

UNIVERSITY OF WOLLONGONG

DOCTORAL THESIS

Thesis Title

Author:

Supervisors:
Dr. Jenny FISHER

*A thesis submitted in fulfillment of the requirements
for the degree of Doctor of Philosophy*

in the

Centre of Atmospheric Chemistry
Chemistry Department

December 12, 2018

Declaration of Authorship

I, Jesse GREENSLADE, declare that this thesis titled, "Thesis Title" and the work presented in it are my own. I confirm that:

- This work was done wholly or mainly while in candidature for a research degree at this University.
- Where any part of this thesis has previously been submitted for a degree or any other qualification at this University or any other institution, this has been clearly stated.
- Where I have consulted the published work of others, this is always clearly attributed.
- Where I have quoted from the work of others, the source is always given. With the exception of such quotations, this thesis is entirely my own work.
- I have acknowledged all main sources of help.
- Where the thesis is based on work done by myself jointly with others, I have made clear exactly what was done by others and what I have contributed myself.

Signed:

Date:

“Thanks to my solid academic training, today I can write hundreds of words on virtually any topic without possessing a shred of information, which is how I got a good job in journalism.”

Dave Barry

Contents

Declaration of Authorship	iii
Abstract	viii
Acknowledgements	ix
1 Introduction and Literature Review	1
1.1 The atmosphere	1
1.1.1 Structure	2
1.1.2 Composition and chemistry	3
1.1.3 Radiative Forcing	3
1.2 Ozone	4
1.2.1 Stratospheric ozone	4
1.2.2 Tropospheric ozone	7
1.2.3 Stratosphere to troposphere transport	9
1.2.4 Chemical production	10
1.3 Volatile Organic Compounds	11
1.3.1 Emissions	13
1.3.2 Isoprene	14
1.3.3 Isoprene chemistry	15
1.3.3.1 Oxidation	15
1.3.3.2 High NO _x pathway	17
1.3.3.3 Low NO _x pathway	18
1.3.3.4 Night time processes	19
1.4 Formaldehyde	19
1.4.1 Sources and sinks	19
1.4.2 Measurement techniques	21
1.4.2.1 Satellite measurements	22
1.5 Atmospheric Chemistry Modelling	23
1.5.1 Box models	23
1.5.2 Chemical transport models	24
1.5.3 Emissions	25
1.5.4 Uncertainties	26
1.5.4.1 Emissions Inventories	26
1.5.4.2 Resolution	27
1.5.4.3 Chemistry mechanisms	27
1.5.4.4 Clouds	28
1.5.4.5 Soil Moisture	28
1.6 Australia and the southern hemisphere	28

1.6.1	Ozone	31
1.6.2	VOCs	31
1.6.3	Measurements	32
1.7	Aims	33
2	Data and Modelling	35
2.1	Introduction	35
2.2	Datasets	36
2.2.1	Satellite	36
2.2.1.1	Formaldehyde	37
2.2.1.2	Nitrogen dioxide	37
2.2.1.3	Aerosol optical depth	38
2.2.1.4	Active fires	40
2.2.1.5	Carbon monoxide	40
2.2.1.6	Uncertainties	40
2.2.2	Model datasets	41
2.2.2.1	GEOS-Chem output	41
2.2.2.2	Meteorological reanalysis	41
2.2.2.3	Surface temperatures	41
2.2.3	Campaign datasets	41
2.2.3.1	Measurements of Urban, Marine and Biogenic Air (MUMBA)	42
2.2.3.2	Sydney Particle Studies (SPS1, SPS2)	45
2.2.3.3	Ozonesondes	45
2.2.3.4	Uncertainties	47
2.3	Satellite formaldehyde	47
2.3.1	Pixel filtering	49
2.3.2	DOAS	51
2.3.3	Air mass factor (AMF)	52
2.3.4	LIDORT	53
2.3.5	Uncertainty	53
2.4	GEOS-Chem	55
2.4.1	Overview	55
2.4.2	Installing and running GEOS-Chem	56
2.4.3	Chemical Mechanism	56
2.4.4	GEOS-Chem isoprene	58
2.4.5	Emissions from MEGAN	59
2.4.6	Rescaling NO _x	61
2.4.7	GEOS-Chem simulations	72
2.4.7.1	GEOS-Chem outputs	72
2.4.7.2	GEOS-Chem runs	73
2.4.7.3	UCX vs tropchem	74
2.4.8	Comparisons with campaign data	81
2.5	Calculating an AMF	82
2.6	Recalculation of OMI HCHO	84
2.6.1	Outline	85
2.6.2	Creating new shape factors	86
2.6.3	Reading satellite data	88

2.6.4	Creating the new AMF	88
2.6.5	Recalculating the AMF using PP code	89
2.6.6	Vertical columns from AMF	90
2.6.7	Reference sector correction	90
2.6.8	Binning the results daily	94
2.6.9	Difference between new and old OMI HCHO columns	95
2.7	Filtering Data	95
2.7.1	Fire and smoke	98
	2.7.1.1 Checking that fire masks are influencing pyrogenic HCHO	103
2.7.2	NO _x	110
2.8	Data Access	110
3	Biogenic Isoprene emissions in Australia	119
3.1	Introduction	119
3.1.1	Aims	120
3.1.2	Top-down isoprene emissions estimates	120
3.1.2.1	Bayesian	121
3.1.2.2	Linear	122
3.1.3	MEGAN emission model	124
3.1.4	satellite measurements	124
3.2	Methods	125
3.2.1	Outline	125
3.2.2	Masks and reprocessed satellite HCHO	126
3.2.3	Calculating modelled slope	128
3.2.4	Calculation of Emissions	133
3.2.5	Accounting for smearing	133
3.2.5.1	Calculation of smearing	135
3.2.5.2	Sensitivity to smearing	136
3.2.5.3	Smearing length scale	138
3.2.5.4	NO _x dependence	140
3.2.6	Running GEOS-Chem using a posteriori emissions	140
3.3	Results	143
3.3.1	HCHO Products and yield	143
3.3.2	Emissions comparisons	143
3.3.3	Comparison with measurements	148
3.4	Uncertainty	154
3.4.1	Summary	154
3.4.2	Top down emissions	154
3.4.3	Model Uncertainty	156
3.4.4	Satellite Uncertainty	156
3.4.4.1	OMI Retrieval	157
3.4.4.2	Satellite vertical column recalculation	157
3.4.5	Fire Filtering	158
3.5	Conclusions and implications	158
3.5.1	Effects from scaling emissions	158
3.5.1.1	HCHO levels	158
3.5.1.2	Ozone levels	160

4 Stratospheric ozone intrusions	159
4.1 Introduction	159
4.2 Data and Methods	161
4.2.1 Ozonesonde record in the Southern Ocean	161
4.2.2 Model description	164
4.2.3 Characterisation of STT events and associated fluxes	165
4.2.4 Biomass burning influence	167
4.2.5 Classifying synoptic conditions during STT events	168
4.3 STT event climatologies	168
4.4 Simulated ozone columns	172
4.5 Stratosphere-to-troposphere ozone flux from STT events	176
4.5.1 Method	176
4.5.2 Results	178
4.5.3 Comparison to literature	178
4.6 Sensitivities and limitations	183
4.6.1 Event detection	183
4.6.2 Flux calculations	184
4.7 Conclusions	185
4.8 Contributions and Acknowledgements	186
5 Conclusions	187
5.1 Ozone over Australia	187
5.2 Isoprene link to ozone	187
5.3 Current trends	187
5.4 Potential future work	187
A Supplementary Notes	189
A.1 Measurement Techniques	189
A.1.1 MAX-DOAS	189
A.2 Data sets	189
A.2.1 SPEI	189
A.2.2 GOME	191
A.2.3 NPI	191
A.3 Chemistry	191
A.3.0.1 SOA	191
A.3.1 Relationship to Glyoxyl TODO: remove if never used	195
A.4 CAABA/MECCA	195
A.4.0.1 CAABA/MECCA outputs	196
A.4.1 CAABA/MECCA Box model: isoprene source classifications	196
A.5 Satellite Stuff	198
A.5.1 OMI Algorithm BOAS	198
A.5.2 AMF recaulcation using 72 level output	199
A.5.3 Old Fire Product MYD14C8H	201
A.6 Modelling	201
A.6.1 Emissions drivers	201
A.7 Campaigns	202
A.7.1 Daintree	202

B Appendix A	205
B.1 Grid Resolution	205
C Frequently Asked Questions	207
C.1 How do I change the colors of links?	207
Bibliography	209

Chapter 2

Data and Modelling

2.1 Introduction

In this thesis the word model is most often used to represent a chemical transport model (CTM), which simulates chemistry and chemical transport through the atmosphere. Models of the atmosphere can be used to interpret measurements, estimate chemical concentrations at any scale, and predict atmospheric composition in the future. In remote sensing measurements, modelling is required in order to produce useful outputs. Models of ozone in the atmosphere are used broadly for international assessments of ozone precursor emissions, and estimating effects from related processes (such as radiation) (Young et al. 2017). Models provide an estimate of many trace gas concentrations, however verification is required, and generally performed using results from measurement campaigns. In situ measurements from campaigns or measurement stations can be used to examine what is happening at a particular location. These data are used to determine how accurate models or estimates are - however the utility is limited to where and when the measurements took place. In this thesis data from several campaigns are compared against model outputs and satellite datasets. Satellite datasets provide large amounts of data over most of the planet. However, they can have high uncertainty due to instrument limitations. Many datapoints can be averaged in order to reduce uncertainty. In this chapter several satellite datasets are combined to estimate biogenic HCHO amounts over Australia.

The first goal is to analyse Australia-specific HCHO concentrations measured by satellite, and determine isoprene sensitivity and any model bias. This leads into chapter 3 where biogenic HCHO columns are used to estimate isoprene emissions. The second goal is to quantify ozone transported from the stratosphere down into the troposphere (Chapter 4). The focus in this chapter is to describe and analyse model outputs and measurements along with how they are recalculated and compared. Section 2.2 details satellite and campaign datasets, and additionally describes model outputs. Measurement techniques used to retrieve the most utilised satellite dataset are outlined in Section 2.3. Section 2.4 describes the GEOS-Chem model, how it is run and what setup and outputs are used in this thesis. In Section 2.5 the process of using model outputs to recalculate satellite vertical columns is defined and analysed. In order to compare satellite data with other datasets, some work must be undertaken to avoid introducing bias (e.g., Palmer et al. 2001; Eskes and Boersma 2003; Marais et al. 2012; Lamsal et al. 2014). One key step is to recalculate the satellite information using modelled data, detailed in section 2.6. The effects of these recalculations

on satellite HCHO is also examined. The creation and effects of filters used to remove non-biogenic influences are described in section 2.7.

2.2 Datasets

This section describes the datasets used in this thesis, along with an overview of the measurement techniques used for each. This includes modelled output, satellite measurements, and measurement campaigns. These datasets serve four purposes:

1. Model output validation in this chapter
2. Calculation of biogenic HCHO distribution over Australia in this chapter
3. Recalculated OMI formaldehyde columns are used as a basis for estimating isoprene emissions in Chapter 3
4. Extrapolation of ozone transport in chapter 4

I will also give details on filtering and interpolations which are undertaken when reading data, as each dataset has its own resolution. While I have not made any measurements myself, it is important to understand the techniques used in datasets I have utilised in order to understand possible anomalous datapoints or trends.

Uncertainty (or error) is present in each dataset and where possible the causes are explained. There are two types of error: systematic and random. Arguably the worst of these is systematic error (or bias). Bias normally indicates a problem in calculation or instrumentation. If the systematic error is known, it can be corrected for by either offsetting data in the opposite direction, or else fixing the cause. A proper fix can only be performed if the sources of error are known and there is a way of correcting or bypassing it. Random error is often reported as some function of a datasets variance, or uncertainty. It can be reduced through averaging either spatially or temporally. Temporal and/or spatial averaging decreases uncertainty by a factor of $1/\sqrt{N}$ where N is the number of observations being averaged.

2.2.1 Satellite

Satellite data products are generally classed into several categories, level 0 through to level 3. Level 0 products are sensor counts and orbital swath data, level 1B data calibrates and geo-locates the level 0 data. Level 2 products additionally have temporal, spatial, solar, and viewing geometry information, as well as quality flags. To create level 2 data slant column density is determined and then translated into vertical column density. Level 3 data is a temporally aggregated subset of level 2 data, for instance monthly or yearly averages.

Satellites record near nadir (vertical) reflected spectra between around 250-700 nm split into spectral components at around 0.3 nm in order to calculate trace gases including O₃, NO₂, and HCHO (e.g., Leue et al. 2001). Satellite measurements are generally performed using spectral fitting followed by conversion to vertical column densities. Several public data servers are available which include products from satellites, including NASAs Earthdata portal (<https://earthdata.nasa.gov/>) and the Belgian

Institute for Space Aeronomy (IASB-BIRA) Aeronomie site (<http://h2co.aeronomie.be/>).

Rayleigh and Mie scattering describe two kinds of particle effects on radiation passing through a medium. Rayleigh scattering is heavily wavelength dependent, and is the dominant form of scattering from particles up to roughly one tenth of the wavelength of the scattered light. Mie scattering more generally involves larger particles, and has less wavelength dependence. The effects of scattering are what gives us the information about substances in the atmosphere. The different particles and gases in the air have measurable properties seen by remote sensing devices such as a satellite. Although instruments will be more or less sensitive to various properties depending on altitude, radiation, and other parameters (e.g., Martin et al. 2002b).

Difficulties can arise when aerosols interfere with recorded spectra (e.g., clouds, smoke, dust), however some of these can be detected and filtered out. Instruments including MODIS on board the Aqua and Terra satellites are able to determine aerosol optical depth (AOD), a measure of atmospheric scatter and absorbance. An AOD under 0.05 indicates a clear sky, while values of 1 or greater indicate increasingly hazy conditions. This is important in order to determine where measurements from other instruments may be compromised by high interference. Cloud filtering is performed on several satellite products used in this thesis, due to the uncertainty introduced by cloud interference. This has been seen to introduce a clear-sky bias in monthly averages since measurements do not include cloudy days (Surl, Palmer, and Abad 2018).

Satellite measured AOD requires validation by more accurate ground based instruments like those of AERONET which uses more than 200 sun photometers scattered globally. Soon much more satellite data will be available in the form of geostationary satellite measurements (Kwon et al. 2017). Geostationary satellites can provide temporally rich measurements over an area, as they are not sweeping around the earth but fixed relative to one latitude and longitude.

2.2.1.1 Formaldehyde

OMI spectra are used in several products used in this thesis, including OMHCHO, OMNO2d, and OMAERUVd. Satellite based formaldehyde measurements from the OMI instrument on board AURA are stored in the OMHCHO product. OMHCHO data is used and modified extensively throughout this thesis, and so is discussed in more detail in Section 2.3. Calculation of column density and AMF are discussed respectively in sections 2.3.2 and 2.3.3.

2.2.1.2 Nitrogen dioxide

OMNO2d is a gridded daily level three NO₂ product with good satellite pixels averaged into 0.25x0.25° horizontally resolved bins. An example figure from Jan 29, 2005 is shown in figure 2.1, while an average for 2005 (global) is shown in figure 2.2. OMNO2 pixel resolution is 40 km by 130 km. NO₂ measured by OMI is used to check whether NO₂ is well represented by GEOS-Chem (see section 2.4.6 for the comparison between this product and GEOS-Chem calculations). It is also used to form the anthropogenic influence filter for OMHCHO (See section 2.7.2).

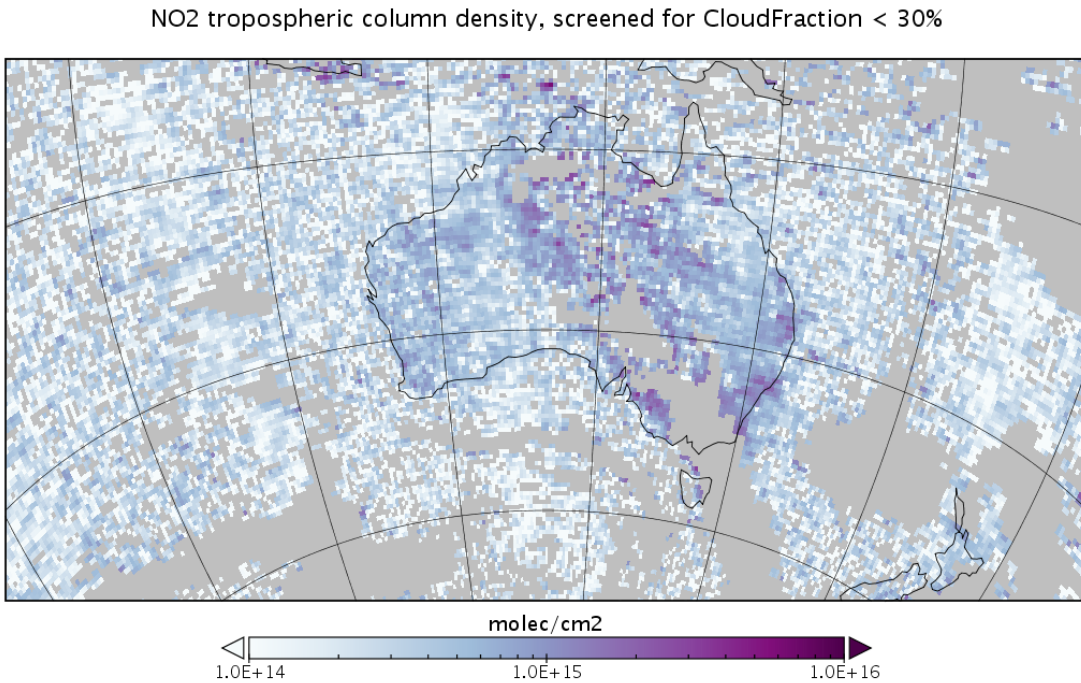


FIGURE 2.1: Example of NO₂ tropospheric columns taken from the OMNO2d product.

Like other satellite products, OMNO2d is influenced by a priori modelling which is required to convert slant path radiance to vertical columns. These models are generally low resolution (~ 110 km by 110 km), which leads to column smearing and difficulty detecting point sources of high NO emissions (Goldberg et al. 2017). Uncertainty in this product arises mostly from the calculation of the AMF (up to 50% of total error) (Lorente et al. 2017).

2.2.1.3 Aerosol optical depth

Aerosols in the atmosphere can be seen through their affects on light. Smoke and dust can be seen as an increase in aerosol optical depth (AOD) (see section 2.3.2). This is due these particles scattering and absorbing UV radiation (Ahn2008). A data product provided by Earthdata (https://disc.gsfc.nasa.gov/datasets/OMAERUVd_V003/summary) called OMAERUVd (DOI: 10.5067/Aura/OMI/DATA3003) is used in this thesis.

OMAERUVd provides a useful dataset which allows detection of areas which may be smoke affected. The product contains AOD and aerosol absorption optical depths (AAOD) at three wavelengths (354, 388, and 500 nm), along with UV aerosol index (UVAI). The OMAERUVd product is level three gridded daily data, based on quality filtered level two swath pixels which are then gridded by averaging. The product is most sensitive to error in the form of sub-pixel scale cloud interference, so I select AAOD as the basis for my smoke filter as it is least affected by clouds (Ahn2008).

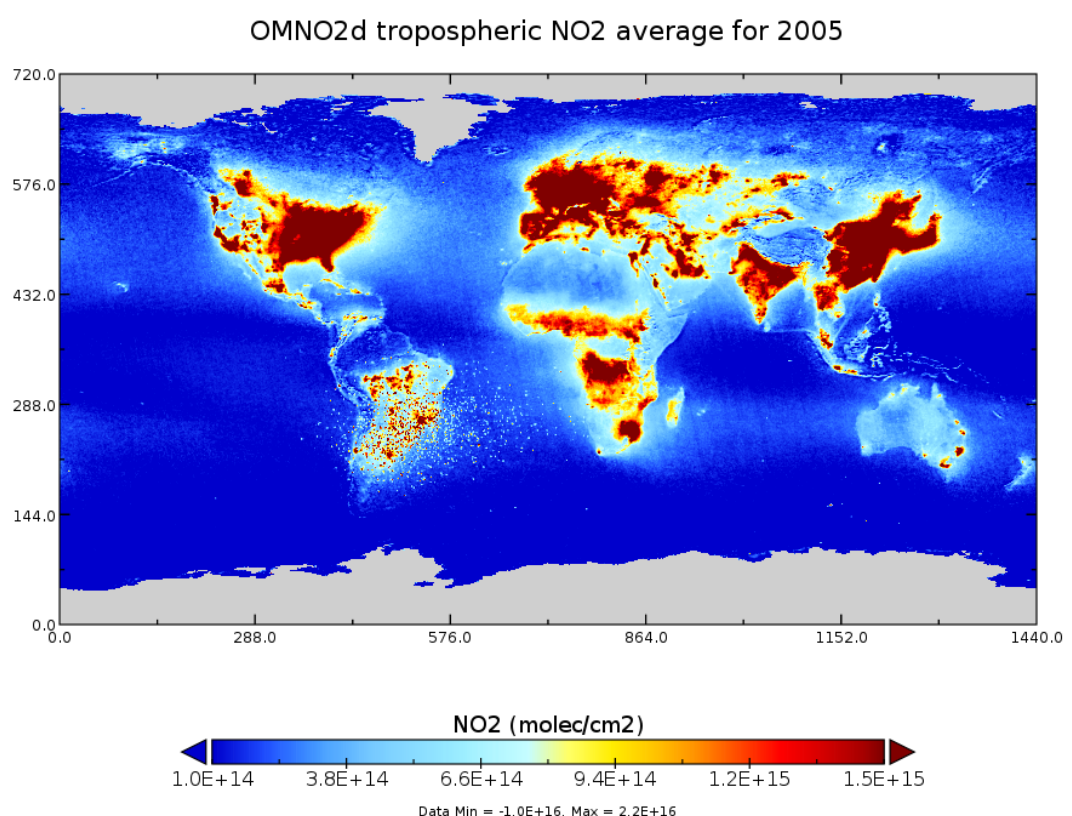


FIGURE 2.2: Average 2005 tropospheric NO₂ from OMNO2d with pixels screened for < 30% cloud cover.

In this work AAOD is mapped from $1 \times 1^\circ$ horizontal resolution to $0.25 \times 0.3125^\circ$ using nearest value mapping. The AAOD at 500 nm wavelength is used to determine smoke influence, although any of the provided wavelengths would be affected by smoke plumes and could also be used. This daily AAOD is compared to a threshold to create a daily smoke filter, any areas with $\text{AAOD} > 0.03$ are considered to be potentially smoke plume affected (see section 2.7.1).

2.2.1.4 Active fires

MOD14A1 is a gridded daily satellite based dataset of fire counts at $1 \times 1 \text{ km}^2$ horizontal resolution. Fire observations are performed four times daily from Terra (10:30 LT, 22:30 LT) and Aqua (01:30 LT, 13:30 LT). The fire pixels are detected based on parameters including apparent pixel temperature and the nearby background temperature. The dataset is obtained from NASA Earth Observations (NEO) that is part of the EOS Project Science Office at the NASA Goddard Space Flight Center https://neo.sci.gsfc.nasa.gov/view.php?datasetId=MOD14A1_M_FIRE. This product is downloaded and binned into a lower resolution (using the sum of fire pixels) to create an active fire influence mask (see section 2.7.1).

2.2.1.5 Carbon monoxide

In chapter 4, potential biomass burning plumes are identified using satellite observations of CO from the AIRS (Atmospheric Infra-red Sounder) instrument aboard the Aqua satellite (Texeira 2013). CO is used as a proxy for biomass burning plumes, and used to qualitatively attribute ozone intrusion events as explained in section 4.2.5. This is a separate method of detecting fire influence near specific sites through visual analysis.

2.2.1.6 Uncertainties

While satellite data is effective at covering huge areas (the entire earth) it only exists at a particular time of day, is subject to cloud cover, and generally does not have fine horizontal or vertical resolution. Concentrations retrieved by satellites have large uncertainties, which arise in the process of transforming spectra into total column measurements, as well as instrument degradation (satellite instruments are hard to tinker with once they are launched). Uncertainty in transforming satellite spectra comes from a range of things, including measurement difficulties introduced by clouds, and instrument sensitivity to particular aerosols (Millet et al. 2006). Many products require analysis of cloud and aerosol properties in order to estimate concentration or total column amounts (Palmer et al. 2001; Palmer 2003; Marais et al. 2012; Vasilkov et al. 2017). The main source of error in satellite retrievals of HCHO are due to instrument detection sensitivities, and calculation of the air mass factor (AMF) which converts slanted light path concentrations into a vertical profile (Millet et al. 2006). Calculations of the AMF performed by different groups tend to agree fairly well, as long as all the a priori and ancillary data is similar. Large differences can occur depending on the a priori vertical profile, trace gas concentrations, and cloud properties (Lorente et al. 2017). Choice of RTM and interpolation operations have a relatively small affect compared

to the assumed state of the atmosphere, with high structural uncertainty introduced at this stage of AMF calculation - as shown in Lorente et al. (2017).

A common way of reducing satellite uncertainty is through oversampling or temporal averaging. This is done frequently for trace gases (which are often near to the detection limit over much of the globe). For example: Vigouroux et al. (2009) reduce the measurement uncertainty (in SCIAMACHY HCHO columns) by at least a factor of 4 through averaging daily over roughly 500km around Saint-Denis, and only using days with at least 20 good measurements. Another example of this can be seen in Dufour et al. (2008), where monthly averaging is used to decrease the measurements uncertainty at the cost of temporal resolution.

In cloudy, hazy or polluted areas measurements are more difficult to analyse (e.g., Palmer 2003; Marais et al. 2014). Recent work by Vasilkov et al. (2017) showed that updating how the surface reflectivity is incorporated into satellite measurements can change the retrievals by 50 % in polluted areas.

2.2.2 Model datasets

2.2.2.1 GEOS-Chem output

GEOS-Chem model output is used extensively in this thesis and is discussed in more detail in section 2.4. Section 2.4.7.1 specifically describes the model outputs used in this thesis. These are generally resolved to 47 vertical levels from the ground up to 0.01 hPa, at 2x2.5°horizontal resolution.

2.2.2.2 Meteorological reanalysis

Synoptic scale weather patterns are taken from the European Centre for Medium-range Weather Forecasts (ECMWF) Interim Reanalysis (ERA-I) (Dee et al. 2011). These are used in chapter 4 to determine typical weather systems for stratospheric ozone intrusions. The version used was ERA-Interim, which was the most up to date at the time (2016) but has since been superseded by ERA5.

2.2.2.3 Surface temperatures

The Climate Prediction Center (CPC) provides a product with maximum daily land-surface temperature at 0.5x0.5°horizontal resolution. This data is used to check the correlation between HCHO and temperature at a higher resolution than is provided by GEOS-Chem output. A full description of the data can be found at <https://www.esrl.noaa.gov/psd/data/gridded/data.cpc.globaltemp.html>. CPC Global Temperature data is provided by the NOAA/OAR/ESRL PSD, Boulder, Colorado, USA, from their web site at <https://www.esrl.noaa.gov/psd/>. An example of one day of land temperature output is shown in figure 2.3.

2.2.3 Campaign datasets

In this thesis data from several measurement campaigns are used to examine accuracy of modelled data at specific sites. Figure 2.4 shows the locations of BVOC measurement sites in the top panel, and release sites for ozonesondes in the bottom panel.

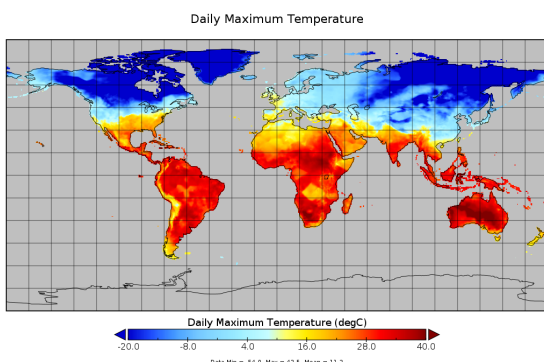


FIGURE 2.3: CPC daily maximum temperature dataset output for 1, Jan, 2005.

TABLE 2.1: Detection limits for MUMBA

Dates	HCHO (ppb)	Isoprene (ppb)	Ozone (ppb)
21/Dec/2012 - 29/Dec/2012	0.205	0.003	0.5
29/Dec/2012 - 18/Jan/2013	0.105	0.005	0.5
19/Jan/2013 - 15/Feb/2013	0.186	0.003	0.5

These took place over disparate times, and are in situ measurements which are hard to directly compare against GEOS-Chem output which is averaged over a large horizontal space.

The campaign datasets provide three separate time series for brief periods of both isoprene and formaldehyde. Figure 2.5 shows these along with the detection limits and also shows isoprene measurements superimposed over a single year. It is apparent that more measurements are required to see more than the daily cycles.

2.2.3.1 Measurements of Urban, Marine and Biogenic Air (MUMBA)

The MUMBA campaign (Paton-Walsh et al. 2017) measured various compound abundances including isoprene, formaldehyde, and ozone from 21 December 2012 to 15 February 2013. These measurements took place in Wollongong, 10 m above ground level (40 m above sea level). Ozone was measured by Thermo UV absorption with 1-minute time resolution averaged into hourly outputs. Isoprene and HCHO were measured by Ionicon Proton-Transfer-Reaction Mass spectrometer (PTR-MS), with a time resolution of 3-minutes, averaged each hour. Detection limits varied due to instrument conditions, and are listed in table 2.1. The full dataset has been published on PANGAEA (DOI:10.1594/PANGAEA.871982) (Guérette et al. 2018).

In this thesis we assume uncertainty in this product is as estimated by Dunne et al. (2018) at (50%). Although the uncertainty determined through calibration measurements was only 15% (Guérette et al. 2018), this does not account for competing trace gas interference (such as furan). The readings are re-sampled to hourly averages. Measurements below the detection limit are set to half of the detection limit when reading this dataset.



FIGURE 2.4: Locations of VOC measurements (top panel) and ozonesonde release sites (bottom panel). Inlaid in top panel is the flight paths over Australia of the HIPPO campaign.

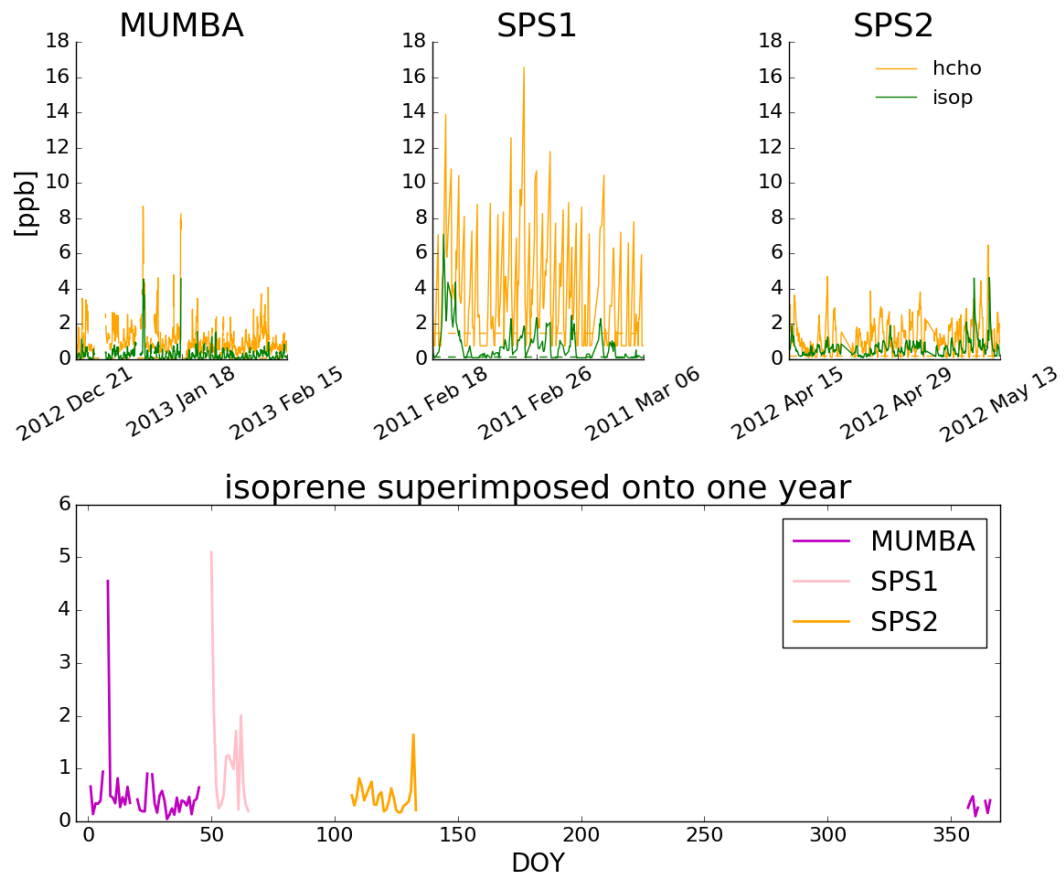


FIGURE 2.5: Top: MUMBA, SPS1, and SPS2 time-series for HCHO (orange) and isoprene (magenta), along with detection limits (dashed).
Bottom: isoprene measurements superimposed onto a single year.

2.2.3.2 Sydney Particle Studies (SPS1, SPS2)

Two trace gas measurement campaigns took place at the Westmead air quality station. Stage 1 (SPS1) from 5 February to 7 March, 2011 and stage 2 (SPS2) from 16 April to 14 May, 2012. Two instruments measured VOC concentrations: a PTR-MS, and a gas chromatographer (GC) with a flame ionisation detector (FID). The PTR-MS uses chemical ionisation mass spectrometry and can quantify VOCs at high temporal resolution (< 1 s). It was calibrated several times per day against HCHO, isoprene, α -pinene, and several other VOCs, further measurement specifics can be found in Dunne et al. (2018).

The output lists hourly averaged ppbv concentrations of trace gases based on the mass to charge ratio (m/z), which for isoprene is 69. It is possible that other chemicals (such as furan, with the same m/z) interfered with this value, especially at low ambient isoprene concentrations and towards the end of autumn (SPS2) when wood fires start to become frequent (Guérette et al. 2018). The GC-FID analysed samples collected in multi-absorbent tubes, with lower temporal resolution but no interference. Further details for this method can be found in Cheng et al. (“Factors controlling volatile organic compounds in dwellings in Melbourne, Australia”). GC-FID data is averaged from 0500-1000 LT, and 1100-1900 LT, while PTR-MS data is averaged hourly. This includes significant differences between measurement devices when detecting isoprene, potentially due to interfering compounds in the PTR-MS (Dunne et al. 2018).

Figure 2.6 shows isoprene and formaldehyde over the course of these two campaigns, as well as the detection limits (dashed lines), as measured by PTR-MS. In order to compare with GEOS-Chem output (see section 2.4) a daily average and an midday time (13:00-14:00 LT) average are both created from these data. In averaging, any measurements below the machine detection limit are set to half of the detection limit, as done in Lawson et al. (2015). This should minimise any introduced bias.

2.2.3.3 Ozonesondes

Ozonesonde data come from the World Ozone and Ultraviolet Data Centre (WOUDC). Ozonesondes are weather balloons which measure from the surface to around 35km. Ozonesondes provide a high vertical resolution profile of ozone, temperature, pressure, and humidity. Generally the instrument will perform 150-300 measurements in the troposphere with ozone mixing ratios quantified by an electrochemical concentration cell (<http://www.ndsc.ncep.noaa.gov/organize/protocols/appendix5/>).

Ozonesondes are launched approximately weekly from Melbourne (38° S, 145° E), Macquarie Island (55° S, 159° E) and Davis (69° S, 78° E). Melbourne, a major city with more than 4 million residents (ABS 2013), may be affected by anthropogenic pollution in the lower troposphere. Actual releases are north of the central business district in the Broadmeadows suburb. Macquarie Island is in the remote Southern Ocean and unlikely to be affected by any local pollution events. Davis (on the coast of Antarctica) is also unlikely to experience the effects of anthropogenic pollution. More information on this dataset is given in section 4.2.

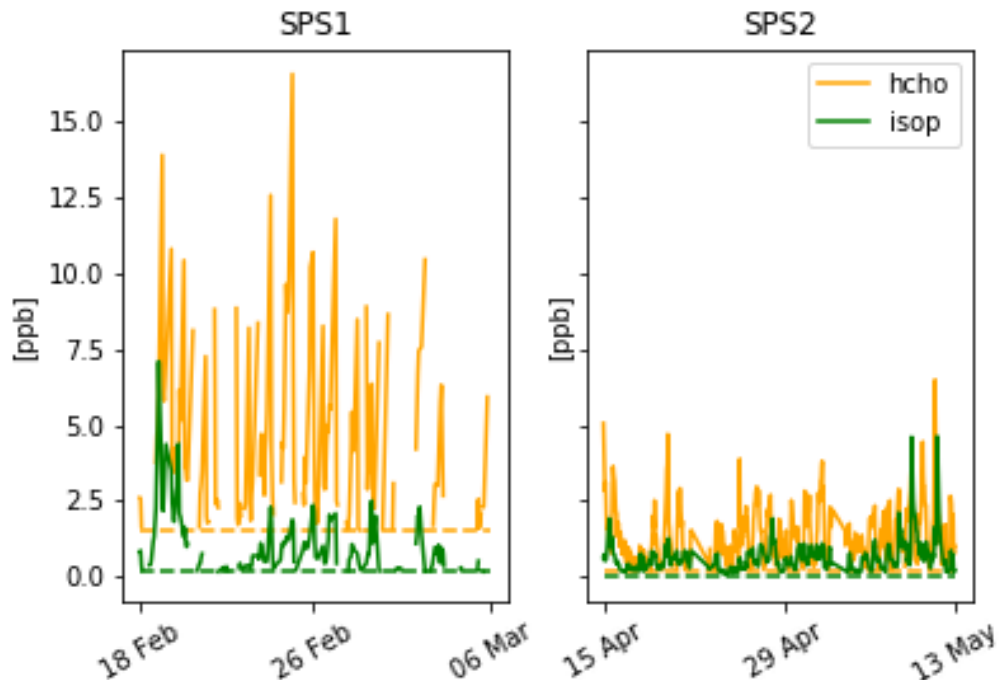


FIGURE 2.6: SPS HCHO (yellow) and isoprene (green) time series, along with detection limits (dashed). SPS 1 (left) took place in late summer 2011, while SPS 2 (right) occurred during autumn 2012.

2.2.3.4 Uncertainties

In situ measurements contain errors, and depending on the device used and chemical being measured this error can be significant. The major sources of uncertainty in measurement techniques included interference from non-target compounds and under-reporting (e.g., Dunne et al. 2018; Guérette et al. 2018). Overall isoprene uncertainty in measurements analysed by Dunne et al. (2018) was a factor of 1.5 to 2. This can feed into uncertainties in modelling and satellite retrievals, as verification and correlations are affected.

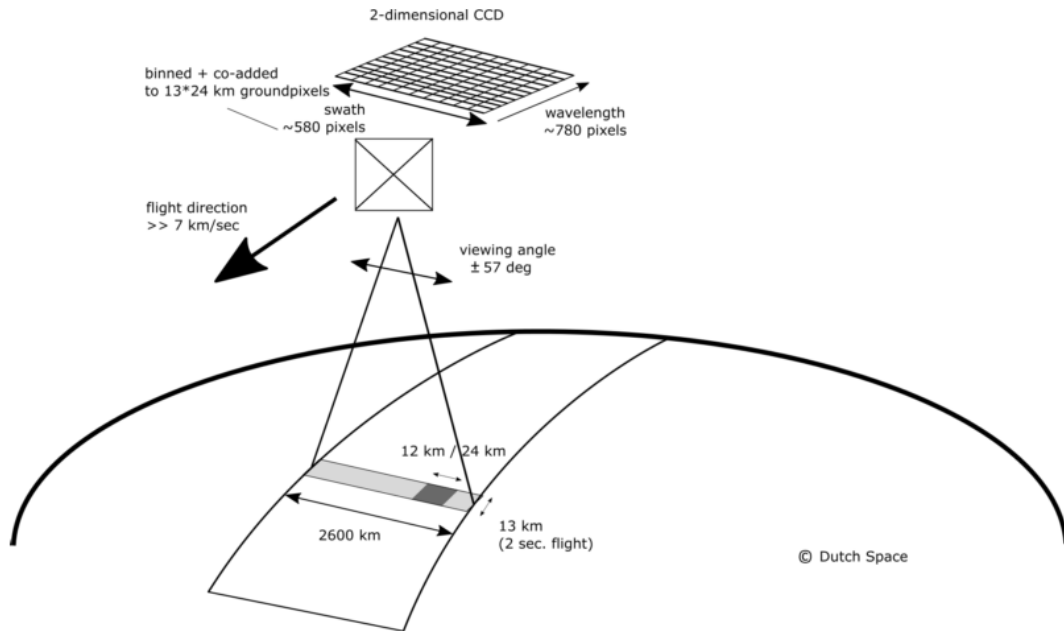
2.3 Satellite formaldehyde

One satellite product used extensively in this thesis is named OMHCHO: from NASA's Earth Observing System's "Aura", which provides several other useful datasets (products). Aura orbits the earth in a polar sun-synchronous pattern, circling the earth on a plane coincident with the sun and the poles. Aura houses the Ozone Monitoring Instrument (OMI), a near-UV/Visible Charged Coupled Device (CCD) spectrometer. The OMI instrument on board AURA has been active since July 2005, it records spectra from 264-504 nm using an array of 60 detectors with mid-resolution (0.4-0.6 nm). This band of wavelengths allows measurements of trace gases (among other quantities) and the formaldehyde product is detailed here.

From here on the word pixel is used to describe one data point retrieved by OMI, each pixel includes a latitude and longitude within OMI's data product. Figure 2.7 shows the details of OMI's detector array and measurement resolutions. OMI measures atmospheric trace gases including NO₂, SO₂, BrO, HCHO, O₃, and aerosols. OMI measurements occur from right to left on a band covering 115°, resulting in swaths of around 2600 km, with pixel sizes from 13x24 km² at nadir to 26x135 km² at the swath edges (Gonzalez Abad et al. 2015). The swaths cover Earth daily, both on the light and dark side of the planet, only daytime measurements provide useful near-UV/Visible information.

The latest OMHCHO algorithm uses a shape factor determined from GEOS-Chem using 47 vertical levels at monthly temporal resolution and 2° latitude by 2.5° longitude horizontal resolution (Gonzalez Abad et al. 2015). The GEOS-Chem model has been substantially updated since then. In this thesis the more recent version V10.01 is used to recalculate the vertical column HCHO (details are shown in section 2.6).

OMI uses a Differential Optical Absorption Spectroscopy (DOAS) based technique to read HCHO along the path of light which reaches the satellite instrument. The first step is to determine how much HCHO is in the path of light between the sun and detector. Measurements done using DOAS often apply a forward radiative transfer model (RTM) such as LIDORT (see section 2.3.4) in order to determine a trace gas' radiative properties at various altitudes. The forward RTM used for satellite data products also involve functions representing extinction from Mie and Rayleigh scattering, and the effect of these on spectra. These RTM are also required to account for (often estimated) atmospheric parameters such as albedo. The next step is to transform the calculated amounts along the non-vertical light path into vertical column amounts. This is done by applying an AMF. In the absence of atmospheric scattering a simple



Channel	Wavelength range	Spectral resolution	Spectral sampling	Ground pixel size
UV1	264–311 nm	0.63 nm = 1.9 px	0.33 nm px ⁻¹	13 × 48 km
UV2	307–383 nm	0.42 nm = 3.0 px	0.14 nm px ⁻¹	13 × 24 km
VIS	349–504 nm	0.63 nm = 3.0 px	0.21 nm px ⁻¹	13 × 24 km

FIGURE 2.7: Figure 1 and Table 1 from Schenkeveld et al. (2017), with the following caption “An impression of OMI flying over the Earth. The spectrum of a ground pixel is projected on the wavelength dimension of the charge-coupled device (CCD; the columns). The cross-track ground pixels are projected on the swath dimension of the CCD (the rows). The forward speed of 7 kms^{-1} and an exposure time of 2 s lead to a ground pixel size of 13 km in the flight direction. The viewing angle of 114° leads to a swath width on the ground of 2600 km.” The table shows the optical properties for OMIs three channels.

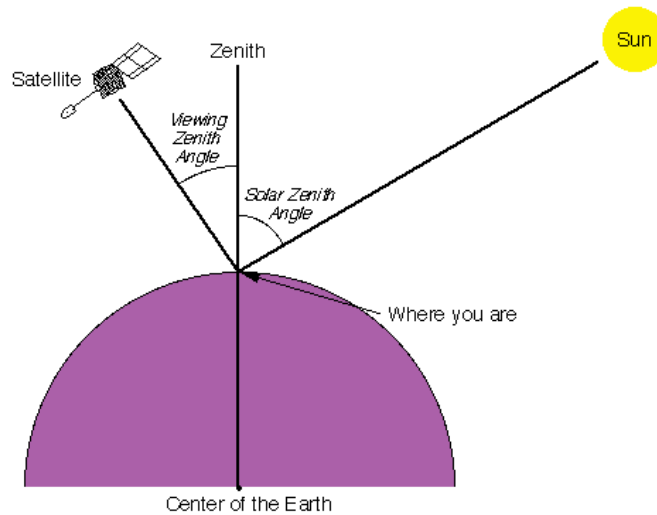


FIGURE 2.8: Solar and viewing zenith angles, image copied from Wikipedia (2016), originally from a NASA website.

geometric AMF can be defined as a function of the solar zenith angle. The solar zenith angle (θ_s) and the satellite viewing angle (θ_v) are shown in image 2.8. However, in the UV-VIS region of the spectrum, Rayleigh and Mie scattering (see section 2.3.2) must be accounted for.

Atmospheric HCHO detected by satellite requires that other trace gases with similar features near the HCHO affected wavelengths are accounted for. A DOAS fit determines the total column amount of a trace gas along the path that the instrument views. This uses the Beer-Lambert law where radiance is reduced as light travels through a medium. I use the NASA OMHCHOv003 data product (Gonzalez Abad et al. 2015), with HCHO determined using the spectral window 328.5 nm–356.5 nm. The algorithm used is based on direct fitting of radiances, and accounts for competing absorbers, under-sampling, and Ring effects. An OMI radiance measurement over the remote Pacific ocean is used instead of an irradiance measurement. This means that the slant columns (Ω_s) are formed from the spectra differential with respect to the radiance reference column over the Pacific. The full method details for slant column retrieval by OMI are outlined in supplemental section A.5.1, or in the technical document (DOI: 10.5067/Aura/OMI/DATA2015). Slant columns range from $\sim 4 \times 10^{15}$ to $\sim 6 \times 10^{16}$ molec cm^{-2} , with uncertainties from 30% (larger columns) to over 100% (smaller columns) (Gonzalez Abad et al. 2015).

2.3.1 Pixel filtering

This thesis uses the level 2 product swath output from the NASA earth data web portal. OMHCHO level two data includes 14-15 daily swaths of measurements. Each swath contains roughly 9×10^4 pixels, each of which includes latitude, longitude vertical column HCHO, along with all the ancillary data required to make the vertical column and several data quality metrics. The OMHCHO dataset has a quality flag

TABLE 2.2: OMI quality flag values table from Kurosu and Chance (2014)

Value	Classification	Rational
0	Good	Column value present and passes all quality checks; data may be used with confidence.
1	Suspect	Caution advised because one or more of the following conditions are present: <ul style="list-style-type: none"> • Fit convergence flag is < 300 but > 0: Convergence at noise level • Column $+2\sigma$ uncertainty $< 0 <$ Column $+3\sigma$ uncertainty • Absolute column value $>$ Maximum column amount ($1e19$ molec cm^{-2})
2	Bad	Avoid using as one of the following conditions are present: <ul style="list-style-type: none"> • Fit convergence flag is < 0 : No convergence, abnormal termination • Column $+3\sigma$ uncertainty < 0
< 0	Missing	No column values have been computed; entries are missing

which can be used to remove unlikely or poor satellite measurements. The states represented by this quality flag are shown in table 2.2 which is taken from Kurosu and Chance (2014). Filtering bad or missing measurement pixels is performed prior to any other filtering, this includes the datapoints affected by the row anomaly. This anomaly (`rowanomaly_url`) affects radiance data at particular viewing angles, corresponding to a row on the CCD detectors, and is dynamic over time. The slant columns affected are flagged and removed before any further processing.

Each ~ 90 minutes the AURA satellite sweeps over the sunny side of the planet of which around 50 k – 80 k of the roughly 90 k pixels are classified as good. Each pixel contains several important pieces of data which are needed for recalculation of the HCHO vertical column: the total column of HCHO (Ω ; molec cm^{-2}), cloud fraction, associated shape factor, AMF, geometric AMF, scattering weights and their vertical altitudes (hPa), viewing zenith angle, solar zenith angle, latitude, longitude, OMI sensor track, main data quality flag, cross track flag, and total column uncertainty. All of these data are needed in order to reconstruct the total vertical column using a modelled a priori shape factor rather than NASA's included a priori shape factor. Each pixel includes an estimate of the cloud fraction created using the OMI cloud product OMCLDO2. If greater than 40% of a pixel measurement is cloudy (ie. cloud fraction > 0.4) then the pixel is removed from subsequent analysis. This removes around 30% of the pixels which remain after filtering out the bad or missing data.

One more filter is applied before any calculations, to remove unreasonable column amounts. Due to numerous highly negative vertical columns (beyond what is expected) a screen is applied to remove any pixels with vertical columns outside the range of -5×10^{15} to 1×10^{17} . This has been performed previously in TODO

2.3.2 DOAS

The DOAS technique uses solar radiation absorption spectra to measure trace gases through paths of light. Beer's law states

$$T = I/I_0 = e^{-\tau} \quad (2.1)$$

with T being transmittance, τ being optical depth, and I , I_0 being radiant flux received at instrument and emitted at source respectively. The Beer-Lambert law of extinction allows spectroscopic measurement of absorbing chemical species (absorbers) in the atmosphere:

$$I_B = I_{B_0} e^{-\tau_s} \quad (2.2)$$

where I_B , I_{B_0} is backscattered intensity with and without the absorber respectively, and τ_s is the optical thickness of the absorber along the measured path between source and instrument.

τ can be described using the scattering and absorption cross section area (α , cm²) and density (η , molec cm⁻³) of an absorber as follows:

$$\tau = \int \alpha(s) \eta(s) ds \quad (2.3)$$

τ through a medium is the sum of optical thicknesses of each absorber within the measured path (s) substituting equation 2.3 into equation 2.2 leads to

$$I = I_0 \exp \left(\sum_i \int \eta_i \alpha_i ds \right)$$

Where i represents a chemical species index, and the integral over ds represents integration over the path from light source to instrument.

Another way of describing optical depth (also called optical thickness) is the natural logarithm of the ratio of incident radiant power to transmitted radiant power through a material (from equation 2.2). In the atmosphere we are interested in the optical depth of various chemical species, and we use incoming solar radiation to determine this. The difference between solar radiation at the top of the atmosphere and the earth's surface defines the atmospheric optical depth along the path of observation.

$$\tau = \ln \frac{\phi_e^i}{\phi_e^t}$$

where ϕ_e^i is radiant flux seen at the earth surface, ϕ_e^t is the solar radiant flux which arrives at the top of the atmosphere. In the atmosphere, optical depth can be due to several factors including scattering, chemical absorbance, and aerosols.

2.3.3 Air mass factor (AMF)

To convert the trace gas profile from a reflected solar radiance column (slanted along the light path) into a purely vertical column requires calculations of an air mass factor (AMF). In satellite data, the AMF is typically a scalar value for each horizontal grid point which will equal the ratio of the total vertical column density to the total slant column density. This value requires calculations to account for instrument sensitivities to various wavelengths over resolved altitudes, and is unique for each trace gas under consideration. An AMF characterises measurement sensitivity to a trace gas at various altitudes Palmer et al. 2001, e.g., Lorente et al. (2017) show that AMF calculations can be the largest source of uncertainty in satellite measurements. Another way of describing AMFs are as measures of how radiance at the top of the atmosphere (TOA) changes with trace gas optical depths at specific altitudes (Lorente et al. 2017). Calculation of the AMF is important as it is multiplied against the estimated slant columns in order to give vertical column amounts.

DOAS column retrievals are an integration of a trace gas over the instruments viewing path, in order to convert this total to a vertically distributed column a few assumptions and estimates are required. The vertical profile of a trace gas is assumed or estimated via a CTM, while its scattering and radiative properties are calculated at prescribed altitudes using an RTM. These properties are combined into a single array called the AMF. Two examples of this are GOME-2 (on the MetOp-A satellite) products (http://atmos.caf.dlr.de/gome/product_hcho.html), and OMI products which respectively use LIDORT combined with IMAGESv2 and GEOS-Chem for processing (Instrument 2002; Gonzalez Abad et al. 2015). AMFs are unique to each trace gas and due to their complexity and the influence of cloud cover they remain one of the largest error sources in remote sensing of BVOCs (Palmer et al. 2001; Millet et al. 2006)). Lam-sal et al. (2014) recommends that when comparing satellite data to models, the AMF should first be recalculated using the model as an a priori. This is in order to remove any a priori bias between model and satellite columns.

Related to the AMF is the averaging kernal (AK), which is used to handle instrument measurements which are sensitive to gas concentrations at different altitudes through the atmosphere. DOAS methods can be heavily influenced by the initial estimates of a trace gas profile (the a priori) which is often produced by modelling, so when comparing models of these trace gases to satellite measurements extra care needs to be taken to avoid introducing bias from differing a priori assumptions. One way to remove these a priori influences is through the satellite AK (or AMF), which takes into account the vertical profile of the modelled trace gas and instrument sensitivity to the trace gas (Eskes and Boersma 2003; Palmer et al. 2001). This process is called deconvolution ($\Omega = AK \times VC_{satellite} + \times(I - AK)VC_{apriori}$) of the AK of the satellite instrument. The AK represents sensitivities to each species at multiple altitudes through the atmosphere and in the case of OMI, can be approximated from the scattering weights ($\omega(z)$) function as follows:

$$AK(z) = \frac{\omega(z)}{AMF} \quad (2.4)$$

This is an approximation for the OMI product, which does not include the AK but does include the ω and AMF, as explained in Gonzalez Abad et al. (2015).

2.3.4 LIDORT

LIDORT is a model of LInearized Discrete Ordinate Radiative Transfer, used to determine backscatter intensities and weighting functions at arbitrary elevation angles (Spurr, Kurosu, and Chance 2001). The model solves radiative transfer equations and can be used to determine various atmospheric column measurement attributes such as optical depth, ring effects, and scattering. These radiative properties (or at least estimates thereof) are required when measuring trace gases in the atmosphere through a long path such as seen by satellites (e.g., Palmer et al. 2001; Martin et al. 2002a; De Smedt et al. 2015; Gonzalez Abad et al. 2015).

2.3.5 Uncertainty

Uncertainty in a single pixel for OMHCHO is roughly the same magnitude as HCHO background levels. Each pixel has $\sim 2 \times 10^{14}$ molec cm $^{-2}$ uncertainty, which is 5 \times higher than GOME. However, there are $\sim 100 - 200\times$ as many measurements allowing a greater reduction of uncertainty with averaging. This is due to the smaller footprint and better temporal resolution of OMI (Instrument 2002; Millet et al. 2008). The finer nadir resolution of OMI (13 by 24 km 2) compared to other satellites also reduces cloud influence (Millet et al. 2006; Millet et al. 2008). The top row in figure 2.9 shows OMI HCHO columns binned to at 0.25°longitude by 0.3125°latitude averaged over one day and one month (with and without filtering). Row two shows uncertainty of the satellite data after averaging. It is clear that one day of satellite data is too uncertain when binned at 0.25x0.3125°horizontal resolution, however after a month (with or without filtering) the uncertainties become manageable. If we assume the uncertainty is random error, and not bias introduced through calculation techniques, then we are able to reduce the uncertainty through averaging. High resolution low detection limit estimates can be built up using “oversampling”, which averages satellite measurements over time (e.g., Zhu et al. 2014). Uncertainty in satellite recalculations, along with other factors is analysed in section ??.

In this thesis, HCHO columns (pixels) with cloud fractions over 40% are filtered as done in Palmer et al. (2001), which introduces a clear-sky bias to any monthly averages. This is due to HCHO being lower on unrecorded cloudy days. This bias has been measured as a 13% positive monthly mean bias (Palmer et al. 2001; Surl, Palmer, and Abad 2018).

Recently Schenkeveld et al. (2017) analysed the performance over time of the instrument and found irradiance degradation of 3-8%, changed radiances of 1-2%, and a stable wavelength calibration within 0.005-0.020 nm. These changes are measured excluding the row anomaly (RA) effect, which is relatively stable since 2011, although it is still growing and remains the most serious concern. Their analysis of OMI concludes that data is still of high quality and will deliver useful information for 5-10 more years, with radiance only changing by 1 – 2% outside of RA impacted areas. An analysis of the row anomaly by Huang et al. (2017) state that measurements remain suitable for scientific use, with recommendation for further evaluation. The RA began in June 2007, with some cross-track rows seemingly blocked. The most likely cause is some instrument insulation partially obscuring the radiance port (Schenkeveld et al. 2017).

OMI HCHO and uncertainty for 200501

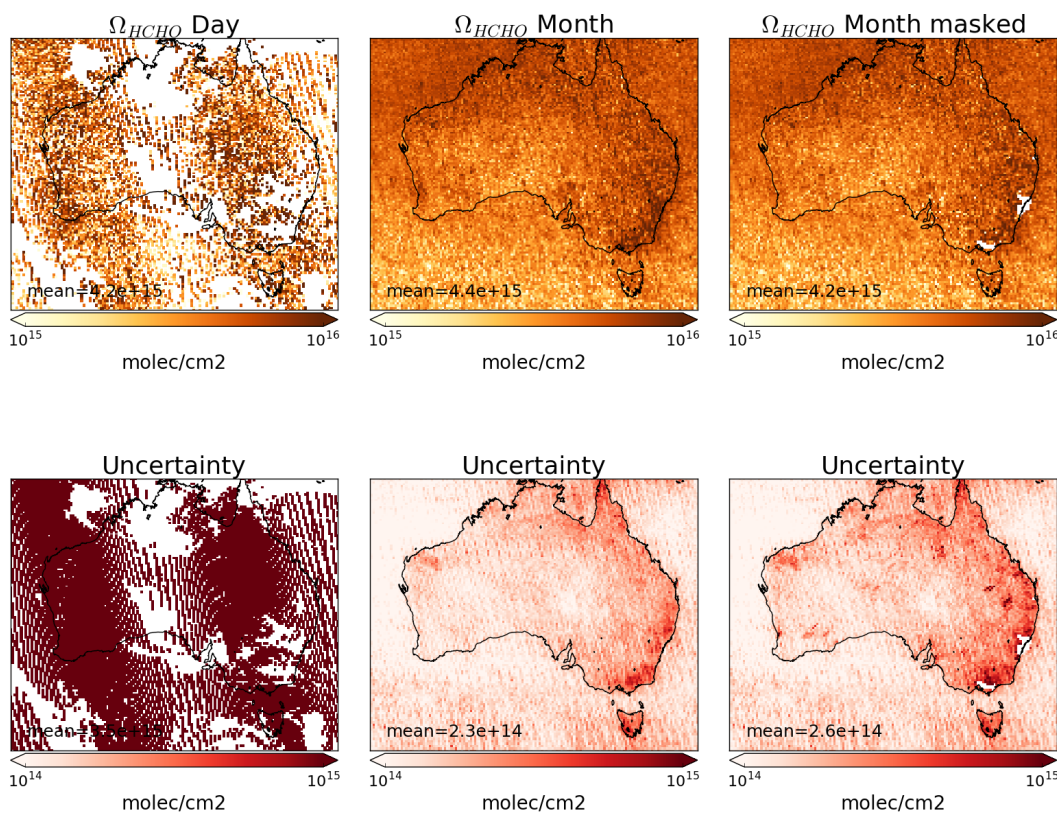


FIGURE 2.9: Top row shows 0.25° by 0.3125° binned OMHCHO columns with one day, one month, and one month with non-biogenic masking applied from left to right respectively. Bottom row shows the uncertainty for each gridsquare after averaging.

In satellite HCHO products, concentrations over the remote pacific ocean are sometimes used to analyse faulty instrument readings. This is due to the expected invariance of HCHO over this region. For instance GOME (an instrument which measures trace gases on board the ERS-2) corrects for an instrument artefact using modelled HCHO over the remote pacific (Shim et al. 2005). OMI HCHO products use a similar technique to account for sensor plate drift and changing bromine sensitivity (Gonzalez Abad et al. 2015). Uncertainty in the OMI satellite instrument is calculated by the Smithsonian Astrophysical Observatory (SAO) group using the uncertainty in backscattered radiation retrievals (Gonzalez Abad et al. 2015; Abad et al. 2016). Another method of calculating the uncertainty is used by the Belgian Institute for Space Aeronomy (BIRA) group, who determine uncertainty from the standard deviation of HCHO over the remote pacific ocean (De Smedt et al. 2012; De Smedt et al. 2015).

For many places the tropospheric column HCHO measured by satellite is biased low, Zhu et al. (2016) examine six available datasets and show a bias of 20 - 51% over south east USA when compared against a campaign of aircraft observations (SEAC⁴RS). De Smedt et al. (2015) also found OMI and GOME2 observations were 20 - 40% lower than ground based vertical profiles, and Barkley et al. (2013) determine OMI to be 37% low compared with aircraft measurements over Guyana. These bias can be corrected by improving the assumed a priori HCHO profiles which are used to calculate the AMFs of the satellite columns. Millet et al. (2006) examine OMI HCHO columns over North America and determine overall uncertainty to be 40%, with most of this coming from cloud interference. Millet et al. (2008) shows that there also exists some latitude based bias, as well as a systematic offset between the OMI and GOME instruments. This does not appear to be due to the different overpass times of the two instruments.

AMF calculation often dominates the total uncertainty in satellite retrievals, especially in polluted regions (Lorente et al. 2017). In scenarios where the gas is enhanced in the lower troposphere, AMF calculation is the largest uncertainty in satellite measurements. In polluted environments the structural uncertainty is estimated at 42 %, or 31 % over unpolluted environments (Lorente et al. 2017). Another impact often not included in uncertainty calculations is the structural uncertainty of retrieval methods. The structural uncertainty of AMF calculation approaches used by different retrieval groups comes from how the AMF is calculated, rather than uncertainty in the calculation components. The importance of a priori and ancillary data (such as surface albedo and cloud top height) sharply affects the structural uncertainty (Lorente et al. 2017).

2.4 GEOS-Chem

2.4.1 Overview

GEOS-Chem is a well supported global, Eulerian CTM (see section 1.5.2) with a state of the science chemical mechanism, with transport driven by meteorological input from the Goddard Earth Observing System (GEOS) of the NASA Global Modeling and Assimilation Office (GMAO). Chemistry, transport, and meteorology are simulated at 15 minute time steps within a global set of 3-D boxes. Emissions are either prescribed

by inventories or modelled (e.g., biogenic emissions are created using the Model of Emissions of Gases and Aerosols from Nature (MEGAN)).

GEOS-Chem simulates more than 100 chemical species from the earth's surface up to the edge of space (0.01 hPa) and can be used in combination with remote and in situ sensing data to give a verifiable estimate of atmospheric gases and aerosols. It was developed, and is maintained, by Harvard University staff as well as users and researchers worldwide. In this thesis I use version 10.01 of GEOS-Chem, which outputs up to 66 chemical species (tracers) in the standard run, at 2 by 2.5° horizontal resolution, with 47 levels up to the top of the atmosphere (TOA at 0.01 hPa).

Global CTMs are often run using one or several emission models (or the output from them) to determine boundary conditions. Some of the inventories used by GEOS-Chem are described here. Meteorological fields are taken from NASA's GEOS-5 dataset (0.5°x 0.666°) (Chen et al. 2009), which exists up to April 2013. GEOS-5 meteorological fields are used as the boundary conditions driving transport. Fire emissions come from the global fire emissions database (GFED4) product (Giglio, Rander son, and Van Der Werf 2013). Anthropogenic VOC emissions come from the Emission Database for Global Atmospheric Research (EDGAR) inventory, while biogenic VOC emissions are simulated using the MEGAN model (see section 2.4.5). MEGAN is used to determine biogenic emissions for our default GEOS-Chem simulation. The estimated biogenic VOC emissions are important for accurately simulating chemistry within models, as discussed in Section 1.1.2.

2.4.2 Installing and running GEOS-Chem

GEOS-Chem instructions for download, compilation, and running can be found in the user guide provided by Harvard: <http://acmg.seas.harvard.edu/geos/doc/man/>. In order to build and run GEOS-Chem a high-speed computing system is optimal, as globally gridded chemical calculations can take a long time to perform (for us ~ 70 computation hours per month). I installed GEOS-Chem onto a suitably configured workspace on the Raijin supercomputer at the National Computational Infrastructure (NCI, <http://nci.org.au/>). This workspace included access to compilers and libraries which are needed to build the Fortran based GEOS-Chem source code, and IDL, Python, and various editors and scripting languages to read, run, edit, and analyse both GEOS-Chem and its output. After downloading GEOS-Chem, the code can be compiled with different options for resolution and chemical mechanisms.

2.4.3 Chemical Mechanism

A chemical mechanism is the name for a closed system of chemical reactions and the rates of each reaction. Chemical reactions are represented by systems of differential equations to be solved for each gridbox in GEOS-Chem. Simplifications are required due to the massive amount of reactions which occur in the atmosphere, and the coupled and stiff nature of these reactions which serve to slow down computation of the solutions (Brasseur and Jacob 2017). Stiffness in chemical systems of differential equations is due to the massively differing reaction rate time scales - for instance hydroxyl radicals react within seconds while methane has an atmospheric lifetime of 8-10 years (Wuebbles and Hayhoe 2002).

Some of the important reactions involving isoprene are reproduced here, including reaction rates (k) in the form $k = A \exp -E/RT$, where T is temperature, E is activation energy, and R is the gas constant, A , E , and R is defined for each reaction. Equation 2.5 lists the main isoprene and sundry reactions, with terms defined in 2.3. Some tracers are defined in order to allow the model to keep track of extra information such as the tracers source. For instance LISOPOH keeps track of how isoprene lost to OH reactions. The full current mechanism is described online at http://wiki.seas.harvard.edu/geos-chem/index.php/New_isoprene_scheme.

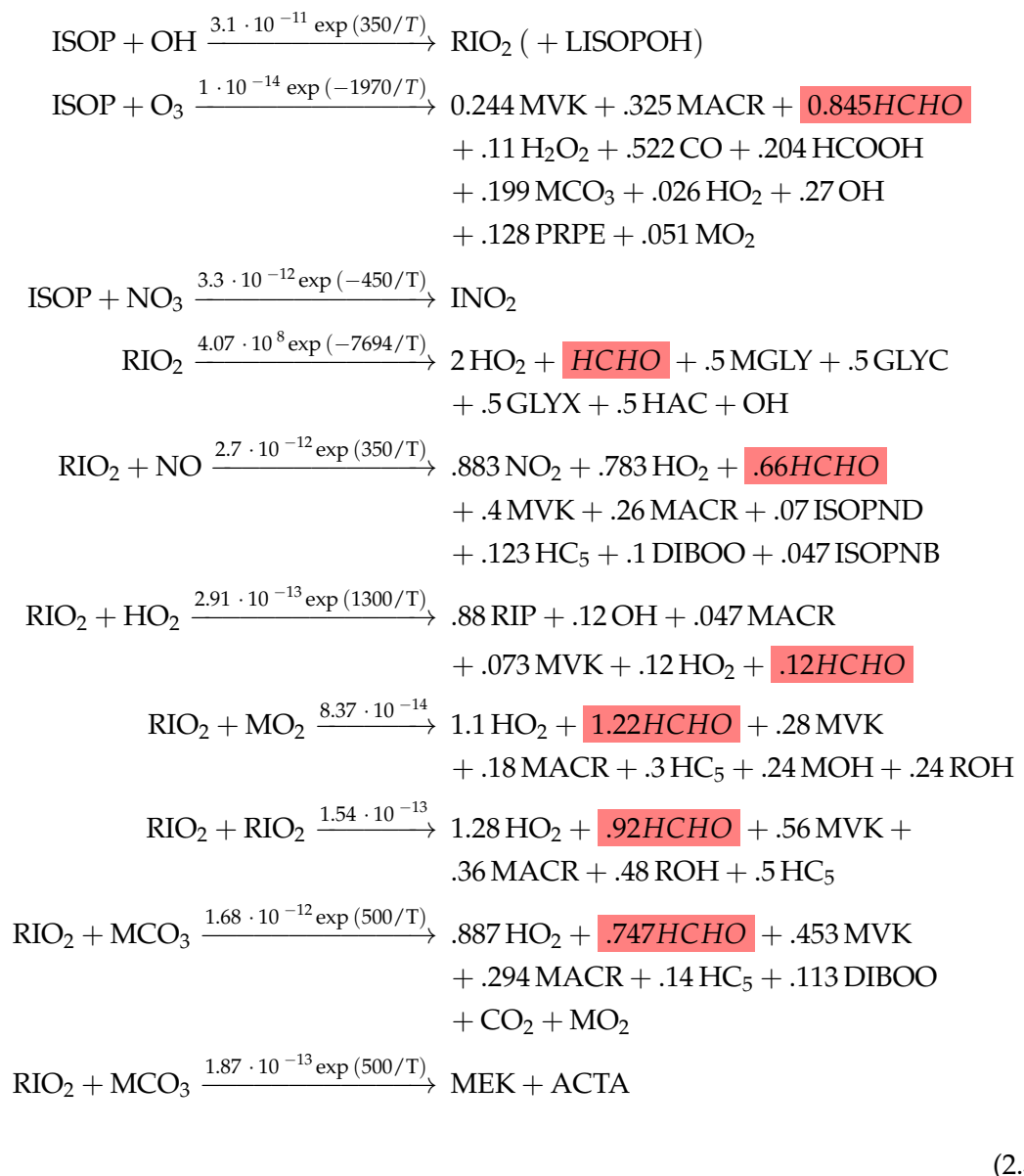


TABLE 2.3: Species or classes from the GEOS-Chem mechanism.

Name	Definition
ACTA	Acetic acid: CH ₃ C(O)OH
DIBOO	Dibble peroxy radical
GLYC	Glycoaldehyde: HOCH ₂ CHO
GLYX	Glyoxal: CHOCHO
HAC	Hydroxyacetone: HOCH ₂ C(O)CH ₃
INO2	RO ₂ from ISOP+NO ₃
ISNP	an isoprene nitrate
ISOPNB	β isoprene nitrates
ISOPND	δ isoprene nitrates
MACR	Methacrolein: CH ₂ =C(CH ₃)CHO
MCO3	Peroxyacetyl radical: CH ₃ C(O)OO
MEK	Methyl ethyl ketone: RC(O)R
MGLY	Methylglyoxal: CH ₃ COCHO
MO2	Methylperoxy radical: CH ₃ O ₂
MOH	Methanol: CH ₃ OH
MVK	Methylvinylketone: CH ₂ =CHC(=O)CH ₃
PRPE	>C ₃ alkenes: C ₃ H ₆ , ...
RIO2	isoprene peroxy radical: ROO
ROH	>C ₂ alcohols

2.4.4 GEOS-Chem isoprene

The isoprene reactions simulated by GEOS-Chem were originally based on Horowitz et al. (1998). The mechanism was subsequently updated by Mao et al. (2013), who change the isoprene nitrate yields and add products based on Paulot et al. (2009a) and Paulot et al. (2009b). Further mechanistic properties, like isomerisation rates, are based on results from four publications: (Peeters, Nguyen, and Vereecken 2009; Peeters and Muller 2010; Crounse et al. 2011; Crounse et al. 2012).

Crounse et al. (2011) examined the isomerisations associated with the oxidation of isoprene to six different isomers of ISOPOO formed in the presence of oxygen. The primary oxidation pathway of isoprene is reaction with the OH radical (*ISOP + OH* \rightarrow *ISOPOO*). Following are seven potential ROO reactions (RIO2 in 2.5), depending on reactant concentrations and local temperature. They determine rates and uncertainties involved in these reactions, and study the rate of formation of C₅-hydroperoxyenals (C5-HPALD) by isomerisation. Prior to 2012, oxidation chamber studies were performed in high NO or HO₂ concentrations, giving peroxy lifetimes of less than 0.1 s (Crounse et al. 2012; Wolfe et al. 2012). In most environments NO and HO₂ concentrations are not so high, GEOS-Chem uses production rates for different NO concentrations and peroxy radical lifetimes determined by Crounse et al. (2012). OH regeneration through photolysis of HPALDs in areas with high isoprene emissions are included from Peeters and Muller (2010). Photolysis of photolabile peroxy-acid-aldehydes creates OH and improved model agreement with continental observations. OH and HPALD interactions are central to maintaining the OH levels in pristine and moderately polluted environments, which makes isoprene both a source and a sink of

OH (Peeters and Muller 2010; Taraborrelli et al. 2012).

Formation of isoprene nitrates (ISOPN) affect ozone levels through NO_X sequestration, and the yields and fate of these nitrates was analysed in Paulot et al. (2009a). In a chamber with clean air and high NO concentrations, isoprene photooxidation is initially driven by OH addition, followed by NO_X chemistry (150 min - 600 min), and finally HO_X dominated chemistry. GEOS-Chem uses these the yields of various positional isomers of isoprene nitrates, and pathways of their oxidation products, and reactions within its suite of chemical mechanisms determined by Paulot et al. (2009a) and Mao et al. (2013).

GEOS-Chem models both high and low NO_X scenarios using NO_X dependent reactions as derived by Paulot et al. (2009a) and Mao et al. (2013). In low NO_X ISOPOO reacts with HO₂ (70% yield of hydroxy hydroperoxides, ISOPOOH), RO₂ (producing mainly MACR, MVK, and HCHO), or isomerises (1,5-H shift producing MACR, MVK, HCHO, or 1,6-H shift producing HPALDs). ISOPOOH can be oxidised (by OH) to produce epoxydiols (IEPOX), recycling OH (Paulot et al. 2009b). HPALDs can photolyse to regenerate OH and small VOCs (Crounse et al. 2011; Wolfe et al. 2012; Jozef et al. 2014). Under low NO_X conditions production of HCHO, MVK, and MACR is 4.7%, 7.3%, and 12% respectively. Refer to section 1.3.3 for more information. Under high NO_X conditions, isoprene undergoes OH addition at the 1 and 4 positions, becoming β (71%) or δ (29%) hydroxyl peroxy radicals (ISOPO₂). The β -hydroxyl reacts with NO_X and produces HCHO (66%), methylvinylketone (40%) (MVK), methacrolein (26%), and β -hydroxyl nitrates (6.7%) (ISOPNB). The δ -hydroxyl reacts with NO to form δ -hydroxyl nitrates (24%) (ISOPND), and ISOPNB (6.7%). ISOPNB and ISOPND yield first generation isoprene at 4.7% and 7% respectively.

The isoprene mechanism in GEOS-Chem includes OH regeneration from oxidation of epoxydiols and slow isomerisation of ISOPO₂ (Mao et al. 2013). In older models isoprene produced ISOPOOH which then titrated OH, however, the loss of OH had not been seen in measurements (Paulot et al. 2009b; Mao et al. 2013). Mao et al. (2013) show that a lower (factor of 50) rate constant for ISOPO₂ isomerisation leads to better organic nitrate agreements with ICARTT. The chemistry updates have led to more accurate modelling of OH concentrations, especially in low NO_X conditions common in remote forests. Prior to Mao et al. (2012), measurements of OH in high VOC regions may have been up to double the real atmospheric OH levels, due to formation of OH inside the instrument. The updates to isoprene chemistry by Mao et al. (2013), and those shown in Crounse et al. (2011) and Crounse et al. (2012) are the last before version 11.

2.4.5 Emissions from MEGAN

MEGAN is a global model with resolution of around 1 km, and is used to generate the BVOC emissions used in various global chemistry models such as GEOS-Chem. MEGAN uses leaf area index, global meteorological data, and plant functional types (PFTs) to simulate terrestrial isoprene emissions. The model includes global measurements of leaf area index, plant functional type, and photosynthetic photon flux density, from remote sensing databases (Kefauver, Filella, and Peñuelas 2014). The various PFTs are used to generate emission factors which represent quantities of a compound

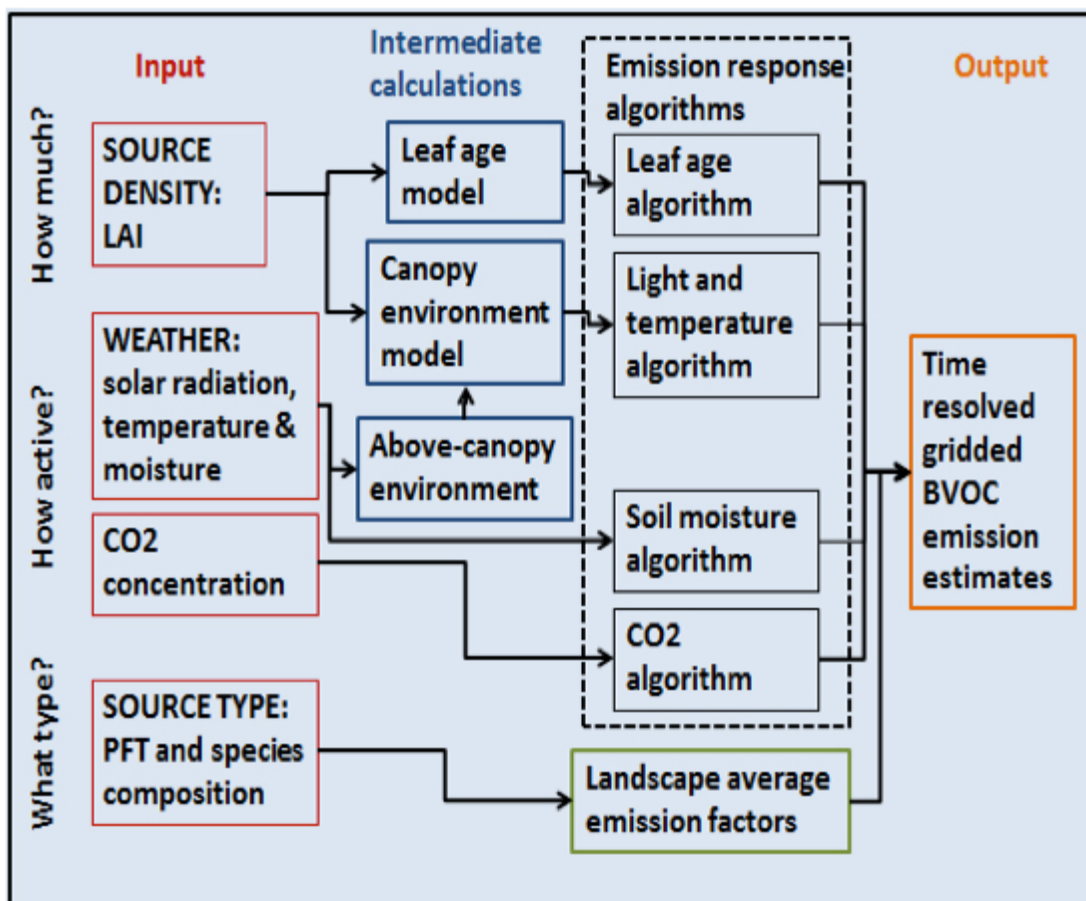


FIGURE 2.10: MEGAN schematic, copied from Guenther (2016)

released to the atmosphere through an associated activity. For example, the emission factor for isoprene is tied to available sunshine, suitable temperature, etc. The schematic for MEGAN, taken from Guenther (2016), is shown in figure 2.10

GEOS-Chem V10.01 uses MEGAN V2.1 with biogenic emissions from Guenther et al. (2012). It computes some emissions using predefined EF maps from MEGAN source code, and others using PFT maps and associated EFs. MEGAN “is a modelling framework for estimating fluxes of biogenic compounds between terrestrial ecosystems and the atmosphere to account for the major known processes controlling biogenic emissions” (Guenther et al. 2012). It allows parameterisation of various BVOC emissions, with descriptions given in Guenther et al. (2012).

MEGAN was developed as a replacement for two earlier canopy-environment emission models (BIES and GEIA), and initially included a simple canopy radiative transfer model, which parameterised sun-lit and shaded conditions through a canopy. Early models did not account for abiotic stresses, such as drought, prior rainfall and development processes. These stresses influenced species-specific emissions by more than an order of magnitude (Niinemets et al. 1999). Isoprene emissions were based on temperature, leaf area, and light, but have since been updated to include leaf age activity (Guenther et al. 2000), and a leaf energy balance model (Guenther et al. 2006)

in MEGANv2.0. This update included a parameter for soil moisture, to account for drought conditions, however this parameter is currently (as of version 2.1) not applied to isoprene (Sindelarova et al. 2014). Soil moisture effects on isoprene emission are important, and can affect estimates.

Instructions to run version 2.1 are available at http://lar.wsu.edu/megan/docs/MEGAN2.1_User_GuideWSU.pdf, and a version using the Community Land Model (CLM) is available at <http://www.cesm.ucar.edu>. It uses meteorological fields from the Weather Research and Forecasting (WRF) modelling system. Version 2.1 (updated from 2.0 (Guenther et al. 2006)) includes 147 species, in 19 BVOC classes, which can be lumped together to provide appropriate output for mechanisms in various chemical models.

2.4.6 Rescaling NO_x

NO_x concentrations affect atmospheric oxidative capacity, which changes many factors important in estimating isoprene emissions including isoprene to HCHO yield, isoprene lifetime, and isoprene oxidation pathways. This means that if the model is poorly simulating NO_x, yields and the effects of transport may be poorly estimated. In order to determine if re-scaling the NO emissions over Australia is necessary in GEOS-Chem, modelled NO₂ amounts are compared to satellite data for most of 2005.

Simulated GEOS-Chem tropospheric NO₂ columns averaged from 1300-1400 LT are compared against OMNO2d data. Figure 2.11 shows the direct comparison between these datasets averaged over the months of January and February, 2005. The top row shows (from left to right) GEOS-Chem NO₂, OMI NO₂ at 0.25x0.3125°, and OMI NO₂ at 2x2.5°. The bottom row shows the difference (absolute, and relative) between GEOS-Chem and OMI, as well as the RMA linear correlation. The OMNO2d product shows Sydney and Melbourne as NO₂ hotspots, which are underestimated by GEOS-Chem due to averaging over the 2x2.5°horizontal resolution. Over much of the country GEOS-Chem overestimates NO₂ by 10-60%, except in NA and northern Queensland where up to 50% underestimation occurs. The comparison is repeated for winter (JJA) of 2005 in Figure 2.12.

This comparison is expanded, including against modelled emissions, and repeated for autumn (MAM), winter (JJA), and spring (SON) in figures 2.13 to 2.20. These show an analysis of GEOS-Chem NO emissions and their correlations with the bias between GEOS-Chem NO₂ mid-day columns and the OMNO2d product, averaged over each season in 2005. The scatter plots have one datapoint for each land square over Australia. The correlation between the bias (GEOS-Chem - OMNO2d) with anthropogenic or soil emissions (E_{NO}) is shown in the bottom right of these figures. The correlation between model and satellite NO₂ columns is OK throughout the year over Australia, with some overestimation in the north during non-summer months. There is also slight underestimation over Sydney and Melbourne throughout the year. These figures show the visible biases are not driven by modelled emissions of NO. While the correlation between column NO₂ and emitted NO is clear, emissions do not appear to bias the model in either direction away from the satellite data. The poor correlations for anthropogenic NO suggest that blanket alterations over Australia would not lead to improved NO₂ fit.

The conclusion drawn is that modelled anthropogenic and soil NO emissions do not show sufficient evidence of biasing GEOS-Chem NO₂ columns away from satellite

GC NO vs OMNO2d 20050101-20050228

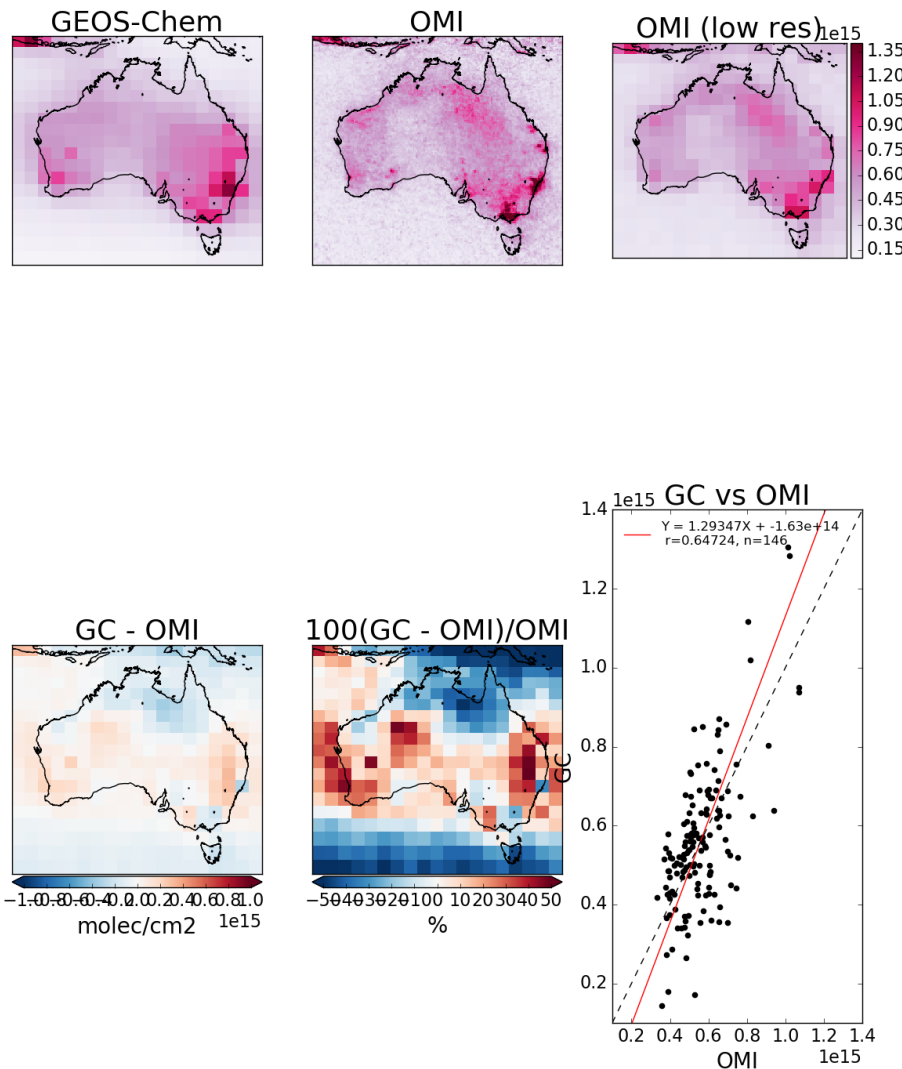


FIGURE 2.11: Row 1 shows the tropospheric columns in molec cm⁻², GEOS-Chem, OMNO2d, and OMNO2d averaged onto the lower resolution of GEOS-Chem from left to right. Row 2 shows the correlations of GEOS-Chem (X axes) between daily anthropogenic emissions, and mid-day OMNO2d columns. Row 3 shows the differences with OMNO2d columns averaged into the lower resolution of GEOS-Chem.

GC NO vs OMINO2d 20050601-20050831

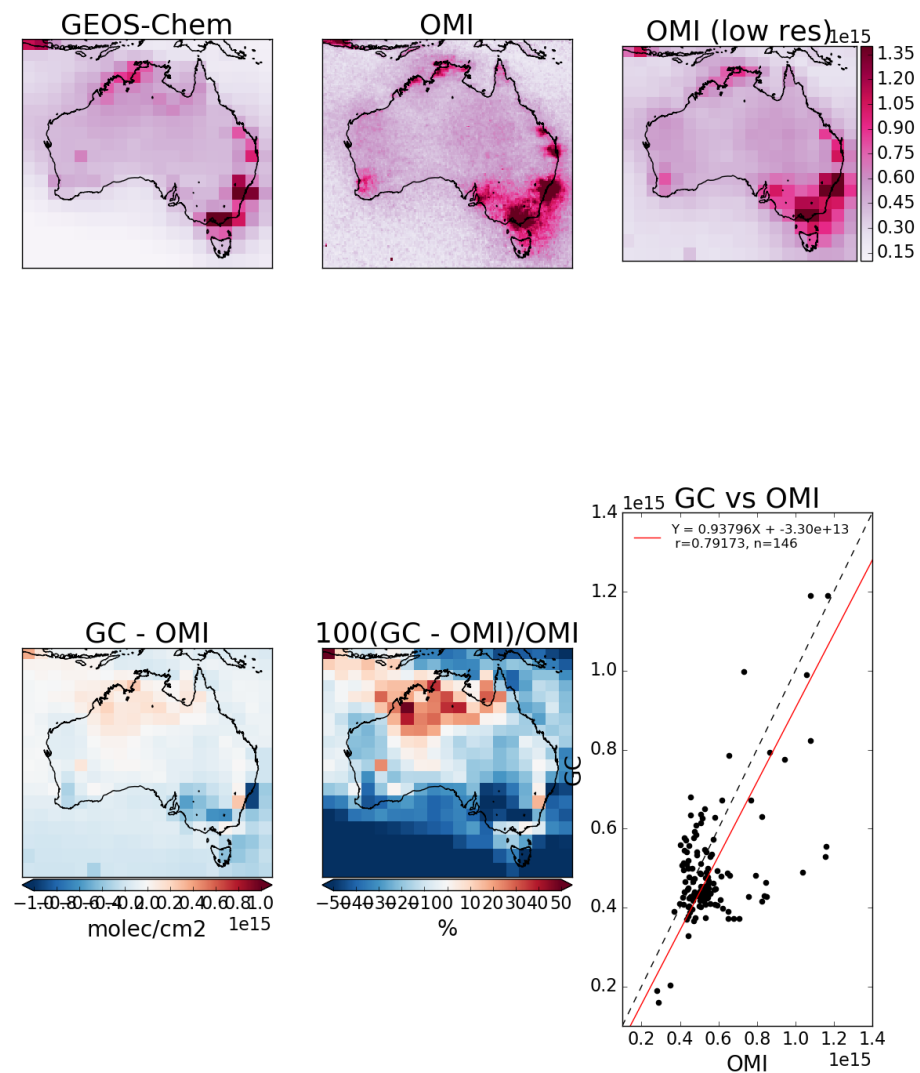


FIGURE 2.12: As figure 2.11, for winter 2005.

GEOS-Chem vs OMNO2d Jan-Feb 2005

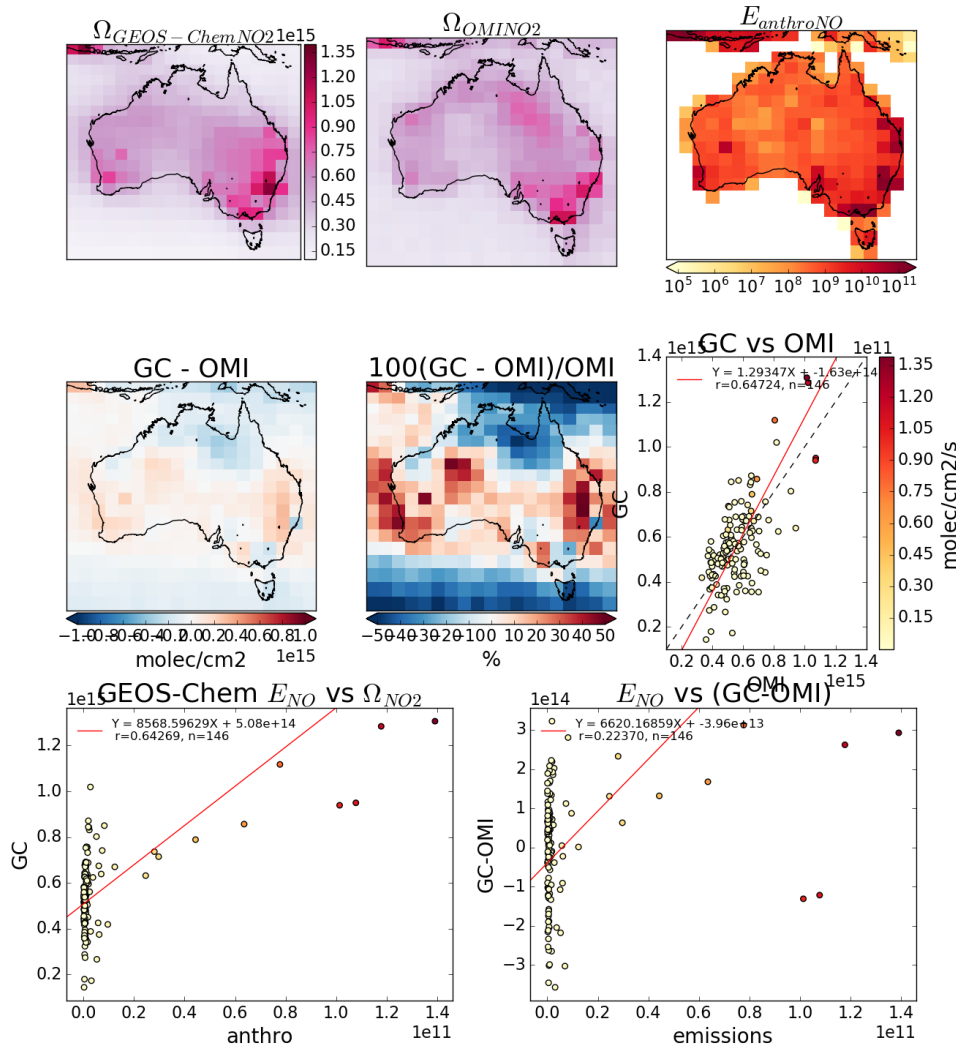


FIGURE 2.13: Top row (left to right): GEOS-Chem NO₂ mid-day tropospheric columns, OMNO2d NO₂ columns, modelled anthropogenic NO emissions. Second row: absolute and relative difference between GEOS-Chem and OMI NO₂ data, and the correlation. Third row: correlation between GEOS-Chem tropospheric column NO₂ and emitted NO, then between the model-satellite bias and the emissions. All correlation plots are coloured by NO emission rates.

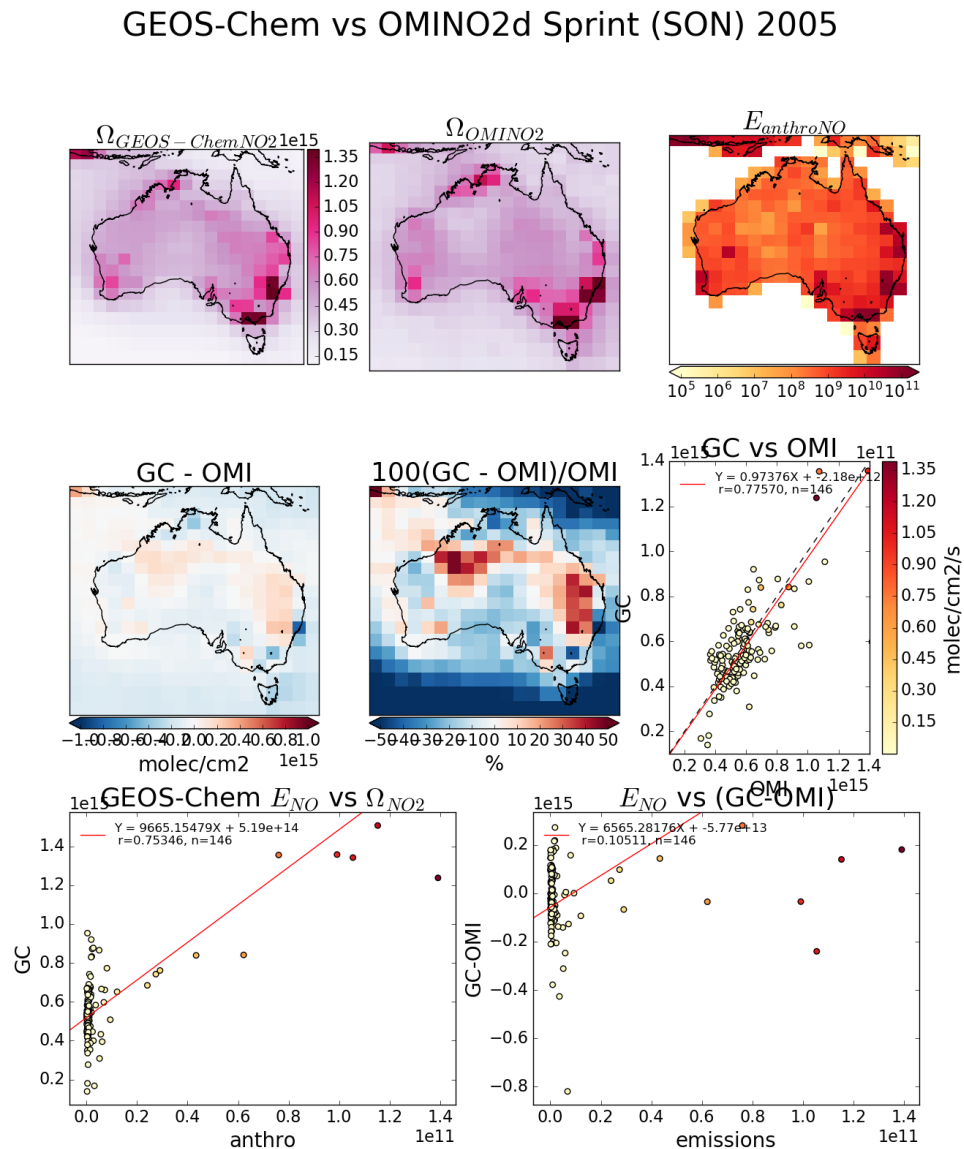


FIGURE 2.14: As figure 2.13, for Autumn 2005.

GEOS-Chem vs OMINO2d Winter (JJA) 2005

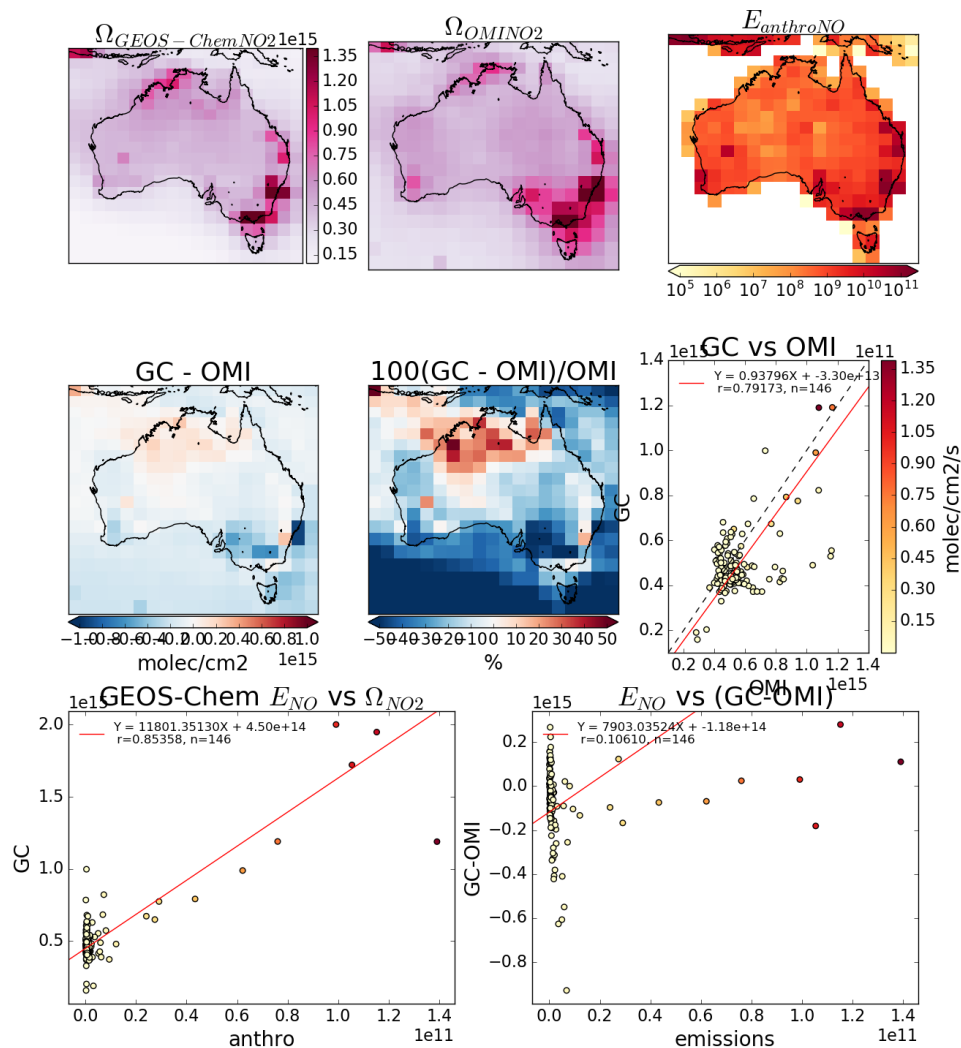


FIGURE 2.15: As figure 2.13, for Winter 2005.

GEOS-Chem vs OMINO2d Autumn (MAM) 2005

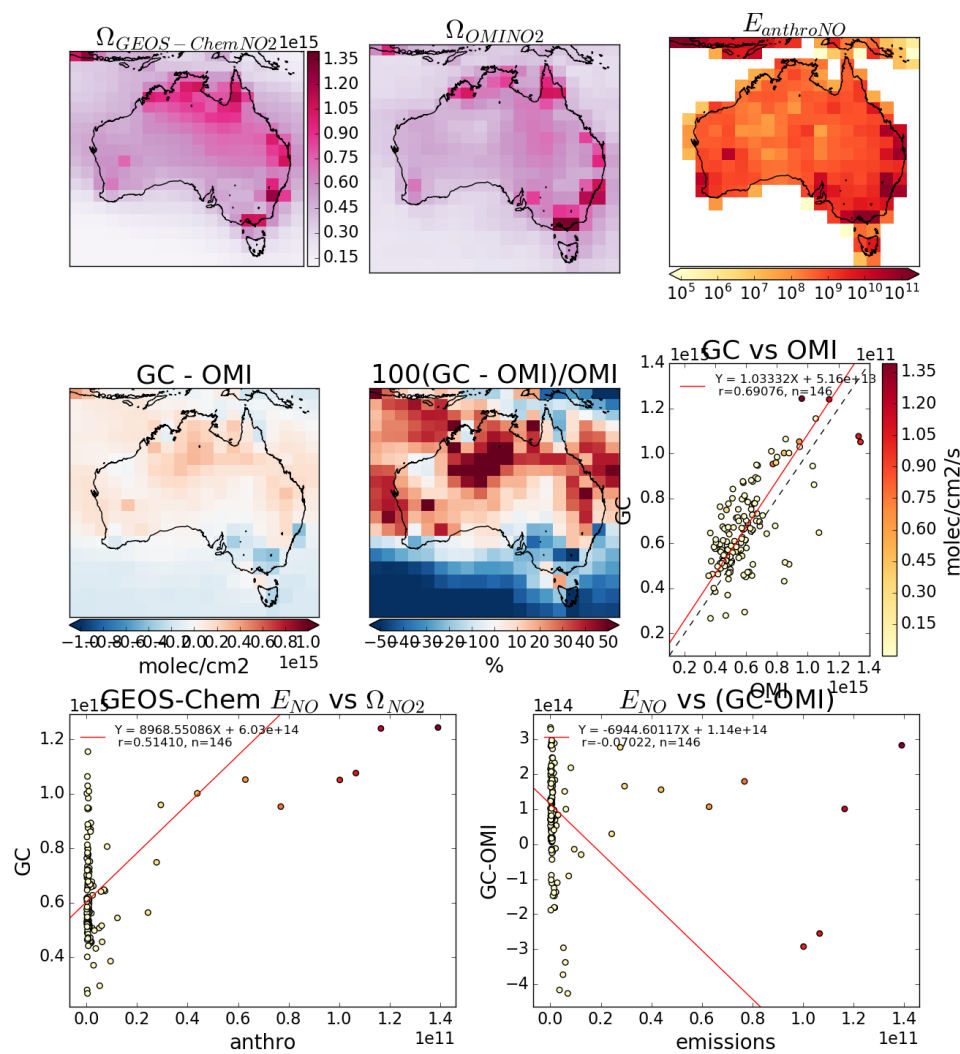


FIGURE 2.16: As figure 2.13, for Spring 2005.

GEOS-Chem vs OMINO2d 20050101-20050228

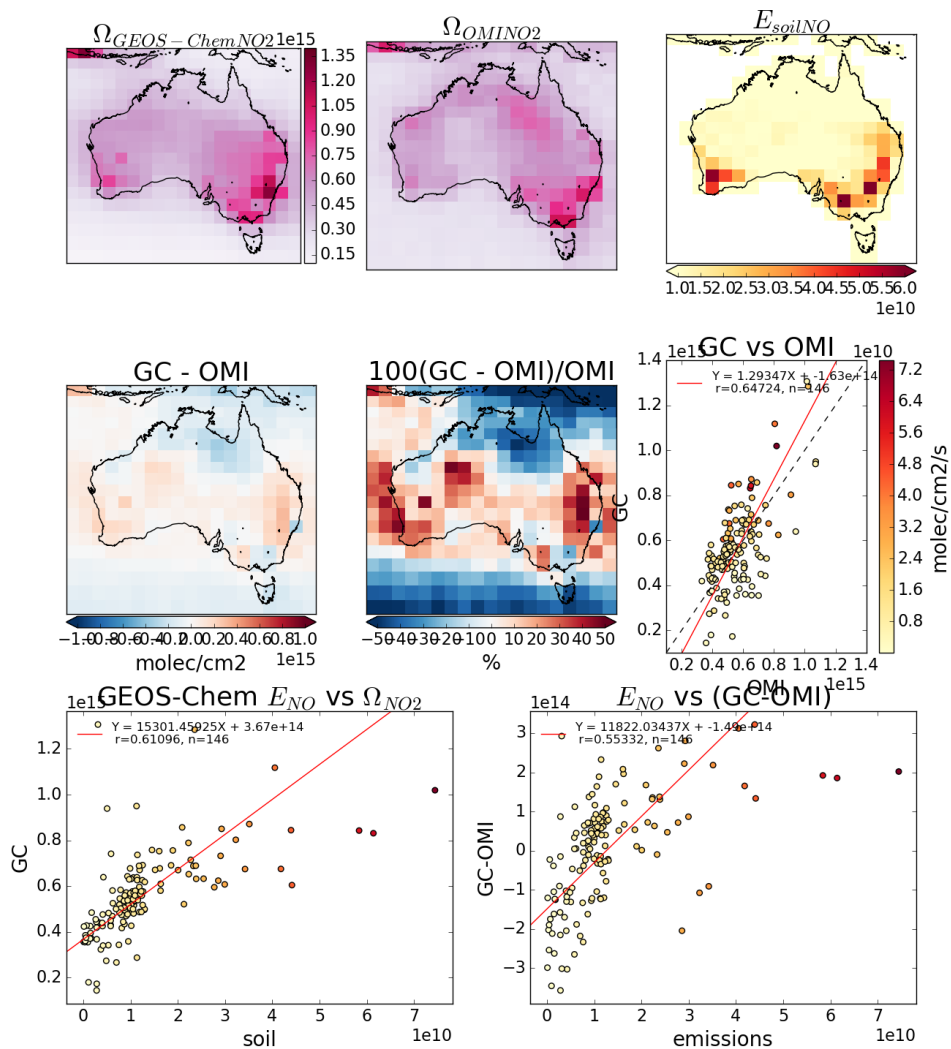


FIGURE 2.17: As figure 2.13, except anthropogenic NO emissions are replaced by soil NO emissions.

GEOS-Chem vs OMINO2d 20050301-20050531

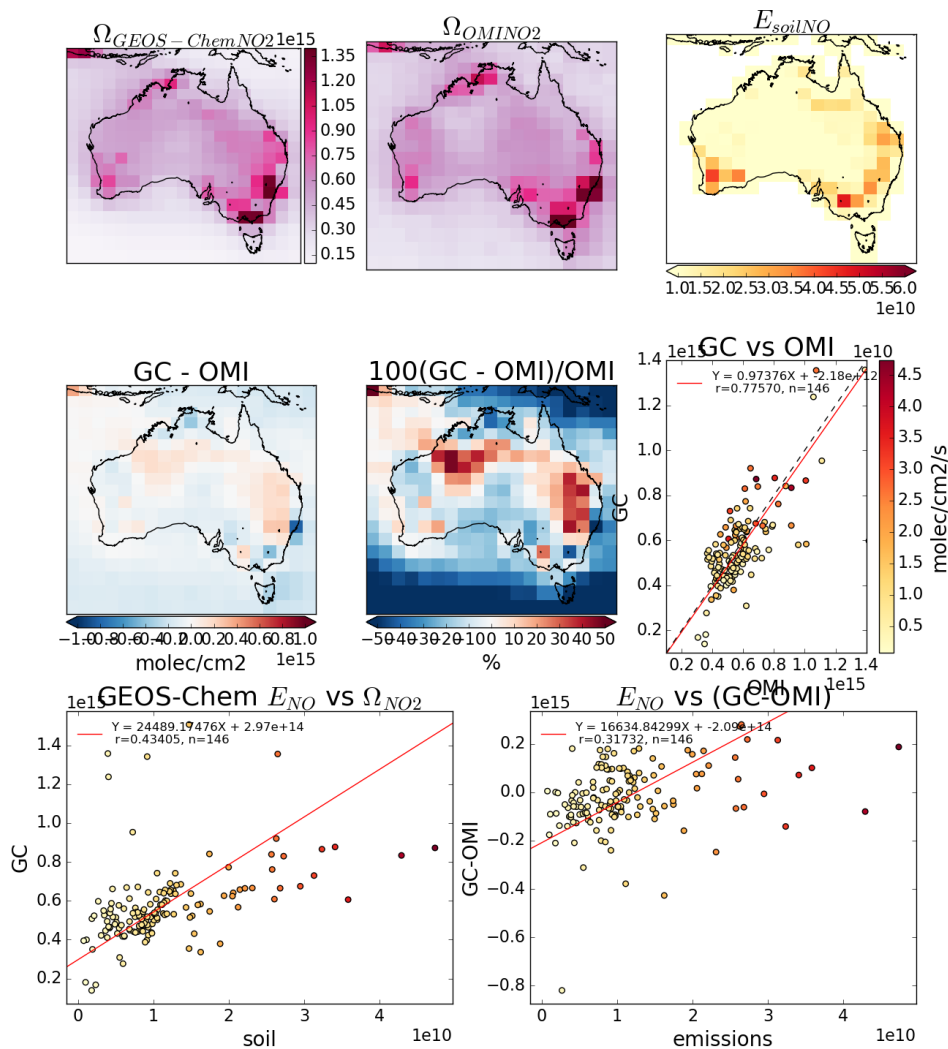


FIGURE 2.18: As figure 2.13, for Autumn 2005, with soil NO emissions replacing anthropogenic NO emissions.

GEOS-Chem vs OMINO2d Winter (JJA) 2005

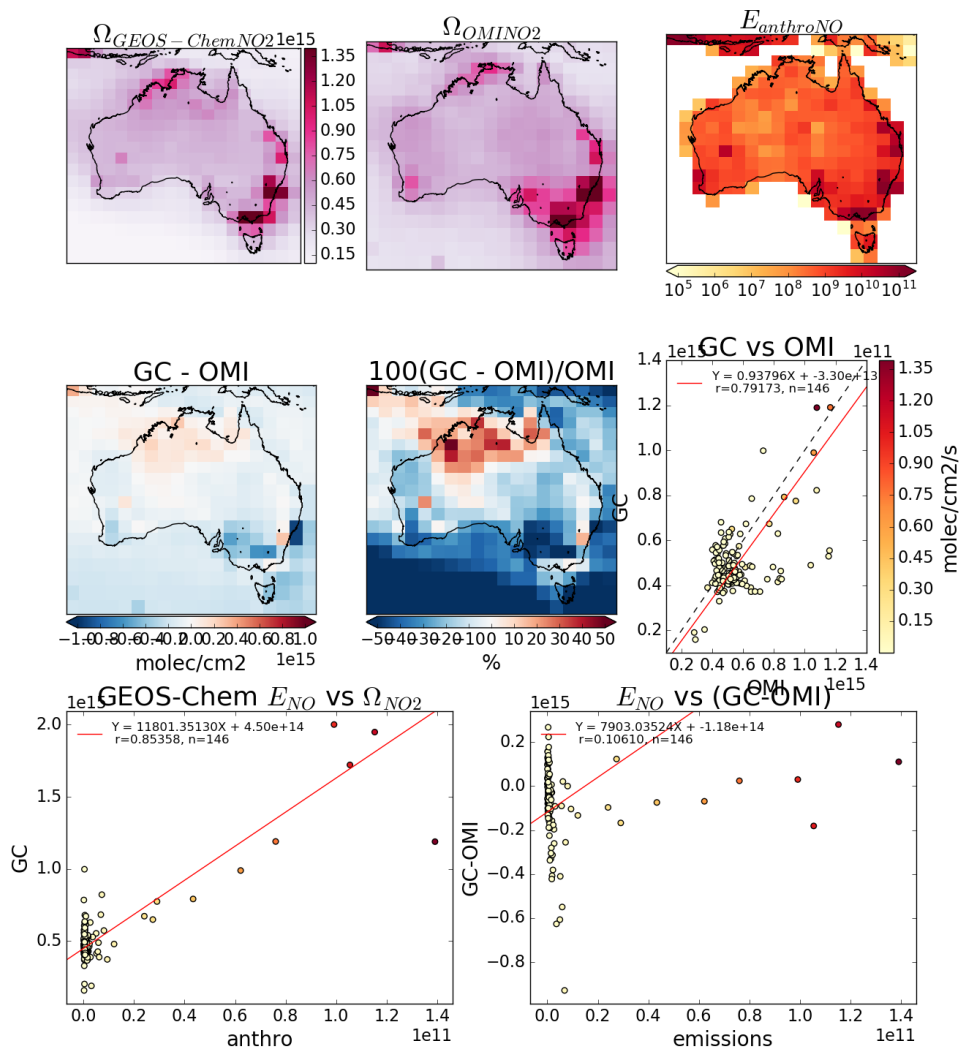


FIGURE 2.19: As figure 2.13, for Winter 2005, with soil NO emissions replacing anthropogenic NO emissions.

GEOS-Chem vs OMINO2d Autumn (MAM) 2005

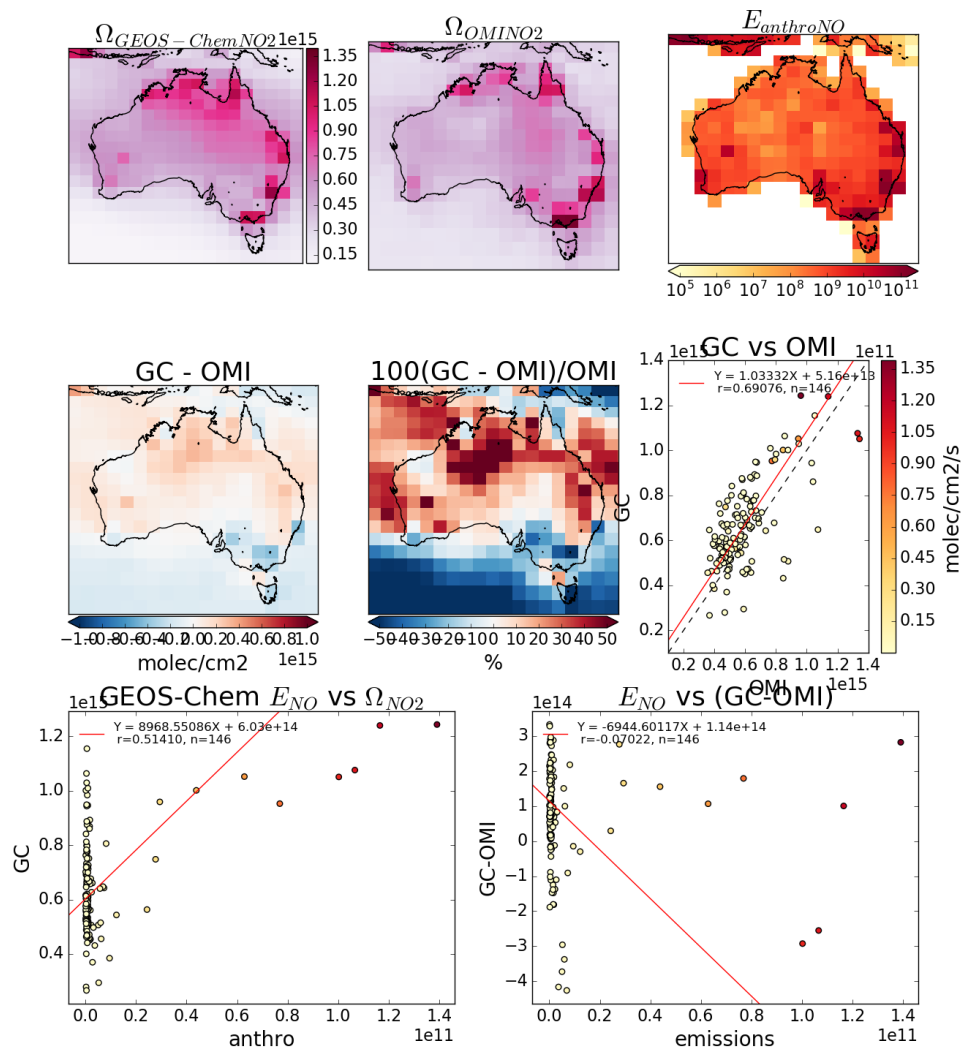


FIGURE 2.20: As figure 2.13, for Spring 2005, with soil NO emissions replacing anthropogenic NO emissions.

measurements over Australia. For this reason modelled NO emissions are not scaled in model runs in this thesis.

2.4.7 GEOS-Chem simulations

GEOS-Chem is run four independent times in this thesis, with different outputs from each simulation used to determine specific information. In this section the different output types are first described (section 2.4.7.1). Following this is the list of model runs, including a summary of the run, which outputs are created, and a summary of how they are used (section 2.4.7.2). Finally a brief comparison between a subset of the runs is performed (section 2.4.7.3).

2.4.7.1 GEOS-Chem outputs

There are various outputs available when running GEOS-Chem, some of which require manipulation in order to compare against observations. GEOS-Chem in this thesis is run with a 15 minute time step for both chemistry and transport, at 2x2.5°horizontal resolution over 47 vertical levels. Output is the average of these time steps either over an entire month, or else per day, or else for the daily local time window of 1300-1400. For example: in this thesis, estimation of model isoprene to HCHO yields uses daily averaged HCHO columns compared against colocated isoprene emissions from MEGAN. Optionally one can save high temporally resolved data for a single (or list of) column(s). This has been used here to compare modelled ozone with ozonesonde profiles at three sonde release sites discussed in Chapter 4.

Satellite output is output from averaging over a window of local time for each gridbox. Output averaged between 1300-1400 LT is saved to match with Aura satellite measurements, as Aura overpasses at ~1330 LT each day. Satellite output is saved both for comparison with, and recalculation of, satellite measurements.

HEMCO diagnostics are output by the HEMCO module, which deals with emissions inventories used in GEOS-Chem. When working with globally gridded data, handling local time offsets becomes more important. The hourly averaged output emissions of isoprene is saved using GMT, which needs to be offset based on longitude in order to retrieve local time. This is done by setting up a latitude by longitude array which matches the horizontal resolution of the data, filling each gridbox with its local time offset. This offset is determined as one hour per 15°(as 360°is 24 hours), and then used to retrieve global data at any specific local time. The retrieval of a daily local time global array is done by index matching the GMT+LT (modulo 24) with the desired hour on this grid over the 24 GMT hours.

Tracer averages are daily or monthly averaged gridbox concentrations.

Time series list of vertical columns with diagnostics saved at a temporal resolution of up to 15 minutes.

2.4.7.2 GEOS-Chem runs

The following list summarises each model run as well as enumerating the outputs (described above), and how the run is used in the thesis.

UCX Universal tropospheric-stratospheric Chemistry eXtension (UCX) mechanism is run with 72 vertical levels from the surface to the top of the atmosphere (TOA \sim 0.1 hPa). UCX runs a chemistry mechanism with combined tropospheric and stratospheric reactions, with an increased number of stratospheric calculations performed online (Eastham, Weisenstein, and Barrett 2014).

1. Satellite output, daily tracer averages, time series over three stations
2. Satellite output used to check how shape factors for AMF recalculation are affected by vertical resolution and stratospheric chemistry TODO: Make a plot of AMF with and without 72 vertical levels
3. Check if the stratospheric chemistry has much influence over tropospheric isoprene or HCHO concentrations.
4. daily tracer averages are used for ozone intrusion quantification (section 4.5.1), and ozone seasonality (section 4.4).
5. Time series are compared against ozonesonde releases (section 4.4) both over time and vertically.

Tropchem (standard) default settings for GEOS-Chem 10.01, using 47 vertical levels at 2x2.5°horizontal resolution. Additional satellite output is created to allow pp code to run on OMI satellite measurements (section 2.6.5).

1. Satellite output, daily tracer averages, HEMCO diagnostics
2. Used in recalculation of the satellite AMF (section 2.5), and the modelled background HCHO over the remote pacific which is used in the reference sector correction for OMI column retrievals (section 2.6.7)
3. Also used to determine isoprene to HCHO yield, after removing days with high biomass burning emissions (section ??)
4. Additional satellite outputs used to determine a separate AMF.
5. Satellite output is combined from two different runs in order to determine smearing (section ??)
6. HEMCO diagnostics output used to determine isoprene to HCHO yields (section ??), and to compare against top-down estimations of isoprene emissions (section ??)
7. TODO: Compare total yearly ozone concentrations before and after implementing top-down estimate.

Tropchem (isoprene emissions halved) identical to standard tropchem except isoprene emissions are halved.

1. Satellite output, monthly tracer averages
2. Check modelled ozone sensitivity to isoprene emissions TODO: plot ozone between the two runs and reference here

3. Combined with standard run to determine model sensitivity transport (section ??)

Tropchem (biogenic emissions only) identical to standard tropchem except all non-biogenic emissions inventories are disabled.

1. Satellite output, hourly biogenic emissions from MEGAN
2. Used to determine the biogenic yield from isoprene to HCHO over Australia, described in section ??
3. Compared to run with updated emissions (??)

Tropchem (altered MEGAN scaling factor)

1. Satellite output, time series, daily averaged tracers
2. Compare to campaign datasets after altering isoprene emissions (see chapter 3)
3. Compare against satellite column HCHO as a sanity check on improving isoprene emissions

2.4.7.3 UCX vs tropchem

Here we compare the model output with and without enabling the Universal tropospheric-stratospheric Chemistry eXtension (UCX). Both runs use 2° latitude by 2.5° longitude, however the UCX mechanism is run with 72 vertical levels from the surface to the top of the atmosphere (TOA~0.1 hPa), while the standard (tropchem) run uses 47 levels. The extra vertical levels are added in the stratosphere, providing finer vertical resolution from around 70 hPa to the top of the atmosphere. For both runs the input parameters such as MEGAN emissions and GEOS-5 meteorological fields are identical.

Figure 2.21 shows an example of surface HCHO amounts, averaged over Jan and Feb, 2007, with (A) and without (B) UCX turned on. Surface HCHO (first model level; up to ~ 100 m) does not differ much between runs. The differences do not exceed 3% over Australia, and absolute differences are exceedingly minor (note the scale in A-B). The major notable difference occurs over northern Africa, where HCHO is around 20% lower in the UCX run. Additionally a slight ($< 8\%$) decrease in Ω_{HCHO} over the oceans can be seen. The comparison is repeated using total columns (instead of surface values) in figure 2.22, showing that differences affecting HCHO between the model run are spread over the entire vertical column.

Figure 2.24 shows the differences in surface isoprene concentrations over Australia, averaged over 1, Jan to 28, Feb, 2007. Here we start to see a higher relative difference in concentrations, although this is generally over the areas with less absolute concentrations. Very little isoprene is seen away from the continents (4-5 orders of magnitude less), due to its short lifetime and lack of oceanic sources. Generally isoprene is 0-30% higher over mid to western Australia when the UCX mechanism is turned on, however this increase is lower in the regions with high isoprene emissions (north-east to south-east coastline). This enhancement can be seen throughout the entire tropospheric column as shown by Figure 2.24. There is a greater effect in Africa

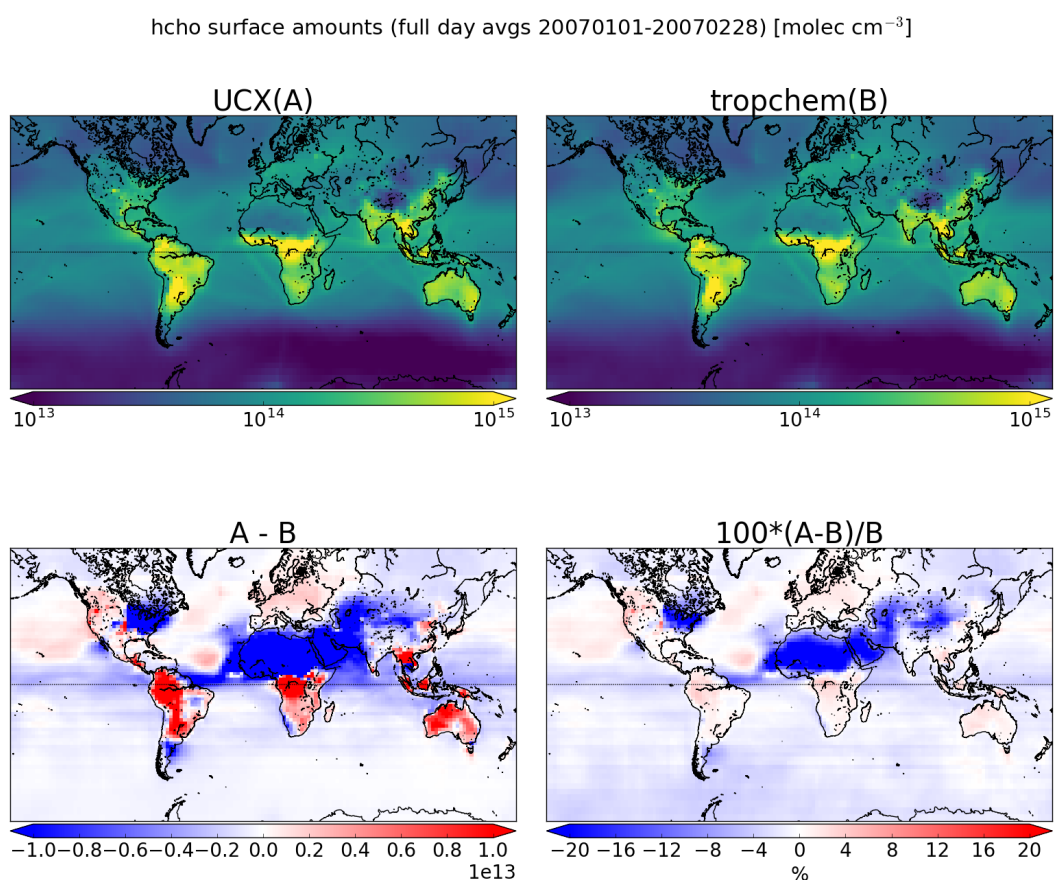


FIGURE 2.21: Surface HCHO simulated by GEOS-Chem with UCX (top left), and without UCX (top right), along with their absolute and relative differences (bottom left, right respectively). Amounts are the average of all times between 1, Jan and 28, Feb, 2007.

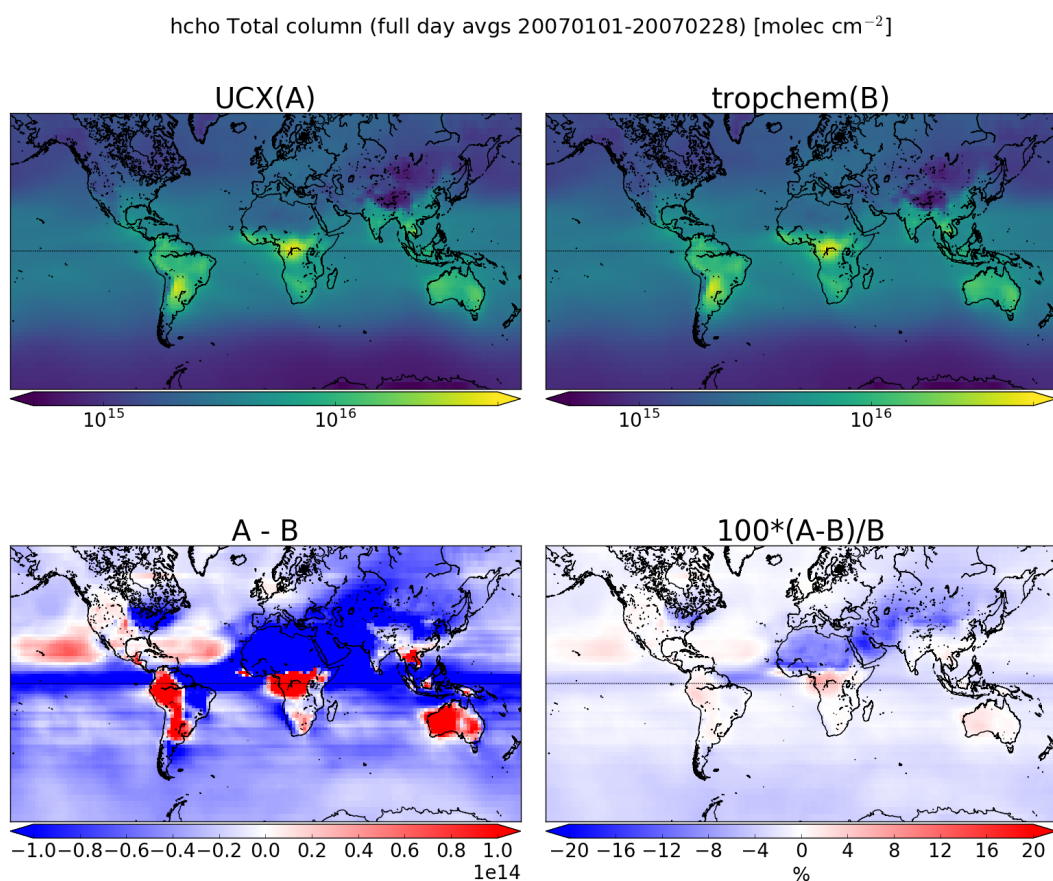


FIGURE 2.22: As figure 2.21 except using total column amounts instead of surface concentrations.

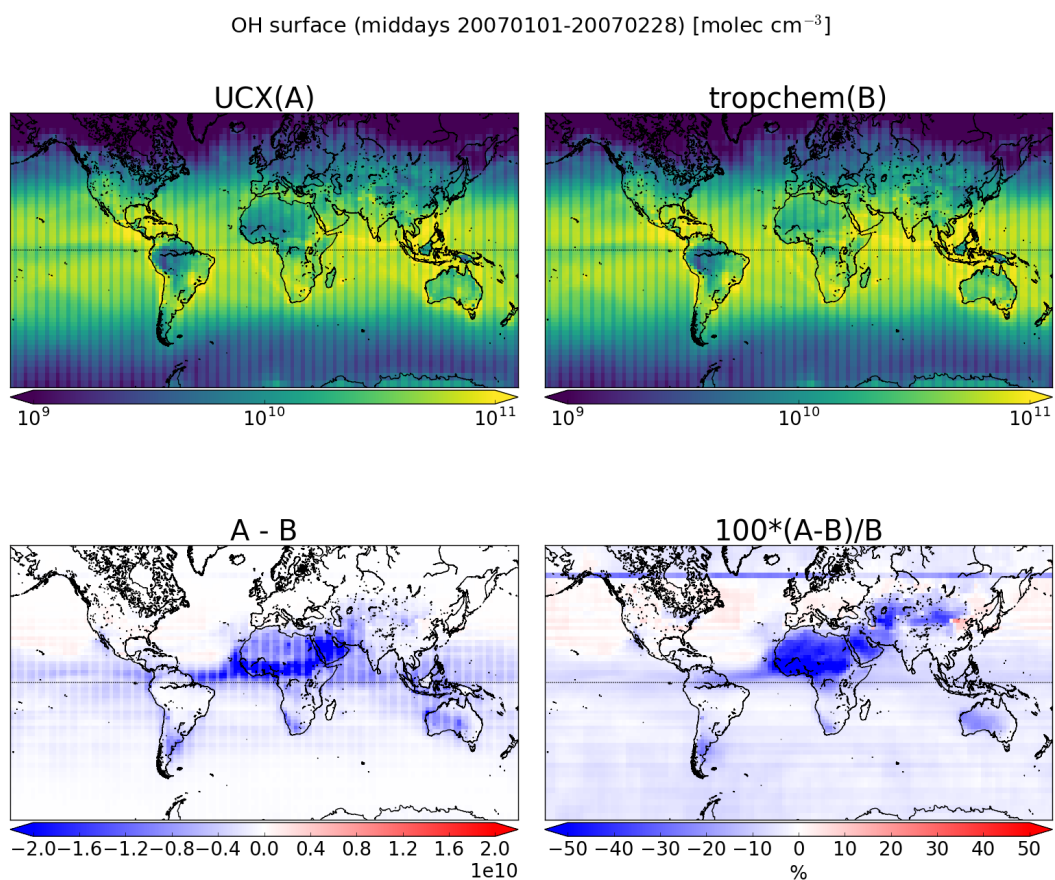


FIGURE 2.23: Midday (1300-1400 LT) surface OH concentrations averaged over Jan-Feb, 2007. Absolute and relative differences are shown on the bottom row.

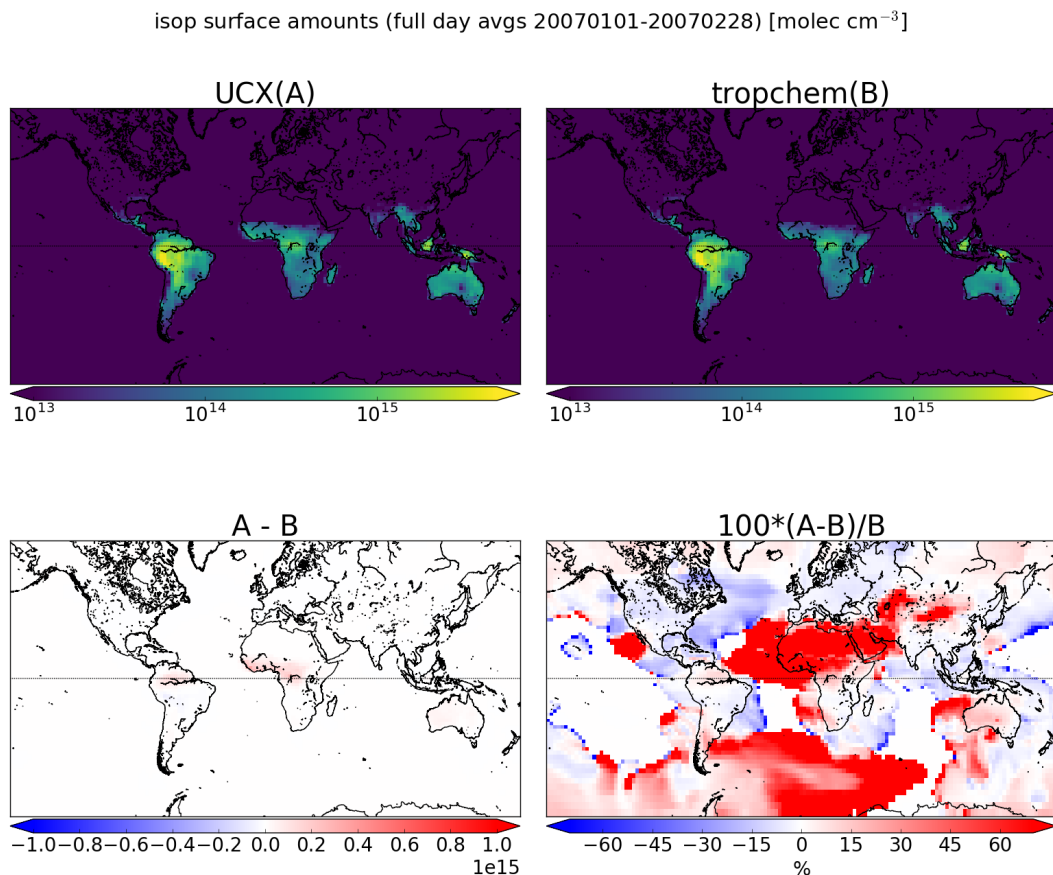


FIGURE 2.24: As figure 2.21, except looking at isoprene.

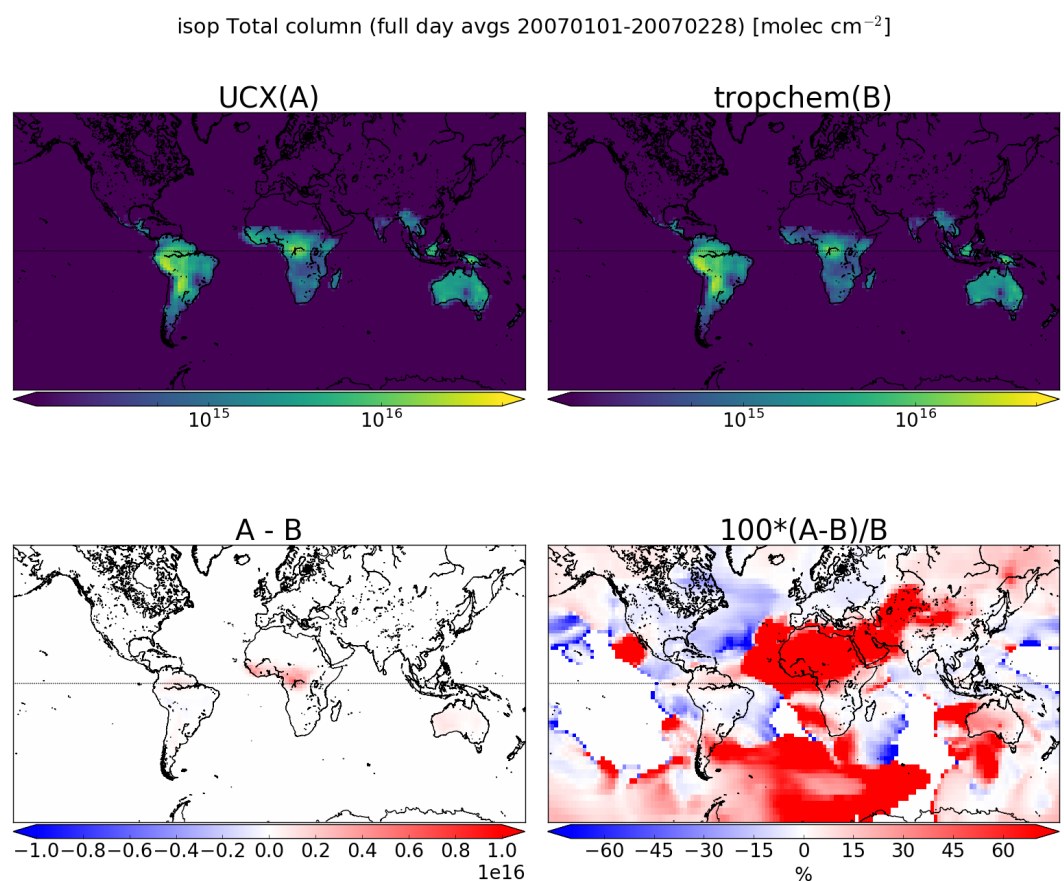


FIGURE 2.25: As figure 2.24, except looking at isoprene total column amounts.

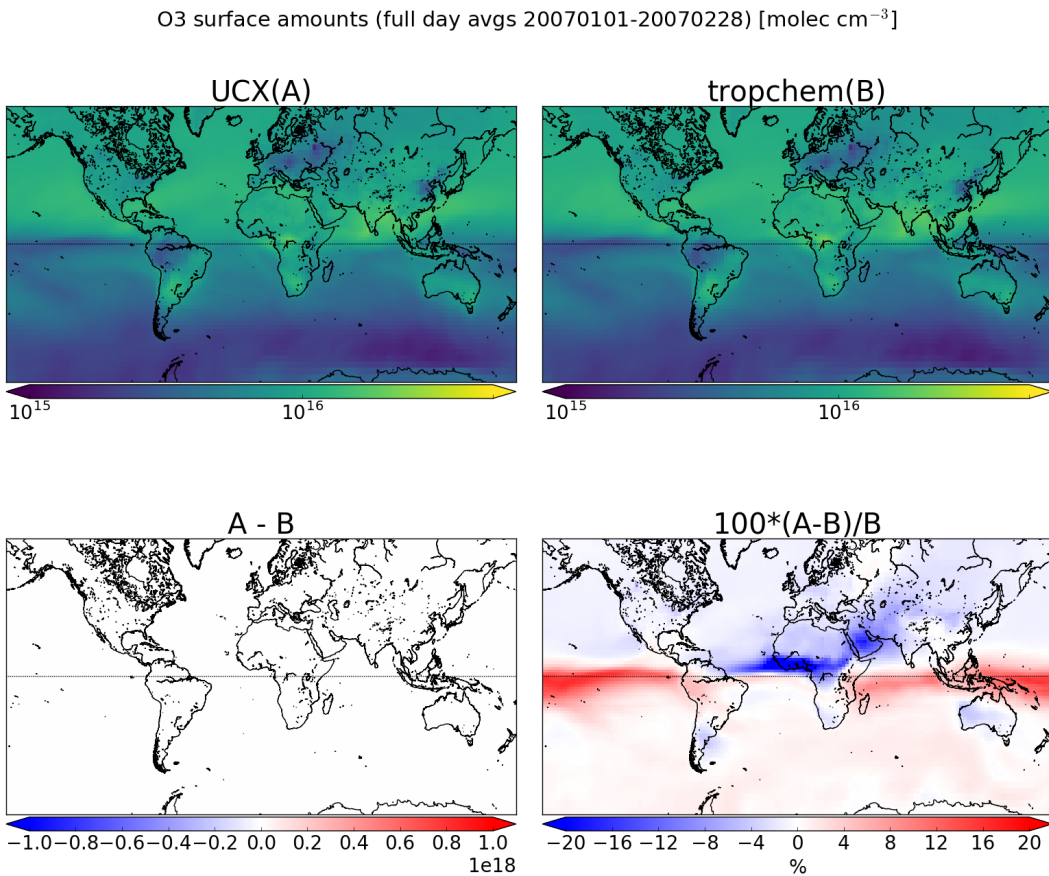


FIGURE 2.26: As figure 2.21, except looking at ozone.

and South America in the tropics, with high relative differences in many regions with low absolute amounts.

The difference in isoprene between UCX and tropchem is likely caused by differences in the modelled radiation reaching the troposphere due to differences in simulated ozone in the stratosphere. With higher stratospheric ozone levels, less radiation would reach the troposphere, changing the photochemistry. Figure 2.23 shows how OH at midday is changed between runs. This figure shows a marked striping which is due to how OH is handled in GEOS-Chem. The most notable difference is again over northern Africa into eastern Europe, with some small decrease in the UCX OH over Australia everywhere except the east coast. Figure ?? shows the total column ozone between UCX and non-UCX runs, using full day averages. This shows that UCX ozone is lower everywhere except for a thin band just north and south of the equator. Decreased O₃ could lead to lower OH and the other differences between the runs over Australia.

The differences are minimal compared to other uncertainties in both AMF calculation and emissions estimation.

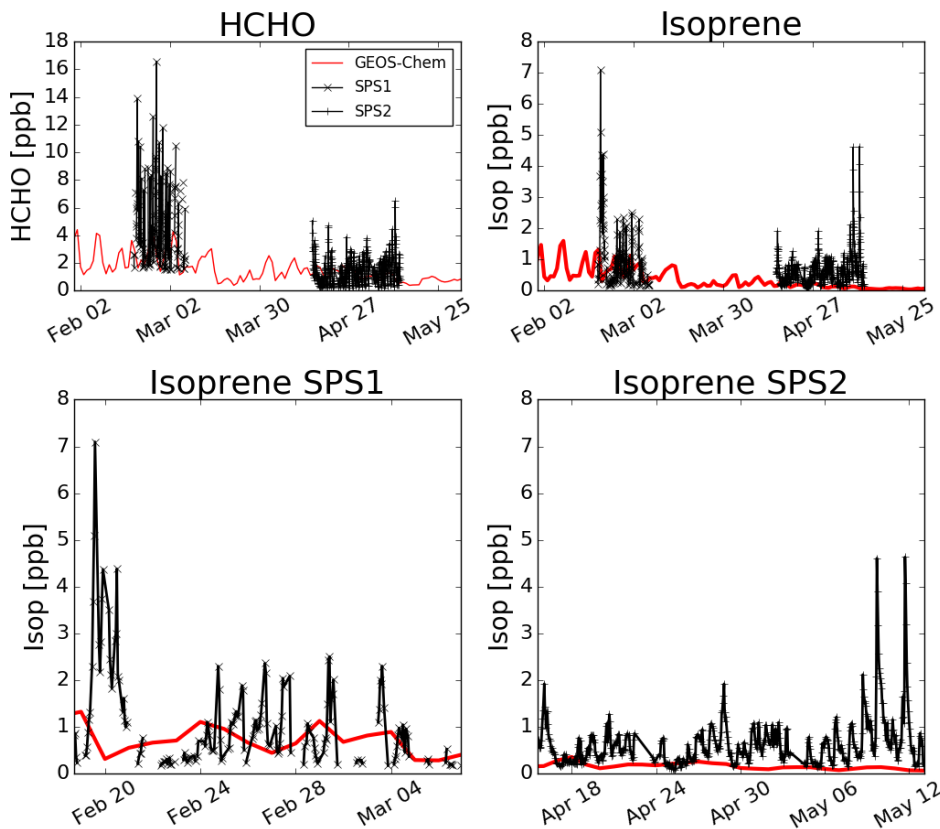


FIGURE 2.27: Comparison between GEOS-Chem HCHO concentrations in the gridsquare containing Sydney for the duration of the SPS 1 and 2 campaigns

2.4.8 Comparisons with campaign data

Figure 2.27 shows GEOS-Chem output in the gridsquare containing Sydney overlaid on SPS measurement data. Superficially the comparison is not too bad between these two datasets, however GEOS-Chem output is the daily average over $2 \times 2.5^\circ$ (latitude by longitude). The SPS data is point-source and taken during the daytime when isoprene is higher, so it is very likely that GEOS-Chem HCHO and isoprene output is in fact too high since the daily average should not match the peak of the measurements.

Figure TODO: shows Wollongong FTIR measurement profiles of HCHO with an assumed averaging kernel and then one calculated from GEOS-Chem, along with the two averaging kernel mean and standard deviation. TODO: Discuss this conversion and results seen here... The bottom panel shows the time series of total column HCHO of both GEOS-Chem and the FTIR instrument in molecules cm^{-2} .

MUMBA data captured concentration at the surface in Wollongong, and is compared in figure TODO against simulated HCHO concentrations at the first level ($\sim 0 - 150$ metres) over corresponding dates. GEOS-Chem midday and day average concentrations are shown, along with Wollongong bottom-level FTIR measurements to

compare against the MUMBA data. TODO Discussion of comparison.

2.5 Calculating an AMF

The AMF is the ratio of the slant column (Ω_s) to the vertical column (Ω_v)

$$AMF = \frac{\Omega_s}{\Omega_v} = \frac{\tau_s}{\tau_v} \quad (2.6)$$

with τ being the optical depth or thickness of the absorber through the slant (s) or vertical (v) path of light.

The OMI instrument records spectra of light which enters the viewing lens on board the Aura satellite. The spectra provide backscattered intensity (I_B) at various wavelengths (see section 2.3), with the light source (I_{B_0}) being the sun. Using the log of Beers law (equation 2.1) we get

$$\tau_s = \ln I_{B_0} - \ln I_B$$

which can be subbed into equation 2.6 to give an expression for the AMF which includes scattering:

$$AMF = \frac{\ln I_{B_0} - \ln I_B}{\tau_v} \quad (2.7)$$

We use $\nabla I = I_B - I_{B_0}$ to represent the change in intensity due to the absorber. For optically thin absorption, $\nabla I/I_B \ll 1$, and we can use:

$$AMF = \frac{\ln \left(1 - \frac{\nabla I}{I_B}\right)}{\tau_v} \approx \frac{-\frac{\nabla I}{I_B}}{\tau_v} \quad (2.8)$$

This is due to the logarithmic property $\ln(1 - x) \approx -x$ for $x \ll 1$. ∇I can also be expressed as the integral of the absorption slices over optical depth increments:

$$\nabla I = \int_0^{\tau_v} \frac{\partial I_B}{\partial \tau} d\tau \frac{\nabla I}{I_B} = \int_0^{\tau_v} \frac{\partial \ln I_B}{\partial \tau} d\tau$$

which can be placed into equation 2.8 leading to

$$AMF \approx \frac{-1}{\tau_v} \int_0^{\tau_v} \frac{\partial \ln I_B}{\partial \tau} d\tau$$

We can then convert $d\tau$ to our path using equation 2.3 leading to

$$AMF = \frac{-1}{\tau_v} \int_0^{\infty} \frac{\partial \ln I_B}{\partial \tau} \alpha(z) \eta(z) dz \quad (2.9)$$

where $\alpha(z)$ and $\eta(z)$ represent absorption cross section in $m^2 \text{ molecule}^{-1}$, and number density in molecules m^{-3} respectively. This uses the attenuation cross section relationship to optical depth (see section 2.3.2).

To represent an average cross section weighted by the absorbing species' vertical distribution, the effective cross section (α_e) is used. This is to account for temperature

and pressure dependence of $\alpha(z)$, and is defined as:

$$\begin{aligned}\alpha_e &= \frac{1}{\Omega_v} \int_0^\infty \alpha(z) \eta(z) dz \\ &= \frac{\tau_v}{\Omega_v}\end{aligned}$$

Then replacing the τ_v in equation 2.9 we obtain:

$$AMF = - \int_0^\infty \frac{\partial \ln I_B}{\partial \tau} \frac{\alpha(z)}{\alpha_e} \frac{\eta(z)}{\Omega_v} dz \quad (2.10)$$

Often the integrand of this AMF formula (equation 2.10) is broken apart into two defining terms: the scattering weights $\omega(z)$ and the shape factor $S(z)$, described here:

- ω The scattering weights describing sensitivity of the backscattered spectrum to the abundance of an absorber at altitude z:

$$\omega(z) = - \frac{1}{AMF_G} \frac{\alpha(z)}{\alpha_e} \frac{\partial \ln I_B}{\partial \tau} \quad (2.11)$$

It is worth noting that in the OMI satellite product, the provided $\omega(z)$ term does not include the $\frac{1}{AMF_G}$ term and the calculations which follow therefor do not include this term when utilising the provided ω . This is not noted in any of the papers which recalculate the AMF from the OMI product, due to them recalculating the ω term themselves with a radiative transfer model such as LIDORT.

- ω the shape factor describes the profile of an absorber ($\eta(z)$) normalised by its total vertical column amount (Ω_v):

$$S(z) = \frac{\eta(z)}{\Omega_v} \quad (2.12)$$

Plugging equations 2.11 and 2.12 into equation 2.10 gives us:

$$AMF = AMF_G \int_0^\infty \omega(z) S(z) dz \quad (2.13)$$

Since we are using the ω provided by OMI, the AMF_G term is removed from this calculation as it is not part equation 2.11 leading to

$$AMF = \int_0^\infty \omega(z) S(z) dz \quad (2.14)$$

Additionally the AMF can be determined using the sigma (σ) coordinate system. A conversion to the σ vertical coordinate is performed using $P = \sigma(P_S - P_T) + P_T$, where P_T is pressure at the top of the atmosphere and P_S is surface pressure. This can be useful when running global atmospheric models as the ground altitude is always at $\sigma = 1$ and we need not worry about topography. S_σ is a dimensionless normalised shape factor on the σ coordinate system. In the sigma coordinate system we calculated

the shape factor as defined in Palmer et al. (2001):

$$S_\sigma(\sigma) = \frac{\Omega_a}{\Omega_v} C_{HCHO}(\sigma) \quad (2.15)$$

where Ω_a is the vertical column of air from the surface to the top of the atmosphere and $C_{HCHO}(\sigma)$ is the mixing ratio of HCHO. The hydrostatic relation $P = -\rho_a g z$, with ρ_a , g , being density of air, and gravity respectively lets us integrate over the sigma coordinates:

$$\begin{aligned} \rho_a g z &= \sigma (P_S - P_T) + P_T \\ d\sigma &= -\frac{\rho_a g}{P_S - P_T} dz \end{aligned}$$

Substitution into 2.14 gives AMF using the sigma coordinates:

$$AMF = \int_0^1 w(\sigma) S_\sigma(\sigma) d\sigma \quad (2.16)$$

2.6 Recalculation of OMI HCHO

The AMF is needed to transform the slant column (SC) viewed by the satellite into a vertical column (Ω):

$$AMF = \frac{SC}{\Omega} \quad (2.17)$$

A slant or vertical column is expressed in molecules cm^{-2} . OMI HCHO vertical columns are calculated using modelled a priori HCHO profiles (see section ??). When comparing satellite measurements against models it is important to recognise the impact of this a priori on the total column values. This is complicated by how OMI is differently sensitive to HCHO (and other trace gases) vertically throughout the atmosphere. When comparing OMI vertical columns (Ω_O) to GEOS-Chem (Ω_G), the satellite AMF needs to be recalculated using GEOS-Chem modelled vertical gas profiles as the a prioris. Without performing this step a bias between modelled and measured total column values may be due to the a priori rather than chemistry or measurements (Palmer et al. 2001; Lamsal et al. 2014).

Here, two new AMFs are calculated, both using GEOS-Chem HCHO profiles as the new a priori. The first (AMF_{GC}) uses the original satellite scattering weights while recalculating the shape factor, whereas the second (AMF_{PP}) also recalculates scattering weights. AMF_{PP} is created using code initially written by Professor P. Palmer (see sections ?? and 2.6.5 for more details). A reference sector correction is determined using the method described in Abad et al. (2016), (see section 2.6.7). This correction is unique for each of the 60 *measurement tracks* used by OMI. Finally the correction is applied to each pixel to create the corrected vertical column. The end product is three sets of corrected vertical columns: the original (Ω_{OC}), one using GEOS-Chem shape factors (Ω_{GC}), and one from Palmer's code (Ω_{PC}).

2.6.1 Outline

An outline in computational order of what takes place when recalculating the Ω from OMI follows:

1. GEOS-Chem satellite overpass output (see section 2.4.7.1) is used to create new shape factors (S_z and S_σ).
 - (a) Pressure edges and geometric midpoints are determined, along with altitudes (z), and box heights (H).
 - (b) Number density and mixing ratio of HCHO (n_{HCHO} , C_{HCHO} respectively) are taken or created from model outputs HCHO(ppb), air density (molec cm^{-3}), and box heights ($H(z)$)
 - (c) Total column HCHO from GEOS-Chem (Ω_G) is calculated $\Omega_G = \Sigma_z (n_{HCHO}(z) \times H(z))$ along with total column air (Ω_A , calculated similarly)
 - (d) The shape factor $S_z(z)$ is calculated on each altitude $S_z(z) = n_{HCHO}/\Omega_{HCHO}$.
 - (e) Pressures (p) are used to create sigma coordinates $\sigma(z) = (p(z) - p_{TOA})/(p(0) - p_{TOA})$
 - (f) $S_\sigma(z)$ is calculated on each altitude: $S_\sigma(z) = C_{HCHO}(z) \times \Omega_A/\Omega_{HCHO}$
2. Satellite pixels (SC, scattering weights ($\omega(z)$), pressure levels, latitude and longitude) are read from the OMHCHO dataset
3. For each pixel, a new AMF (AMF_{GC}) is created using the GEOS-Chem shape factors and satellite scattering weights:
 - (a) scattering weights (ω) are interpolated onto the same vertical dimensions (z and σ) as the shape factors.
 - (b) Integration (approximated using rectangular method) is performed along the vertical dimension to calculate the new AMF on both coordinate systems:

$$\text{AMF}_z = \Sigma_z (\omega(z) \times S_z(z) \times H(z)) \quad (2.18)$$

$$\text{AMF}_s = \Sigma_\sigma (\omega(\sigma) \times S_\sigma(\sigma) \times d\sigma) \quad (2.19)$$

4. These two AMFs represent the same thing using different coordinates, and either one can be used as the AMF_{GC}
5. The AMF_{PP} (created separately) and AMF_{GC} are used to determine the new vertical columns (Ω_P , Ω_G respectively): $\Omega = SC / AMF$
6. A reference sector correction (RSC) is defined each day using these AMFs along with modelled HCHO over the remote pacific:
 - (a) GEOS-Chem satellite overpass output ($\Omega_{GEOS-Chem}$ from 140°W to 160°W) are averaged monthly and longitudinally to provide a modelled reference sector $\Omega_0[lat]$
 - (b) The modelled reference slant columns (MRSC) are calculated using $MRSC = \Omega_0 \times AMF$ for each AMF

- (c) For each satellite pixel between 140°W and 160°W , the correction is calculated as the measured SC minus the MRSC at the nearest latitude:
- $$\text{corr}[\text{lat}, \text{track}] = \text{SC}[\text{lat}, \text{track}] - \text{MRSC}[\text{lat}]$$
- (d) These corrections are binned by satellite detector (track: 1-60), and latitude (0.36° ; 500 latitudes from 90°S to 90°N)
- (e) The median entry of each bin is determined and this forms the RSC[lat,track] (e.g., figure 2.31)
7. VCC are determined using $\text{VCC} = (\text{SC} - \text{RSC}[\text{lat}, \text{track}]) / \text{AMF}$ for each measured SC and using each AMF, with the RSC linearly interpolated to the latitude of the satellite pixel
8. The VCC (along with most of the pixel and GEOS-Chem data) are binned onto a 0.25° by 0.3125° grid along with how many pixels have been binned, and the average pixel uncertainty in product OMHCHORP

Figure 2.28 shows an overview of how these profiles are used in this thesis. Output from GEOS-Chem is combined with OMHCHO swath data to produce a gridded HCHO file which contains HCHO vertical columns recalculated with GEOS-Chem a prioris. PP code is run on a subset of the globe covering Australia and the pacific ocean, producing AMF_{PP} . The output keeps the original AMF as well as those recalculated using GEOS-Chem (AMF_{OMI} , AMF_{GC} , and AMF_{PP}). Additionally, MOD14A1, OMAERUVd and OMNO2d data are used to create masks which are also stored in the OMHCHORP dataset. The creation of fire, smoke, and anthropogenic influence masks is described in section 2.7.

2.6.2 Creating new shape factors

In order to visualise and analyse OMI HCHO columns, slant columns are transformed into vertical columns using the AMF. The shape factor (S) is one of the key components in creation of the AMF (see section 2.5, equation 2.14). The shape factor is calculated using GEOS-Chem satellite output (see section 2.4.7.1) which provide simulated HCHO concentration profiles ($\eta(z)$) and total columns (Ω) at $2\times2.5^{\circ}$ horizontal resolution. Using equation 2.12 to determine the shape factor is straightforwards $S(z) = \frac{\eta(z)}{\Omega}$. The associated OMI per-pixel scattering weights are not changed in this calculation (unlike in section 2.6.5).

Model output is in molecules per billion molecules of air (ppb), and is converted before being used in the shape factor calculation. The following equation converts model profile output from ppb into number densities:

$$\eta_{\text{HCHO}} = \text{ppb}_{\text{HCHO}} \times \eta_a \times 10^{-9} \quad (2.20)$$

where η_{HCHO} is the number density of a HCHO, η_a is the number density of air (from model output), and ppb_{HCHO} is the molecules of that species per billion molecules of air. The modelled total vertical column Ω_{HCHO} is determined by:

$$\Omega_{\text{HCHO}} = \sum_z (\eta_{\text{HCHO}} \times H(z))$$

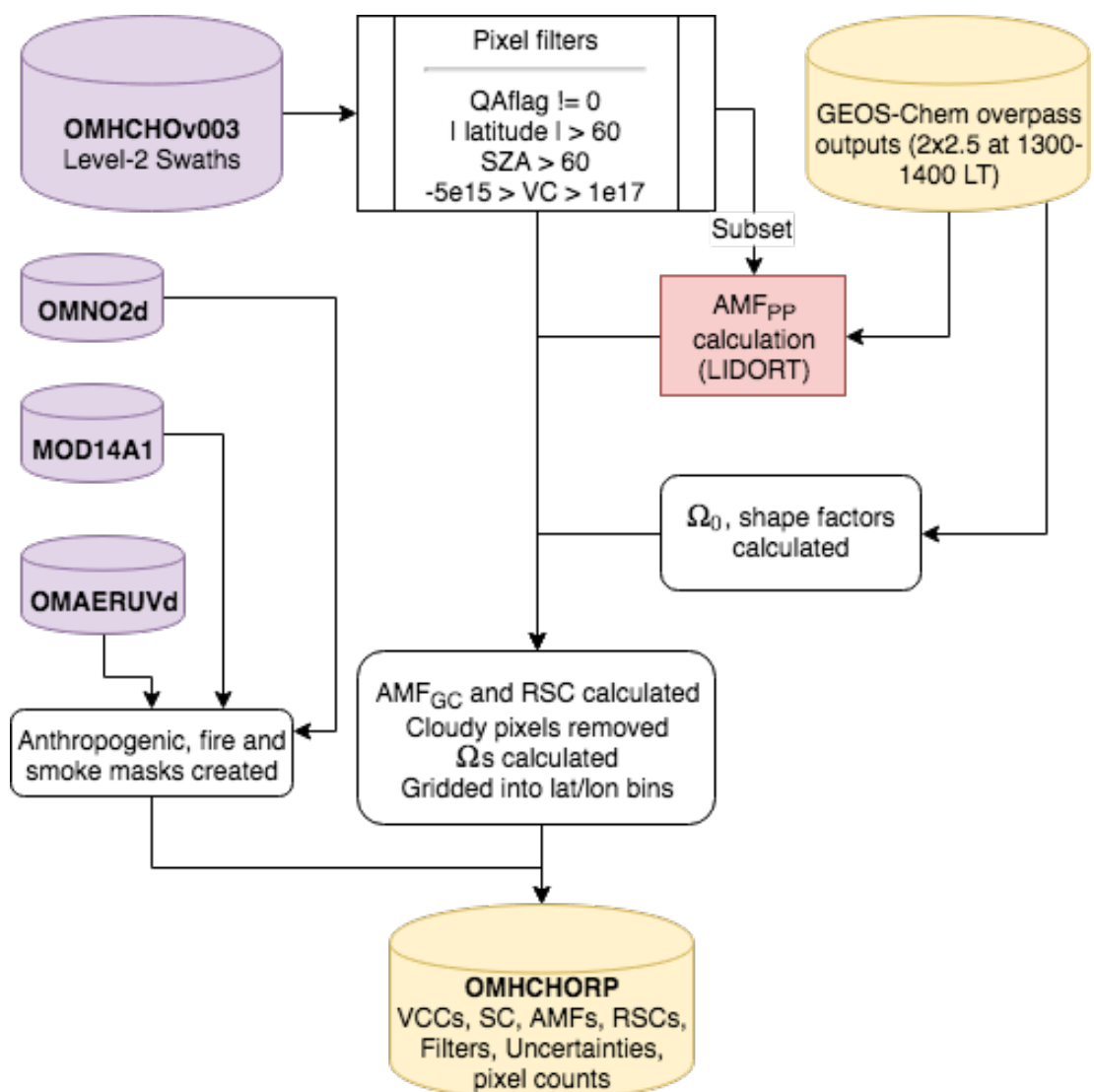


FIGURE 2.28: Flow diagram showing how OMHCHO level two swath data is read, processed, and gridded in this thesis

where $H(z)$ is the box height for level z . In effect this equation sums over the molecules per cm^2 in each altitude level.

As a sanity check S_σ is calculated (through equation 2.15) to confirm that these shape factors are equivalent. Comparing the resulting AMFs created by equations 2.16 and 2.14 for each pixel provides confidence in the unit conversions (and other factors) applied. For example see figure TODO: plot showing correlation between AMF_z and AMFs - or state that these are exactly one to one if that is the case..

2.6.3 Reading satellite data

First satellite slant columns of formaldehyde for the years January 1st, 2005 - April 1st, 2013 are downloaded (see section ??). The data set used is from the Ozone Monitoring Instrument (OMI) on board the Aura satellite, as it has data for the entire time line and sufficiently covers the southern hemisphere. When reading OMHCHO level 2 swath files, several factors are taken into account in order to filter uncertain and erroneous pixels. The process is outlined in figure 2.28 for a single day. First all *good* pixels (those with QA flag equal to 0) are read into a long list (roughly 1 million per day). These are then filtered by solar zenith angle (SZA) and latitude, similarly to other works (Marais et al. 2012; Barkley et al. 2013; Bauwens et al. 2016; Zhu et al. 2016, e.g.). This filtering removes highly uncertain pixels, along with those for which instrument problems such as the OMI row anomaly (see section ??) may have affected.

Satellite measurements polewards of 60° north or south are removed as well as measurements with SZA greater than 60° . Pixels with cloud fraction greater than 40% are removed after being used in determining the reference sector correction (see section 2.6.7), as is done in Gonzalez Abad et al. (2015) and De Smedt et al. (2015). Further filtering is performed to remove the measurements which are most likely to be unrealistic: those with column density outside the range -0.5×10^{16} to 10^{17} molec cm^{-2} , as is performed by Zhu et al. (2016). This filter is required due to currently unexplained large negative values which occur in the OMI HCHO product increasingly over time. Figure 2.29 shows how unfiltered HCHO columns are affected by a small set of highly negative values which heavily affect the mean column amount over any region. The histograms here show the negative (left) and positive (right) total column HCHO measurements from a subset of swaths over Australia, on the 18th of March 2013. The highly negative values can be seen around the -10^{19} molecules cm^{-2} region.

Additional information is added to each pixel, including the new AMFs (see the following subsections). Each pixel and its relevant data are saved in a long list for subsequent gridding. The shape factors and scattering weights for each pixel lie along a z-axis which is vertically resolved to 47 layers.

2.6.4 Creating the new AMF

From equation 2.14 we have:

$$\text{AMF} = \int_0^\infty \omega(z)S(z)\text{dz}$$

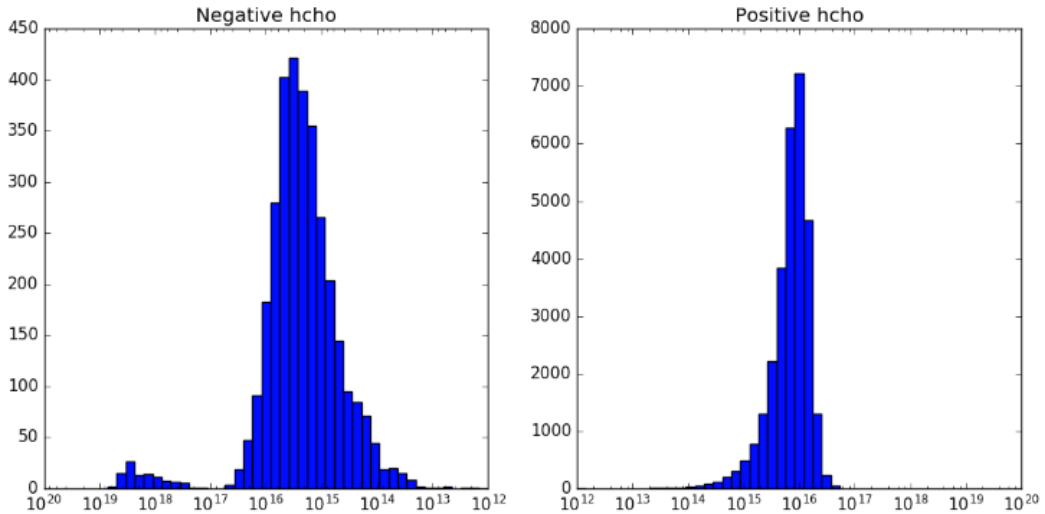


FIGURE 2.29: Column density histograms for a subset of OMI swaths over Australia on the 18th of March 2013. Negative entries are shown in the left panel, positive in the right, note the different scale between negative and positive panels.

then using the $\omega(z)$ from satellite output, along with our calculated S_z interpolated linearly onto the same vertical grid as $\omega(z)$, the AMF can be determined through integration. The integration is performed using a simple rectangular method, which multiplies the integrand midpoints by the change in height, and then takes the sum for each vertical box. This assumes that the provided scattering weights and shape factors are linear between the 47 resolved values.

2.6.5 Recalculating the AMF using PP code

Some of the pixels (those covering Australia and most of the zonal band) have their AMFs recalculated using Fortran code written by Paul Palmer, and Randal Martin, subsequently updated by Luke Surl. I will refer to this as the PP code, and subscript the VCs and AMFs with PP when referring to those calculated through this method. Running this code is computationally expensive, and is subset to within the region ($50\text{--}10^\circ \text{S}$, $160^\circ \text{W}\text{--}160^\circ \text{E}$). The code uses a combination of GEOS-Chem a priori profile information and satellite measurement data to calculate the AMF by using LIDORT radiative transfer calculations to determine scattering. The instrument sensitivity (or scattering weights; ω) and shape factors for each pixel are calculated within the PP code, which outputs AMF_{PP} .

Code for recalculating AMFs using satellite swaths and modelled aerosol optical depths and gas profiles can be found at http://fizz.phys.dal.ca/~atmos/martin/?page_id=129. The original method for HCHO is layed out in Palmer et al. (2001), with modifications for clouds and use of the LIDORT RTM (Spurr 2002) as described by Martin et al. (2003). This code does not work as is when using OMI satellite data,

and requires modifications performed by Luke Surl at Edinburgh University. Additionally the tropopause heights averaged within satellite overpass times are required, and provided by modifying the GEOS-Chem diagnostic output.

Mie scattering and clouds can complicate the calculation of $\omega(z)$, however tables of values for this function at various parameter inputs can be used with modeled vertical shape factors for local AMF calculations. This has been done in the PP code and the AMF look-up-table (LUT) can be found in the source code at (<https://github.com/LukeSurl/amf581g>). In order to run, output is required from GEOS-Chem: the HCHO concentration profile averaged between 1300 and 1400 LT, including optical depths at 550 nm, and dust concentrations. A subset of the OMI pixel information is also required, which is coalesced from OMHCCHO daily swath files into csv files (one per day), and read by the PP code in conjunction with the GEOS-Chem outputs for each day. The PP code then produces a list of recalculated AMFs which is read by my python code and associated with the corresponding pixel (outlined in 2.28).

2.6.6 Vertical columns from AMF

All that remains for recalculating the total vertical column using our new a priori shape factor is to apply the new AMF to the slant columns and grid them onto our chosen resolution. Each satellite pixel at this stage has an associated SC along with three AMFs: the original (AMF_O), one with recalculated shape factors (AMF_G), and one completely recalculated using PP code (AMF_{PP}). These are used to create vertical columns (Ω) through equation 2.6: $\Omega = SC / AMF$.

Figure TODO shows a comparison between the three Ω over Australia for 2005. The first row shows the yearly average column amounts, as well as coloured rectangles describing regions which are averaged over time in row 3. Row two from left to right shows the relative differences between Ω_P and Ω_G , Ω_O and Ω_G , and Ω_O and Ω_P .
TODO: Add this plot here.

2.6.7 Reference sector correction

Each satellite slant column measurement is corrected by its divergence from a modelled reference sector. HCHO products from OMI and SCIAMACHY both use a median daily remote pacific ocean radiance reference spectrum, over 15°S-15°N, 140°-160°W where it is assumed that the only significant source of HCHO is methane oxidation (De Smedt et al. 2008; Barkley et al. 2013; Kurosu and Chance 2014).

The RSC method corrects for several problems, however it introduces some a priori model influence. One of the problems removed through this correction method is instrument degradation, which can introduce bias over time. Another is the possible influence of varying dead/hot pixel masks across 2-D detector arrays such as OMI (De Smedt et al. 2015). This method also corrects for the errors introduced through correlations between BrO and HCHO absorption cross sections, which are especially significant at high latitudes (Gonzalez Abad et al. 2015).

Here a new reference sector correction (RSC) is created using modelled and measured HCHO columns over the remote pacific, to produce corrected vertical columns (VCC). This follows Abad et al. (2016), and defines the remote pacific as the band

between 140°W to 160°W. It uses the difference between slant columns (Ω_S) and reference slant columns (Ω_{S_0}) divided by the AMF, plus the modelled reference sector column (Ω_{V_B}):

$$VCC = \frac{(\Omega_S - \Omega_{S_0})}{AMF} + \Omega_{V_B}$$

This method is used in several works, including De Smedt et al. (e.g., 2008), De Smedt et al. (2012), De Smedt et al. (2015), Barkley et al. (2013), and Bauwens et al. (2016). Recently this correction was expanded (for OMI data) to include latitudinal and instrument track influence by Gonzalez Abad et al. (2015).

To get the modelled slant columns, each of the AMFs (calculated in prior sections) is applied to the modelled vertical columns using equation 2.17. The longitudinal average is taken within the remote pacific, as corrections are assumed to be longitudinally invariant. The modelled reference sector is averaged over the month and interpolated latitudinally to 500 equidistant bins. Figure 2.30 shows the simulated reference sector VCs as an example, calculated for January 1st 2005. In this figure the vertical resolution is increased from 2° to 0.36°, through linear interpolation, in order to form 500 vertical bins which are used in correcting the satellite data. Each day, satellite measurements (pixels) over the remote pacific are used to determine a correction array. The model does not produce slant columns associated with each measurement, however one is created by multiplying the vertical column with the associated slant columns AMF.

For OMI swaths, each row of measured data contains 60 “Across track”(track) measurements. The track index (i) relates the measurement to one of the 60 columns of data. Corrections (molecules cm⁻²) for each measurement are calculated by taking the difference between the measured slant column and the a priori slant column as follows:

$$Correction(i, j) = SC_{HCHO}(i, j) - VC_{GEOS-Chem}(lat(j)) \times AMF(i, j) \quad (2.21)$$

where j represents a latitude index and $VC_{GEOS-Chem}(lat)$ represents the a priori reference sector vertical column HCHO at the latitude corresponding to j . The RSC is independently calculated for each of the 60 tracks, at each latitude in the 500 0.36°bins. This provides a different RSC for each of the three AMFs.

Due to incomplete latitudinal coverage, the correction for each track is interpolated linearly between measurements, with corrections outside of the highest measured latitudes being equal to the corrections at the highest measured latitudes. Figure 2.31 shows an example of the 60 track corrections for January 1st 2005, the points are satellite measurements longitudinally averaged over the remote pacific, coloured by track number. Another way to look at this correction is given in the OMI corrections panel of figure 2.30, which has the sensors along the x axis, and latitude on the y axis, and shows how for this example 8-day period, the corrections are distributed with more negative values towards the left or right sensors, especially in the tropics.

One correction is associated with every good satellite measurement which is used to create a reference sector corrected measurement (Vertical Column Corrected or

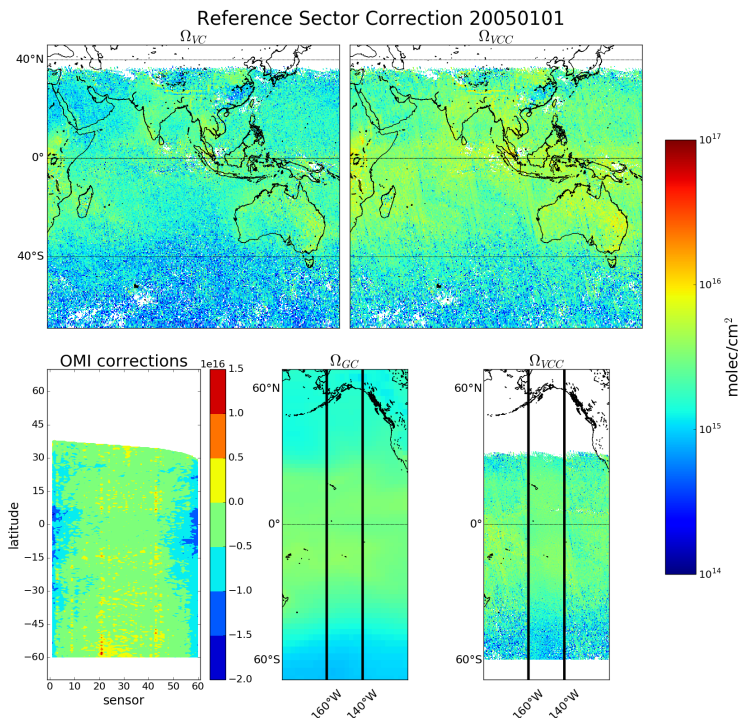


FIGURE 2.30: Example of remote pacific RSC using 8-day average measurements and one month modelled data. Ω_{VC} shows the uncorrected vertical columns, while Ω_{VCC} shows the corrected vertical columns. OMI corrections shows the correction applied globally based on latitude and OMI track number(sensor). Ω_{GC} shows the GEOS-Chem modelled HCHO VC over the RSC, with Ω_{VCC} showing the corrected VC over the same area.

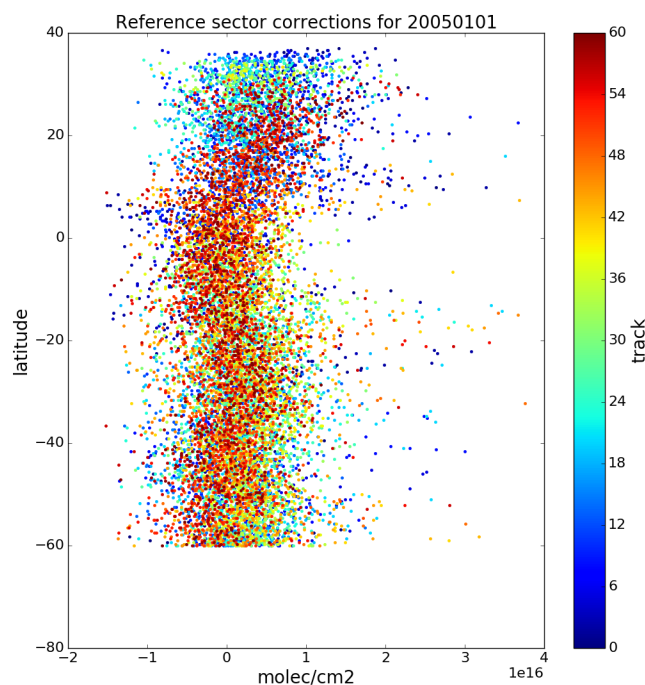


FIGURE 2.31: Example of track correction interpolations for January 1st 2005, points represent the difference between satellite slant column measurements and modelled slant columns over the remote pacific.

VCC) through the following equation:

$$VCC(i,j) = \frac{SC_{HCHO}(i,j) - Correction(i, lat(j))}{AMF(i,j)} \quad (2.22)$$

For each day, good satellite measurements and associated SC, VC, VCC, and AMFs are listed.

2.6.8 Binning the results daily

Finally the pixels are binned into a gridded dataset named OMHCHORP, as shown in figure 2.28. The resolution is chosen to match the native resolution of GEOS-Chem ($0.25 \times 0.3125^\circ$) and the GEOS met data fields. A bin entry count is used to allow easy re-binning, and can be used to check for sparse data days due to filtering or poor weather. Data averaged into this dataset are as follows:

1. satellite SC
2. satellite AMF
3. satellite VC
4. satellite RSC VC
5. GEOS-Chem recalculated AMF
6. GEOS-Chem recalculated VC
7. GEOS-Chem recalculated RSC VC
8. GEOS-Chem AMF recalculated using Paul Palmer code (AMF_{PP})
9. GEOS-Chem RSC VC based on AMF_{PP}
10. Smoke AAOD from OMAERUVd (mapped into bins from $1 \times 1^\circ$ resolution)
11. satellite pixel counts (summed into bins)
12. fire counts (summed into bins)

This whole process requires some processing time as well as RAM and computer storage space, and has been performed on the National Computing Infrastructure (NCI) supercomputer cluster. In order to reprocess one year of swath files, ~ 162 GB ($142 + 16 + 4$ OMHCHO, MOD14A1, and OMNO2d respectively) of daily data was downloaded and then transformed into ~ 8 GB (per year) of daily gridded data. This takes around 90 minutes per day, and is very parallelisable as each day is completely independent once the model has run in each required configuration. Initially parallelism was built into the python code, however simply sending separate jobs to NCI's process queue was simpler and more scalable. As much as possible, processing is done using the HDF-5 or NetCDF-4 formats, with some GEOS-Chem output being read from bitpunch. The scripts to regrid and reprocess the swath data set are available from github at TODO.

2.6.9 Difference between new and old OMI HCHO columns

New corrected vertical columns (VCC) of HCHO are created at global $0.25 \times 0.3125^\circ$ horizontal resolution. These calculations are compared over Australia in figure(s) 2.32, TODO: regression, and time series. Figure 2.32 shows how the recalculated columns compare to the original (OMI, left). Recalculation increases the January column amounts while also slightly flattening the distributions (row 3). The effect of not recalculating the ω_z can also be seen in figure 2.33 which shows the altered satellite vertical columns using each method.

Figure 2.33 shows vertical columns of HCHO for: column 1) the original satellite swaths, column 2) recalculated without changing the provided scattering weights, and column 3) fully recalculated vertical columns. Each grid square (at $0.25 \times 0.3125^\circ$ resolution) has been created by binning the recalculated satellite pixels within the month. The average number of pixels per land square is inset as text, changing due to how the fire filter is applied. Each row has a stricter fire filter applied from top to bottom, with no fire filter on the first row up to filtering pixels from squares with fires up to 8 days prior. This figure looks at March 2005 with biomass burning filtered differently in each row. Active fires over the last 0, 1, 2, 4, and 8 days are filtered as the row number increases.

Figure TODO shows an analysis of the differences between running the recalculations with and without updating the ω_z .

TODO: compare how many nans from palmers code to my code. The AMF calculated using professor Palmer's produces TODO: MORE OR FEWER reasonable (within screening range of -5×10^{15} to 1×10^{17}) vertical column amounts. Stricter filtering must be balanced against both coverage and the sensitivity of the AMF determination to recalculating ω_z .

Figure TODO: shows global and Australian HCHO averaged total column maps for January 2005, along with the reduced major axis (RMA) regression correlation and percentage difference. This comparison shows how reprocessing with an updated model can have a systematic influence on the total column.

2.7 Filtering Data

In order to examine only biogenic processes, pyrogenic and anthropogenic influences need to be removed from modelled and measured data. Biomass burning can be a large local or transported (via smoke plumes) source of HCHO, CHOCHO, glyoxal, and other compounds which influence levels of both HCHO and isoprene. Anthropogenic emissions from power generation, transport, and agriculture can influence these levels as well. Where possible these influences need to be removed so that calculations of purely biogenic emissions are not biased. In GEOS-Chem we can simply turn off pyrogenic and anthropogenic emissions, however in satellite datasets we need to mask potentially affected pixels.

Influence from biomass burning can be removed through measurements of acetonitrile and CO (e.g., Wolfe et al. 2016; Miller et al. 2016), or else removal of scenes coincident with satellite detected fire counts and aerosol absorption optical depth as done in Marais et al. (2014). Marais et al. (2012) remove pixels collocated with non zero

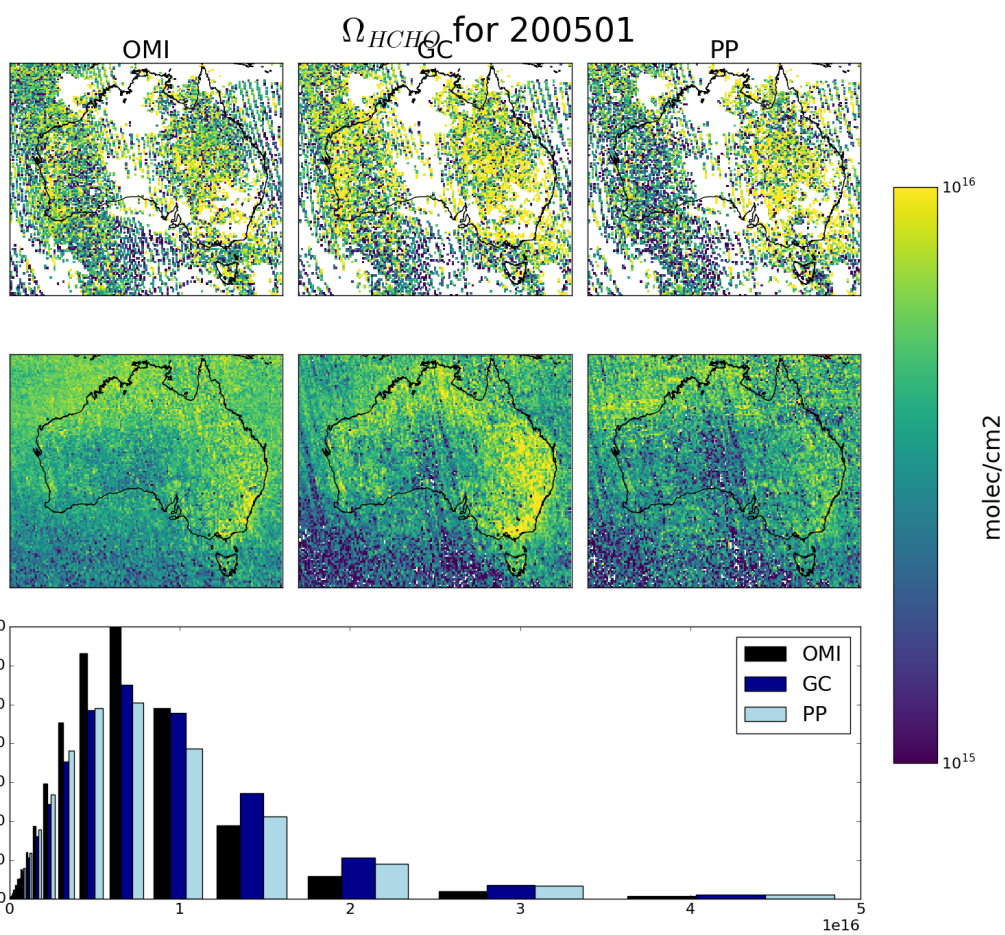


FIGURE 2.32: Row 1: regridded corrected Ω_{HCHO} from OMHCHO on January 1, 2005: original (left), recalculated using new shape factors (middle), and additionally using updated scattering weights (right). Row 2: shows the monthly average for January 2005. Row 3: shows the distribution over the month for each of the three column amounts.

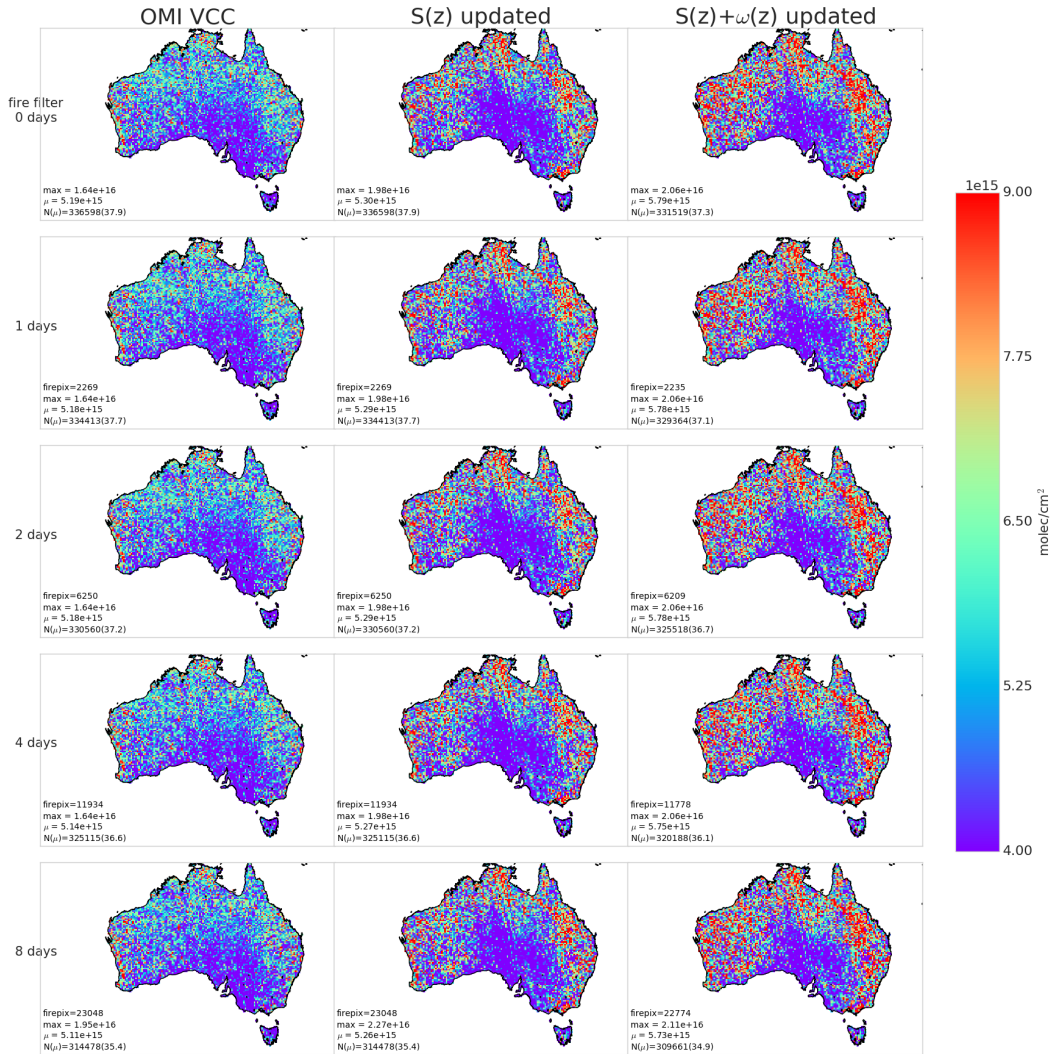


FIGURE 2.33: Column 1: Reference sector corrected HCHO vertical columns Ω from OMHCVOv003. Column 2: Ω with recalculated a priori shape factors using GEOS-Chem v10.01. Column 3: Ω with recalculated a priori shape factors and scattering weights using GEOS-Chem v10.01 and LIDORT. Row 1-5: increasing number of prior days which have active fires are included when masking fire influence.

TABLE 2.4: How many satellite pixels are filtered by pyrogenic and anthropogenic masking. Left to right the columns display year, how many land pixels are read over Australia, how many of these pixels are removed by the pyrogenic filter, how many are removed by the anthropogenic filter, and how many are removed in total. In parenthesis are the portion of pixels filtered.

Year	Pixels	Pyro	Anthro	Total
2005	3.9e+06	4.1e+05(10.7%)	5.0e+04(1.3%)	4.4e+05(11.5%)
2006	3.8e+06	5.1e+05(13.5%)	9.2e+04(2.4%)	5.6e+05(14.7%)
2007	3.7e+06	4.4e+05(11.9%)	7.5e+04(2.0%)	4.9e+05(13.0%)
TODO				
TODO				

fire counts in any of the prior eight days, within grid squares with $1 \times 1^\circ$ resolution. Barkley et al. (2013) use fires from the preceding and concurrent day, within local or adjacent grid squares, with grid resolution of $0.25 \times 0.3125^\circ$. Wolfe et al. (2016) disregard HCHO measurements when acetonitrile > 210 pptv and CO > 300 ppbv, while acetonitrile > 200 pptv is used to determine fire influence in Miller et al. (2016). TODO: look at yearly correlation, compare to exponential curve and look for fire outliers As seen in TODO: citation, HCHO concentrations scale exponentially with temperature. This allows another method for detecting the influence of non-biogenic HCHO emission/creation by looking for outliers above the curve at low temperature. Zhu et al. (2013) has a similar analysis over south-eastern USA showing an exponential correlation of $HCHO = \exp(0.15 \times T - 9.07)$.

I use satellite data to account for anthropogenic and pyrogenic influences on the OMHCHO satellite HCHO columns. MODIS fire counts are used in conjunction with smoke AAOD enhancements (from OMI) to remove data points which may be affected by fires or fire smoke plumes. OMI NO₂ measurements are used to mask potential anthropogenic influence. These masks negatively affect uncertainty, as fewer measurements are available to be averaged. This section describes the creation and effects of filters used on satellite data.

A quick summary of how much data is filtered over Australian land squares is provided in table 2.4, and an quick check of how many pixels are filtered in January 2006 can be seen in Figure 2.34. The anthropogenic filter completely removes grid squares over Sydney and Melbourne, and high removal rates over Brisbane. Other major cities in Australia either do not emit enough NO₂ or are too spread out and do not breach the threshold to be filtered as anthropogenic.

2.7.1 Fire and smoke

The method used in this thesis follows that of Marais et al. (2012), and Barkley et al. (2013), with active fires filtered using fire counts, and smoke filtered out using smoke AAOD. We use the MODIS fire counts, detected from space using the combined product from Terra and Aqua (Terra at 10:30, 22:30 LT; Aqua at 13:30, 01:30 LT). Smoke plumes are filtered using smoke AAOD from product OMAERUVd, with the threshold determined through analysis of Australian AAOD distributions.

Anthro and Fire filters applied on 20060101-20060131

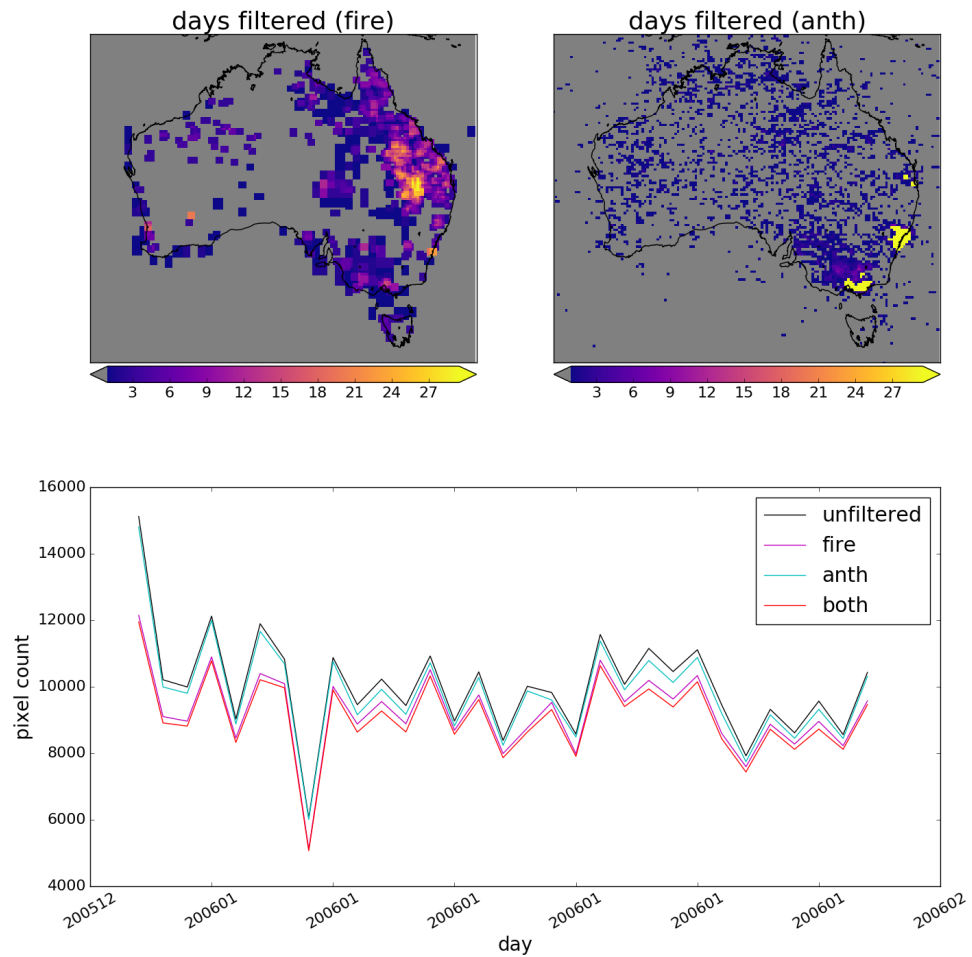


FIGURE 2.34: Top row shows grid squares filtered out by pyrogenic(left) and anthropogenic(right) influence masks during January 2006. Along the bottom is the time series of total pixels over Australian land squares with and without filtering the data.

OMHCHO total column HCHO Ω is processed into a $0.25 \times 0.3125^\circ$ horizontal daily grid. Pyrogenic filters are interpolated to the same horizontal resolution as Ω to simplify application. The following steps are performed in order to create the pyrogenic influence mask:

1. MOD14A1 daily gridded Aqua/Terra combined fire counts ($1 \times 1 \text{ km}^2$) are read, and binned into $0.25 \times 0.3125^\circ$ bins (matching the resolution of binned Ω).
2. A rolling mask is formed which removes Ω if one or more fires are detected in a grid square, or in the adjacent grid square, up to 2 days previously. This includes the current day, making 3 days of fires in total being filtered out on each day.
3. AAOD at 500 nm is mapped from OMAERUVd ($1 \times 1^\circ$ resolution) onto the $0.25 \times 0.3125^\circ$ resolution.
4. An AAOD threshold of 0.03 is determined through visual analysis of AAOD distributions over several days, including days with and without influence from active fires, dust, and transported smoke plumes (see figure 2.35).
5. Grid squares with AAOD over this threshold are considered potentially affected by transported fire smoke.

Determining the AAOD due to smoke can be difficult since both smoke and dust absorb UV radiation (Ahn2008; Marais et al. 2012). AAOD is less sensitive to cloud contamination than AOD, and I use AAOD from the daily gridded level 3 satellite product OMAERUVd (Ahn2008) described in section 2.2.1.3 to provide a filter for smoke plumes. Although removing gridsquares with dust reduces how much data is available to analyse, dust in Australia is highly episodic and should not affect more than a few days per year, especially over regions with high tree coverage (Shao et al. 2007).

Filtering fire smoke using AAOD is done by removing OMHCHO gridsquares where the AAOD is above a 0.03, after the AAOD is mapped from $1 \times 1^\circ$ to the same $0.25 \times 0.3125^\circ$ resolution as our OMHCHO gridded product. The threshold is determined through analysing AAOD over Australia in 4 scenarios: normal conditions, active local fires, during influence from transported fire smoke, and large scale dust storms. Figure 2.35 shows AAOD (columns 1 and 2), with AAOD distribution in column 3, along with satellite imagery on the same day in column 4 (from <https://worldview.earthdata.nasa.gov/>). The scenarios listed are shown from row 1 to 4, and AAOD = 0.03 is demarcated by a horizontal line in the density plots in column 3. Figure 2.36 shows how the smoke filter compares to the fire filter over 2005. The left panel shows how many days are filtered using the AAOD threshold, while the right panel shows how many are filtered using the combined smoke and active fire masks. The time series shows pixels available for analysis before being filtered (black), after smoke filtering (cyan) and after the full fire filter is applied (magenta). The Ayre basin is the dominant area filtered by smoke detection, likely due to dust influence in the arid region.

Figure ?? shows what portion of pixels are filtered out by the pyrogenic filter. The top panel shows the spatial distribution of fire masks, with most pixels removed along the northern and eastern coastlines. A large portion of the filtered areas appear to correspond with forested areas (see figure ??), which suggests that forest fires are being

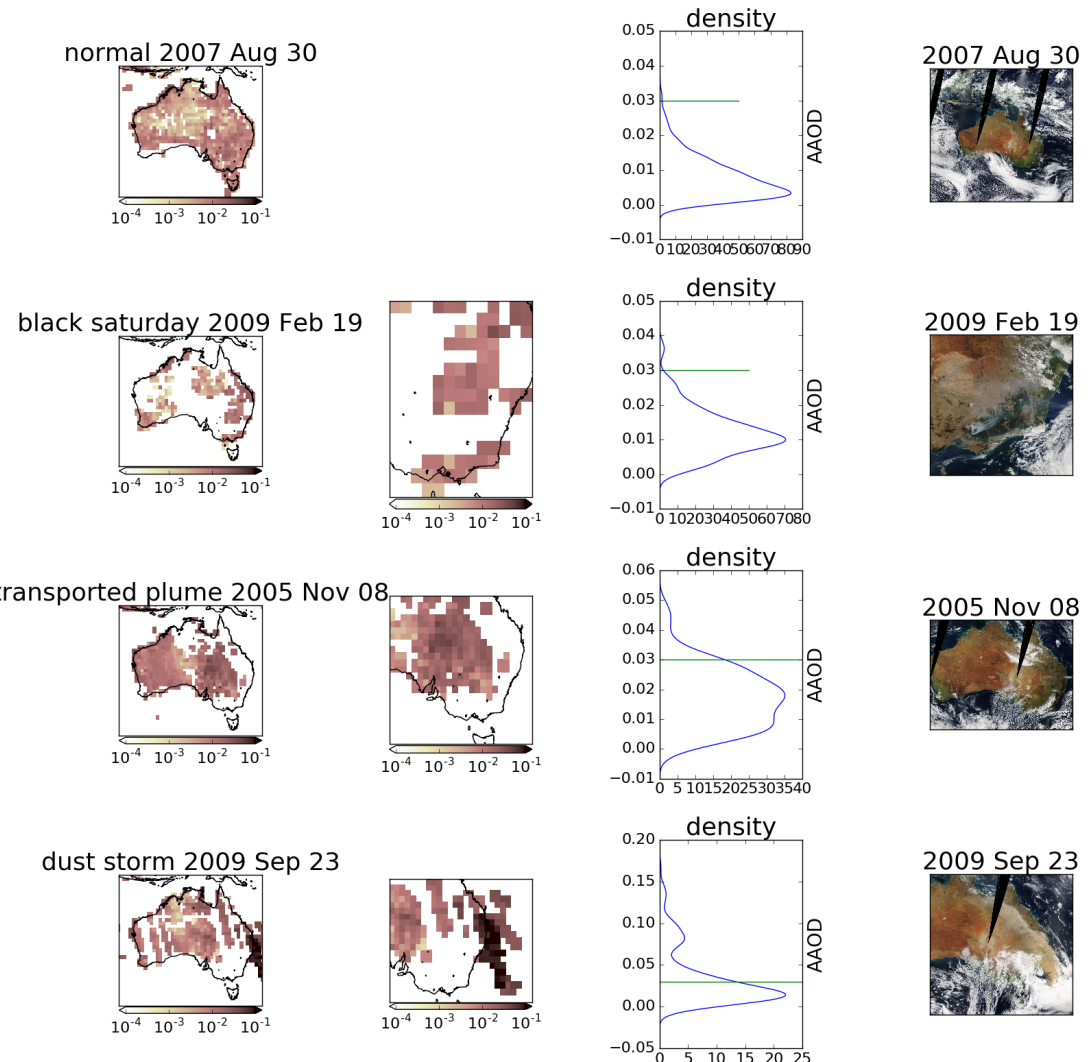


FIGURE 2.35: AAOD from OMAERUVd (columns 1, 2, 3) over Australia for four different scenarios (rows 1-4). Scenes from the same day are taken from the EOS Worldview website <https://worldview.earthdata.nasa.gov/>.

Fire and smoke filters applied on 20050101-20051231

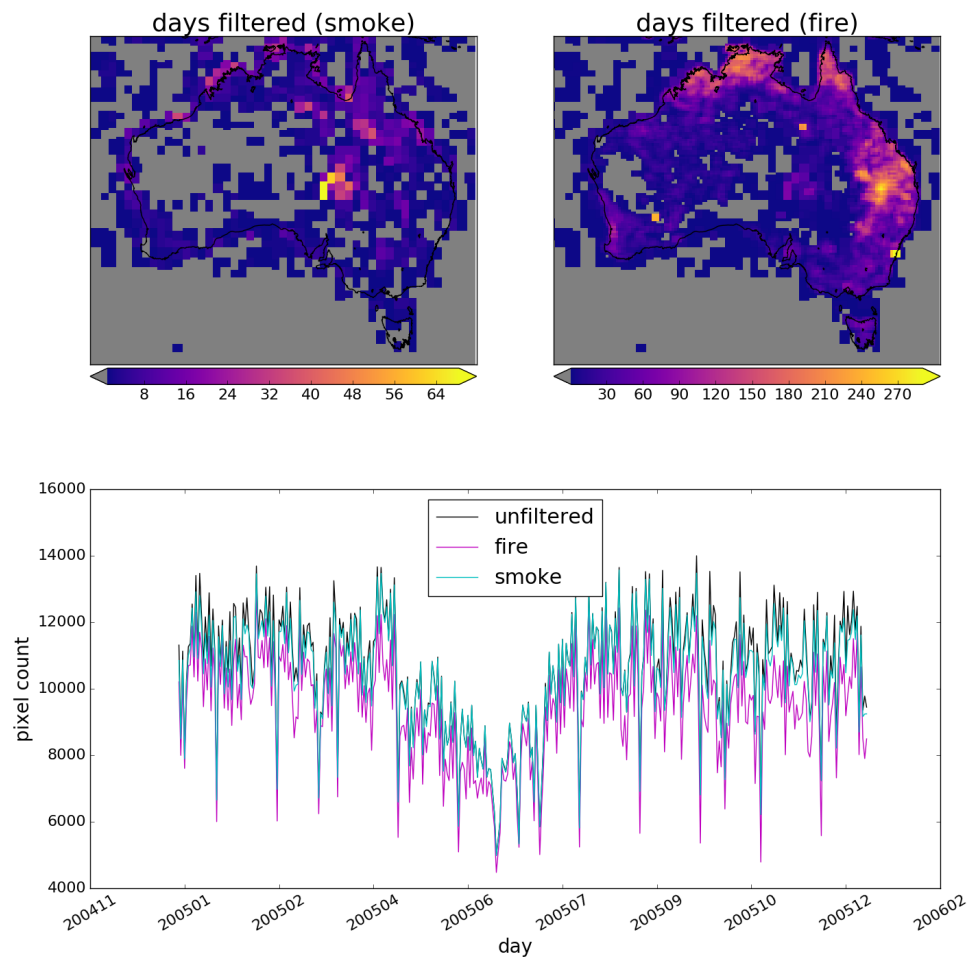


FIGURE 2.36: Smoke (top left) filtered days using AAOD > 0.03 compared to the combined (smoke and active fires) fire filter (top left). Time series shows how many pixels are available for analysis before and after filtering.

masked properly. Central Australia is largely unmasked, which could be due to a lack of sufficient vegetation to create a large enough fire to be seen by satellite. The other potential cause of pyrogenic filtering is the proliferation of petrol or gas wells (see figure 2.38 and figure 2.39). The filtering shown here is for 2005, when 388 gas wells existed in Queensland, however more than 2000 wells (cumulative) were approved by 2013, so this may cause more filtering over the course of this thesis' timeline (Carlisle 2012). To check this the filtering portion for 2012 is also plotted in Figure TODO: plot map of filtered squares for 2012 when it has been run by NCI. One clear hotspot is located over port Kembla (south of Sydney), most likely due to the flame which burns over the blast furnace stack throughout the year. Another hotspot can be seen in Western Australia over Kalgoorlie, where a large open cut gold mine "super pit" is always open and blasting daily. In Western Queensland over Mount Isa there is again a mining related hotspot. A large area in southern Queensland/northern NSW is also heavily filtered, potentially due to gas flaring in the Surat Basin, which has thousands of petrol and gas wells.

2.7.1.1 Checking that fire masks are influencing pyrogenic HCHO

Looking at temperature can provide evidence of pyrogenic HCHO. HCHO precursors are heavily tied to temperature (TODO:cite), and model output shows how higher temperature leads to an increase in HCHO levels. Figures 2.43 - 2.45 show the relationship between modelled temperature, and satellite HCHO for January 2005 within subsets of Australia. A reduced major axis regression is used to determine the correlation between surface temperature (X axis) and HCHO (Y axis). Using the natural log of HCHO we can take the linear regression and then exponentiate each side in the equation $\ln Y = mX + b$ to get $Y = \exp mX + b$. This gives us the exponential fit as shown, with the correlation coefficient between $\ln HCHO$ and temperature. The distributions of exponential correlation coefficients and m terms is shown in the embedded plot, with one datapoint available for each grid square where the regression is performed.

Figures 2.41 and 2.42 show the regressions between OMI HCHO total columns and temperature from GEOS-Chem output and CPC daily maximum temperatures respectively. Comparing against GEOS-Chem modelled surface temperatures first requires deresolution from 0.25×0.3125 to $2 \times 2.5^\circ$ latitude by longitude resolution. The left column in figure 2.41 shows scatter and RMA correlation within a single gridbox over 2 months from Jan 1 to Feb 28, 2005, without having applied either the fire nor anthropogenic masks to OMI HCHO columns. The right column shows the same correlation after applying the fire filter, affected datapoints are marked in teal (matching the red marked points in the left column). The analysis is repeated for Sydney, Canberra, and three gridsquares to the north-west, west, and southwest of Sydney (w1, w2, w3 respectively). Figure 2.42 shows the same analysis at higher resolution using CPC daily maximum temperatures (see 2.2).

One cause of high HCHO at lower temperatures is direct or transported emissions and subsequent products from biomass burning. One potential problem with showing this is that days with fire enhanced HCHO are also likely to be hot. Another problem with correlating heat and HCHO is that increased temperature accelerates HCHO destruction (Zheng et al. 2015). We test the fire mask by examining the relationship

Pyrogenic filter: 20050101-20060101

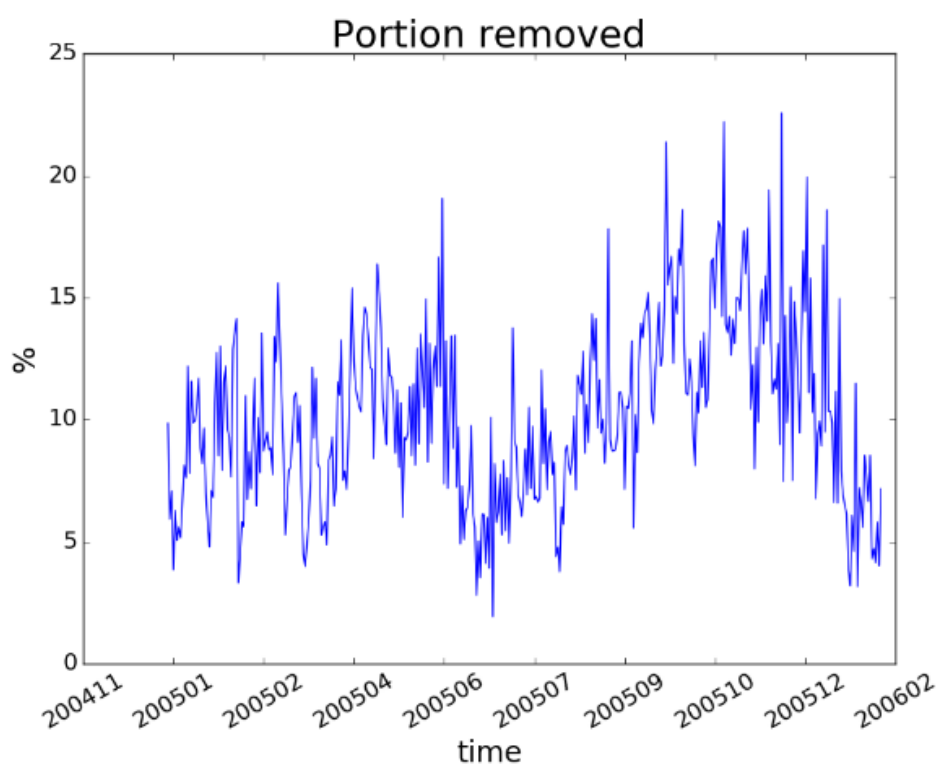
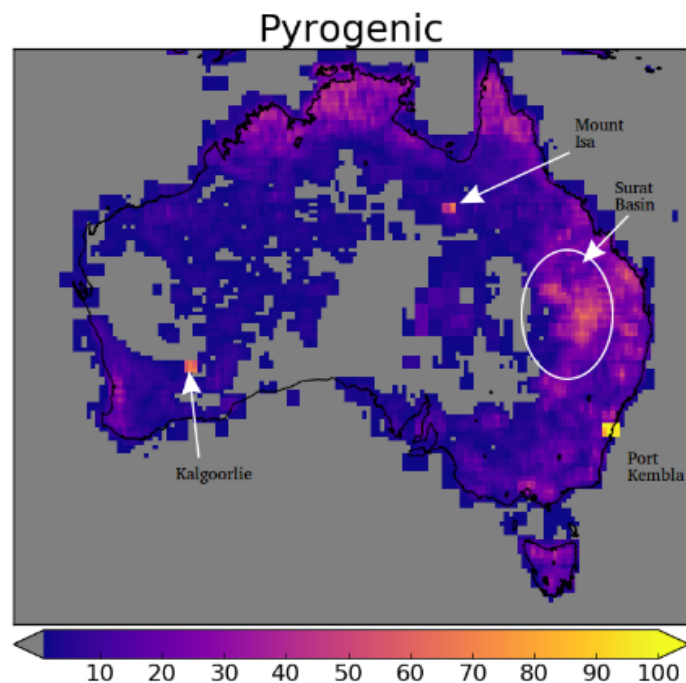


FIGURE 2.37: Top: Portion of 2005 filtered out by fire and smoke masks.
Bottom: portion filtered out each day from land squares in Australia.

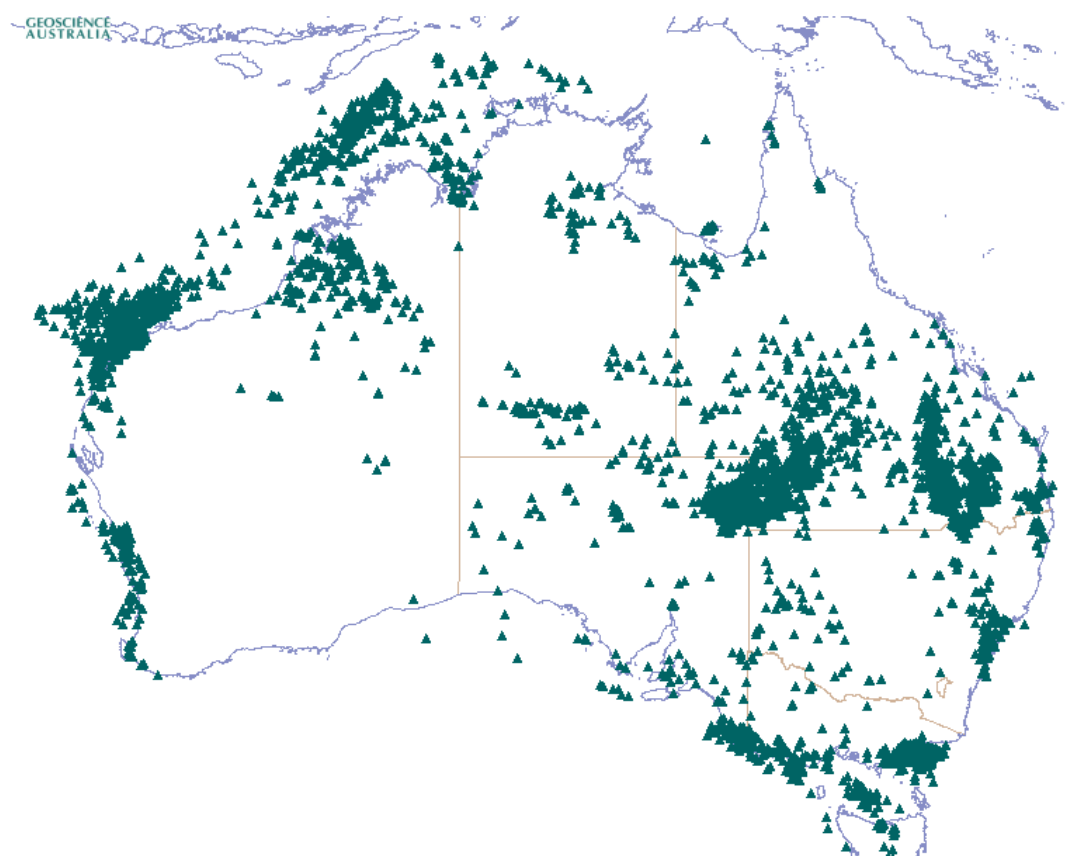


FIGURE 2.38: Petrol Well locations over Australia (current-2018) (<http://dbforms.ga.gov.au/www/npm.well.search>)

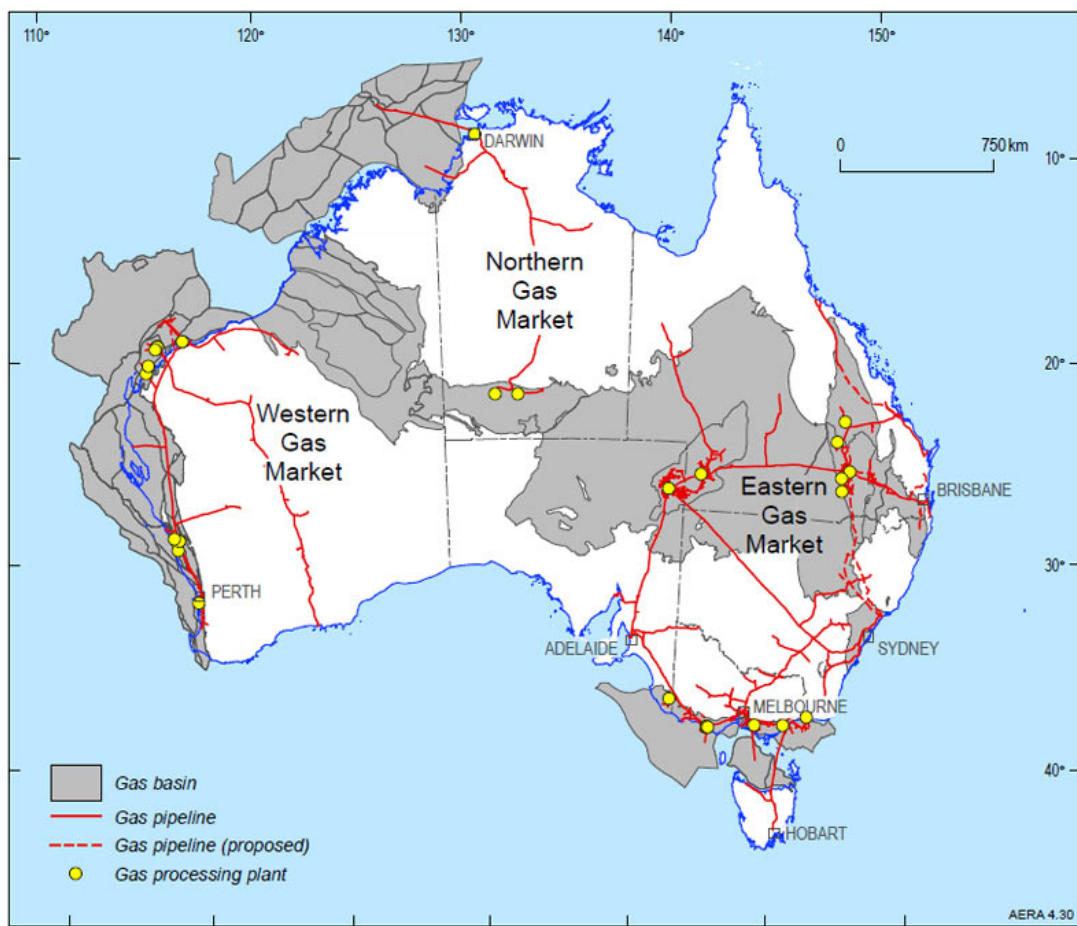
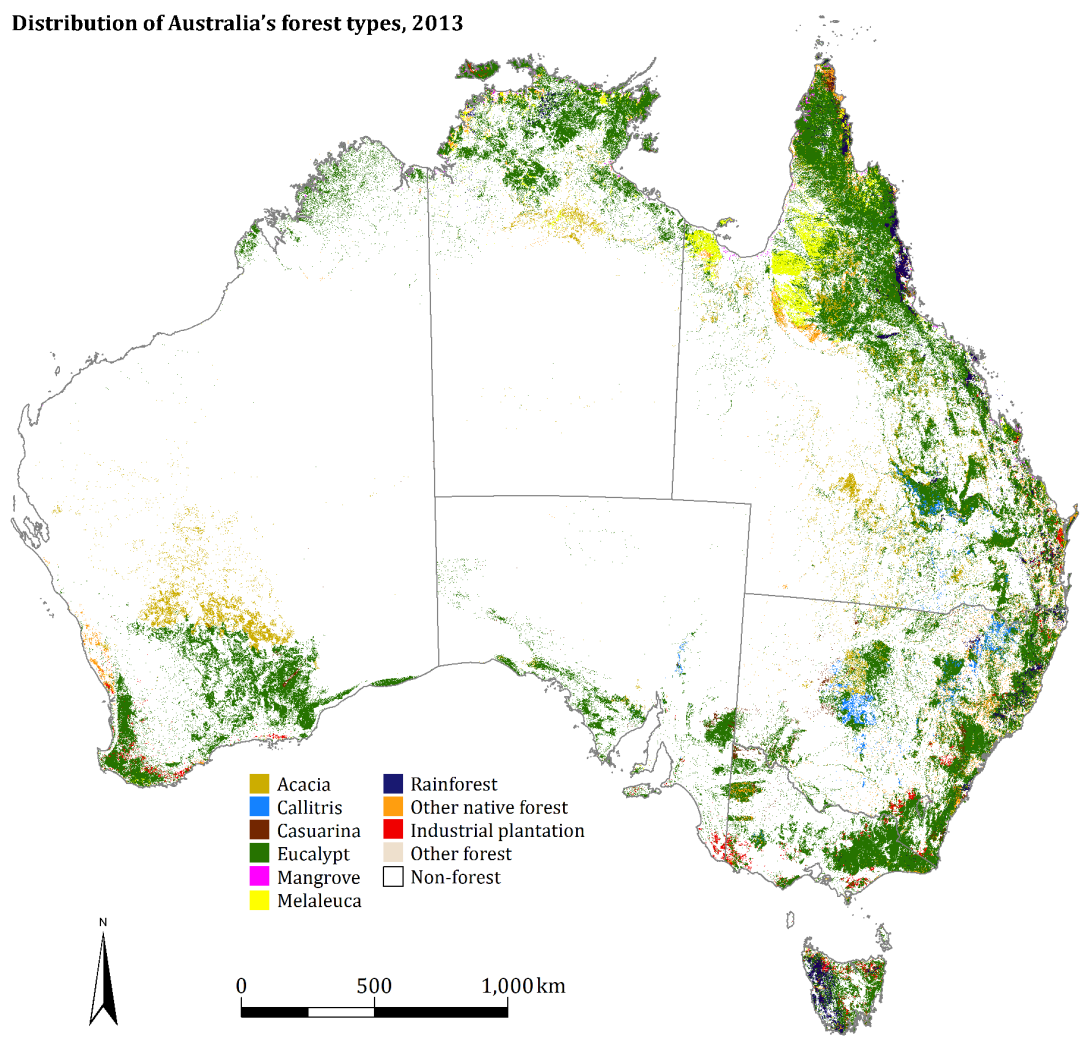


FIGURE 2.39: Gas fields and pipelines (2018) for Australia
(<http://www.ga.gov.au/scientific-topics/energy/resources/petroleum-resources/gas>)



Source: ABARES (2016) Map compiled by ABARES 2016

© Commonwealth of Australia 2016. This material is licensed under a Creative Commons Attribution 3.0 Australia Licence.

FIGURE 2.40: Forest coverage, coloured by predominant tree species.

??

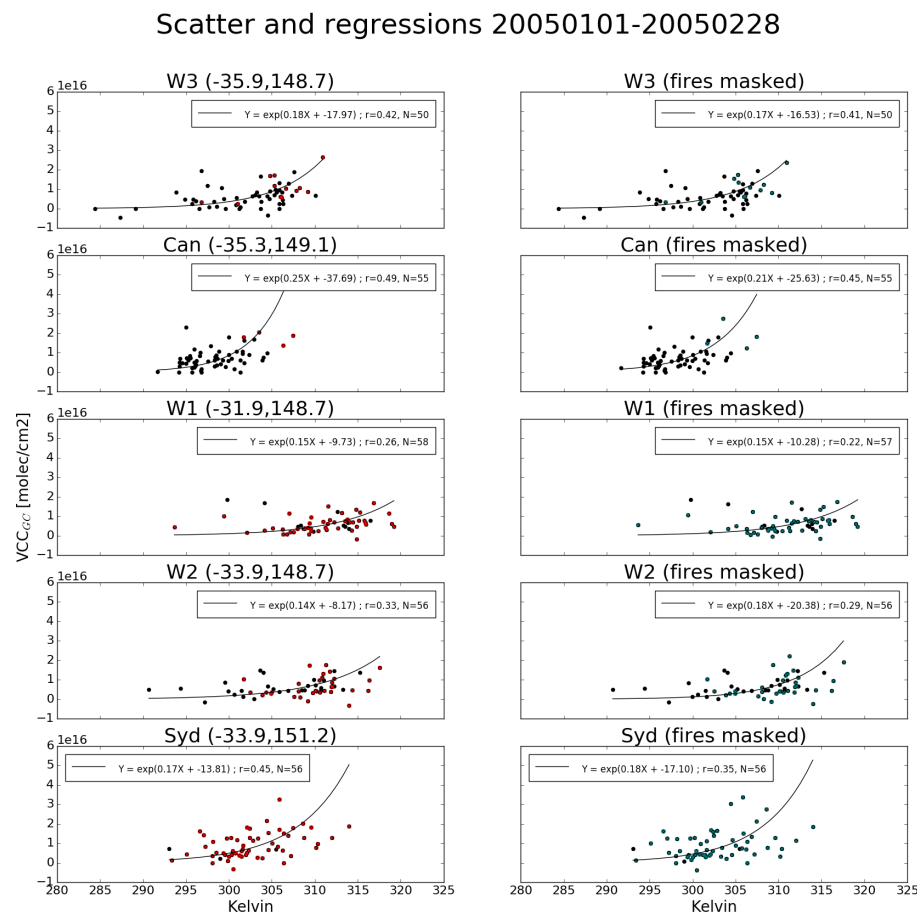


FIGURE 2.41: HCHO vs GEOS-Chem daily midday temperatures
TODO add longer caption

Scatter and regressions (CPC temperature) 20050101-20050228

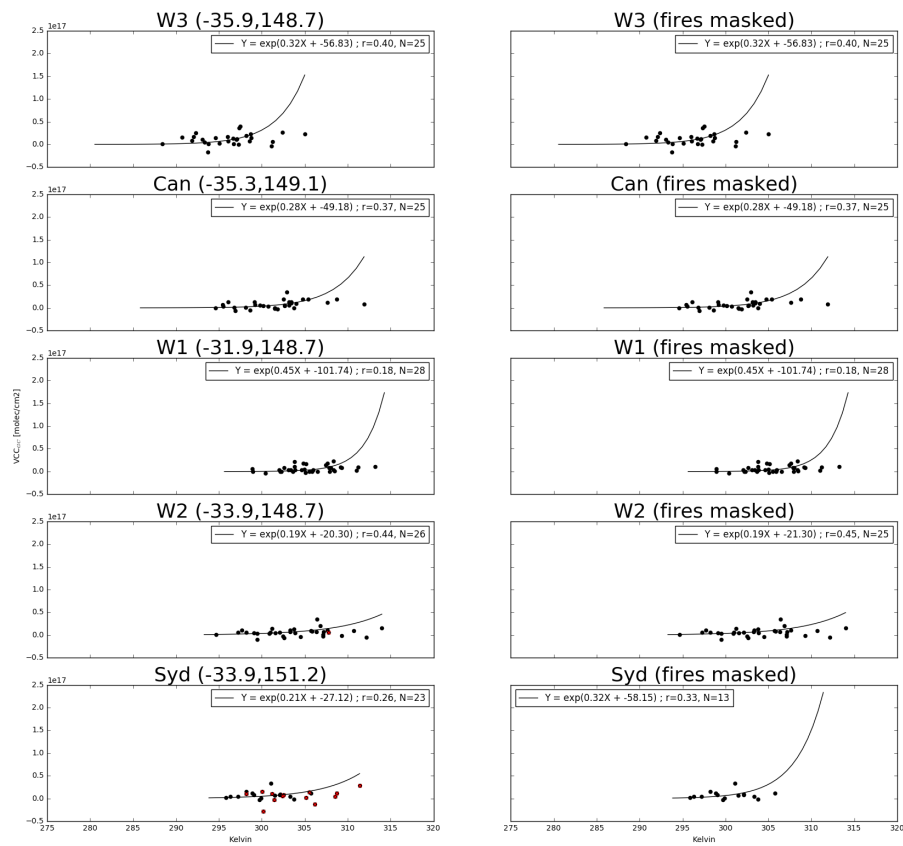


FIGURE 2.42: HCHO vs CPC daily maximum temperatures TODO add longer caption

between modelled temperature and satellite HCHO with and without applying the filters for smoke and active fires. Figures TODO-TODO show the exponential fits for one month of datapoints (January 2005) in Northern, Southeastern, and Southwestern Australia respectively. Each grid square (2 by 2.5°) provides one datapoint per day, with satellite HCHO initially averaged onto the lower resolution of the GEOS-Chem modelled surface (from 0 to ~ 100 m) temperature. The scatter between HCHO and temperature is coloured by fire counts, and we see TODO. The TODO lines show the exponential fit before and after filtering fire and smoke. TODO plot showing how fire mask affects HCHO - Temperature relationship

2.7.2 NO_x

Enhanced NO₂ concentrations can indicate anthropogenic influence over Australia. In order to filter out these influences on satellite HCHO measurements, a filter is designed using the OMNO2d product which includes tropospheric NO₂ columns.

OMNO2d from 2005 is used to determine a suitable threshold for anthropogenic influence by looking at NO₂ columns near several major cities in the south eastern sector of Australia. The mean, standard deviation, and time series over Australia of tropospheric NO₂ seen by Aura is shown in figure 2.46. The average tropospheric NO₂ column averaged within all of Australia and then each region shown in this figure is listed in table TODO 2.5.

Anthropogenic influences on the NO₂ columns are clearly visible near major cities in Australia. A filter is created each year from the OMNO2d product in two steps:

1. Daily gridsquares with NO₂ greater than 10^{15} molec cm⁻² are flagged as anthropogenic.
2. After taking the yearly average over Australia, any gridsquares greater than 1.5×10^{15} molec cm⁻² are flagged for the whole year.

This removes both the gridsquares close enough to cities to be affected by their emissions year round, as well as effects from transported pollution plumes. The affects of applying this filter to the OMNO2d product itself can be seen in figure 2.47

The same regions as in figure 2.46 are shown again in figure 2.48, with NO₂ pixels densities for each region shown, along with the threshold of 1×10^{15} molec cm⁻². This led to a reduction of TODO gridsquares from the total available measurement space over Australia. The removal of gridsquares which went above the yearly averaged limit of 1.5×10^{15} molec cm⁻² further reduced the available data by TODO gridsquares.

2.8 Data Access

TODO: ADD MORE HERE

OMHCHO Satellite swaths of HCHO slant columns downloaded from <https://search.earthdata.nasa.gov>, with DOI 10.5067/Aura/OMI/DATA2015

OMNO2d Daily satellite NO₂ product downloaded from <https://search.earthdata.nasa.gov/search>, DOI:10.5067/Aura/OMI/DATA3007. For more information in refer to section

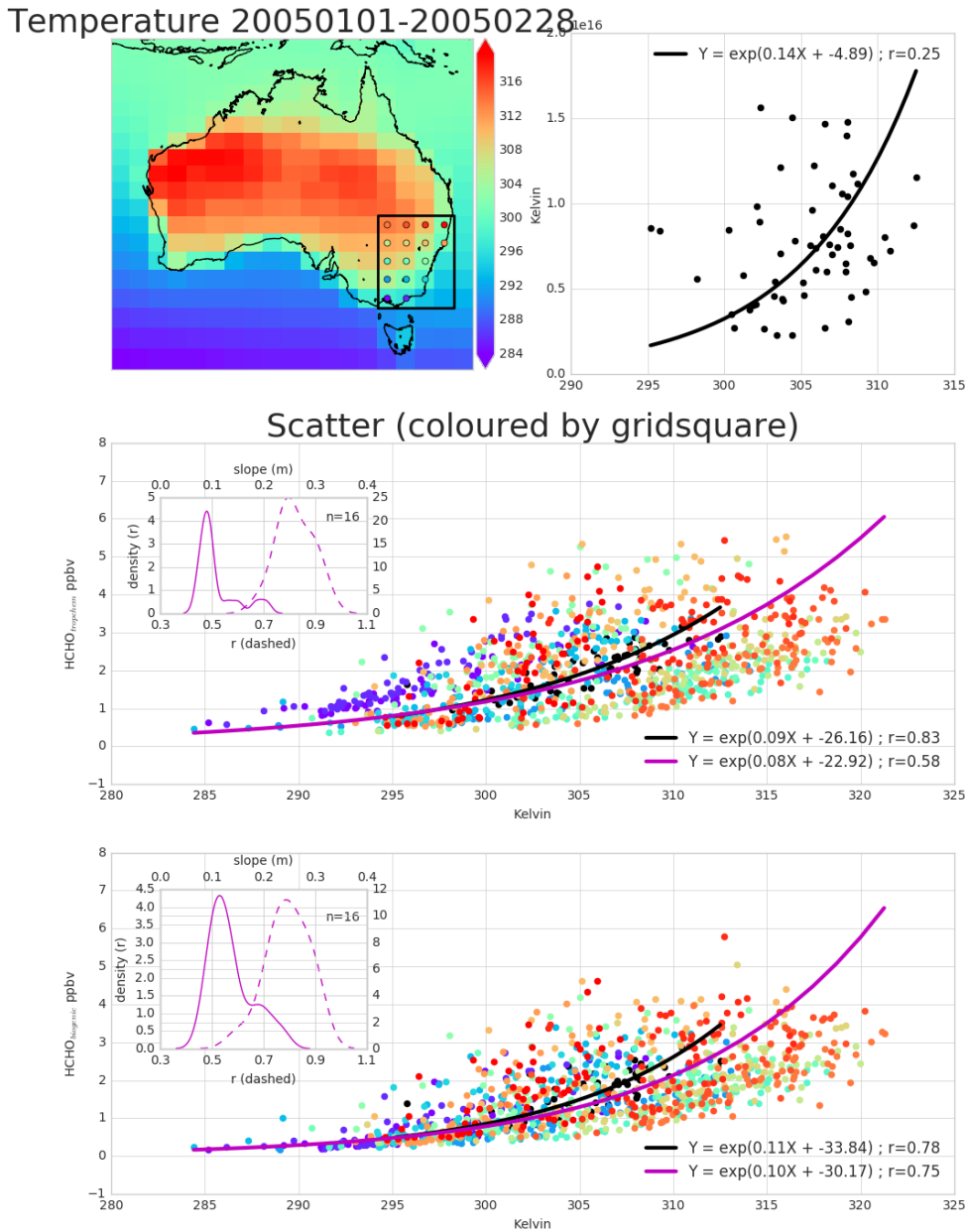


FIGURE 2.43: Top panel: surface temperature averaged over January and February 2005. Bottom panel: surface temperature correlated against temperature over, with different colours for each gridbox, and the combined correlation. A reduced major axis regression is used within each gridbox (shown in top panel) using daily overpass time surface temperature and HCHO amounts (ppbv). The distribution of slopes and regression correlation coefficients (one datapoint per gridbox) for the exponential regression is shown in the embedded plot.

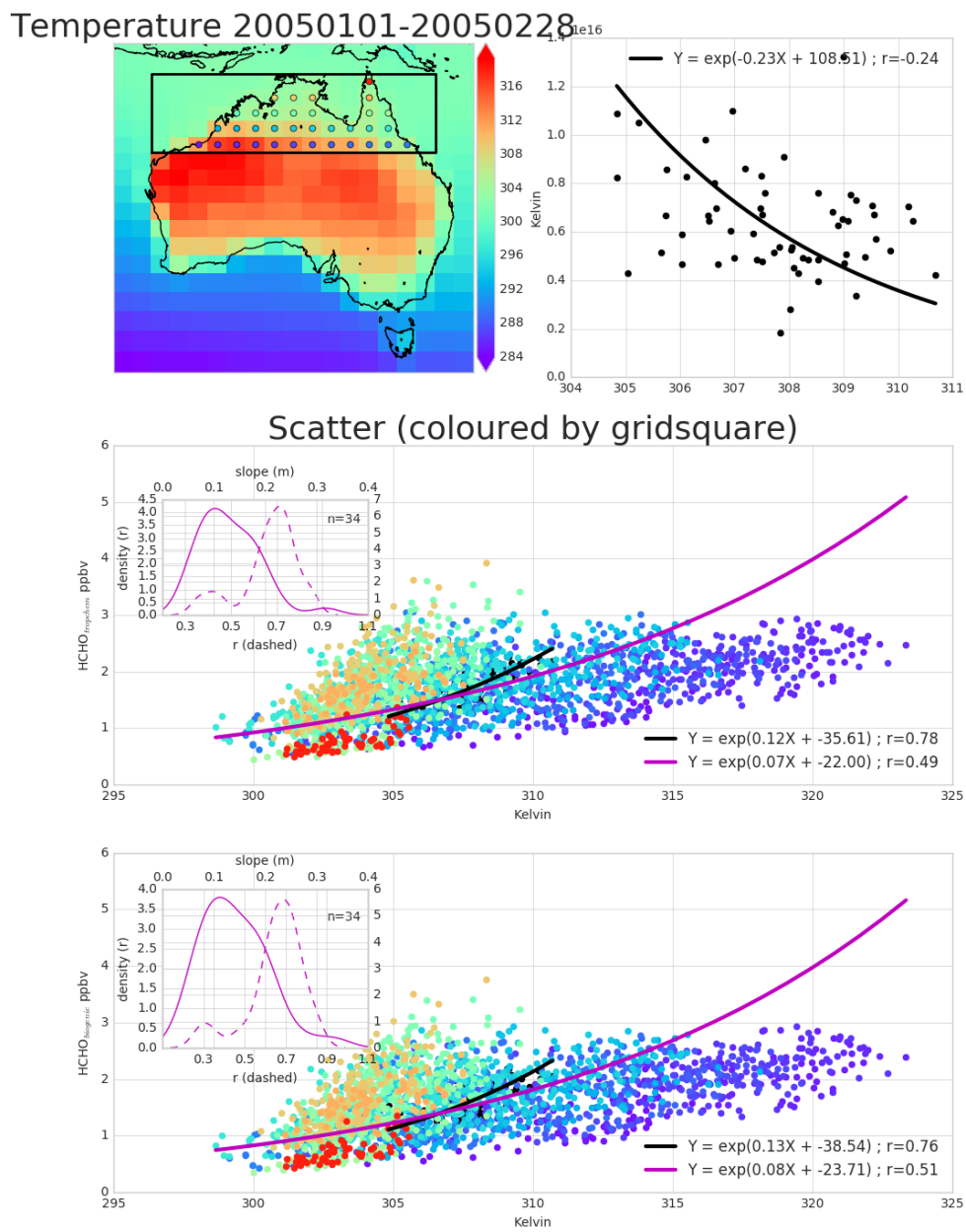


FIGURE 2.44: As figure 2.43 but for northern Australia.

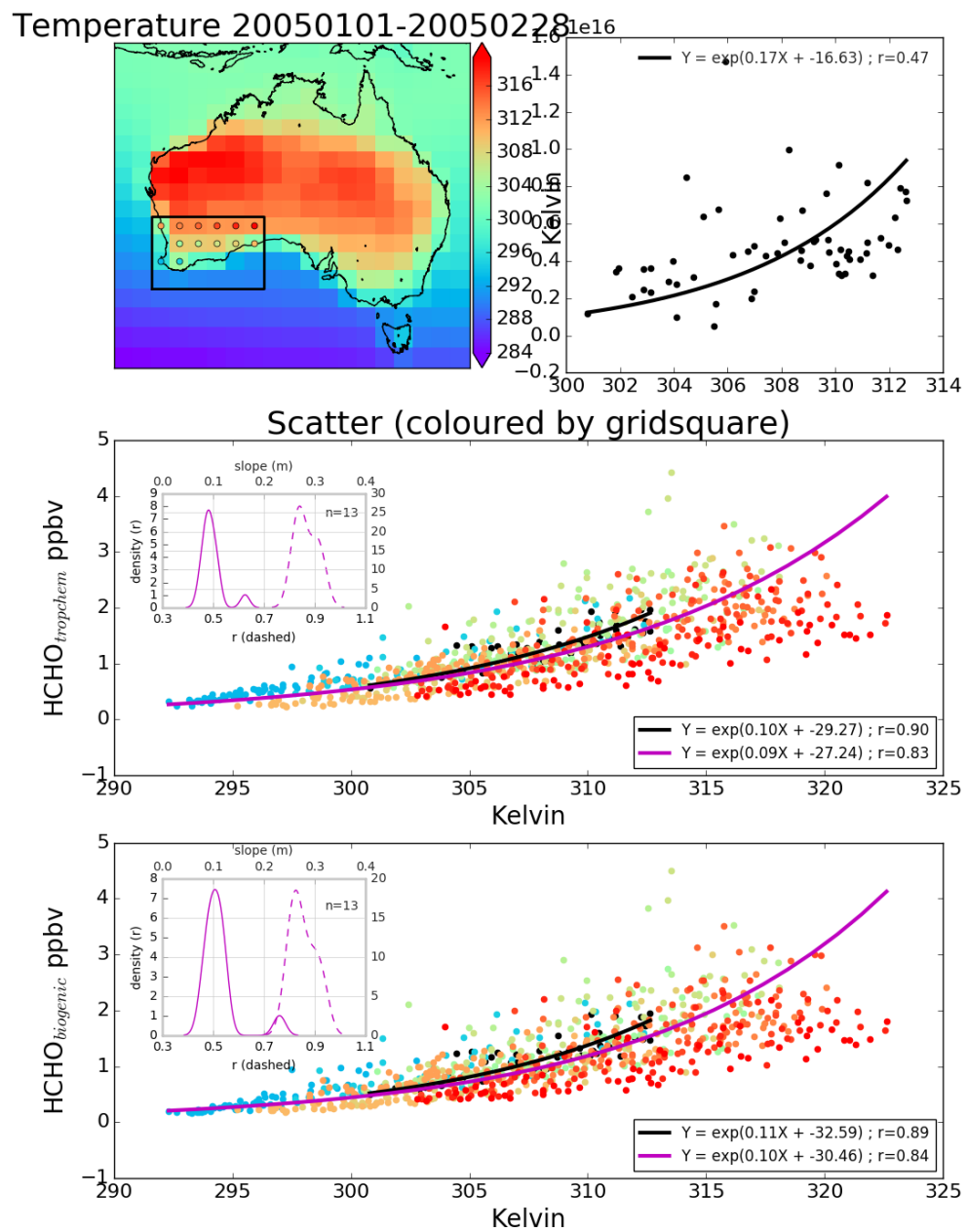


FIGURE 2.45: As figure 2.43 but for south-western Australia.

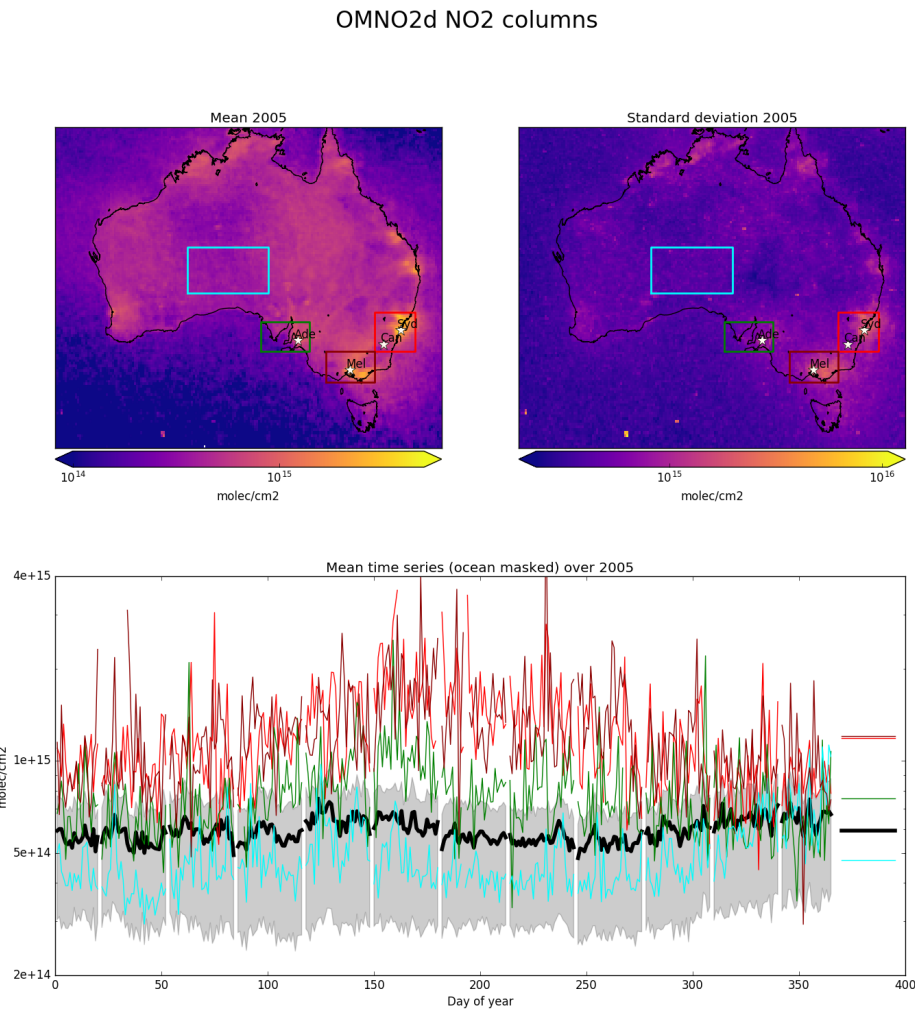


FIGURE 2.46: Mean (top left) and standard deviation (top right) of OMNO2d daily $0.25^\circ \times 0.25^\circ$ tropospheric cloud filtered NO₂ columns. Time series for Australia, and each region (by colour) shown in the bottom panel, with mean for that region shown on the right. A grey shaded area depicts the 25th to 75th percentiles of Australia averaged NO₂ columns for each day in the time series, with a thicker black line showing the Australia-wide mean value.

TABLE 2.5: NO₂ averages by region before and after filtering for anthropogenic emissions using 2005 data from the OMNO2d product.

Region	NO ₂	NO ₂ after filtering	% Data lost
Aus	1	2	3
BG	1	2	3
Syd	1	2	3
Melb	1	2	3
Adel	1	2	3

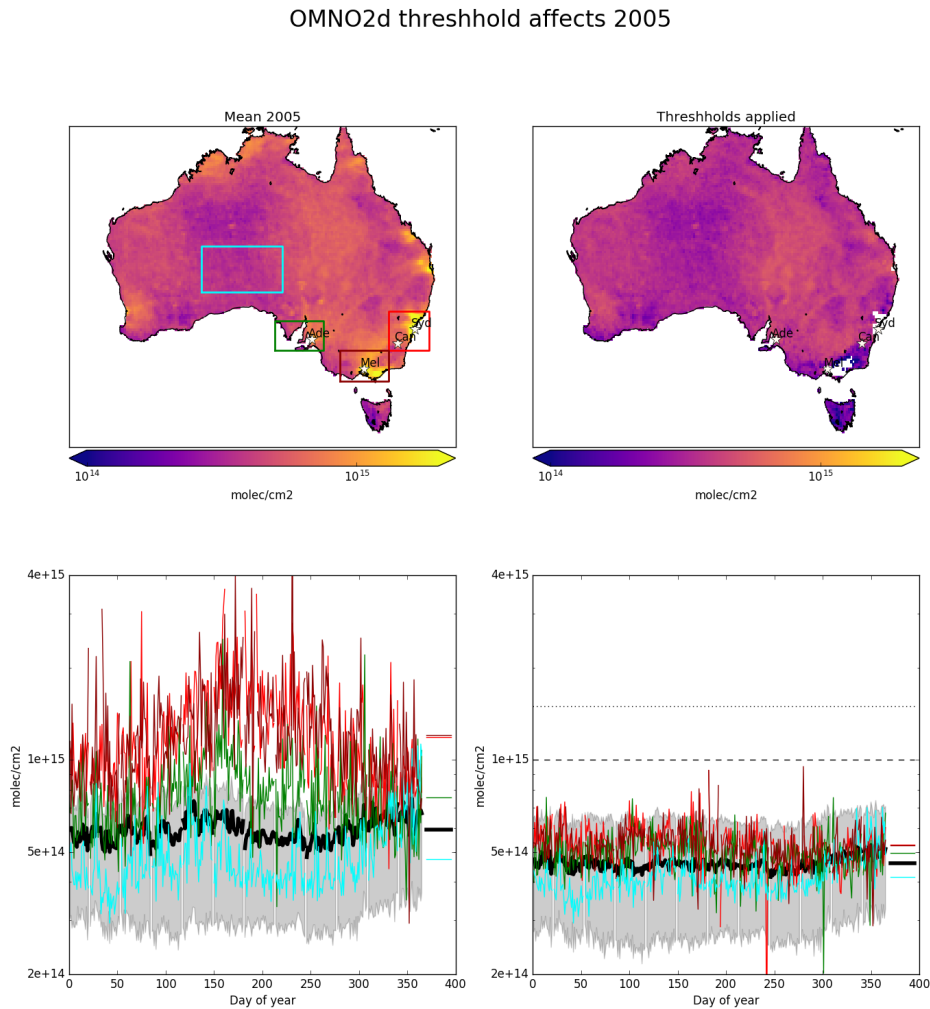


FIGURE 2.47: 2005 OMNO2d NO₂ column mean before (left) and after (right) applying the threshhold filters as described in the text. Time series for Australia, and each region (by colour) shown in the bottom panel, with mean for that region shown on the right.

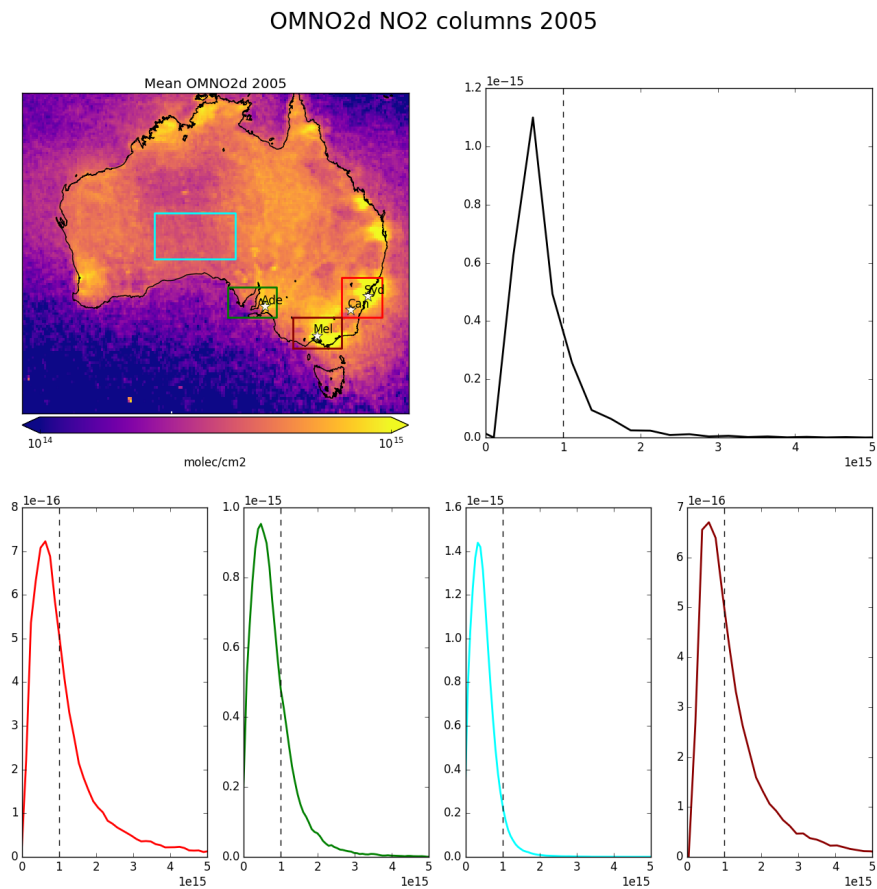


FIGURE 2.48: 2005 OMNO2d NO₂ column means (top left), along with column amount distributions for Australia (top right) and each region shown in the area map (by colour)

OMAERUVd Gridded satellite based AAOD measurements downloaded from <https://search.earthdata.nasa.gov>, DOI 10.5067/Aura/OMI/DATA3003.

SPEI Monthly standardised precipitation evapotranspiration index (metric to determine drought stress) downloaded from <http://hdl.handle.net/10261/153475> with DOI:10.20350/digitalCSIC/8508. See more information in section

Chapter 3

Biogenic Isoprene emissions in Australia

3.1 Introduction

Australian forests are strong emitters of both isoprene and monoterpenes. However emissions are poorly understood due to poor measurement coverage. The lack of measurements makes it difficult to estimate important subsequent processes such as ozone and secondary organic aerosol (SOA) formation. Isoprene has a large impact on the oxidative properties of the atmosphere, as it reacts quickly with the OH radical. One frequently used model of biogenic volatile organic compound (BVOC) emissions is MEGAN (Guenther et al. 2000) which estimates $\sim 1150 \text{ Tg yr}^{-1}$ globally. The primary BVOC emission is isoprene, globally modelled at $\sim 465\text{-}500 \text{ Tg C yr}^{-1}$ (Guenther et al. 2006; Messina et al. 2016). The emission models used to derive these estimates are estimate fluxes from different plant species (phenotypes), which are seldom well understood within Australian forests. Isoprene emissions may be overestimated in Australia since they are based on measurements of taken from a few heavily emitting young eucalyptus trees which are not representative (Winters et al. 2009; Fortems-Cheiney et al. 2012).

Satellite based emissions estimates allow us to improve the models without requiring other expensive measurements over the large data sparse continent of Australia. Kefauver, Filella, and Peñuelas (2014) reviews remote sensing of BVOC emissions, examining the last 20 years of data and analysis of the satellite products. Their review reinforces the message that BVOCs affect the oxidative capacity of the atmosphere and are largely driven by and sensitive to vegetation. In the troposphere, BVOC emissions affect the hydroxyl radical (OH) cycling, ozone (O_3) and secondary organic aerosol (SOA) production, and methane longevity. The chemistry involved is complex and still suffers from relatively large uncertainties in both measurement and chemistry mechanisms.

In this chapter we use and describe a technique using satellite measurements of HCHO to estimate surface isoprene emissions. In-situ isoprene concentration measurements are costly and sparse within Australia, while satellite HCHO data are plentiful and freely available, making this technique very attractive. Such techniques have informed isoprene emission inventories in North America (Abbot 2003; Palmer 2003; Palmer et al. 2006; Millet et al. 2006; Millet et al. 2008), South America (Barkley et al. 2013), Europe (Dufour et al. 2008; Curci et al. 2010), Africa (Marais et al. 2012), Asia

(Fu et al. 2007; Stavrakou et al. 2014), India (Surl, Palmer, and Abad 2018), and even globally (Shim et al. 2005; Fortems-Cheiney et al. 2012; Bauwens et al. 2016). HCHO is the dominant product of most BVOCs and is measured by remote sensing. HCHO products can be found in four satellite instruments: GOME on ERS-2, SCIAMACHY on ENVI-SAT, OMI on EOS AURA, and GOME2 on MetOp-A. These satellites have slightly different spectral and spatial resolutions, as well as using varied processes to estimate HCHO from detected radiances. This leads to different estimates between instruments as described in Lorente et al. (2017), and both validation and comparison become more important when using these remotely sensed data. In this thesis the OMHCHO dataset from the OMI instrument (see section 2.3) is used as the basis for HCHO amounts.

3.1.1 Aims

In a prior chapter (chapter 2), the OMI HCHO total columns are recalculated using an updated estimate of HCHO profiles from GEOS-Chem v10.01 . These estimates are compared to available datasets of isoprene or HCHO (SPS1, SPS2, MUMBA, Wollongong FTIR). Sensitivity satellite AMF calculation is examined and quantified for some scenarios. In this chapter we outline why current isoprene emissions estimates are inadequate and how they can be improved. We discuss literature which shows how the estimates may be too high, and describe how emissions may be calculated using satellite datasets. Section 3.2 lays out how new isoprene emissions are estimated, with results examined in Section 3.3. In section 3.5 we examine how these changes in emissions would affect ozone concentrations in Australia, along with some other chemical processes. Uncertainties for each step along the way are quantified in section 3.4.

Recent work suggests that modelled emissions may be overestimated in southeastern Australia, while emissions of monoterpenes ($C_{10}H_{16}$, two units of isoprene) appear to be underestimated (Emmerson et al. 2016). This could lead to the unique scenario of neither emission type dominating VOC chemistry over the forests. This work tries to improve the understanding of isoprene emissions over the whole of Australia, clarifying the spatial distribution of bias and how these biases impact modelled chemistry. We estimate isoprene emissions in Australia using top-down estimates based on OMI HCHO measurements and modelled isoprene to HCHO yields. This a posteriori top-down estimate is used to determine if model fit against sparse available ground-based measurements can be improved. GEOS-Chem model output is examined before and after updating isoprene emissions which are used as inputs. Wellness of fit between in-situ (at Wollongong) HCHO, satellite (OMI), and modelled (GEOS-Chem) HCHO is determined with and without updated emissions estimates.

3.1.2 Top-down isoprene emissions estimates

In the remote troposphere HCHO production is dominated by methane oxidation, while in the continental boundary layer (CBL) production is largely due to non-methane VOCs (NMVOCs) (Abbot 2003; Kefauver, Filella, and Peñuelas 2014). This leads to the technique of using a linear regression between enhanced HCHO and NMVOC emissions. In the CBL, HCHO enhancement is generally driven by short lived (< 1 hr) precursors (most importantly isoprene). HCHO itself has a lifetime of a few hours

(Kefauver, Filella, and Peñuelas 2014). Isoprene is emitted and enters the atmosphere in the gas phase, where it begins a complex series of reactions. Formaldehyde is produced with high yields in many of the isoprene reactions, which are discussed in more detail in Section 1.3.3. HCHO measurements are often used as a check on how well isoprene reactions are simulated, as model output can then be compared against them (Marvin et al. 2017).

We broadly follow the method of Palmer et al. (2001) to create an emissions estimate of isoprene over Australia. In their work isoprene emissions fluxes were derived using the Global Ozone Monitoring Experiment (GOME) satellite instrument, however here we use OMI (on board the AURA satellite) as it has better temporal coverage and increased pixel counts. Palmer's method improved biogenic isoprene emissions estimates (compared with in-situ measurements) over two available inventories: the U.S. EPA Biogenic Emissions Inventory System (BEIS2) and the Global Emissions Inventory Activity (GEIA). Here we try to improve MEGAN emissions estimates over Australia and analyse some of the technique sensitivities.

Recently Bauwens et al. (2016) estimated isoprene emissions with a top-down technique using the IMAGESv2 global CTM. They calculate emissions which create the closest match between model and satellite vertical columns, and compare these a posteriori data with their a priori (satellite data) and independent data sets. They examine global emissions seen by three models and a top-down inversion, showing a wide range of estimated values for Australia. In this thesis we prioritise the analysis of a top-down emissions estimate compared against MEGAN, along with flow on effect of changed emissions on modelled ozone levels.

3.1.2.1 Bayesian

Bayesian inversion corrects biased biogenic isoprene emissions by optimising emission parameters in order to reduce the difference between observed HCHO and model output. In-depth inversions can account for effects from transport and allow source attribution (Fortems-Cheiney et al. 2012).

For example this method is used by Shim et al. (2005) who optimise GEOS-Chem isoprene emissions in areas with high HCHO concentrations to improve comparison against GOME HCHO observations. They show that the original model underestimates isoprene emissions and HCHO concentrations by 14-46%, with the corrected VOC emissions reducing model biases to 3-25%. The Bayesian inversion is also used in Curci et al. (2010), where a regional CTM (CHIMERE) simulates HCHO, which is compared against OMI observed HCHO and shown to be regionally biased. The model is run initially with emissions of BVOCs and reactive anthropogenic VOCs turned off in order to work out the background (b) values of these compounds. Curci et al. (2010) uses CHIMERE as the forward model to determine the relationship between HCHO (y), isoprene and reactive anthropogenic VOCs (x), using

$$y = \mathbf{K}x + b + \epsilon \quad (3.1)$$

where ϵ are the (assumed) independent errors in measurements. K is the Jacobian matrix determined from CHIMERE representing the sensitivity of y to the state variable

x. This K matrix is used in conjunction with error covariance in x to determine the Maximum A Posteriori solution to calculate the optimal estimate of x.

The Bayesian method is computationally expensive due to the requirement that model runs take place using many permutations of changed inputs. An advantage of the Bayesian method is that it can account for pyrogenic and anthropogenic emissions rather than filtering them out. Biases may still arise due to errors in modelled emission estimation (Curci et al. 2010). In this work we do not use the Bayesian method due to the heavy computational costs involved.

3.1.2.2 Linear

This technique is the simplest, and is performed in this thesis. Using vertical columns of biogenic HCHO one can infer the local (grid space) isoprene emissions using effective molar formaldehyde yield (In other continents around 2-3, or 1 in low NO_x conditions) (Palmer 2003; Marais et al. 2012; Bauwens et al. 2016). If one assumes fast HCHO yield, so that the effect of chemical transport is minimal, and that HCHO and isoprene are at steady states, then one may calculate local yield from a CTM.

In this work yield is calculated from the modelled slope between isoprene emissions and HCHO tropospheric columns within each gridbox over Australia, as performed in Palmer (2003), using modelled values between 1300-1400 LT which is around the overpass time of the OMI. This modelled yield is then used in conjunction with the recalculated OMI measurements in order to estimate isoprene emissions. To calculate this yield we use a reduced major axis (RMA) regression between modelled average values of the total columns and isoprene emission rates, an example is shown in figure 3.1 shows the modelled regression between emissions and tropospheric columns for January, 2005. Also shown is the time series for these two quantities averaged over Australia, and the squared correlation coefficient along with a sample from four grid-squares. The top down estimation process in this thesis is further explained in section 3.2.

This technique suffers from the assumptions of fast HCHO yield and no transport, which requires filtering areas with low NO_x, high winds, or low emissions. Since we use an estimate of the yield from biogenic isoprene to HCHO, we must also filter out areas where HCHO may be coming from anthropogenic or pyrogenic sources. On the plus side, the simple nature of the inversion requires very little computational power after acquiring satellite and model datasets, even over large amounts of gridded data. Both the linear and Bayesian techniques assume that modelled chemistry is accurate and only try to correct precursor emissions, which may be a problem if the chemistry is uncertain.

In high NO_x environments where HCHO has a lifetime on the order of 30 minutes, it can be used to map isoprene emissions with spatial resolution from 10-100 kms. Horizontal transport *smears* the HCHO signal so that source location would need to be calculated using wind speeds and loss rates (Palmer et al. 2001; Palmer 2003). Smearing requires analysis and filtering due to the importance of transport and NO_x on forming robust and accurate estimates. Over Australia NO_x levels are generally not high enough to ensure quick HCHO formation and we must take care to account for resultant smearing. Details on smearing analysis and filtering are in Section 3.2.5.

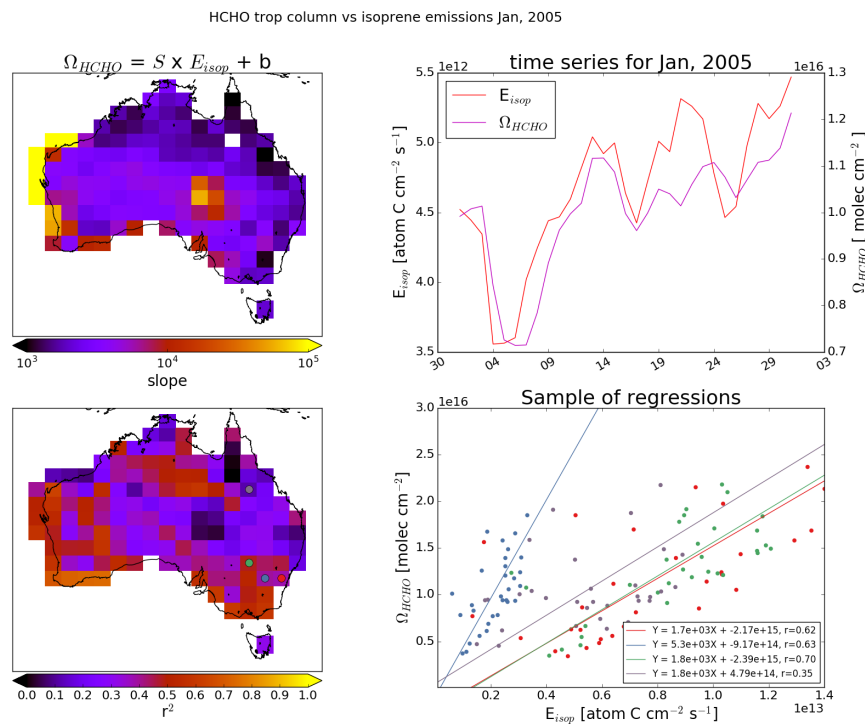


FIGURE 3.1: Top left: RMA slope between modelled tropospheric column HCHO (Ω_{GC}) and isoprene emissions (E_{GC}) using midday (13:00-14:00 LT) values over for January 2005, per gridsquare at 2x2.5°horizontal resolution. Top right: Australia-wide average of midday emissions and tropospheric columns. Bottom left: Squared RMA correlation coefficient for regression in top left. Coloured dots correspond to colour of regressions shown in bottom right panel. Bottom right: Sample of correlations from four gridsquares.

3.1.3 MEGAN emission model

The Model of Emissions of Gases and Aerosols from Nature (MEGAN) is one of the most popular emissions inventories for biogenic isoprene. Global atmospheric studies often use MEGAN along with a chemical transport model (CTM) to examine transport, emission, deposition, and other chemical processes in the atmosphere. Emissions of Biogenic Volatile Organic Compounds (BVOCs) including isoprene are often the subject of studies as they are still relatively uncertain, as well as being drivers for important oxidation and pollution events. In this work MEGAN is run as a module within GEOS-Chem, a global CTM which uses emissions inventories and meteorological data to simulate atmospheric gas concentrations and transport.

MEGAN is poorly calibrated for Australian conditions. Emissions of isoprene (C_5H_8) may be overestimated in some regions within Australia. Sindelarova et al. (2014) showed how the isoprene emissions could be as much as halved by accounting for lower soil moisture. Stavrakou et al. (2015) saw isoprene emissions overestimated by a factor of 2-3 in January. Emmerson et al. (2016) discuss the suitability of MEGAN's isoprene and monoterpene emission factors over southeast Australia, and suggest isoprene emissions are estimated 2-6 times too high. They also show that no blanket increase or decrease in emission factors is appropriate for the entire southeast of Australia. Additionally, emissions of monoterpenes ($C_{10}H_{16}$, two units of isoprene) appear to be underestimated (Emmerson et al. 2016). This could lead to the unique scenario of neither emission type dominating VOC chemistry over the forests.

3.1.4 satellite measurements

Top-down estimates look at how much of a chemical is in the atmosphere and try to work out how much of its major precursors were emitted. This generally takes advantage of longer lived products which may reach a measurable equilibrium in the atmosphere. For isoprene this is done by looking at atmospheric HCHO enhancement, which can be largely attributed to isoprene emissions once transport and other factors are accounted for. Since 1997, when GOME measurements were first used to measure HCHO over Asia (Thomas et al. 1998), satellites have been used to provided a total column measurement of HCHO, allowing isoprene emissions estimates by proxy (Palmer et al. 2001; Bauwens et al. 2016). Using satellite information to improve biogenic emissions is pinpointed as a valuable use of satellite derived datasets (Streets et al. 2013). In this work we use NASA's OMHCCHO product, using measurements from OMI on board the AURA satellite (see section 2.3).

Satellites recording reflected solar spectra use DOAS to measure various trace gases in the atmosphere, including formaldehyde. While satellite measurements can only be used during daytime hours, HCHO lifetimes are sufficiently short that any night-time chemistry will not affect midday observations (Wolfe et al. 2016). Satellite records are often compared with modelled estimates of HCHO and also used as a proxy to estimate isoprene emissions. Total HCHO is measured by satellite over the entire world. The technique used to determine precursor emissions suffers from uncertainties, not the least of which are the uncertainties in the satellite measurements themselves. Zhu et al. (2016) use SEAC⁴RS aircraft HCHO measurements over the southeastern US as model validation. They show that a bias in the assumed OMI

shape factor leads to a bias between satellite and SEAC⁴RS measurements. Satellite based chemical concentrations often require both remote and in-situ measurements combined with modelled data for validation (Marais et al. 2014). There is less information available from satellite measurements at higher latitudes due to increased error in measurements over the more slanted column paths (De Smedt et al. 2015). Validation is important due to the various uncertainties in the satellite remote sensing process, with a priori assumptions having the greatest effect on structural uncertainty between measurements techniques Lorente et al. (2017).

3.2 Methods

3.2.1 Outline

This section provides an overview of the steps involved in creating a top-down emissions estimate. This process is summarised in figure 3.2.

1. Corrected vertical columns (Ω ; saved in OMHCHORP dataset) are calculated using level two OMI HCHO satellite data (see section 2.3), along with GEOS-Chem model runs (see section 2.4.7) at 0.25° by 0.3125° horizontal resolution (see section 2.6).
2. Level three satellite data are used to make anthropogenic, fire, and smoke influence masks (see section 2.7). These are applied to remove Ω which may be influenced by non biogenic sources.
 - (a) The fire mask is created daily from non-zero (MODIS) fire counts over the prior 2 days which occur in local or adjacent grid squares at 0.25° latitude by 0.3125° longitude
 - (b) Influence from transported smoke plumes is removed by filtering OMI aerosol absorption optical depth (AAOD, from OMAERUVd) greater than 0.03
 - (c) A filter for anthropogenic influence is created daily using OMNO2d NO₂ tropospheric column amounts; masking any grid squares with greater than 2×10^{15} molec cm⁻² on any particular day, along with grid squares where the yearly average is above 1.5×10^{15} molec cm⁻²
3. GEOS-Chem modelled biogenic emissions of isoprene (E_{GC}) along with total biogenic columns of HCHO (Ω_{GC}), both averaged over $2 \times 2.5^\circ$ horizontally and 1300-1400 LT temporally, are used to calculate a linear regression slope ($\Omega_{GC} = SE_{GC} + \Omega_{GC,0}$)
 - (a) Hourly gridded model output E_{GC} atoms C cm⁻² s⁻¹ is read, and 13:00 LT daily values are extracted.
 - (b) Daily 13:00-14:00 LT Ω_{GC} molec cm⁻² output is read.
 - (c) A reduced major axis regression slope is determined between Ω_{GC} and E_{GC} using a month of modelled output (one value per day) for each gridsquare (eg. see figure 3.3)

4. Ω are used to create a top-down estimate of biogenic isoprene emissions (E_{OMI} atoms C cm⁻² s⁻¹)
 - (a) Background total columns (Ω_0) are calculated by averaging longitudinally the Ω between 180 and 120°W
 - (b) Emissions are calculated using

$$E_{OMI} = \frac{\Omega - \Omega_0}{S} \quad (3.2)$$
5. Modelled slope (S) calculations depend on several assumptions which are not always valid. A mask is created for where the HCHO production is not dominated by local isoprene emissions. This is determined by calculating smearing over Australia using two model runs with differing isoprene emissions. This smearing value is determined as $\hat{S} = \Delta\Omega_{GC}/\Delta E_{GC}$: the ratio of the differences between model runs of HCHO columns and isoprene emissions. The acceptable range for \hat{S} over Australia is determined as 800 - 4600 s. A full description of the creation of this smearing filter is given in section 3.2.5
6. Top-down emissions E_{OMI} are compared against MEGAN estimated emissions, as well as analysed in conjunction with concentration measurement campaigns (MUMBA, SPS, and one set of airplane measurements (HIPPO)). TODO: do these things
 - (a) Top-down isoprene emissions are calculated for the time window 1300-1400 LT, matching the peak of the diurnal cycle
 - (b) A monthly scaling factor (α) for isoprene emissions is created based on the difference between peak MEGAN emissions and our top-down estimates
 - (c) GEOS-Chem is run using the a posteriori emissions, and HCHO, O₃, isoprene, and NO_x outputs are compared to campaign measurements

3.2.2 Masks and reprocessed satellite HCHO

Satellite data pixels are read from the OMHCHO level 2 satellite dataset, AMFs are recalculated, and then pixels are gridded daily into 0.25x0.3125°horizontal bins. This forms the intermediate product OMHCHORP, which is fully described in section 2.6.1. This dataset includes gridded satellite HCHO columns (Ω), along with pixel counts (how many satellite datapoints were used for each gridbox) to allow averaging and resolution changes.

In order to determine biogenic HCHO enhancements from Ω , we require filters for non-biogenic sources. Anthropogenic, fire, and smoke influence masks are created from three satellite products: NO₂ from OMNO2d, fire counts from MOD14A1, and AAOD from OMAERUVd respectively (see section 2.7). These masks are binned using daily averaged or summed values within our 0.25x0.3125°horizontal resolution. The recalculated corrected vertical columns are saved to OMHCHORP dataset both before and after applying the filters, to allow filter analysis. While one primary source

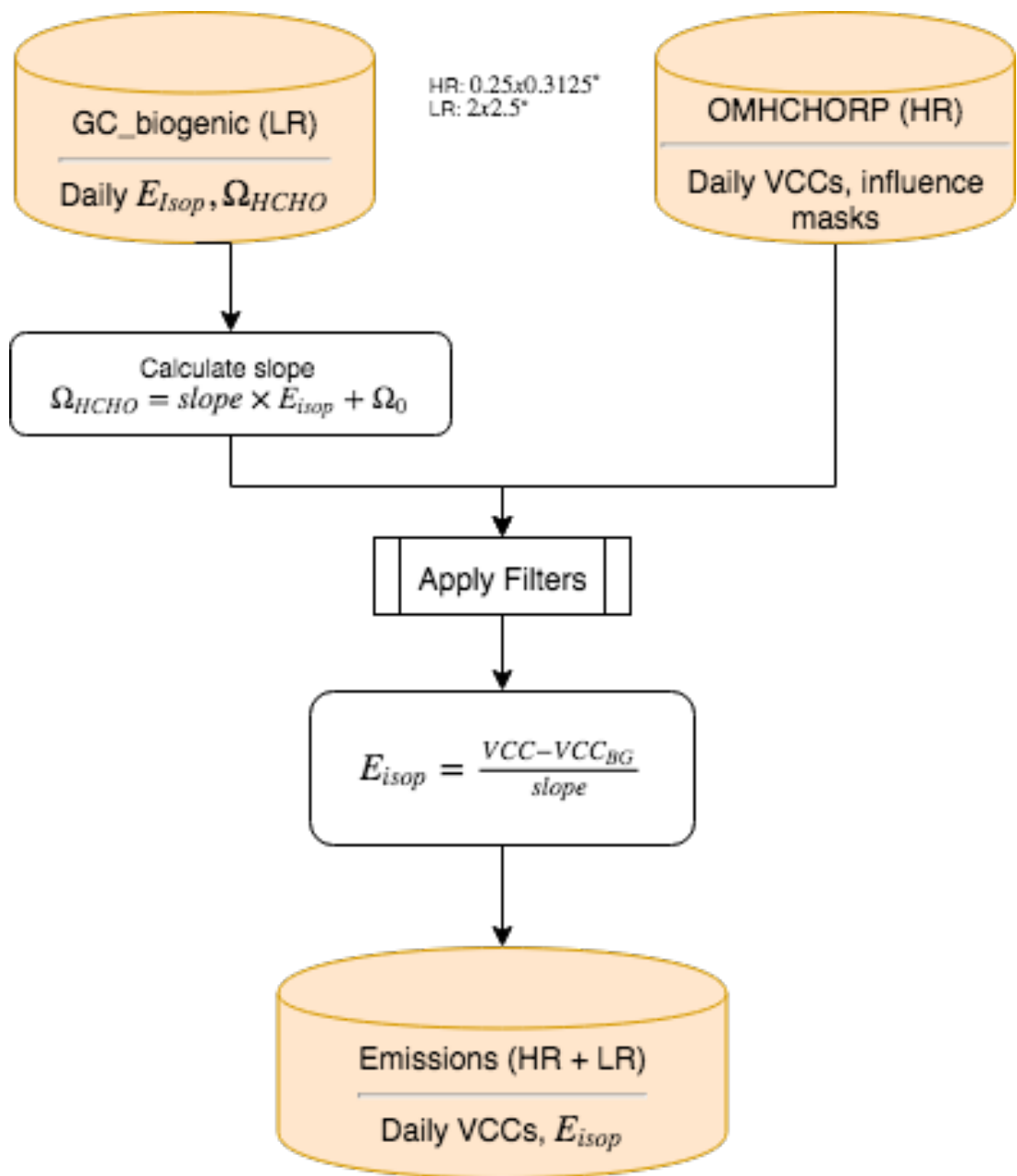
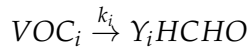


FIGURE 3.2: Creation of isoprene emissions dataset using OMH-CHORP and biogenic GEOS-Chem outputs.

of HCHO production is methane oxidation, the linear regression used to estimate isoprene emissions effectively ignores this source as part of the background, which means a methane filter is not required.

3.2.3 Calculating modelled slope

By assuming a simple linear steady-state relationship between HCHO and its precursors (Palmer 2003; Palmer et al. 2006; Millet et al. 2006), one may calculate isoprene emissions using measured HCHO. The calculation requires reaction rates and yields from isoprene to HCHO, which can be determined most readily using chemical modelling. The methodology for calculating isoprene emissions from HCHO is laid out in Palmer (2003), and takes into account the expected lifetime and reaction rates of the precursor VOCs and HCHO. Assuming HCHO is produced quickly from short-lived intermediates:



Where i indexes a chemical species, Y_i is HCHO yield per C atom, and k_i is the reaction rate. Then assuming a steady state of atmospheric HCHO (Ω) in molec cm⁻² produced by oxidation of VOCs (VOC_i) and no horizontal transport:

$$\Omega = \frac{1}{k_{\text{HCHO}}} \sum_i Y_i E_i$$

Where k_{HCHO} is the HCHO loss rate due to OH and photolysis, Y_i is the molar HCHO yield from oxidation (of i), and E_i is emission fluxes (C atoms cm⁻²s⁻¹). We assume isoprene is the most important precursor and lump other terms into the background Ω_0 so that our equation becomes

$$\begin{aligned} \Omega_{\text{HCHO}} &= \frac{Y_{\text{isop}}}{k_{\text{HCHO}}} \times E_{\text{isop}} + \Omega_0 \\ &= S \times E_{\text{isop}} + \Omega_0 \end{aligned} \quad (3.3)$$

The equations above come from several assumptions that are important to understand. The first assumption is that HCHO is at steady state, which implies productions and losses are equivalent. Then we assume that loss is only due to photolysis and oxidation (first order, $k_{\text{HCHO}} = 1/\tau_{\text{HCHO}}$). Production of HCHO above a background is due to the sum of the precursor emissions (E_i) multiplied by their yields to HCHO (Y_i).

$$\begin{aligned} \frac{d[\text{HCHO}]}{dt} &= 0 = \text{Prod}(\text{HCHO}) - \text{Loss}(\text{HCHO}) \\ \text{Loss}(\text{HCHO}) &= k_{\text{HCHO}}[\text{HCHO}] \\ \text{Prod}(\text{HCHO}) &= \Sigma_i Y_i E_i \end{aligned}$$

Now instead of concentrations we use total column amounts for HCHO, with emissions being in units of molecules cm⁻² s⁻¹. And then lumping together non-isoprene

precursors, and assuming that enhancements above the background are only due to isoprene emissions we have:

$$\begin{aligned} k_{HCHO}\Omega_{HCHO} &= Y_{isop}E_{OMI} + \sum_{i \neq isop} Y_i VOC_i \\ \Omega_{HCHO} &= SE_{OMI} + \Omega_0 \end{aligned}$$

Estimates of Y_{isop} or S are attained through modelling (e.g. Millet et al. 2006). We look at each 2×2.5 °grid box from daily GEOS-Chem (biogenic only) output of $\Omega_{HCHO} \equiv \Omega_{GC}$ and $E_{OMI} \equiv E_{GC}$ within Australia, and calculate the (RMA) correlation for each month. Modelled background concentrations can be ignored here as they do not affect slope calculation. This effectively gives us monthly gridded isoprene to HCHO slope (S) in units of molecules HCHO / atom C × seconds (seconds). Figure 3.3 (top left) shows the RMA regression slope between modelled HCHO columns and isoprene emissions calculated within each grid square over January 2005, averaged between 1300-1400 LT each day. Also shown are the regression coefficients (bottom left), Australia averaged E_{GC} and Ω_{GC} time series (top right), and a sample of the regressions (bottom right). Each regression is for a single grid box, over the course of one month, and is coloured by location (matching dots shown in the bottom left panel). The slopes shown in the bottom right panel can range widely due to differences in emission and yield parameters, which plays a role in the smearing filters applied in section 3.2.5. Due to the low horizontal resolution of GEOS-Chem (2 by 2.5°, latitude by longitude), calculations from grid boxes on the coast which are largely oceanic need to be discarded as the change in HCHO is not dominated by emissions of isoprene, as is assumed for equation 3.3.

One issue with slope calculation is the potential transport of isoprene emissions before the resulting HCHO is formed. The effects of this are dealt with by forming a smearing filter (see section 3.2.5 Accounting for smearing). In order to decide if this filter should be applied before or after calculating the monthly slope, a quick analysis is performed on how the filter affects monthly slope, correlation, and uncertainty. Figure 3.4 shows the calculated monthly slope for 2005-2012, along with its 95% confidence interval over Sydney. The difference between the left and right columns is application of the smearing filter. The bottom two rows show how the slope calculation looks when using multiple years of data for each month. This plot has been repeated for several grid squares over Australia (not shown).

There are a couple of ways to determine the modelled background HCHO concentration, one of which involves running the model with isoprene emissions turned off, which allows us to see exactly how much the modelled isoprene emissions alter each vertical column of HCHO. This is effective since we have assumed variation in HCHO columns only depends on isoprene emissions, so our background term is theoretically identical to the emission free simulated HCHO. The other way involves looking at HCHO over the remote pacific at matching latitudes and times, which emulates how the background is determined for the satellite measured HCHO. Figure 3.5 shows GEOS-Chem total column HCHO with and without isoprene emissions along with amounts over the remote pacific at the same latitudes. Background HCHO for any latitude in this thesis are calculated by averaging longitudinally (140°W to 160°W) the matching latitudes over the remote pacific.

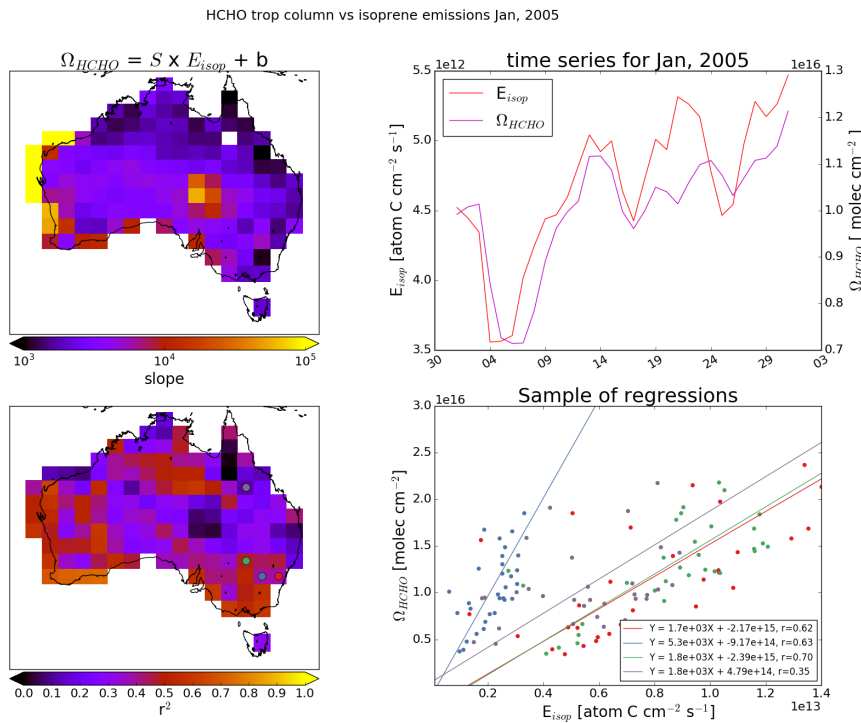


FIGURE 3.3: Top left: the RMA regression slope between modelled HCHO columns and isoprene emissions calculated within each grid box over January 2005. Bottom left: the square of the regression coefficients. Top right: Australia averaged time series Bottom right: a sample of the regressions coloured by latitude and longitude pairs, matching dots in the bottom left panel.

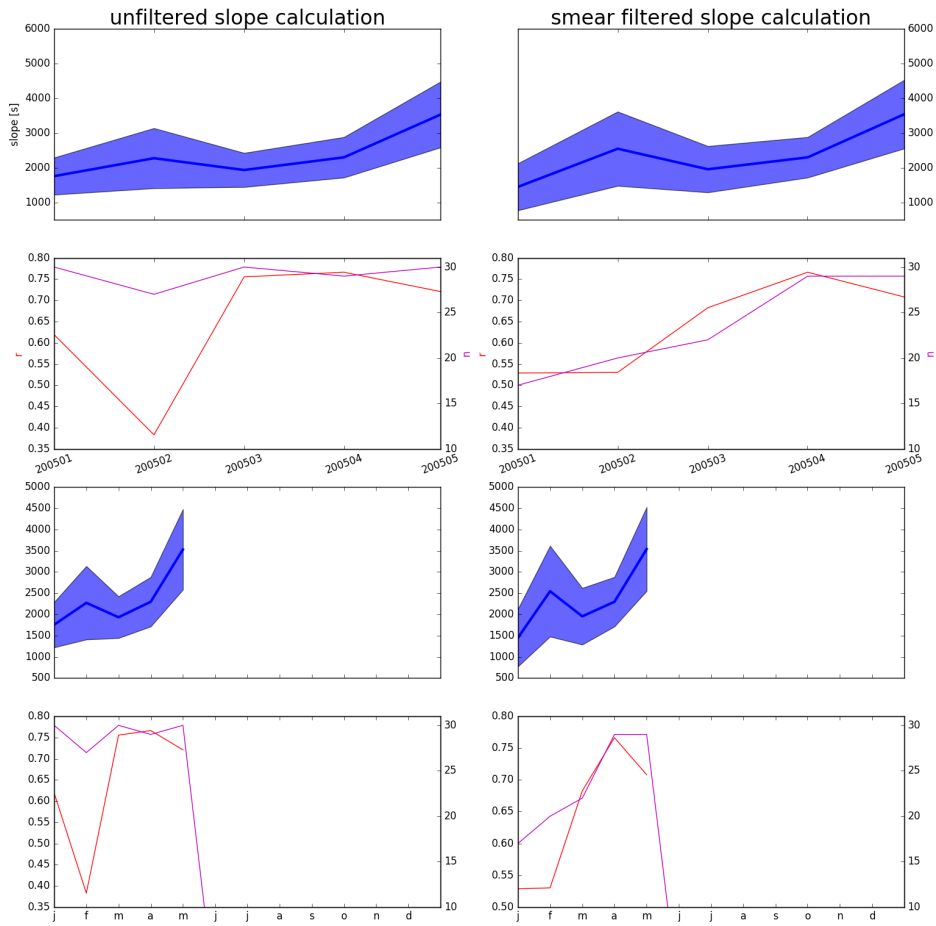


FIGURE 3.4: Row 1: monthly slope along with 95% confidence interval both with (left) and without (right) applying the smear filter for the model grid square containing Sydney over 2005-2012. Row 2: regression coefficient and data-point counts for row 1. Row 3: slope and confidence interval using the multi-year dataset for each month. Row 4: regression coefficient and data-point counts for row 3.

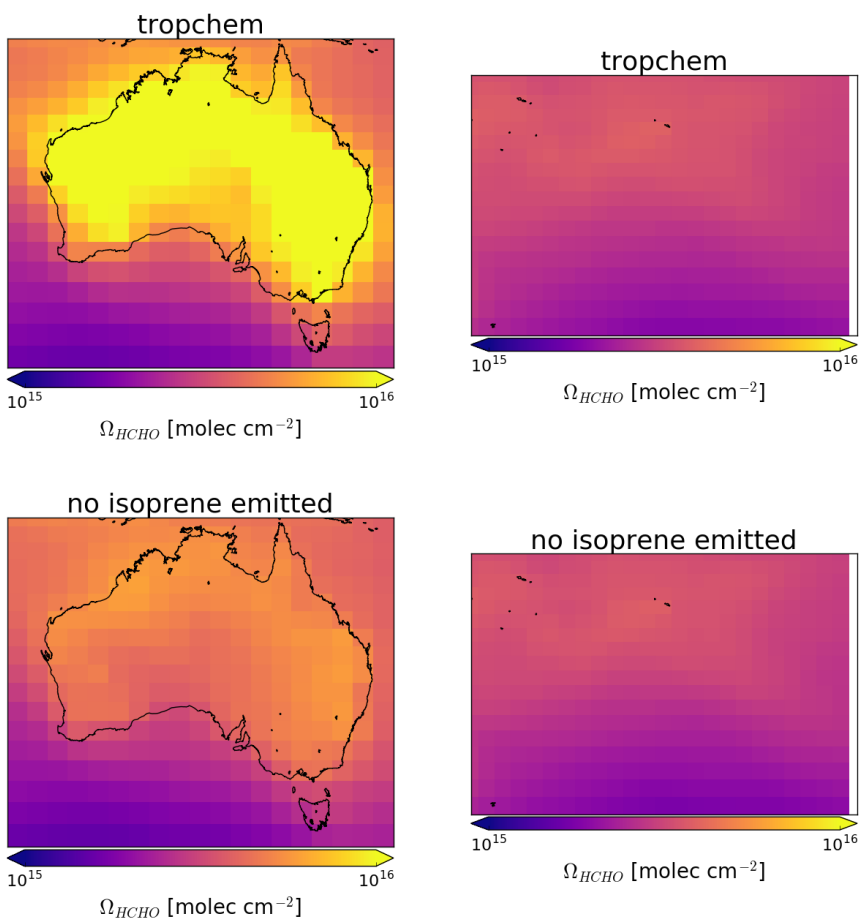


FIGURE 3.5: Total column HCHO over Australia (left) and the remote pacific region (right) using GEOS-Chem with (top) and without (bottom) isoprene emissions.

3.2.4 Calculation of Emissions

As is done in Palmer (2003), Millet et al. (2006), and Bauwens et al. (2016), we assume that HCHO and isoprene columns are in a steady state, with no horizontal transport. We also assume that isoprene is the only compound enhancing the HCHO levels, which requires that we filter out influence from fires, smoke, and anthropogenic emissions. Emissions of precursors are easy to calculate using the slope S calculated in the prior section from modelled HCHO and isoprene columns:

$$\Omega = S \times E_{OMI} + \Omega_0$$

This is the same equation 3.3, except now we use the modelled slope along with satellite HCHO (Ω , and Ω_0). The background HCHO is calculated using measurements in the remote pacific at the same time and latitude as Ω . This leaves E_{OMI} as the only unknown once the satellite measurements are processed to match the temporal and horizontal resolution of S . Figure 3.6 shows the emissions calculated this way along with the modelled emissions output by GEOS-Chem E_{GC} averaged over January, 2005.

The Background (Ω_0) from OMI is determined using the mean column HCHO measured over the remote pacific ocean. For this term we use remote ocean measurements averaged monthly and longitudinally. This gives us a background which is appropriate for any latitude. Figure TODO: figure with background region highlighted and a time series of background values. One potential issue is the low number of valid measurements at high latitudes (especially during winter). When calculating the E_{OMI} from our modelled slope, negative emissions result when using OMI measured columns are lower than the background amounts (as $E_{OMI} = \frac{\Omega - \Omega_0}{S}$). These are set to zero, which increases the average by TODO: $\sim X\%$.

Top-down emission rates calculated in this work are in units of molecules $\text{cm}^{-2} \text{s}^{-1}$. In order to calculate the emissions in kg, each gridsquare is multiplied by the area, and then daily emissions are assumed to follow a sine wave peaking at the estimated rate. Figure 3.7 shows how the daily approximation of total emitted isoprene per grid square is calculated. Daytime hours are estimated per month, from 14 hrs (Jan) to 10 hrs(Jul).

3.2.5 Accounting for smearing

Accounting for transport of the precursors is important, especially in low NO_x conditions in which isoprene has a longer lifetime (hours-days). When estimating emissions of isoprene using one of its products, it is often assumed that isoprene has a short lifetime. This is a problem in Australia where low NO_x environments abound, as detected formaldehyde may not be directly above its emission source (as assumed in this top-down estimation technique). An analysis of spatial smearing (smearing from here forwards) can be used to mitigate potential emissions estimation biases by filtering out affected gridsquares. Smearing in this case is a measure of how much formaldehyde is created from isoprene emissions in non-local grid boxes. Smearing has been estimated in various works (eg. Martin et al. 2003; Palmer 2003; Millet et al. 2006; Stavrakou et al. 2009; Marais et al. 2012; Barkley et al. 2013; Zhu et al. 2014; Wolfe et al. 2016; Surl, Palmer, and Abad 2018), often implementing the method designed in

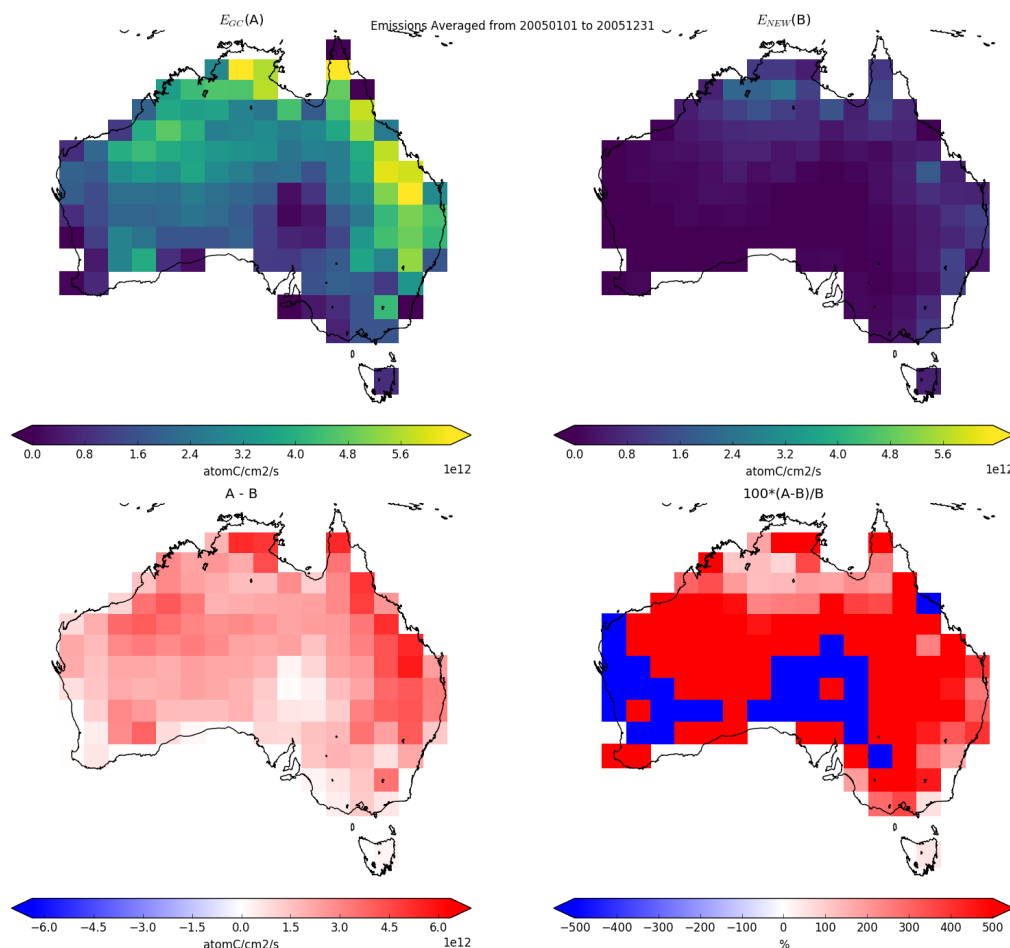


FIGURE 3.6: Top row is isoprene emissions for the month of January, in 2005, from GEOS-Chem and estimated from OMI respectively. Bottom row shows the absolute and relative differences between the two.

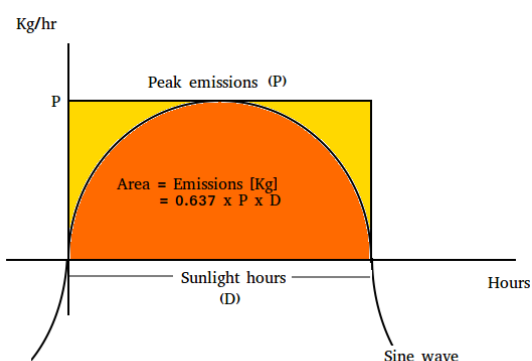


FIGURE 3.7: How daily isoprene emissions (in kg) are calculated.

TABLE 3.1: Smearing filters or slopes (S) seen in literature.

Publication	min. (s)	max. (s)	Notes
Palmer (2003)	1270	2090	Slope ranges seen in North America Summer
Marais et al. (2012)		4000	Smearing limits for Africa
Barkley et al. (2013) ^a	1300	1800	Smearing limits for South America
Surl, Palmer, and Abad (2018)	2200	4900	Slope ranges seen in India

a: Assumed HCHO lifetime of 2.5 hours implies yields from 0.14 to 0.2 per C, consistent with box modelling.

Palmer (2003). This method involves calculating smearing using two almost identical model runs, one of which has isoprene emissions scaled globally by a factor (generally from 0.5 to 2). Another method (eg. Stavrakou et al. 2009) involves the analysis of an adjoint CTM, however this is computationally expensive.

In this work a run of GEOS-Chem using globally halved isoprene emissions (with no other changes) is performed to create a smearing filter. Consider halving the isoprene emitted globally and rerunning the model, one would expect HCHO enhancement (above background levels) to be halved in isoprene emitting gridboxes if no transport has occurred. This idea is behind the method of testing the correlation between HCHO enhancement and isoprene emissions. By assuming no transport and negligible yield and lifetime changes between model runs, an equation can be derived and tested, finding where the assumptions lead to unlikely yields.

In order to filter potential smearing, a daily modelled value for $\hat{S} \approx Y_{isop} / k_{HCHO}$ is determined. By assuming midday HCHO lifetime typically falls within 1.5 to 4 hrs (as seen in the USA), and isoprene to HCHO yield (HCHO per isoprene carbon emitted) lies within the range 0.2 to 0.4 (scenarios estimated in Palmer (2003)): one can set a simple bound on \hat{S} of $[0.2 \times 1.5, 0.4 \times 4]$ hrs or 1080 to 5760 seconds. As NO_x levels across Australia are relatively low, the yield is likely lower than seen in Palmer (2003): and here we reduce the bounds by 20% and round to the nearest hundred to get a bounding range of 800 to 5200 for \hat{S} . This range strikes a balance between unlikely modelled yields and how much data is lost to filtering. A better approximation of lifetimes for HCHO is required to properly account for seasonality and regional NO_x concentrations. TODO: Figure todo shows \hat{S} over Australia for one year, along with where and when the filter has most impact. Table 3.1 shows the smearing filters or typical slopes seen in other works.

3.2.5.1 Calculation of smearing

In order to understand the smearing calculation the underlying equations and assumptions must first be understood. From section 3.2.3, equation 3.3 we have the formulation of a modelled slope (S) being the yield of HCHO per C of emitted isoprene divided by HCHO loss rate per second ($S = \frac{Y_{isop}}{k_{HCHO}}$). Using two runs of GEOS-Chem

with isoprene emissions being the only difference we have:

$$\begin{aligned} Run_1 : \Omega_{HCHO} &= SE_{isop} + \Omega_0 \\ Run_2 : \Omega'_{HCHO} &= S'E'_{isop} + \Omega'_0 \end{aligned} \quad (3.4)$$

There are several assumptions which need to be understood, as these are what is tested by the smearing calculation. The initial assumption is that the system is in a steady state, with no transport of isoprene affecting HCHO columns, this is the basis for equations 3.4. It is assumed that background values (Ω_0) are from oxidation of methane and other long lived VOCs, so that $\Omega_0 = \Omega'_0$. Between these two runs we are only changing the E term, we do not change any chemistry and so we can expect that the yield and loss rate is not changing between the two runs $S = S' = \frac{Y_{isop}}{k_{HCHO}}$ which leads to us being able to combine the runs in equation 3.4 as follows:

$$Run_1 - Run_2 : \Omega_{HCHO} - \Omega'_{HCHO} = SE_{isop} - S'E'_{isop} + \Omega_0 - \Omega'_0 \quad (3.5)$$

$$\Delta\Omega_{HCHO} = S\Delta E_{isop} \quad (3.6)$$

$$\hat{S} \equiv \frac{\Delta\Omega_{HCHO}}{\Delta E_{isop}} \approx \frac{Y_{isop}}{k_{HCHO}} \quad (3.7)$$

And using the output from our two runs we can see if the calculated \hat{S} is wildly different from expected values for S .

Similarly to smearing sensitivity calculations in Marais et al. (2012), we run GEOS-Chem with isoprene emissions halved, then calculate $\hat{S} = \frac{\Delta\Omega_{HCHO}}{\Delta E_{isop}}$. Here Δ represents the departure (daily over 1300-1400 LT) from default run values. If \hat{S} is large, then you can infer sensitivity to non-local isoprene emissions. A relatively large change in Ω_{HCHO} compared to local emissions suggests that HCHO is being formed from non-local isoprene emissions. Alternatively a relatively low value of \hat{S} infers that emissions from a particular grid square are being exported before they form HCHO, which also informs us that local HCHO levels are not due to local emissions.

Smearing is sensitive to how E_{isop} is determined, figure 3.8 shows smearing over two seasons defining E_{isop} as the daily averaged (left column) and midday (1300-1400 LT) isoprene emissions (right column). Essentially the midday isoprene emissions are at the peak of their daily cycle (shown later in figure 3.11) which means the effect of smearing is relatively smaller during these hours. Figure TODO: shows averaged isoprene emissions with added markers showing when the threshold of 800-5200 affects at least one day within the season (cyan or pink diamonds) and where it removes all data for that gridbox (blue or red x).

3.2.5.2 Sensitivity to smearing

Smearing can be dependent on local or regional weather patterns, as greater wind speeds will reduce the time any emitted compound stays within the local grid box. As such smearing sensitivity is both spatially and temporally diverse. Figure TODO: is a picture of the smearing sensitivity over Australia in Summer and Winter, along with where the smearing threshold is exceeded (for one or all days). Large smearing values can be seen near many coastlines as only a fraction of the grid squares actually emit isoprene, which makes transported isoprene relatively more important in these

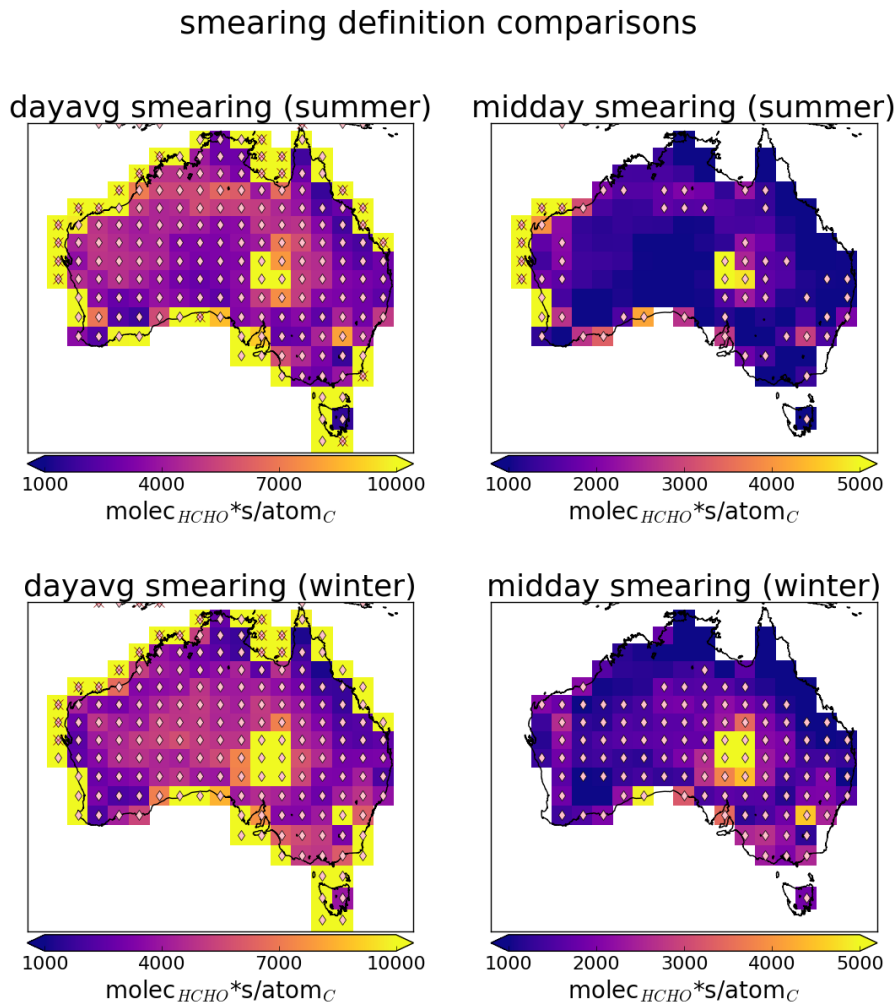


FIGURE 3.8: Smearing (\hat{S} , see text) in summer (DJF, top row) and winter (JJA, bottom row) using averaged isoprene emissions daily (left column) and 1300-1400 LT (right column). The scale changes between left and right columns.

gridboxes. Once the smearing sensitive grid squares are filtered out, application of equation 3.3 is used to estimate isoprene emissions across the nation.

When limiting smearing (\hat{S}) to within 800–4600 s, GEOS-Chem correlation between isoprene emissions and HCHO columns should improve (TODO analysis). A problem arises due to the loss of datapoints used to create monthly gridsquare regressions, and a secondary filter is applied where the confidence interval of the slope exceeds 200%. Figure TODO shows GEOS-Chem midday HCHO columns compared against GEOS-Chem emissions of isoprene, over land squares with (red) and without (grey) filtering for smearing. This smearing range captures isoprene to HCHO yields of around 0.16 to 0.32 C per C if HCHO lifetime is assumed to lie within 1.5 to 4 hours.

3.2.5.3 Smearing length scale

The expected horizontal transport (prior to reaction) of a precursor can be calculated using the smearing length (Palmer 2003). The distance travelled (L) downwind (d) by a precursor (i) before becoming HCHO can be estimated through:

$$L_{d,i} = \frac{U}{k_i - k_{HCHO}} \ln \left(\frac{k_i}{k_{HCHO}} \right)$$

where U is wind-speed. Palmer (2003) further define a smearing length scale: $L_{s,i}$ as the distance downwind where a fraction ($1 - 1/e$) of the precursor is completely transformed into HCHO. This equation uses the initial VOC column concentration ($[VOC]_0$) at the point of emission and mass balance equations as follows:

$$\frac{1}{k_{HCHO} - k_i} \left(k_{HCHO} \exp \left[\frac{-k_i L_{s,i}}{U} \right] - k_i \exp \left[\frac{-k_{HCHO} L_{s,i}}{U} \right] \right) = \frac{1}{e} \quad (3.8)$$

with limiting values $L_{s,i} \rightarrow U/k_i$ for $k_i \ll k_{HCHO}$, and $L_{s,i} \rightarrow U/k_{HCHO}$ for $k_{HCHO} \ll k_i$. Figure TODO: shows a rough estimate of isoprene smearing length(L_{isop}) in Australia using wind speeds from TODO:, and reaction rates k_{isop} , k_{HCHO} from GEOS-Chem.

GEOS-Chem daily averaged HCHO lifetime (τ) is shown for 2005 in figure 3.9. This lifetime is calculated using daily averaged surface loss rates and concentrations of HCHO:

$$\tau = \frac{[HCHO]}{\text{Loss}}$$

The expected lifetime of HCHO is determined by assuming loss is linear (first order) and dividing grid box daily averaged concentrations of GEOS-Chem HCHO ($[HCHO]$ in molecules cm^{-3}) by their modelled losses (Loss in molecules $\text{cm}^{-3} \text{ s}^{-1}$). For each grid square over Australia this daily averaged surface lifetime in summer (Jan., Feb.) and winter (JJA) is shown in figure 3.9. Additionally lifetimes coloured by land grid squares (dots in top right panel) are shown over time in the bottom panel. The problem with this approximation is that we are not interested in daily averaged lifetime, but the midday (13:00–14:00 LT) lifetime. This figure highlights the seasonal nature of HCHO loss rates, although midday numbers are expected to have less seasonality. Another highlighted issue is the potential latitudinal dependence of HCHO lifetimes, since there is less total insolation leading to lower HCHO loss rates at higher latitudes.

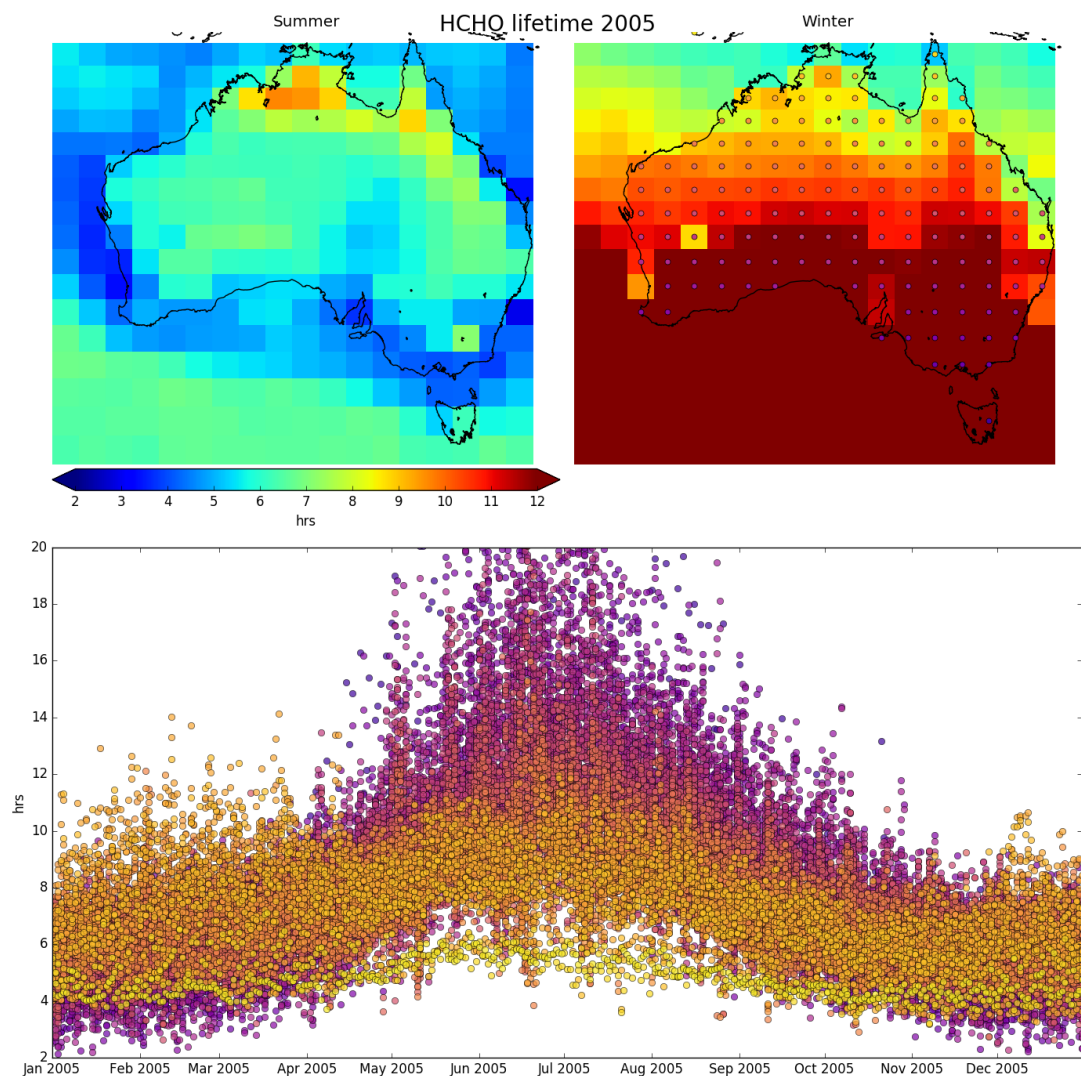


FIGURE 3.9: Top left, right: Summer (Jan., Feb.) and winter (JJA) averaged daily surface HCHO lifetime (τ). Bottom panel: τ over the year, coloured by grid square (see dots in top right panel).

3.2.5.4 NO_x dependence

Isoprene production of HCHO depends on several factors, importantly NO_X levels directly affect the fate of VOCs in the atmosphere. Isoprene first reacts with the hydroxy radical, producing an organic peroxy radical (RO₂). At higher NO mixing ratios (at least a few hundred pptv), RO₂ react mostly with NO. At low NO (less than 50 pptv), RO₂ is more likely to either isomerise, or react with HO₂, or another RO₂. In low NO_X environments, reported HCHO yields from isoprene are around 0.2 - 0.3 C per C, while in high NO_X environments this value becomes two to three times higher (Palmer 2003; Wolfe et al. 2016).

NO₂ measured by OMNO2d gives us a daily mid-day measurement which we can compare to output from GEOS-Chem to determine how well the model does at simulating NO₂ (see section 2.4.6). The affect of NO₂ on smearing can be seen in figure 3.10. This plot shows how smearing over Australia compares to satellite NO₂ levels, with smearing distributions binned by NO₂ both with and without applying a filter for smearing. One feature of the figure is that at lower NO₂ levels the smearing is often 2-4 orders of magnitude above the upper threshold. This abruptly decreases at around 5×10^{14} molec cm⁻² NO₂. There is also a higher number of data points below the lower threshold before that same NO₂ level, suggesting that transport is a bigger issue at NO₂ < 5×10^{14} molec cm⁻².

The half-life of HCHO to photo-oxidation with hydroxyl radicals is around 1 hr depending on environmental conditions (Kaden DA, Mandin C, Nielsen GD 2010). This would make the expected lifetime ($\tau = \text{half-life} / \ln 2$) around 1.4 hours. Over the majority of Australia conditions are relatively clean (low NO_X levels) which extends the expected lifetime. The estimated loss rate of HCHO in GEOS-Chem is up to three times higher in summer and along the north and eastern regions associated with denser forest regions, when compared against other regions. This is largely due to loss rates being proportional to concentrations.

Conversions between HCHO per unit C yield and molar % yield from species X are given by the equation $Y_{\text{molar}\%} = 100 \times C_X \times Y_{HCHO \text{C}^{-1}}$, where C_X is how many carbon are within species X (5 for isoprene). For instance a 200% molar yield of HCHO from isoprene implies 1 mole of C₅H₈ becomes 2 mole HCHO which is a 0.4 HCHO per unit C yield.

3.2.6 Running GEOS-Chem using a posteriori emissions

After creating the top-down estimation of isoprene emissions, we run GEOS-Chem again with emissions scaled to match the new estimate. This is done through taking all the new midday (13:00-14:00 LT) emissions (per grid box) and forming a multi year monthly mean, which can be compared to the MEGAN equivalent. A monthly factor (α at 2x2.5°) that scales MEGAN to match the top-down emissions is then applied within HEMCO (the emissions module in GEOS-Chem). Figure 3.11 shows the multi-year monthly mean daily cycle of isoprene emissions from GEOS-Chem, along with the top-down midday estimate, for an example grid box located 2.5°west of Sydney. First hourly biogenic isoprene emissions are retrieved from GEOS-Chem (estimated using the MEGAN model). Then the midday emissions for each month per gridbox are

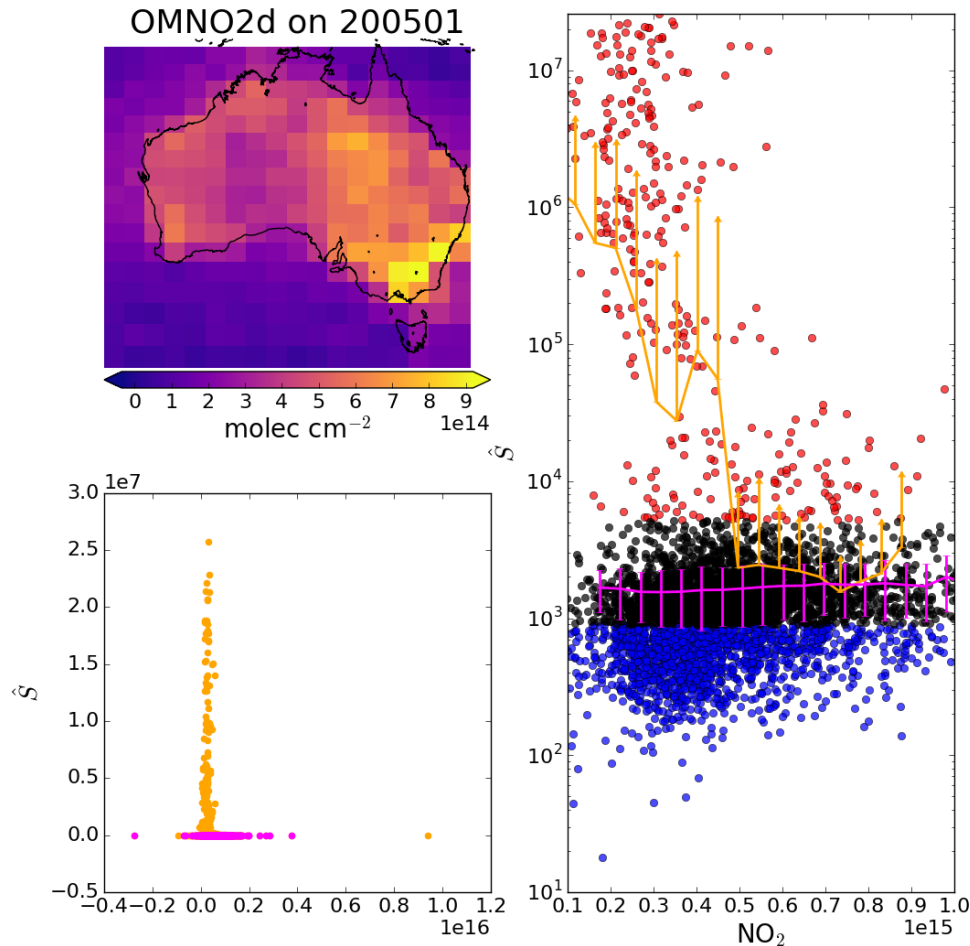


FIGURE 3.10: Top left: OMNO2d tropospheric NO₂ columns (NO₂: molec cm⁻²) averaged into 2x2.5°horizontal bins for over Jan, 2005. Right: Scatter plot of NO₂ against smearing calculations from GEOS-Chem (\hat{S}), with points above and below the smearing threshold range of 900-5200 s coloured red and blue respectively. Points are binned by NO₂ with and without having the smearing filter applied (orange and magenta respectively). Overplotted is the mean and standard deviation (error bars) within each bin. Due to the logarithmic Y scale we only show the positive direction of standard deviations for unfiltered data. Bottom left: Daily NO₂ scattered against smearing with (magenta) and without (orange) applying the smearing filter. This plot is a zoomed out version of the right panel.

TABLE 3.2: HCHO yields from isoprene, and lifetime against oxidation by OH.

HCHO Yield (molar %)	Life vs OH	NO _x background	Source
315±50		High	a
285±30		High	a
225	35 min	High	b
150		Low	b
150		Low	d
450		High	d
235		1 ppbv	e
150		0.1 ppbv	e

a Atkinson and Arey (2003): Table 2, Yield from Isoprene reaction with OH, two values are from two referenced papers therein.

b Palmer (2003): lifetimes assume [OH] is 1e15 mol cm⁻³.

c (Lee et al. 2006b): Calculated through change in concentration of parent and product linear least squares regression. Estimates assume 20° C conditions.

d Wolfe et al. (2016): “prompt yield”: change in HCHO per change in ISOP₀. $[ISOP]_0 = [ISOP] \exp(k_1[OH]t)$; where k_1 is first order loss rate. Effectively relates HCHO abundance with isoprene emission strength.

e Dufour et al. (2008): One-day yields from oxidation modelled by CHIMERE, using MCM reference scheme.

f Calculated using PTR-MS and iWAS on SENEX campaign data.

averaged (see figure TODO) and the multi-year average of these is compared against the top-down estimate.

A scaling factor α is derived which when multiplied with E_{GC} produces the top down emissions estimate E_{OMI} : $\alpha = \frac{E_{GC}}{E_{OMI}}$. This is performed through a small modification of GEOS-chem source code which applies α after calculating emissions for each grid-square based on the default emission factors and meteorology. This scale factor is set to one wherever top-down emissions are not calculated.

3.3 Results

Australia is a large country - roughly 7.7 million km², with heterogeneous environmental conditions. The results presented in this section are frequently split into five regions which are differentiated by colour, as shown in figure 3.12. Top-down emissions estimates (E_{OMI}) shown in this section are calculated using OMHCHO (see section 2.3) slant columns and an updated AMF calculated using code from Paul Palmer's group (see section 2.6.5).

3.3.1 HCHO Products and yield

Isoprene reaction chains are diverse, with many branches forming HCHO. HCHO production yields are often classed into at least two categories: first generation HCHO yield refers to the amount of HCHO produced per unit isoprene consumed by initial oxidation, while total (or molar) yield refers to time dependent yield of HCHO over multiple oxidation stages (Wolfe et al. 2016). Wolfe et al. (2016) define prompt yield as the change in formaldehyde per unit change in initial isoprene emissions. In this work yield (Y_{isop}) is approximately the total yield within 4 hours.

Figure 3.13: shows the GEOS-Chem Y_{isop} and HCHO lifetime (τ) estimated throughout the year. By using an assumed constant Y_{isop} of 0.4, we estimate the midday lifetimes of HCHO using $S = \frac{Y_{isop}}{k_{HCHO}}$ from equation 3.3. Then dividing the slope by this monthly mean lifetime returns an estimate of the Yield. Both of these terms are heavily influenced by the assumed yield, and should not be taken as results, however this technique shows the seasonal cycle and spread of the HCHO yield and lifetime. A clear June (and sometimes March, July and August) increase in HCHO lifetimes is shown, with a matching drop in yield. These are the winter months, when midday temperature and insolation is reduced. Noise in the southwest region may be indicative of heavy filtering, potentially driven by westerly winds which can lead to both smearing and transported pollution.

3.3.2 Emissions comparisons

Guenther et al. (2012) Estimate global biogenic isoprene emissions at roughly 535 Tg yr⁻¹, using MEGAN. Sindelarova et al. (2014) Estimate around 594 Tg yr⁻¹using MEGAN with MACC, showing isoprene as 69.2% of the total BVOC emissions, with monoterpenes at 10.9 Tg yr⁻¹(10.9%). They show 41 Tg yr⁻¹decrease in Australia when introducing soil moisture parameterisation. When comparing the GEOS-Chem (which runs MEGAN) emissions to those calculated using our top-down inversion, we see a

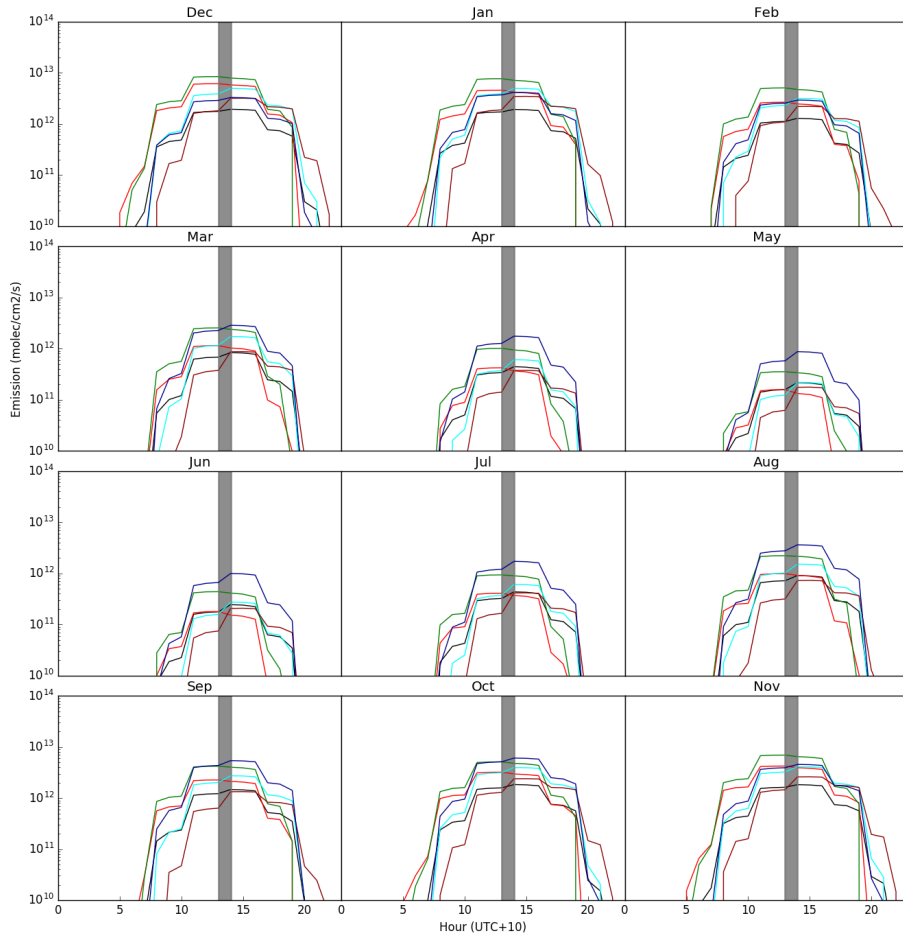


FIGURE 3.11: The diurnal cycle of MEGAN emissions averaged by month over 1, Jan, 2005 to TODO, 2013 are shown with lines, while top-down emissions estimates are shown with plus symbols. MEGAN emissions are estimated hourly per 2x2.5°horizontal grid box, shown here are the averages within several areas (denoted by colour, see figure todo). Top-down estimates are similarly grouped by colour, and shown at the 13:00 LT mark for each month. Rows 1-4 match seasons from austral summer (DJF) through to spring (SON).

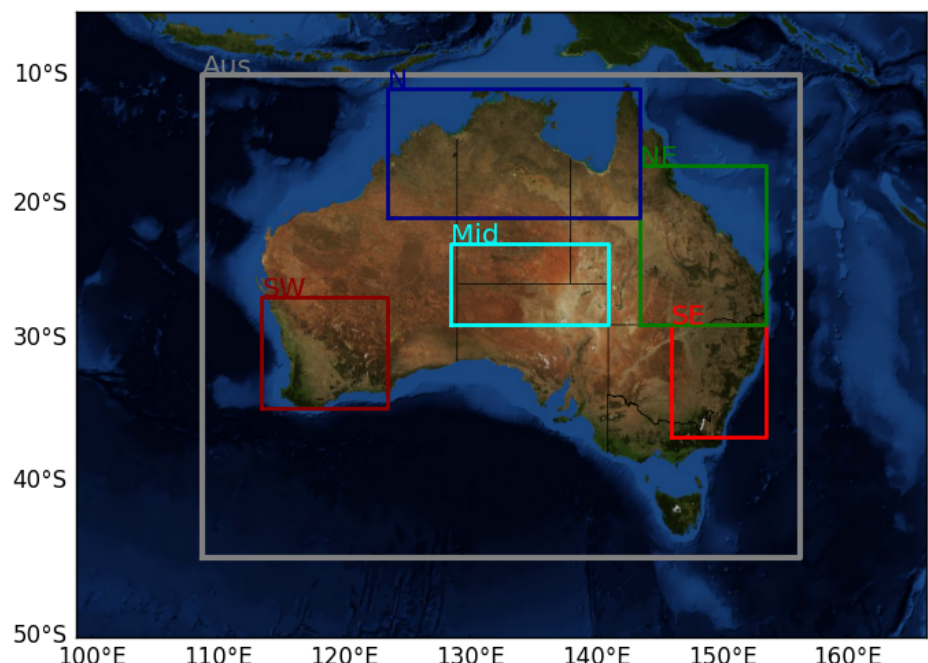


FIGURE 3.12: Sub-regions used in subsequent figures. Averages taken within Australia will be black or grey, while averages from within the coloured rectangles will match the colour shown here.

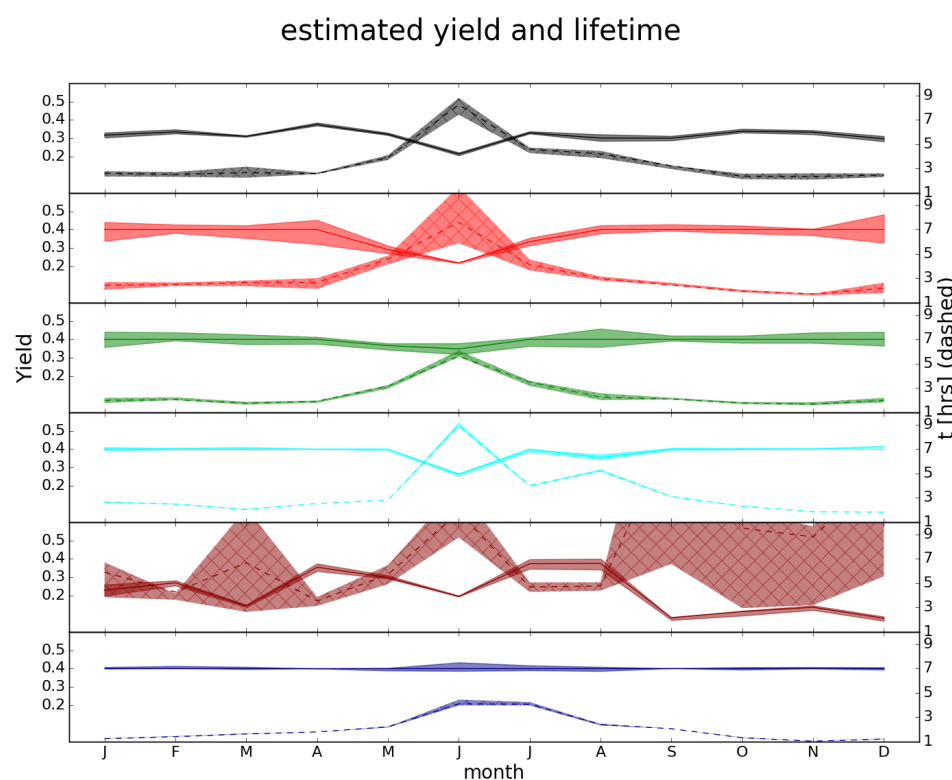


FIGURE 3.13: Monthly area averaged isoprene to HCHO midday yield, and HCHO lifetime. Coloured by regions shown in figure 3.12 Shaded areas show the yield (plain) and lifetime (hatched) IQR.

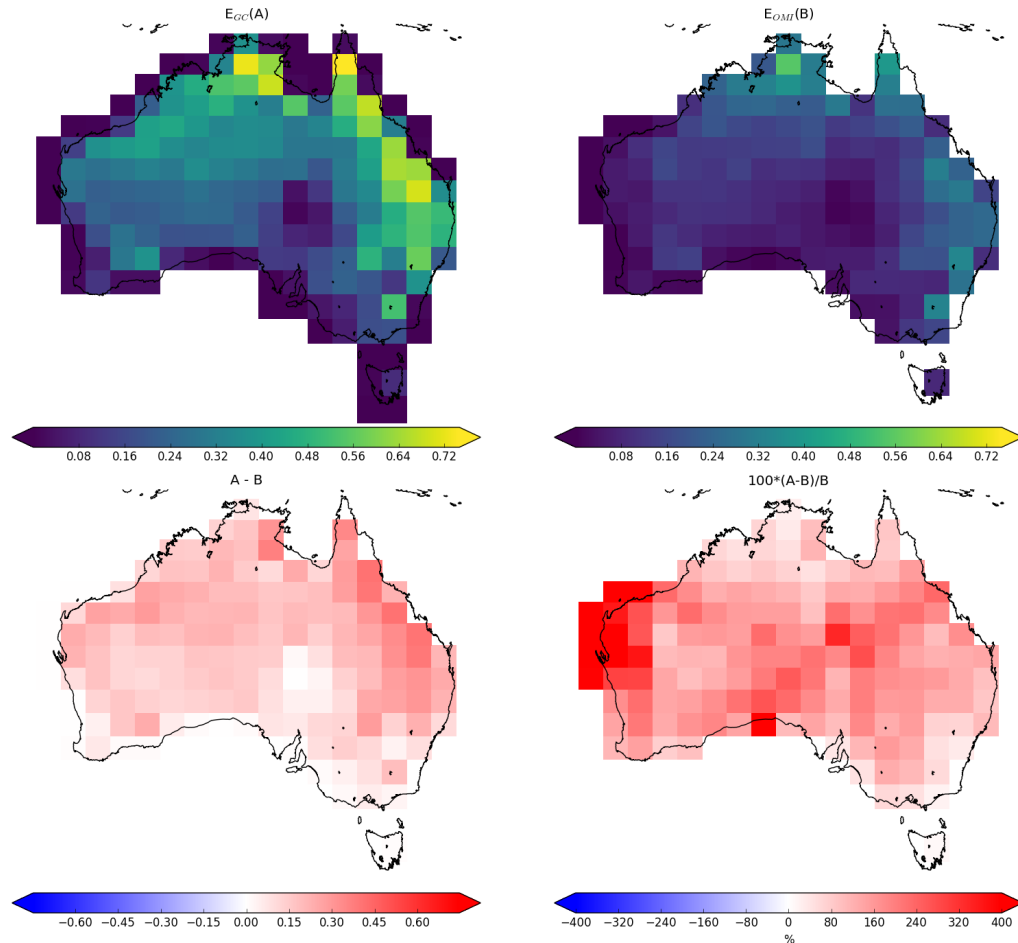


FIGURE 3.14: Top row: multiyear mean emissions in Tg yr^{-1} from E_{GC} (GEOS-Chem; running MEGAN) and E_{OMI} (top-down emissions) respectively. E_{OMI} uses an assumed sinusoidal daily cycle, with daylight hours prescribed for each month: see section 3.2.4 . Bottom left and right shows the absolute and relative differences respectively.

decrease of around 29 Tg yr^{-1} (66%). Table 3.3 shows yearly isoprene emissions from this work and some other works for Australia and globally. Figure 3.14 shows how this decrease is distributed spatially, with E_{GC} and E_{OMI} in Tg yr^{-1} calculated as a multi-year mean. Across all of Australia we see large reductions of total emissions using the new top-down estimate.

Figure 3.17 shows emissions over Australia calculated using the OMI top down estimate (column 1: E_{OMI}) and GEOS-Chem simulated emissions (column 2: E_{GC}). The first row shows the time series (daily midday averages) and the final row shows the absolute differences ($E_{GC} - E_{OMI}$). This figure is repeated using monthly means (of the daily midday estimates) in figure 3.18.

Figure 3.19 shows the multi-year monthly mean and IQR of daily midday isoprene emissions estimates, averaged over several regions (see figure 3.12). Generally months outside of May to August show the a posteriori lower than the a priori, except in the

TABLE 3.3: Isoprene emissions (Tg/yr)

Australia	Global	notes
43(2)	445(18)	a) GEOS-Chem: 2005-2010
19(2)		b) Top-down: 2005-2010
	535	Guenther et al. (2012):
	594	Sindelarova et al. (2014):
26-94	272-570	c) Bauwens et al. (2016): 2005-2013

a: MEGAN diagnostics based on 3-hourly averages

b: Based on daily peak emissions integrated over a sinusoidal daily curve

c: Range shown here based on 3 different models and one top-down inversion

south eastern portion of Australia.

Figures 3.15 and 3.16 show how the distributions of top-down emissions compare to those of MEGAN in each region during summer months (DJF) with zeros and negatives removed from both distributions. Figure 3.15 shows the daily midday distributions, binned hexagonally to show data-point frequency. There is only weak correlation apparent between daily top down and MEGAN estimations, however daily values suffer from large uncertainty. Figure 3.16 displays the regressions between monthly averages of the same data. In the monthly averages more correlation is apparent, with regression coefficients ranging from 0.48 to 0.78 across regions. The portion of this correlation due to seasonality is examined by re-running the regression after subtracting the multi-year monthly average from each dataset. TODO: run regression after removing seasonal average and see how r and slope are affected.

3.3.3 Comparison with measurements

TODO: Analyse comparison of gridbox with campaigns of measurements

Comparison between ground-based measurements and large ($2 \times 2.5^\circ$) averaged grid squares suffers from heavy representational error. Figure 3.20 shows the SPS and MUMBA measurement sites, along with the outline of the $2 \times 2.5^\circ$ model gridbox. The urban footprint of Sydney and Wollongong are clearly shown, along with some ocean, forest, and rural regions, which are all averaged within calculations made here. Due to high uncertainty in components of the top-down emissions estimate, temporal resolution is also limited. MUMBA, SPS1 and SPS2 each provide only a couple of comparable data points, and these campaigns measured isoprene concentrations while our estimate is of emissions.

Figure TODO shows how isoprene compares against measurements from the MUMBA and SPS campaigns (described in section 2.2) both before and after scaling isoprene emissions to match the top-down estimation. TODO: discuss results and differences, does isoprene improve?

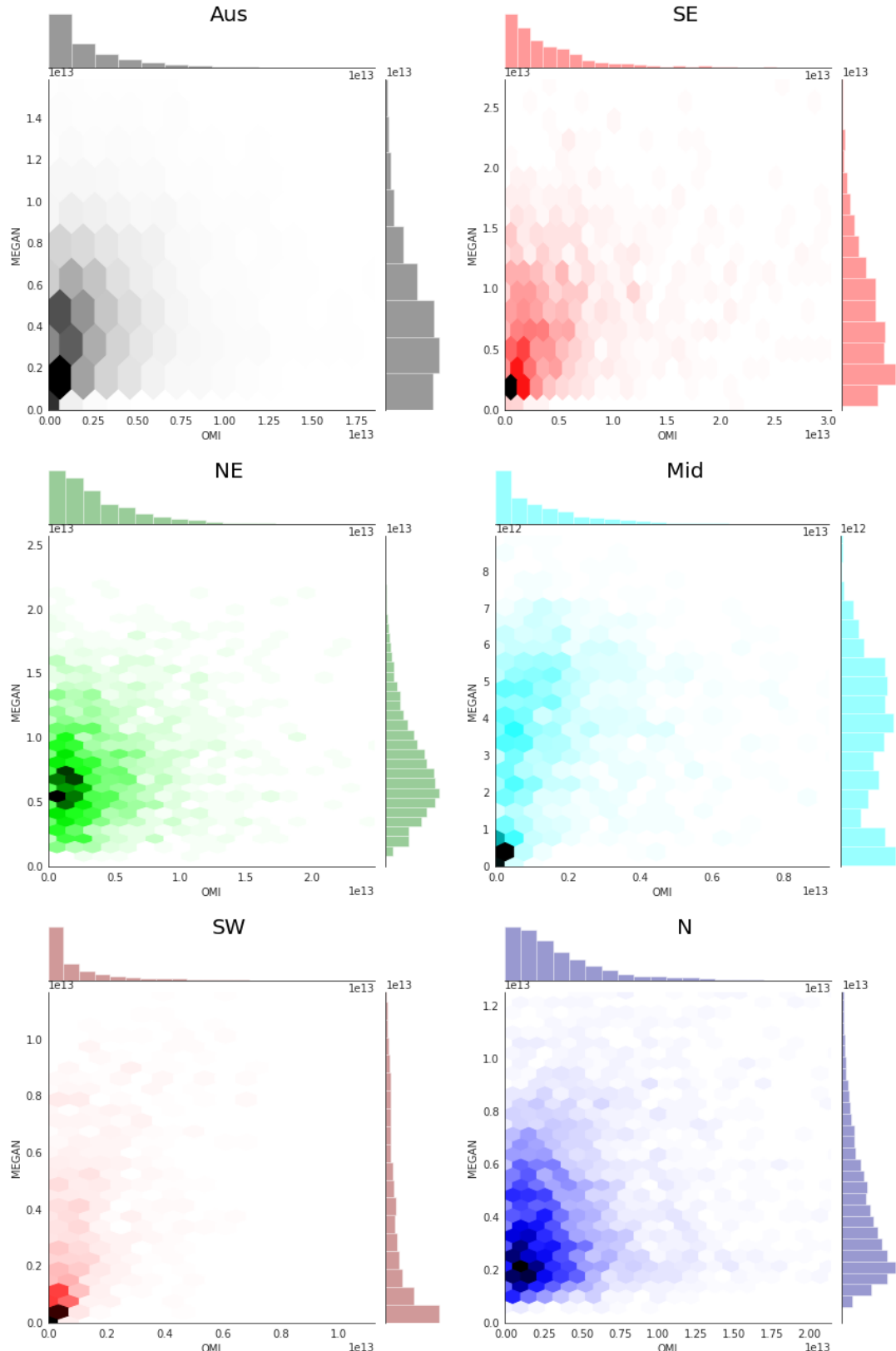


FIGURE 3.15: Scatter plot (binned hexagonally to show data-point frequency) along with the distributions of MEGAN (y axis) and the top down estimate (x axis). This figure is based on summer (DJF) midday values over multiple years. Coloured by regions shown in figure 3.12.

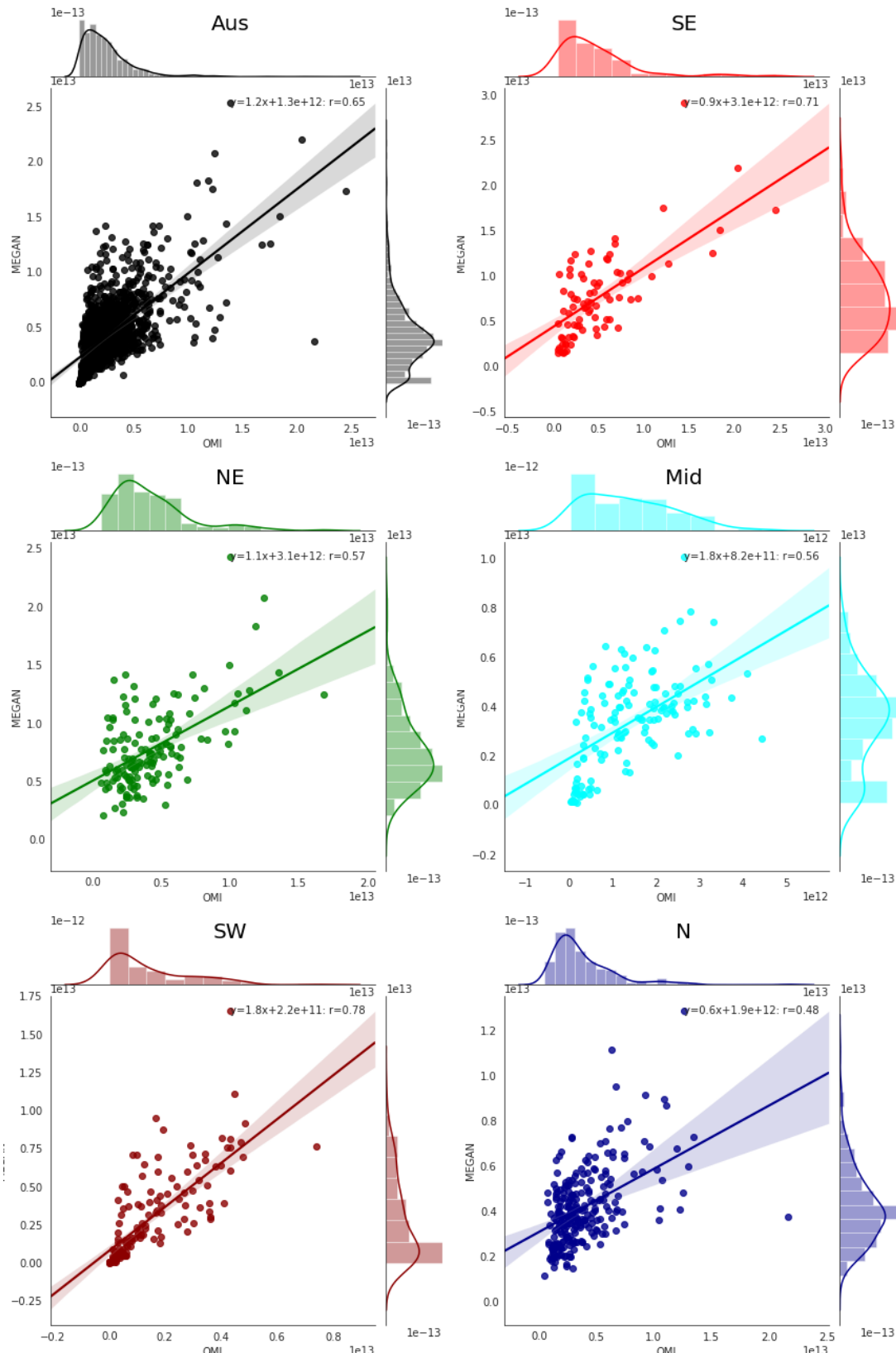


FIGURE 3.16: Scatter plot of MEGAN emissions against top down emissions using monthly averaged gridsquares as regression datapoints. Figures use multiple years of summer (DJF) midday values averaged monthly within each region shown. Coloured by regions shown in figure 3.12.

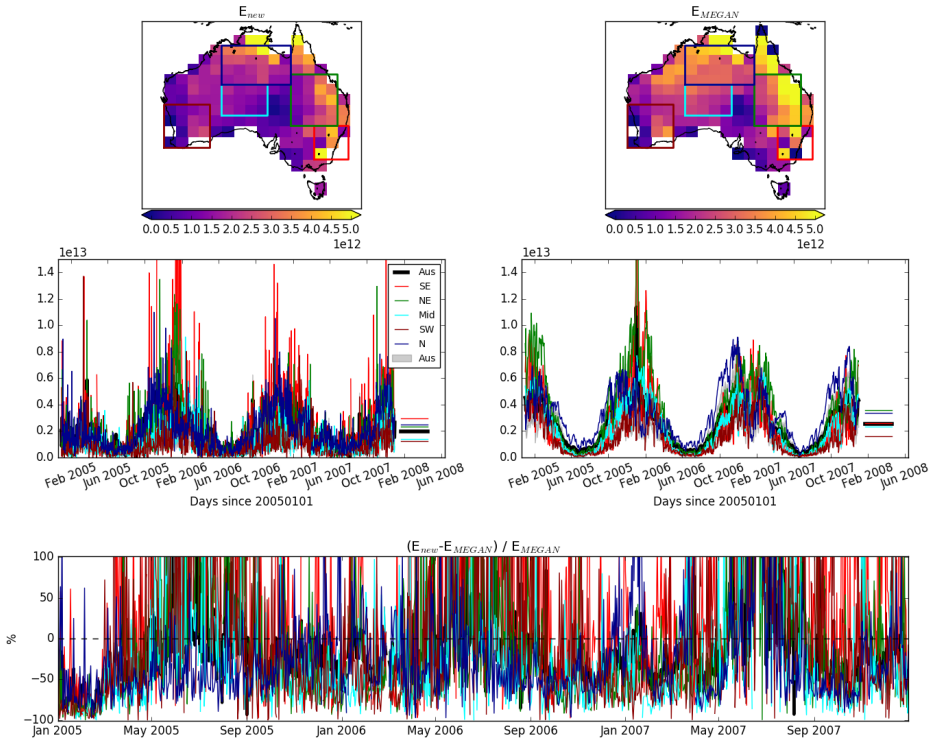


FIGURE 3.17: Emissions of isoprene estimates using OMI top down inversion (column 1: E_{OMI}) and MEGAN (column 2: E_{GC}). Row 1: overall averaged daily midday emission rates, from 1, Jan, 2005 to 1, May, 2013. Row 2: time series of daily midday averages for all of Australia along with several subregions (shown in row 1). Row 3: relative differences: $\frac{E_{MECHAN} - E_{OMI}}{E_{MECHAN}}$. The black lines and grey areas show the Australian mean and inter-quartile range respectively, while the coloured lines show the mean within the rectangles (of matching colours) shown in the first row.

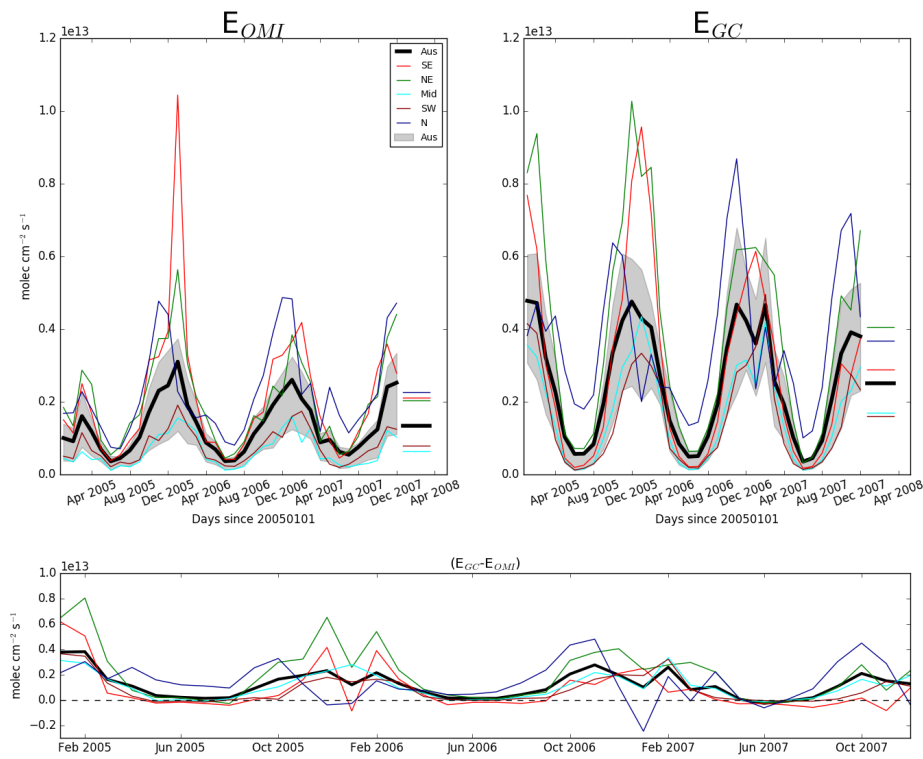


FIGURE 3.18: As figure 3.17 using monthly medians of the daily mid-day emissions estimates.

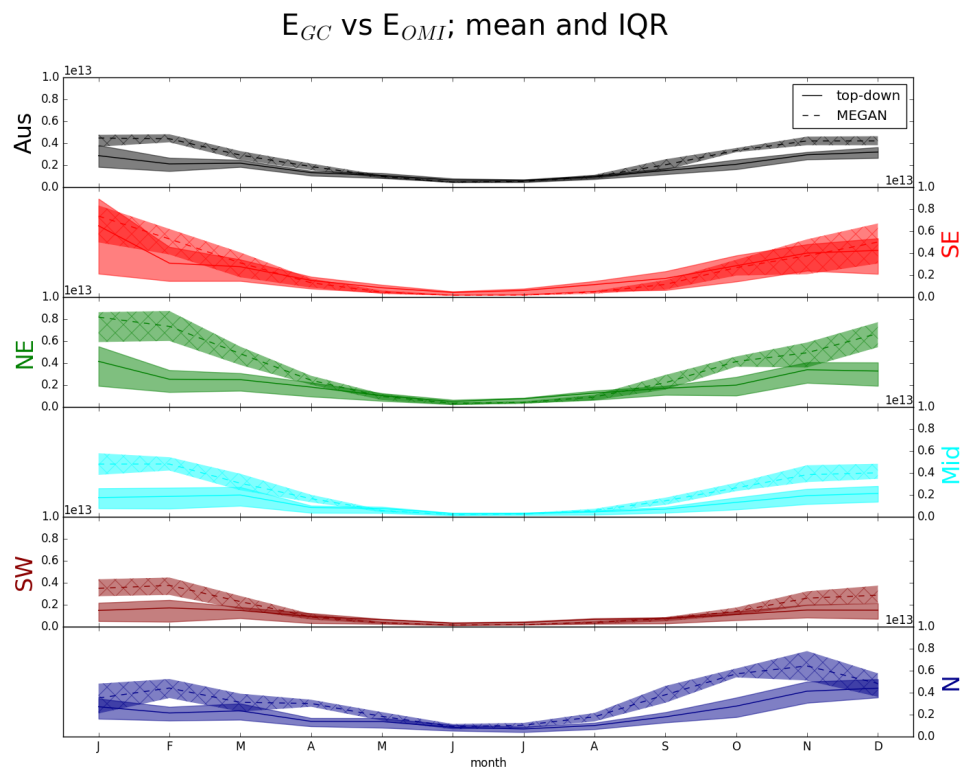


FIGURE 3.19: The multi-year monthly mean (lines) and IQR (shaded) of midday (13:00-14:00 LT) isoprene emissions estimates. Estimates come from MEGAN run by GEOS-Chem (E_{GC}), and the OMI top-down technique (E_{OMI}). The mean E_{GC} is shown by the dashed lines and hatched shaded areas show the IQR. E_{OMI} means are shown using the solid lines, with IQR shown by unhatched shaded areas. Colours denote the region over which the monthly average was taken, as shown in Figure 3.12.



FIGURE 3.20

3.4 Uncertainty

3.4.1 Summary

Uncertainties introduced through the inversion process are hard to adequately quantify. We can identify the uncertainties in the linear regression used to relate HCHO to isoprene emissions, as well as in the satellite data product, however these uncertainties lack verification against measurements. Even as this top-down inversion attempts to remedy the lack of measurement over Australia, it suffers from the lack of data-points against which it can be verified.

This section identifies the overall uncertainties of calculating isoprene emissions using OMHCHO and GEOS-Chem in the top-down method. The major source of uncertainty lies in TODO, and calculations are more or less uncertain in the Winter. This limits temporal resolution of isoprene emissions estimates. Table TODO shows each term calculated in this work and the corresponding uncertainty estimate in summer and winter.

3.4.2 Top down emissions

There are several factors which need to be considered when looking at the uncertainty in our emissions estimate. Things with their own inherent uncertainty include the modelled a-priori, modelled relationship between HCHO and isoprene, and satellite measurements. Important factors which need to be analysed for confidence in results

TABLE 3.4: Uncertainties in literature and here.

product	uncertainty	location	notes
satellite HCHO top-down E_{OMI}	40%	North America	(a) mostly due to cloud interference
	X%	where	(b)
	Y%	where	(c)
	X%	Australia	accumulated uncertainty in calculation
	X%	Australia	range found when scaling satellite HCHO

a: Millet et al. (2006) and Palmer et al. (2006)

b:

include the steady state assumptions, filtering techniques for fire and human influences, and the regression model for determining the isoprene to HCHO yield.

Uncertainty in satellite HCHO, along with top down emissions estimates E_{OMI} from literature is listed in table 3.4. The final determination of top-down emissions comes from equation 3.2: $E_{OMI} = \frac{\Omega - \Omega_0}{S}$. Assuming each term is independent, we use the following equations to estimate random error in E_{OMI} :

$$\begin{aligned} z = x + y : \Delta z &= \sqrt{(\Delta x)^2 + (\Delta y)^2} \\ z = x/y : \Delta z &= z \sqrt{\left(\frac{\Delta x}{x}\right)^2 + \left(\frac{\Delta y}{y}\right)^2} \\ \Omega - \Omega_0 = \Phi & \\ \Delta \Phi &= \sqrt{(\Delta \Omega)^2 + (\Delta \Omega_0)^2} \\ \Delta E_{OMI} &= E_{OMI} \times \sqrt{\left(\frac{\Delta \Phi}{\Phi}\right)^2 + \left(\frac{\Delta S}{S}\right)^2} \end{aligned}$$

In order to quantify ΔE_{OMI} we need to find the uncertainty in the underlying terms: ΔS , $\Delta \Omega$, and $\Delta \Omega_0$. For ΔS ($\Omega_{GC} = S \times E_{isop} + \Omega_0$ from equation 3.3) we examine related GEOS-Chem output in section 3.4.3, since S comes directly from the monthly linear regression of modelled isoprene emissions and column HCHO. Uncertainty in terms Ω , and Ω_0 come from both the OMHCHO slant columns (SC) and the AMFs calculated to transform them into vertical columns ($VC = SC / AMF$ from equation 2.6). Section ?? describes these calculations.

The summation of these uncertainties through standard quadrature rules provides an estimate of random error in the calculation of E_{OMI} . In order to calculate the bias or systematic error, an understanding of biases in the underlying terms is required, since there is little in the way of comparable measurements. Known biases:

OMHCHO up to 40% underestimated HCHO in the OMI satellite product (pixel bias, (Zhu et al. 2016; De Smedt et al. 2015; Barkley et al. 2013))

OMHCHO around 13% overestimation of monthly averaged HCHO (cloud-free bias, (Surl, Palmer, and Abad 2018))

GEOS-Chem HCHO TODO under/over estimation of modelled HCHO due to coarse resolution (over prediction of low- NO_x oxidation pathway TODO:citation)

Figure TODO shows the average summer and winter random uncertainty over Australia, along with a time series of total emissions and the error bars using monthly averaged data and MEGAN emissions for reference.

3.4.3 Model Uncertainty

E_{OMI} estimation depends partly on the product it is trying to improve, using modelled yields based on MEGAN. Model uncertainty is difficult to accurately ascertain, generally an analysis of the model compared to in-situ measurements is performed, however there are few of these measurements over Australia. Here GEOS-Chem output is compared against the campaign datasets with the caveat that in-situ and point measurements are quite different to modelled (large) area averages.

Uncertainty in modelled yield is estimated through uncertainty in the regression slope (TODO:). Prior works use flight campaigns and in-situ data to verify HCHO columns in various locations (TODO: redo cite list from lit review). Figures X to D TODO: make figures comparing campaigns to model HCHO Yield calculations are performed at low resolution ($2^\circ \times 2.5^\circ$) which may lead to overestimation (Yu et al. 2016). TODO: how do I check this? Isoprene to HCHO yield between low and high NO_x (0.1 to 1 ppbv respectively) conditions has been estimated through box modelling to be 1.9 to 2.4 mol mol^{-1} in Bauwens et al. (2016).

3.4.4 Satellite Uncertainty

There are three main sources of error in the satellite HCHO columns:

- a Fitting error from the OMI retrieval.
- b Uncertainty in AMF calculations.
- c Uncertainty of HCHO background.

a) is available in the OMI product and reduced through spatial and temporal averaging. Taking the eight day gridded average with horizontal resolution of 0.25 by 0.3125 degrees (latitude by longitude) typically reduces uncertainty by a factor of 1.5 to 4. b) could be determined through comparison of GEOS-Chem output to measured HCHO columns, if they existed. Palmer et al. (2006) calculate the error in AMF through combining estimates of error in the UV albedo database ($\sim 8\%$), model error based on in-situ measurements, cloud error (20 – 30%) (Martin et al. 2003), and aerosol errors (< 20%), totalling AMF error of around $\sim 30\%$ (calculated in quadrature). Here we use 30% as a rough estimate of error in this term. TODO:Paul palmer calculation and combination for overall Satellite VC uncertainty per pixel and gridded. c) is also determined through a study of GEOS-Chem output, in relation to in-situ measurements. Since we expect oceanic background HCHO to be invariant, then variance in remote ocean HCHO can be used as a rough estimate of background uncertainty. TODO: calculate this uncertainty. Compare this error estimate with that of Curci et al. (2010), where the error in b) and c) are respectively found to be 30% and 15% based on their

analysis of CHIMERE. Millet et al. (2008) also examine this uncertainty and determine an overall uncertainty (1σ) of 25 – 27% in HCHO vertical columns with calculated AMFs where cloud fraction < 0.2 .

Two simple methods of looking at overall uncertainty from satellite measurements are performed here.

1. using the variance over the remote pacific ocean to provide relative uncertainty globally (e.g. De Smedt et al. 2012)
2. scaling up HCHO columns by 40% as an upper bound on satellite uncertainty

Analysing variance over the remote pacific gives a quick measure of uncertainty if we assume HCHO levels within the region are stable. This region should be relatively invariant throughout any month so each month the standard deviation of the midday total column HCHO amounts from 15°S to 15°N , and 180°W to 120°W . Other literature has found satellite HCHO columns to be up to 40% too low, so scaling them up 40% is another way of quickly analysing how sensitive our calculations are to the satellite HCHO columns.

3.4.4.1 OMI Retrieval

TODO: Calculate remote pacific variance (also bin by latitudes) and plot over time.

Provided with the OMI product is the measurement of uncertainty in each pixel, calculated by SAO from the backscattered solar radiation fit (Gonzalez Abad et al. 2015; Abad et al. 2016). Uncertainty introduced through AMF calculation needs to be additionally determined to give a representation of the confidence in vertical column amounts. BIRA use another method, and calculate the standard deviation of HCHO over the remote pacific ocean as the uncertainty (De Smedt et al. 2012; De Smedt et al. 2015). In the remote pacific, it can be assumed that HCHO variations are weak, with concentrations remaining steady in the short term (~ 1 month). This means the standard deviation over this region can be used as a proxy for determination of the instrument error.

TODO: uncertainty calculation on remote pacific OMI.

Satellite measured HCHO has been found to be biased low in several studies (eg. Zhu et al. 2016; De Smedt et al. 2015; Barkley et al. 2013). These papers use in-situ data to scale up the satellite HCHO columns for their areas of interest, however Australia lacks sufficient HCHO measurements to do this. Satellite bias is seen to be as high as 40%, which we use as a simplistic method of quantifying potential satellite uncertainty. If satellite HCHO was scaled up by 40% our isoprene emissions estimates would increase by the same, as our estimate is proportional to satellite HCHO.

OMI is scaled up by up to 40% in several papers (cite) we consider HCHO scaled by 1 and 1.4 to be boundaries for modelled yield. If we infer from this that there is 40% bias and random uncertainty remains unchanged, then in the S term, we find TODO increase or decrease in ΔE_{OMI} of some amount through changing $\Delta S = .$

3.4.4.2 Satellite vertical column recalculations

OMI HCHO vertical columns are recalculated using GEOS-Chem V10.01 a priori HCHO and air density profiles (see chapter 2). The recalculation is considered assumed to be

no more or less uncertain than that used to calculate the default AMF, and uncertainty in the AMF recalculation is not used to alter the pixel uncertainty from the OMH-CHO product. Here we examine the sensitivity of the isoprene emissions estimation technique to the AMF recalculation method. Through looking at how the emissions change based on whether we use the AMF provided (AMF_{OMI}), the AMF with shape factor recalculated but the default scattering weights (AMF_{GC}), or the fully recalculated AMF (AMF_{PP}).

Figure todo shows the emissions over Australia averaged within January 2005. This figure shows estimates from MEGAN (top), and top down estimates using OMH-CHO Ω s (row 1: OMI), Ω recalculated using GEOS-Chem shape factors (row 2: GC), and using the code from Paul Palmer's group (row 3: PP). Column 2 is emissions without applying anthropogenic or pyrogenic filters, Column 3 is calculated at the lower resolution of $2 \times 2.5^\circ$.

Figure todo shows emissions over time from a single grid square, estimated by MEGAN (black) and the three top-down estimates, using $2 \times 2.5^\circ$ horizontal resolution.

3.4.5 Fire Filtering

Figure 3.21 shows emissions estimates for January 2005, using three different HCHO columns as the basis: the original OMI satellite HCHO columns (Ω), those with AMF recalculated using a new a priori (Ω_{GC}), and those with AMFs recalculated using PP code (Ω_{PP}). The first row shows top-down emissions estimates, while the second row runs the same calculations without applying any fire or smoke filter. The Third row is the absolute difference between them: fire filtered minus standard emissions.

3.5 Conclusions and implications

3.5.1 Effects from scaling emissions

Using our top-down emissions estimate to recalculate MEGAN isoprene emissions for Australia is detailed in section 3.2 How these changes affect HCHO and ozone model outputs are discussed in this section.

3.5.1.1 HCHO levels

We examine the affect of scaling isoprene emissions on the correlation between modelled and satellite based HCHO columns. Figure TODO: shows the regressions between GEOS-Chem tropospheric column amounts of HCHO and satellite columns for two runs of GEOS-Chem: a) using standard MEGAN emissions, b) using our updated emissions. We interpolated or something (TODO) the emissions over Australia into the inventories used by GEOS-Chem which reduced the emissions by X% per year (over Australia). The resulting simulation output shows that HCHO was reduced by X%, although if we boost monoterpenes by X% where the isoprene emissions were lowered then

Wollongong FTIR measurements (see section ??) provide vertical profiles of HCHO which can be converted to total column amounts using modelled air densities. This is the only non-satellite long-term record of vertical profile HCHO available in Australia

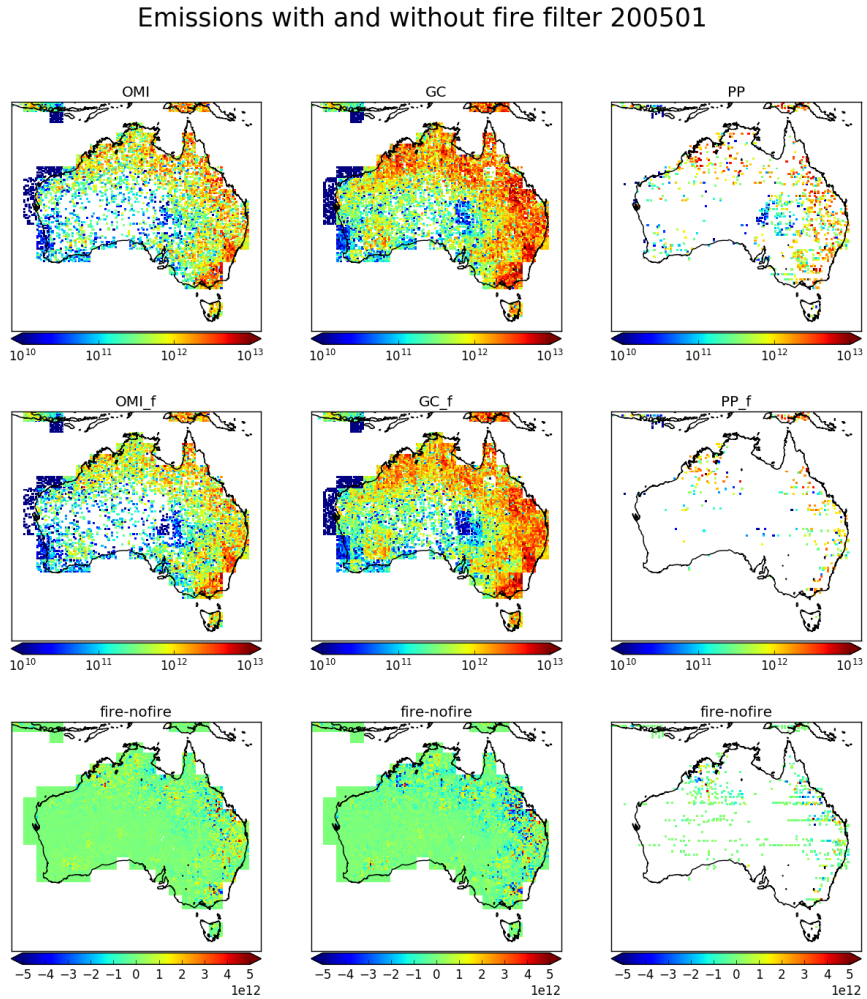


FIGURE 3.21: Emissions estimates using OMI satellite columns (column 1) recalculated with updated shape factor (column 2) and scattering weights (column 3). Turning off the fire and smoke filters gives emissions in row 2, while the difference between row 1 and row 2 is shown in row 3.

and we use it here to examine trends and seasonality. The time series for HCHO is shown in figure TODO, along with GEOS-Chem output before and after updating isoprene emissions. TODO: discuss plot here

TODO: Figure showing campaign data against model and recalculated model.

A long term regression of anomalies from the multi-year monthly average shows that TODO. Figure TODO shows the trend for each month along with co-located HCHO from GEOS-Chem outputs. Figure TODO shows how campaign data compares against GEOS-Chem modelled HCHO before and after isoprene scaling is performed. The regressions show improvement/no improvement TODO however there are relatively few data points for comparison as the campaigns only lasted a few months.

Figure todo shows how the longer term FTIR HCHO measurements compare against modelled HCHO before and after changing isoprene emissions

3.5.1.2 Ozone levels

TODO: compare ozone after changing isoprene emissions in GEOS-Chem Changing isoprene emissions over Australia impacts the cities/coasts TODO determine this. This is likely due to the relatively clean atmosphere over the majority of Australia, which is likely NO_x limited outside of major population centres.

TODO: Figure shows modelled surface ozone concentrations and their differences between model runs over an average summer (DJF). Figure TODO shows the same over an average winter (JJA). Figure TODO compares the summer differences to surface NO emissions (modelled), and total column NO (satellite).

Bibliography

- Brasseur, Guy P and Daniel J Jacob (2017). *Modeling of Atmospheric Chemistry*. Cambridge University Press. DOI: [10.1017/9781316544754](https://doi.org/10.1017/9781316544754).
- Hsieh, Nan-Hung and Chung-Min Liao (2013). "Fluctuations in air pollution give risk warning signals of asthma hospitalization". In: *Atmospheric Environment* 75, pp. 206–216. DOI: [10.1016/j.atmosenv.2013.04.043](https://doi.org/10.1016/j.atmosenv.2013.04.043). URL: <http://dx.doi.org/10.1016/j.atmosenv.2013.04.043>.
- Avnery, Shiri et al. (2013). "Global crop yield reductions due to surface ozone exposure: 2. Year 2030 potential crop production losses and economic damage under two scenarios of O₃ pollution". In: *Atmospheric Environment* 71.13, pp. 408–409. ISSN: 13522310. DOI: [10.1016/j.atmosenv.2012.12.045](https://doi.org/10.1016/j.atmosenv.2012.12.045). URL: <http://dx.doi.org/10.1016/j.atmosenv.2011.01.002>.
- Yue, Xu et al. (2017). "Ozone and haze pollution weakens net primary productivity in China". In: *Atmospheric Chemistry and Physics* 17.9, pp. 6073–6089. ISSN: 1680-7324. DOI: [10.5194/acp-17-6073-2017](https://doi.org/10.5194/acp-17-6073-2017). URL: <https://www.atmos-chem-phys.net/17/6073/2017/>.
- Myhre, G and D Shindell (2013). Chapter 8: *Anthropogenic and Natural Radiative Forcing*, in *Climate Change 2013: The Physical Science Basis, Working Group 1 Contribution to the Fifth Assessment Report of the Intergovernmental Panel on Climate Change*, 2013. Fifth Assessment Report of the Intergovernmental Panel on Climate Change, 2013.
- Monks, P. S. et al. (2015). "Tropospheric ozone and its precursors from the urban to the global scale from air quality to short-lived climate forcer". In: *Atmospheric Chemistry and Physics* 15.15, pp. 8889–8973. ISSN: 1680-7324. DOI: [10.5194/acp-15-8889-2015](https://doi.org/10.5194/acp-15-8889-2015). URL: <https://www.atmos-chem-phys.net/15/8889/2015/>.
- Lelieveld, J. et al. (2013). "Model calculated global, regional and megacity premature mortality due to air pollution". In: *Atmospheric Chemistry and Physics* 13.14, pp. 7023–7037. ISSN: 16807324. DOI: [10.5194/acp-13-7023-2013](https://doi.org/10.5194/acp-13-7023-2013).
- Ayers, James D and William R Simpson (2006). "Measurements of N₂O₅ near Fairbanks, Alaska". In: *Journal of Geophysical Research: Atmospheres* 111.D14, n/a–n/a. ISSN: 2156-2202. DOI: [10.1029/2006JD007070](https://doi.org/10.1029/2006JD007070). URL: <http://dx.doi.org/10.1029/2006JD007070>.
- Lelieveld, J. et al. (2009). "Severe ozone air pollution in the Persian Gulf region". In: *Atmospheric Chemistry and Physics* 9, pp. 1393–1406. ISSN: 1680-7324. DOI: [10.5194/acp-9-1393-2009](https://doi.org/10.5194/acp-9-1393-2009).
- Ashmore, M R, Lisa. Emberson, and Murray Frank (2003). *Air pollution impacts on crops and forests : a global assessment*. Ed. by Lisa Emberson, Mike Ashmore, and Frank Murray. Imperial College Press London ; River Edge, NJ, xiii, 372 p. : ISBN: 186094292.

- Stevenson, D. S. et al. (2013). "Tropospheric ozone changes, radiative forcing and attribution to emissions in the Atmospheric Chemistry and Climate Model Intercomparison Project (ACCMIP)". In: *Atmospheric Chemistry and Physics* 13.6, pp. 3063–3085. ISSN: 16807316. DOI: [10.5194/acp-13-3063-2013](https://doi.org/10.5194/acp-13-3063-2013).
- Selin, N E et al. (2009). "Global health and economic impacts of future ozone pollution". In: *Environmental Research Letters* 4.4, p. 044014. ISSN: 1748-9326. DOI: [10.1088/1748-9326/4/4/044014](https://doi.org/10.1088/1748-9326/4/4/044014).
- Atkinson, Roger (2000). "Atmospheric chemistry of VOCs and NO(x)". In: *Atmospheric Environment* 34.12-14, pp. 2063–2101. ISSN: 13522310. DOI: [10.1016/S1352-2310\(99\)00460-4](https://doi.org/10.1016/S1352-2310(99)00460-4).
- Fuentes, J. D. et al. (2000). "Biogenic Hydrocarbons in the Atmospheric Boundary Layer: A Review". In: *Bulletin of the American Meteorological Society* 81.7, pp. 1537–1575. ISSN: 00030007. DOI: [10.1175/1520-0477\(2000\)081<1537:BHITAB>2.3.CO;2](https://doi.org/10.1175/1520-0477(2000)081<1537:BHITAB>2.3.CO;2). arXiv: [arXiv : 1011.1669v3](https://arxiv.org/abs/1011.1669v3). URL: [http://journals.ametsoc.org/doi/abs/10.1175/1520-0477\(2000\)081%3C1537%3ABHITAB%3E2.3.CO%3B2](http://journals.ametsoc.org/doi/abs/10.1175/1520-0477(2000)081%3C1537%3ABHITAB%3E2.3.CO%3B2).
- Paulot, Fabien et al. (2009b). "Unexpected Epoxide Formation in the". In: *Science* 325.2009, pp. 730–733. ISSN: 0036-8075. DOI: [10.1126/science.1172910](https://doi.org/10.1126/science.1172910).
- Atkinson, Roger and Janet Arey (2003). "Gas-phase tropospheric chemistry of biogenic volatile organic compounds: A review". In: *Atmospheric Environment* 37.SUPPL. 2. ISSN: 13522310. DOI: [10.1016/S1352-2310\(03\)00391-1](https://doi.org/10.1016/S1352-2310(03)00391-1).
- Kanakidou, M et al. (2005). "Physics Organic aerosol and global climate modelling : a review". In: *Atmospheric Chemistry and Physics* 5, pp. 1053–1123.
- Stocker, T.F. et al. *IPCC, 2013: Climate Change 2013: The Physical Science Basis. Contribution of Working Group I to the Fifth Assessment Report of the Intergovernmental Panel on Climate Change*. Tech. rep. Cambridge University Press, Cambridge, United Kingdom and New York, NY, USA. DOI: [10.1017/CBO9781107415324](https://doi.org/10.1017/CBO9781107415324).
- Intergovernmental Panel on Climate Change (IPCC): Climate Change: The Scientific Basis* (2001). Tech. rep. Cambridge University Press. URL: <http://www.ipcc.ch/ipccreports/tar/>.
- Forster, P. et al. (2007). *Changes in Atmospheric Constituents and in Radiative Forcing*. In: *Climate Change 2007: The Physical Science Basis. Contribution of Working Group I to the Fourth Assessment Report of the Intergovernmental Panel on Climate Change* Solomon, S., D. Qin, M. Man. URL: https://www.ipcc.ch/publications_and_data/ar4/wg1/en/ch2.html (visited on 01/14/2016).
- Arneth, A et al. (2008). "Why are estimates of global terrestrial isoprene emissions so similar (and why is this not so for monoterpenes)?" In: *Atmos. Chem. Phys* 8.x, pp. 4605–4620. ISSN: 1680-7375. DOI: [10.5194/acpd-8-7017-2008](https://doi.org/10.5194/acpd-8-7017-2008).
- Emmerson, Kathryn M. et al. (2016). "Current estimates of biogenic emissions from eucalypts uncertain for southeast Australia". In: *Atmospheric Chemistry and Physics* 16.11, pp. 6997–7011. ISSN: 1680-7324. DOI: [10.5194/acp-16-6997-2016](https://doi.org/10.5194/acp-16-6997-2016). URL: <http://www.atmos-chem-phys.net/16/6997/2016/>.
- Hegglin, Michaela I and Theodore G Shepherd (2009). "Large climate-induced changes in ultraviolet index and stratosphere-to-troposphere ozone flux". In: *Nature Geoscience* 2.10, pp. 687–691. DOI: [10.1038/ngeo604](https://doi.org/10.1038/ngeo604). URL: <http://dx.doi.org/10.1038/ngeo604>.

- Jacob, Daniel J (1999). *Introduction to Atmospheric Chemistry*. Ed. by Daniel J Jacob. Princeton University Press. URL: <http://acmg.seas.harvard.edu/people/faculty/djj/book/index.html>.
- Huang, Guanyu et al. (2017). "Validation of 10-year SAO OMI Ozone Profile (PROFOZ) Product Using Aura MLS Measurements". In: *Atmospheric Measurement Techniques Discussions*, pp. 1–25. ISSN: 1867-8610. DOI: [10.5194/amt-2017-92](https://doi.org/10.5194/amt-2017-92). URL: <https://www.atmos-meas-tech-discuss.net/amt-2017-92/>.
- Zeng, Guang et al. (2017). "Attribution of recent ozone changes in the Southern Hemisphere mid-latitudes using statistical analysis and chemistry-climate model simulations". In: *Atmospheric Chemistry and Physics* 17.17, pp. 10495–10513. ISSN: 16807324. DOI: [10.5194/acp-17-10495-2017](https://doi.org/10.5194/acp-17-10495-2017).
- Young, P J et al. (2017). "Tropospheric Ozone Assessment Report (TOAR): Assessment of global-scale model performance for global and regional ozone distributions, variability, and trends". In: *Elementa: Science of the Anthropocene*, pp. 0–84. ISSN: 2325-1026. DOI: [10.1525/elementa.265](https://doi.org/10.1525/elementa.265). URL: http://eprints.lancs.ac.uk/88836/1/TOAR_Model_Performance_07062017.pdf http://www.igacproject.org/sites/default/files/2017-05/TOAR-Model_Performance_draft_for_open_comment.pdf.
- Cape, J. N. (2008). "Surface ozone concentrations and ecosystem health: Past trends and a guide to future projections". In: *Science of the Total Environment* 400.1-3, pp. 257–269. ISSN: 00489697. DOI: [10.1016/j.scitotenv.2008.06.025](https://doi.org/10.1016/j.scitotenv.2008.06.025). URL: <http://dx.doi.org/10.1016/j.scitotenv.2008.06.025>.
- Delmas, R, D Serca, and C Jambert (1997). "Global inventory of NO_x sources". In: *Nutrient cycling in agroecosystems* 48.x, pp. 51–60. ISSN: 1385-1314. DOI: [10.1023/A:1009793806086](https://doi.org/10.1023/A:1009793806086). URL: <http://link.springer.com/article/10.1023/A:1009793806086>.
- Sillman, Sanford (1999). "The relation between ozone, NO and hydrocarbons in urban and polluted rural environments". In: *Atmospheric Environment* 33. DOI: [https://doi.org/10.1016/S1352-2310\(98\)00345-8](https://doi.org/10.1016/S1352-2310(98)00345-8). URL: [http://www-personal.umich.edu/\\$\sim\\\$sillman/web-publications/Sillmanreview99.pdf](http://www-personal.umich.edu/$\sim\$sillman/web-publications/Sillmanreview99.pdf) <https://www.sciencedirect.com/science/article/pii/S1352231098003458>.
- Stohl, Andreas et al. (2003). "A new perspective of stratosphere-troposphere exchange". In: *Bulletin of the American Meteorological Society* 84.11, pp. 1565–1573+1473. ISSN: 00030007. DOI: [10.1175/BAMS-84-11-1565](https://doi.org/10.1175/BAMS-84-11-1565).
- Guenther, A et al. (2006). "Estimates of global terrestrial isoprene emissions using MEGAN (Model of Emissions of Gases and Aerosols from Nature)". In: *Atmospheric Chemistry and Physics* 6.11, pp. 3181–3210. DOI: [10.5194/acp-6-3181-2006](https://doi.org/10.5194/acp-6-3181-2006). URL: <http://dx.doi.org/10.5194/acp-6-3181-2006>.
- Jacobson, M C and H Hansson (2000). "Organic atmospheric aerosols: Review and state of the science". In: *Reviews of Geophysics* 38.38, pp. 267–294. ISSN: 87551209. DOI: [10.1029/1998RG000045](https://doi.org/10.1029/1998RG000045). URL: <http://dx.doi.org/10.1029/1998RG000045>.
- Kuang, Shi et al. (2017). "Summertime tropospheric ozone enhancement associated with a cold front passage due to stratosphere-to-troposphere transport and biomass burning: Simultaneous ground-based lidar and airborne measurements". In: *Journal of Geophysical Research: Atmospheres* 122.2, pp. 1293–1311. ISSN: 21698996. DOI: [10.1002/2016JD026078](https://doi.org/10.1002/2016JD026078). URL: <http://dx.doi.org/10.1002/2016JD026078>.

- Cooper, O. et al. (2004). "On the life cycle of a stratospheric intrusion and its dispersion into polluted warm conveyor belts". In: *Journal of Geophysical Research* 109.23, pp. 1–18. ISSN: 01480227. DOI: [10.1029/2003JD004006](https://doi.org/10.1029/2003JD004006).
- Young, P. J. et al. (2013). "Preindustrial to present-day changes in tropospheric hydroxyl radical and methane lifetime from the Atmospheric Chemistry and Climate Model Intercomparison Project (ACCMIP)". In: *Atmospheric Chemistry and Physics* 13.10, pp. 5277–5298. ISSN: 16807316. DOI: [10.5194/acp-13-5277-2013](https://doi.org/10.5194/acp-13-5277-2013).
- Sprenger, Michael, Mischa Croci Maspoch, and Heini Wernli (2003). "Tropopause folds and cross-tropopause exchange: A global investigation based upon ECMWF analyses for the time period March 2000 to February 2001". In: *Journal of Geophysical Research* 108.D12. ISSN: 2156-2202. DOI: [10.1029/2002JD002587](https://doi.org/10.1029/2002JD002587). URL: <http://dx.doi.org/10.1029/2002JD002587>.
- Ojha, Narendra et al. (2016). "Secondary ozone peaks in the troposphere over the Himalayas". In: *Atmospheric Chemistry and Physics Discussions* 17.November, pp. 1–25. ISSN: 1680-7375. DOI: [10.5194/acp-2016-908](https://doi.org/10.5194/acp-2016-908). URL: <http://www.atmos-chem-phys-discuss.net/acp-2016-908/>.
- Liu, Junhua et al. (2017). "Causes of interannual variability over the southern hemispheric tropospheric ozone maximum". In: *Atmos. Chem. Phys* 17.5, pp. 3279–3299. ISSN: 1680-7324. DOI: [10.5194/acp-17-3279-2017](https://doi.org/10.5194/acp-17-3279-2017). URL: www.atmos-chem-phys.net/17/3279/2017/.
- Lin, Meiyun et al. (2015). "Climate variability modulates western US ozone air quality in spring via deep stratospheric intrusions." In: *Nature communications* 6.May, p. 7105. ISSN: 2041-1723. DOI: [10.1038/ncomms8105](https://doi.org/10.1038/ncomms8105). URL: <http://www.nature.com/ncomms/2015/150512/ncomms8105/full/ncomms8105.html>.
- Christian, Kenneth E. et al. (2018). "Global sensitivity analysis of GEOS-Chem modeled ozone and hydrogen oxides during the INTEX campaigns". In: *Atmospheric Chemistry and Physics* 18.4, pp. 2443–2460. ISSN: 1680-7324. DOI: [10.5194/acp-18-2443-2018](https://doi.org/10.5194/acp-18-2443-2018). URL: <https://www.atmos-chem-phys.net/18/2443/2018/>.
- Marvin, Margaret R. et al. (2017). "Impact of evolving isoprene mechanisms on simulated formaldehyde: An inter-comparison supported by in situ observations from SENEX". In: *Atmospheric Environment* 164, pp. 325–336. ISSN: 13522310. DOI: [10.1016/j.atmosenv.2017.05.049](https://doi.org/10.1016/j.atmosenv.2017.05.049). URL: https://ac.els-cdn.com/S1352231017303618/1-s2.0-S1352231017303618-main.pdf?_tid=3de7eaaa-06ff-11e8-99a9-0000aacb360&acdnat=1517455576_09d7334af609ed43470155c1c42fad5fhttp://www.sciencedirect.com/science/article/pii/S1352231017303618.
- Mazzuca, Gina M. et al. (2016). "Ozone production and its sensitivity to NO_x and VOCs: Results from the DISCOVER-AQ field experiment, Houston 2013". In: *Atmospheric Chemistry and Physics* 16.22, pp. 14463–14474. ISSN: 16807324. DOI: [10.5194/acp-16-14463-2016](https://doi.org/10.5194/acp-16-14463-2016).
- Stevenson, D S et al. (2006). "Multimodel ensemble simulations of present-day and near-future tropospheric ozone". In: *Journal of Geophysical Research* 111.D8. DOI: [10.1029/2005jd006338](https://doi.org/10.1029/2005jd006338). URL: <http://dx.doi.org/10.1029/2005JD006338>.
- Guenther, Alex et al. (2000). "Natural emissions of non-methane volatile organic compounds, carbon monoxide, and oxides of nitrogen from North America". In: *Atmospheric Environment* 34.12-14, pp. 2205–2230. ISSN: 13522310. DOI: [10.1016/S1352-2310\(99\)00465-3](https://doi.org/10.1016/S1352-2310(99)00465-3).

- Guenther, Alex et al. (1995). "A global model of natural volatile organic compound emissions". In: *Journal of Geophysical Research* 100.D5, pp. 8873–8892. ISSN: 0148-0227. DOI: [10.1029/94JD02950](https://doi.org/10.1029/94JD02950). URL: [http://onlinelibrary.wiley.com/doi/10.1029/94JD02950/full](http://onlinelibrary.wiley.com/doi/10.1029/94JD02950/full%5Cnhttp://doi.wiley.com/10.1029/94JD02950http://onlinelibrary.wiley.com/doi/10.1029/94JD02950/full).
- Glasius, Marianne and Allen H. Goldstein (2016). "Recent Discoveries and Future Challenges in Atmospheric Organic Chemistry". In: *Environmental Science and Technology* 50.6, pp. 2754–2764. ISSN: 15205851. DOI: [10.1021/acs.est.5b05105](https://doi.org/10.1021/acs.est.5b05105).
- Yue, X., N. Unger, and Y. Zheng (2015). "Distinguishing the drivers of trends in land carbon fluxes and plant volatile emissions over the past 3 decades". In: *Atmospheric Chemistry and Physics* 15.20, pp. 11931–11948. ISSN: 16807324. DOI: [10.5194/acp-15-11931-2015](https://doi.org/10.5194/acp-15-11931-2015).
- Stavrakou, T. et al. (2014). "Isoprene emissions over Asia 1979–2012: Impact of climate and land-use changes". In: *Atmospheric Chemistry and Physics* 14.9. ISSN: 16807324. DOI: [10.5194/acp-14-4587-2014](https://doi.org/10.5194/acp-14-4587-2014).
- Kwon, Hyeong-Ahn et al. (2017). "Sensitivity of formaldehyde (HCHO) column measurements from a geostationary satellite to temporal variation of the air mass factor in East Asia". In: *Atmospheric Chemistry and Physics* 17.7, pp. 4673–4686. ISSN: 1680-7324. DOI: [10.5194/acp-17-4673-2017](https://doi.org/10.5194/acp-17-4673-2017). URL: <http://www.atmos-chem-phys.net/17/4673/2017/>.
- Aksoyoglu, Sebnem et al. (2017). "Secondary inorganic aerosols in Europe: sources and the significant influence of biogenic VOC emissions, especially on ammonium nitrate". In: *Atmospheric Chemistry and Physics* 17.12, pp. 7757–7773. ISSN: 1680-7324. DOI: [10.5194/acp-17-7757-2017](https://doi.org/10.5194/acp-17-7757-2017). URL: <https://www.atmos-chem-phys.net/17/7757/2017/>.
- Lelieveld, J et al. (2015). "The contribution of outdoor air pollution sources to premature mortality on a global scale". In: *Nature* 525.7569, pp. 367–371. DOI: [10.1038/nature15371](https://doi.org/10.1038/nature15371). URL: <http://dx.doi.org/10.1038/nature15371>.
- Cooper, O R, S Gilge, and D T Shindell (2014). "Global distribution and trends of tropospheric ozone : An observation-based review". In: pp. 1–28. DOI: [10.12952/journal.elementa.000029](https://doi.org/10.12952/journal.elementa.000029). URL: <https://www.elementascience.org/articles/10.12952/journal.elementa.000029/>.
- Hoek, Gerard et al. (2013). "Long-term air pollution exposure and cardio-respiratory mortality: a review". In: *Environmental Health* 12.1, p. 43. DOI: [10.1186/1476-069x-12-43](https://doi.org/10.1186/1476-069x-12-43). URL: <http://dx.doi.org/10.1186/1476-069x-12-43>.
- Krewski, D et al. (2009). "Extended follow-up and spatial analysis of the American Cancer Society study linking particulate air pollution and mortality". In: *Res Rep Health Eff Inst* 140, pp. 5–36. ISSN: 1041-5505 (Print) 1041-5505 (Linking). URL: <http://www.ncbi.nlm.nih.gov/pubmed/19627030>.
- Silva, Raquel A et al. (2013). "Global premature mortality due to anthropogenic outdoor air pollution and the contribution of past climate change". In: *Environ. Res. Lett.* 8.3, p. 34005. DOI: [10.1088/1748-9326/8/3/034005](https://doi.org/10.1088/1748-9326/8/3/034005). URL: <http://dx.doi.org/10.1088/1748-9326/8/3/034005>.
- Kroll, Jesse H. and John H. Seinfeld (2008). "Chemistry of secondary organic aerosol: Formation and evolution of low-volatility organics in the atmosphere". In: *Atmospheric Environment* 42.16, pp. 3593–3624. ISSN: 13522310. DOI: [10.1016/j.atmosenv.2008.02.030](https://doi.org/10.1016/j.atmosenv.2008.02.030).

- atmosenv . 2008 . 01 . 003. URL: <http://www.sciencedirect.com.ezproxy.uow.edu.au/science/article/pii/S1352231008000253>.
- Guenther, A. B. et al. (2012). "The model of emissions of gases and aerosols from nature version 2.1 (MEGAN2.1): An extended and updated framework for modeling biogenic emissions". In: *Geoscientific Model Development* 5.6, pp. 1471–1492. ISSN: 1991959X. DOI: [10.5194/gmd-5-1471-2012](https://doi.org/10.5194/gmd-5-1471-2012).
- Brown, S. S. et al. (2009). "Nocturnal isoprene oxidation over the Northeast United States in summer and its impact on reactive nitrogen partitioning and secondary organic aerosol". In: *Atmospheric Chemistry and Physics* 9.9, pp. 3027–3042. ISSN: 16807316. DOI: [10.5194/acp-9-3027-2009](https://doi.org/10.5194/acp-9-3027-2009).
- Kefauver, Shawn C., Iolanda Filella, and Josep Peñuelas (2014). "Remote sensing of atmospheric biogenic volatile organic compounds (BVOCs) via satellite-based formaldehyde vertical column assessments". en. In: *International Journal of Remote Sensing*. URL: <http://www.tandfonline.com/doi/abs/10.1080/01431161.2014.968690#.VqqEubNM6lM>.
- Millet, Dylan B et al. (2006). "Formaldehyde distribution over North America: Implications for satellite retrievals of formaldehyde columns and isoprene emission". In: *J. Geophys. Res.* 111.D24. DOI: [10.1029/2005jd006853](https://doi.org/10.1029/2005jd006853). URL: TODO.
- Niinemets, U. et al. (2010). "The emission factor of volatile isoprenoids: Stress, acclimation, and developmental responses". In: *Biogeosciences* 7.7, pp. 2203–2223. ISSN: 17264170. DOI: [10.5194/bg-7-2203-2010](https://doi.org/10.5194/bg-7-2203-2010).
- Lathière, J et al. (2006). "Impact of climate variability and land use changes on global biogenic volatile organic compound emissions". In: *Atmospheric Chemistry and Physics* 6.2003, pp. 2129–2146. ISSN: 16807324. DOI: [10.5194/acp-6-2129-2006](https://doi.org/10.5194/acp-6-2129-2006). URL: www.atmos-chem-phys.net/6/2129/2006/.
- Sindelarova, K. et al. (2014). "Global data set of biogenic VOC emissions calculated by the MEGAN model over the last 30 years". In: *Atmospheric Chemistry and Physics* 14.17, pp. 9317–9341. ISSN: 16807324. DOI: [10.5194/acp-14-9317-2014](https://doi.org/10.5194/acp-14-9317-2014). arXiv: [arXiv:1011.1669v3](https://arxiv.org/abs/1011.1669v3).
- Shim, Changsub et al. (2005). "Constraining global isoprene emissions with Global Ozone Monitoring Experiment (GOME) formaldehyde column measurements". In: *Journal of Geophysical Research Atmospheres* 110.24, pp. 1–14. ISSN: 01480227. DOI: [10.1029/2004JD005629](https://doi.org/10.1029/2004JD005629).
- Wagner, V (2002). "Are CH₂O measurements in the marine boundary layer suitable for testing the current understanding of CH₄ photooxidation?: A model study". In: *Journal of Geophysical Research* 107.D3, p. 4029. ISSN: 0148-0227. DOI: [10.1029/2001JD000722](https://doi.org/10.1029/2001JD000722). URL: <http://doi.wiley.com/10.1029/2001JD000722>.
- Nguyen, T. B. et al. (2014). "Overview of the Focused Isoprene eXperiment at the California Institute of Technology (FIXCIT): Mechanistic chamber studies on the oxidation of biogenic compounds". In: *Atmospheric Chemistry and Physics* 14.24. ISSN: 16807324. DOI: [10.5194/acp-14-13531-2014](https://doi.org/10.5194/acp-14-13531-2014).
- Messina, Palmira et al. (2016). "Global biogenic volatile organic compound emissions in the ORCHIDEE and MEGAN models and sensitivity to key parameters". In: *Atmospheric Chemistry and Physics* 16.22, pp. 14169–14202. ISSN: 16807324. DOI: [10.5194/acp-16-14169-2016](https://doi.org/10.5194/acp-16-14169-2016). URL: <http://www.atmos-chem-phys.net/16/14169/2016/acp-16-14169-2016.pdf>.

- Hewitt, C N et al. (2011). "Ground-level ozone influenced by circadian control of isoprene emissions". In: *Nature Geoscience* 4.10, pp. 671–674. DOI: [10.1038/ngeo1271](https://doi.org/10.1038/ngeo1271). URL: <http://dx.doi.org/10.1038/ngeo1271>.
- Fan, Jiwen and Renyi Zhang (2004). "Atmospheric oxidation mechanism of isoprene". In: *Environmental Chemistry* 1.3, pp. 140–149. ISSN: 14482517. DOI: [10.1071/EN04045](https://doi.org/10.1071/EN04045). URL: <http://dx.doi.org/10.1071/en04045>.
- Jiang, Xiaoyan et al. (2018). "Isoprene emission response to drought and the impact on global atmospheric chemistry". In: *Atmospheric Environment* 183, pp. 69–83. ISSN: 1352-2310. DOI: [10.1016/J.ATMOSENV.2018.01.026](https://doi.org/10.1016/J.ATMOSENV.2018.01.026). URL: <https://www.sciencedirect.com/science/article/pii/S1352231018300402>.
- Izci, Alime and Halit L. Hosgün (2007). "Kinetics of synthesis of isobutyl propionate over amberlyst-15". In: *Turkish Journal of Chemistry* 31.5, pp. 493–499. ISSN: 13000527. DOI: [10.1002/kin](https://doi.org/10.1002/kin).
- Mao, Jingqiu et al. (2013). "Ozone and organic nitrates over the eastern United States: Sensitivity to isoprene chemistry". In: *Journal of Geophysical Research Atmospheres* 118.19, pp. 11256–11268. ISSN: 21698996. DOI: [10.1002/jgrd.50817](https://doi.org/10.1002/jgrd.50817).
- Wolfe, G. M. et al. (2016). "Formaldehyde production from isoprene oxidation across NO_x regimes". In: *Atmospheric Chemistry and Physics* 16.x, pp. 2597–2610. ISSN: 16807324. DOI: [10.5194/acp-16-2597-2016](https://doi.org/10.5194/acp-16-2597-2016). URL: www.atmos-chem-phys.net/16/2597/2016/.
- Crounse, John D et al. (2012). "Atmospheric Fate of Methacrolein. 1. Peroxy Radical Isomerization Following Addition of OH and O₂". In: *Physical Chemistry m.*
- Nguyen, Tran B. et al. (2016). "Atmospheric fates of Criegee intermediates in the ozonolysis of isoprene". In: *Phys. Chem. Chem. Phys.* 18.15, pp. 10241–10254. ISSN: 1463-9076. DOI: [10.1039/C6CP00053C](https://doi.org/10.1039/C6CP00053C). URL: <http://xlink.rsc.org/?DOI=C6CP00053C>.
- Crounse, John D. et al. (2013). "Autoxidation of organic compounds in the atmosphere". In: *Journal of Physical Chemistry Letters* 4.20, pp. 3513–3520. ISSN: 19487185. DOI: [10.1021/jz4019207](https://doi.org/10.1021/jz4019207). URL: <http://pubs.acs.org/doi/abs/10.1021/jz4019207>.
- Crounse, John D. et al. (2006). "Measurement of gas-phase hydroperoxides by chemical ionization mass spectrometry". In: *Analytical Chemistry* 78.19, pp. 6726–6732. ISSN: 00032700. DOI: [10.1021/ac0604235](https://doi.org/10.1021/ac0604235). URL: <https://pubs.acs.org/doi/abs/10.1021/ac0604235>.
- Yu, Karen et al. (2016). "Sensitivity to grid resolution in the ability of a chemical transport model to simulate observed oxidant chemistry under high-isoprene conditions". In: *Atmospheric Chemistry and Physics* 16.7, pp. 4369–4378. ISSN: 16807324. DOI: [10.5194/acp-16-4369-2016](https://doi.org/10.5194/acp-16-4369-2016). URL: http://acmg.seas.harvard.edu/publications/2016/Yu_ACP_2016.pdf.
- Marais, E A et al. (2012). "Isoprene emissions in Africa inferred from OMI observations of formaldehyde columns". In: *Atmospheric Chemistry and Physics* 12.3, pp. 7475–7520. DOI: [10.5194/acp-12-6219-2012](https://doi.org/10.5194/acp-12-6219-2012). URL: <http://dx.doi.org/10.5194/acp-12-6219-2012>.
- Liu, Yingjun et al. (2016b). "Isoprene photochemistry over the Amazon rainforest". In: *Proceedings of the National Academy of Sciences* 113.22, pp. 6125–6130. ISSN: 0027-8424. DOI: [10.1073/pnas.1524136113](https://doi.org/10.1073/pnas.1524136113). URL: <http://www.pnas.org/content/113/22/6125.abstract>.

- Paulot, F. et al. (2009a). "Isoprene photooxidation: new insights into the production of acids and organic nitrates". In: *Atmospheric Chemistry and Physics* 9.4, pp. 1479–1501. ISSN: 1680-7324. DOI: [10.5194/acp-9-1479-2009](https://doi.org/10.5194/acp-9-1479-2009).
- Wolfe, Glenn M. et al. (2012). "Photolysis, OH reactivity and ozone reactivity of a proxy for isoprene-derived hydroperoxyenals (HPALDs)". In: *Physical Chemistry Chemical Physics* 14.20, p. 7276. ISSN: 1463-9076. DOI: [10.1039/c2cp40388a](https://doi.org/10.1039/c2cp40388a). URL: <http://xlink.rsc.org/?DOI=c2cp40388a>.
- Liu, Y. J. et al. (2013). "Production of methyl vinyl ketone and methacrolein via the hydroperoxyl pathway of isoprene oxidation". In: *Atmospheric Chemistry and Physics* 13.11, pp. 5715–5730. ISSN: 1680-7324. DOI: [10.5194/acp-13-5715-2013](https://doi.org/10.5194/acp-13-5715-2013). URL: <http://www.atmos-chem-phys.net/13/5715/2013/>.
- Palmer, Paul I et al. (2006). "Quantifying the seasonal and interannual variability of North American isoprene emissions using satellite observations of the formaldehyde column". In: *J.Geophys.Res.* 111, p. D12315. ISSN: 0148-0227. DOI: [10.1029/2005JD006689](https://doi.org/10.1029/2005JD006689). URL: <http://dx.doi.org/10.1029/2005JD006689>.
- Peeters, Jozef and Jean-Francis Muller (2010). "HO_x radical regeneration in isoprene oxidation via peroxy radical isomerisations. II: experimental evidence and global impact". In: *Physical Chemistry Chemical Physics* 12.42, p. 14227. ISSN: 1463-9076. DOI: [10.1039/c0cp00811g](https://doi.org/10.1039/c0cp00811g). URL: <http://pubs.rsc.org/en/content/articlepdf/2010/cp/c0cp00811g>.
- Mao, J. et al. (2012). "Insights into hydroxyl measurements and atmospheric oxidation in a California forest". In: *Atmospheric Chemistry and Physics* 12.17, pp. 8009–8020. ISSN: 16807316. DOI: [10.5194/acp-12-8009-2012](https://doi.org/10.5194/acp-12-8009-2012).
- Chan, A. W. H. et al. (2010). "Role of aldehyde chemistry and NO_x concentrations in secondary organic aerosol formation". In: *Atmospheric Chemistry and Physics* 10.15, pp. 7169–7188. ISSN: 1680-7324. DOI: [10.5194/acp-10-7169-2010](https://doi.org/10.5194/acp-10-7169-2010). URL: <http://www.atmos-chem-phys.net/10/7169/2010/>.
- Surratt, Jason D et al. (2010). "Reactive intermediates revealed in secondary organic aerosol formation from isoprene". In: *PNAS* 107.15, pp. 6640–6645. DOI: [10.1073/pnas.0911114107](https://doi.org/10.1073/pnas.0911114107). URL: <http://www.pnas.org/content/107/15/6640.full.pdf>.
- Lin, Ying-Hsuan et al. (2013). "Epoxide as a precursor to secondary organic aerosol formation from isoprene photooxidation in the presence of nitrogen oxides". In: DOI: [10.1073/pnas.1221150110](https://doi.org/10.1073/pnas.1221150110). URL: <http://www.pnas.org/content/110/17/6718.full.pdf>.
- Peeters, J., T. L. Nguyen, and L. Vereecken (2009). "HO_x radical regeneration in the oxidation of isoprene". In: *Physical Chemistry Chemical Physics* 11.28, p. 5935. ISSN: 1463-9076. DOI: [10.1039/b908511d](https://doi.org/10.1039/b908511d). URL: <http://xlink.rsc.org/?DOI=b908511d>.
- Rollins, A W et al. (2009). "Isoprene oxidation by nitrate radical: alkyl nitrate and secondary organic aerosol yields". In: *Atmos. Chem. Phys. Atmospheric Chemistry and Physics* 9, pp. 6685–6703. URL: www.atmos-chem-phys.net/9/6685/2009/.
- Fortems-Cheiney, A. et al. (2012). "The formaldehyde budget as seen by a global-scale multi-constraint and multi-species inversion system". In: *Atmospheric Chemistry and Physics* 12.15, pp. 6699–6721. ISSN: 16807316. DOI: [10.5194/acp-12-6699-2012](https://doi.org/10.5194/acp-12-6699-2012). URL: <http://www.atmos-chem-phys.net/12/6699/2012/acp-12-6699-2012.pdf>.

- Palmer, Paul I (2003). "Mapping isoprene emissions over North America using formaldehyde column observations from space". In: *J. Geophys. Res.* 108.D6. DOI: [10.1029/2002jd002153](https://doi.org/10.1029/2002jd002153). URL: <http://dx.doi.org/10.1029/2002jd002153>.
- Andreae, M O (2001). "Emission of trace gases and aerosols from biomass burning". In: *Biogeochemistry* 15.4, pp. 955–966. URL: <http://onlinelibrary.wiley.com/doi/10.1029/2000GB001382/epdf>.
- Millet, Dylan B. et al. (2008). "Spatial distribution of isoprene emissions from North America derived from formaldehyde column measurements by the OMI satellite sensor". In: *Journal of Geophysical Research Atmospheres* 113.2, pp. 1–18. ISSN: 01480227. DOI: [10.1029/2007JD008950](https://doi.org/10.1029/2007JD008950).
- Zhu, Lei et al. (2014). "Anthropogenic emissions of highly reactive volatile organic compounds in eastern Texas inferred from oversampling of satellite (OMI) measurements of HCHO columns". In: *Environmental Research Letters* 9.11, p. 114004. ISSN: 1748-9326. DOI: [10.1088/1748-9326/9/11/114004](https://doi.org/10.1088/1748-9326/9/11/114004). URL: <http://stacks.iop.org/1748-9326/9/i=11/a=114004?key=crossref.3d2869ee02fd4f0792f831ac8cbecc117>.
- Fu, Tzung-may et al. (2007). "Space-based formaldehyde measurements as constraints on volatile organic compound emissions in east and south Asia and implications for ozone". In: 112, pp. 1–15. DOI: [10.1029/2006JD007853](https://doi.org/10.1029/2006JD007853).
- Levy, Hiram (1972). "Photochemistry of the lower troposphere". In: *Planetary and Space Science* 20.6, pp. 919–935. ISSN: 00320633. DOI: [10.1016/0032-0633\(72\)90177-8](https://doi.org/10.1016/0032-0633(72)90177-8).
- CRUTZEN, PAUL J, MARK G LAWRENCE, and ULRICH PÖSCHL (1999). "On the background photochemistry of tropospheric ozone". In: *Tellus A* 51.1, pp. 123–146. ISSN: 1600-0870. DOI: [10.1034/j.1600-0870.1999.t01-1-00010.x](https://doi.org/10.1034/j.1600-0870.1999.t01-1-00010.x). URL: <http://dx.doi.org/10.1034/j.1600-0870.1999.t01-1-00010.x>.
- Ayers, G. P. et al. (1997). "Formaldehyde production in clean marine air". In: *Geophysical Research Letters* 24.4. DOI: <https://doi.org/10.1029/97GL00123>.
- Franco, B. et al. (2015). "Retrievals of formaldehyde from ground-based FTIR and MAX-DOAS observations at the Jungfraujoch station and comparisons with GEOS-Chem and IMAGES model simulations". In: *Atmospheric Measurement Techniques* 8.4, pp. 1733–1756. ISSN: 18678548. DOI: [10.5194/amt-8-1733-2015](https://doi.org/10.5194/amt-8-1733-2015).
- Gonzalez Abad, G. et al. (2015). "Updated Smithsonian Astrophysical Observatory Ozone Monitoring Instrument (SAO OMI) formaldehyde retrieval". In: *Atmospheric Measurement Techniques* 8.1, pp. 19–32. ISSN: 18678548. DOI: [10.5194/amt-8-19-2015](https://doi.org/10.5194/amt-8-19-2015).
- Davenport, J. J. et al. (2015). "A measurement strategy for non-dispersive ultra-violet detection of formaldehyde in indoor air : spectral analysis and interferent gases". In: *Measurement Science and Technology* 015802. December 2015, p. 15802. ISSN: 0957-0233. DOI: [10.1088/0957-0233/27/1/015802](https://doi.org/10.1088/0957-0233/27/1/015802). URL: <http://dx.doi.org/10.1088/0957-0233/27/1/015802>.
- Lee, Anita et al. (2006a). "Gas-phase products and secondary aerosol yields from the ozonolysis of ten different terpenes". In: 111.Ci, pp. 1–18. DOI: [10.1029/2005JD006437](https://doi.org/10.1029/2005JD006437).
- Lerner, Brian M. et al. (2017). "An improved, automated whole air sampler and gas chromatography mass spectrometry analysis system for volatile organic compounds in the atmosphere". In: *Atmospheric Measurement Techniques* 10.1, pp. 291–313. ISSN: 18678548. DOI: [10.5194/amt-10-291-2017](https://doi.org/10.5194/amt-10-291-2017). URL: <https://www.atmos-meas-tech.net/10/291/2017/amt-10-291-2017.pdf>.

- Hak, C. et al. (2005). "Intercomparison of four different in-situ techniques for ambient formaldehyde measurements in urban air". In: *Atmospheric Chemistry and Physics Discussions* 5.3, pp. 2897–2945. ISSN: 1680-7316. DOI: [10.5194/acpd-5-2897-2005](https://doi.org/10.5194/acpd-5-2897-2005).
- EUMETSAT (2015). GOME2. URL: <http://www.eumetsat.int/website/home/Satellites/CurrentSatellites/Metop/MetopDesign/GOME2/index.html>.
- Dufour, G. et al. (2008). "SCIAMACHY formaldehyde observations: constraint for isoprene emissions over Europe?" In: *Atmospheric Chemistry and Physics* 8.6, pp. 19273–19312. ISSN: 1680-7324. DOI: [10.5194/acpd-8-19273-2008](https://doi.org/10.5194/acpd-8-19273-2008).
- Bauwens, M et al. (2013). "Satellite-based isoprene emission estimates (2007–2012) from the GlobEmission project". In: *Proceedings of the ACCENT-Plus Symposium, Atmospheric Composition Change-Policy Support and Science, Urbino*, pp. 17–20.
- Bauwens, Maite et al. (2016). "Nine years of global hydrocarbon emissions based on source inversion of OMI formaldehyde observations". In: *Atmospheric Chemistry and Physics* March, pp. 1–45. ISSN: 1680-7375. DOI: [10.5194/acp-2016-221](https://doi.org/10.5194/acp-2016-221). URL: <http://www.atmos-chem-phys-discuss.net/acp-2016-221/>.
- Surl, Luke, Paul I. Palmer, and Gonzalo G. Abad (2018). "Which processes drive observed variations of HCHO columns over India?" In: *Atmospheric Chemistry and Physics* 18.March, pp. 4549–4566. DOI: [10.5194/acp-18-4549-2018](https://doi.org/10.5194/acp-18-4549-2018). URL: <https://doi.org/10.5194/acp-18-4549-2018>.
- Zhang, Yang et al. (2012). "Impact of gas-phase mechanisms on Weather Research Forecasting Model with Chemistry (WRF/Chem) predictions: Mechanism implementation and comparative evaluation". In: *Journal of Geophysical Research: Atmospheres* 117.D1, n/a–n/a. DOI: [10.1029/2011JD015775](https://doi.org/10.1029/2011JD015775). URL: <http://doi.wiley.com/10.1029/2011JD015775>.
- Marais, E A et al. (2014). "Improved model of isoprene emissions in Africa using Ozone Monitoring Instrument (OMI) satellite observations of formaldehyde: implications for oxidants and particulate matter". In: *Atmospheric Chemistry and Physics* 14.15, pp. 7693–7703. DOI: [10.5194/acp-14-7693-2014](https://doi.org/10.5194/acp-14-7693-2014). URL: <http://dx.doi.org/10.5194/acp-14-7693-2014>.
- Miller, C. et al. (2014). "Glyoxal retrieval from the Ozone Monitoring Instrument". In: *Atmospheric Measurement Techniques* 7.11, pp. 3891–3907. ISSN: 1867-8548. DOI: [10.5194/amt-7-3891-2014](https://doi.org/10.5194/amt-7-3891-2014). URL: <http://www.atmos-meas-tech.net/7/3891/2014/>.
- Zeng, G. et al. (2015). "Multi-model simulation of CO and HCHO in the Southern Hemisphere: comparison with observations and impact of biogenic emissions". In: *Atmospheric Chemistry and Physics* 15.13, pp. 7217–7245. ISSN: 1680-7324. DOI: [10.5194/acp-15-7217-2015](https://doi.org/10.5194/acp-15-7217-2015). URL: <http://www.atmos-chem-phys.net/15/7217/2015/>.
- Christian, Kenneth E, William H Brune, and Jingqiu Mao (2017). "Global sensitivity analysis of the GEOS-Chem chemical transport model: ozone and hydrogen oxides during ARCTAS (2008)". In: *Atmos. Chem. Phys* 17, pp. 3769–3784. DOI: [10.5194/acp-17-3769-2017](https://doi.org/10.5194/acp-17-3769-2017). URL: www.atmos-chem-phys.net/17/3769/2017/.
- Niinemets, U. et al. (1999). "A model of isoprene emission based on energetic requirements for isoprene synthesis and leaf photosynthetic properties for Liquidambar and Quercus". In: *Plant, Cell and Environment* 22.11, pp. 1319–1335. ISSN: 01407791. DOI: [10.1046/j.1365-3040.1999.00505.x](https://doi.org/10.1046/j.1365-3040.1999.00505.x).

- Arneth, Almut et al. (2007). "CO₂ inhibition of global terrestrial isoprene emissions: Potential implications for atmospheric chemistry". In: *Geophysical Research Letters* 34.18, p. L18813. DOI: [10.1029/2007GL030615](https://doi.org/10.1029/2007GL030615). URL: <http://doi.wiley.com/10.1029/2007GL030615>.
- Travis, Katherine R et al. (2016). "Why do models overestimate surface ozone in the Southeast United States?" In: *Atmos. Chem. Phys* 16, pp. 13561–13577. DOI: [10.5194/acp-16-13561-2016](https://doi.org/10.5194/acp-16-13561-2016). URL: www.atmos-chem-phys.net/16/13561/2016/.
- Wild, Oliver and Michael J. Prather (2006). "Global tropospheric ozone modeling: Quantifying errors due to grid resolution". In: *Journal of Geophysical Research Atmospheres* 111.11, pp. 1–14. ISSN: 01480227. DOI: [10.1029/2005JD006605](https://doi.org/10.1029/2005JD006605).
- Rowntree, P. R. and J. A. Bolton (1983). "Simulation of the atmospheric response to soil moisture anomalies over Europe". In: *Quarterly Journal of the Royal Meteorological Society* 109.461, pp. 501–526. ISSN: 00359009. DOI: [10.1002/qj.49710946105](https://doi.org/10.1002/qj.49710946105). URL: <http://doi.wiley.com/10.1002/qj.49710946105>.
- Chen, Fei and Jimy Dudhia (2001). "Coupling an Advanced Land Surface–Hydrology Model with the Penn State–NCAR MM5 Modeling System. Part I: Model Implementation and Sensitivity". In: *Monthly Weather Review* 129. URL: <https://journals.ametsoc.org/doi/pdf/10.1175/1520-0493%282001%29129%3C0569%3ACAALSH%3E2.0.CO%3B2>.
- Wang, Yuxuan et al. (2017). "Adverse effects of increasing drought on air quality via natural processes". In: *Atmos. Chem. Phys* 175194, pp. 12827–12843. DOI: [10.5194/acp-17-12827-2017](https://doi.org/10.5194/acp-17-12827-2017). URL: <http://www.atmos-chem-phys.net/17/12827/2017/acp-17-12827-2017.pdf>.
- VanDerA, R J et al. (2008). "Trends seasonal variability and dominant NO x source derived from a ten year record of NO₂ measured from space". In: *J. Geophys. Res.* 113.D4. DOI: [10.1029/2007jd009021](https://doi.org/10.1029/2007jd009021). URL: <http://dx.doi.org/10.1029/2007jd009021>.
- Oltmans, J et al. (2001). "Ozone in the Pacific tropical troposphere from ozonesonde observations". In: *Journal of Geophysical Research* 106.D23, pp. 32503–32525.
- Gloudemans, Annemieke et al. (2007). "Evidence for long-range transport of carbon monoxide in the Southern Hemisphere from SCIAMACHY observations". In: *European Space Agency, (Special Publication)* 33.SP-636, pp. 1–5. ISSN: 03796566. DOI: [10.1029/2006GL026804](https://doi.org/10.1029/2006GL026804).
- Edwards, D. P. et al. (2006). "Satellite-observed pollution from Southern Hemisphere biomass burning". In: *Journal of Geophysical Research* 111.14, pp. 1–17. ISSN: 01480227. DOI: [10.1029/2005JD006655](https://doi.org/10.1029/2005JD006655).
- Pak, B.C.a et al. (2003). "Measurements of biomass burning influences in the troposphere over southeast Australia during the SAFARI 2000 dry season campaign". In: *Journal of Geophysical Research* 108.13, pp. 1–10. ISSN: 0148-0227. DOI: [10.1029/2002JD002343](https://doi.org/10.1029/2002JD002343). URL: <http://www.scopus.com/inward/record.url?eid=2-s2.0-0742322536&partnerID=40&md5=cafafef03b948fb456696583ed3ab9a5>.
- Liu, Junhua et al. (2016a). "Causes of interannual variability of tropospheric ozone over the Southern Ocean". In: *Atmospheric Chemistry and Physics Discussions* October, pp. 1–46. ISSN: 1680-7316. DOI: [10.5194/ACP-2016-692](https://doi.org/10.5194/ACP-2016-692).
- Winters, Anthony J et al. (2009). "Emissions of isoprene, monoterpene and short-chained carbonyl compounds from Eucalyptus spp. in southern Australia". In: *Atmospheric*

- Environment* 43.19, pp. 3035–3043. ISSN: 13522310. DOI: [10.1016/j.atmosenv.2009.03.026](https://doi.org/10.1016/j.atmosenv.2009.03.026).
- Alexander, S. P. et al. (2013). "High resolution VHF radar measurements of tropopause structure and variability at Davis, Antarctica (69 S, 78 E)". In: *Atmospheric Chemistry and Physics* 13.6, pp. 3121–3132. ISSN: 16807324. DOI: [10.5194/acp-13-3121-2013](https://doi.org/10.5194/acp-13-3121-2013). URL: <http://www.atmos-chem-phys.net/13/3121/2013/>.
- Škerlak, B, M Sprenger, and H Wernli (2014). "A global climatology of stratosphere-troposphere exchange using the ERA-Interim data set from 1979 to 2011". In: *Atmospheric Chemistry and Physics* 14.2, pp. 913–937. DOI: [10.5194/acp-14-913-2014](https://doi.org/10.5194/acp-14-913-2014). URL: <http://www.atmos-chem-phys.net/14/913/2014/>.
- Müller, J.-F. et al. (2008). "Global isoprene emissions estimated using MEGAN ECMWF analyses and a detailed canopy environment model". In: *Atmospheric Chemistry and Physics Discussions* 7.6, pp. 15373–15407. DOI: [10.5194/acpd-7-15373-2007](https://doi.org/10.5194/acpd-7-15373-2007). URL: <http://dx.doi.org/10.5194/acpd-7-15373-2007>.
- Stavrakou, T et al. (2009). "Evaluating the performance of pyrogenic and biogenic emission inventories against one decade of space-based formaldehyde columns". In: *Atmospheric Chemistry and Physics* 9.3, pp. 1037–1060. DOI: [10.5194/acp-9-1037-2009](https://doi.org/10.5194/acp-9-1037-2009). URL: <http://dx.doi.org/10.5194/acp-9-1037-2009>.
- Palmer, Paul I et al. (2001). "Air mass factor formulation for spectroscopic measurements from satellites' Application to formaldehyde retrievals from the Global Ozone Monitoring Experiment". In: *Journal of Geophysical Research* 106.D13.
- Dunne, Erin et al. (2018). "Comparison of VOC measurements made by PTR-MS, adsorbent tubes-GC-FID-MS and DNPH derivatization-HPLC during the Sydney Particle Study, 2012: A contribution to the assessment of uncertainty in routine atmospheric VOC measurements". In: *Atmospheric Measurement Techniques* 11.1, pp. 141–159. ISSN: 18678548. DOI: [10.5194/amt-11-141-2018](https://doi.org/10.5194/amt-11-141-2018). URL: <https://www.atmos-meas-tech.net/11/141/2018/amt-11-141-2018.pdf>.
- Brinksma, E. J. et al. (2002). "Five years of observations of ozone profiles over Lauder, New Zealand". In: *Journal of Geophysical Research* 107.D14, pp. 1–11. ISSN: 0148-0227. DOI: [10.1029/2001JD000737](https://doi.org/10.1029/2001JD000737). URL: <http://doi.wiley.com/10.1029/2001JD000737>.
- Baray, Jean-Luc et al. (2012). "One year ozonesonde measurements at Kerguelen Island (49.2S, 70.1E): Influence of stratosphere-to-troposphere exchange and long-range transport of biomass burning plumes". In: *Journal of Geophysical Research* 117.D6. ISSN: 2156-2202. DOI: [10.1029/2011JD016717](https://doi.org/10.1029/2011JD016717). URL: <http://dx.doi.org/10.1029/2011JD016717>.
- Eskes, HJ and K F Boersma (2003). "Averaging kernels for DOAS total-column satellite retrievals". In: *Atmospheric Chemistry and Physics* 3.1, pp. 1285–1291. ISSN: 1680-7324. DOI: [10.5194/acp-3-1285-2003](https://doi.org/10.5194/acp-3-1285-2003). URL: <http://dx.doi.org/10.5194/acpd-3-895-2003>.
- Lamsal, L N et al. (2014). "Evaluation of OMI operational standard NO₂ column retrievals using in situ and surface-based NO₂ observations". In: *Atmos. Chem. Phys* 14, pp. 11587–11609. DOI: [10.5194/acp-14-11587-2014](https://doi.org/10.5194/acp-14-11587-2014). URL: www.atmos-chem-phys.net/14/11587/2014/.

- Leue, C et al. (2001). "Quantitative analysis of NO_x emissions from Global Ozone Monitoring Experiment satellite image sequences". In: *J. Geophys. Res.* 106.D6, p. 5493. DOI: [10.1029/2000jd900572](https://doi.org/10.1029/2000jd900572). URL: <http://dx.doi.org/10.1029/2000jd900572>.
- Martin, Randall V et al. (2002b). "Interpretation of TOMS observations of tropical tropospheric ozone with a global model and in situ observations". In: 107. DOI: [10.1029/2001JD001480](https://doi.org/10.1029/2001JD001480).
- Goldberg, Daniel L. et al. (2017). "A high-resolution and observationally constrained OMI NO₂ satellite retrieval". In: *Atmospheric Chemistry and Physics* 17.18, pp. 11403–11421. ISSN: 16807324. DOI: [10.5194/acp-17-11403-2017](https://doi.org/10.5194/acp-17-11403-2017).
- Lorente, Alba et al. (2017). "Structural uncertainty in air mass factor calculation for NO₂ and HCHO satellite retrievals". In: *Atmospheric Measurement Techniques* 2, pp. 1–35. ISSN: 1867-8610. DOI: [10.5194/amt-2016-306](https://doi.org/10.5194/amt-2016-306). URL: <http://www.atmos-meas-tech-discuss.net/amt-2016-306/>.
- Texeira, Joao (2013). *AIRS/Aqua L3 Daily Standard Physical Retrieval (AIRS-only) 1 degree x 1 degree V006*: Accessed 2/Dec/2015. DOI: [doi:10.5067/AQUA/AIRS/DATA303](https://doi.org/10.5067/AQUA/AIRS/DATA303).
- Vasilkov, A et al. (2017). "Accounting for the effects of surface BRDF on satellite cloud and trace-gas retrievals: a new approach based on geometry-dependent Lambertian equivalent reflectivity applied to OMI algorithms". In: *Atmospheric Measurement Techniques* 10.1, pp. 333–349. DOI: [10.5194/amt-10-333-2017](https://doi.org/10.5194/amt-10-333-2017). URL: <http://www.atmos-meas-tech.net/10/333/2017/>.
- Vigouroux, C. et al. (2009). "Ground-based FTIR and MAX-DOAS observations of formaldehyde at Réunion Island and comparisons with satellite and model data". In: *Atmospheric Chemistry and Physics Discussions* 9, pp. 15891–15957. ISSN: 1680-7316. DOI: [10.5194/acpd-9-15891-2009](https://doi.org/10.5194/acpd-9-15891-2009).
- Dee, D P et al. (2011). "The ERA-Interim reanalysis: configuration and performance of the data assimilation system". In: *Quarterly Journal of the Royal Meteorological Society* 137.656, pp. 553–597. ISSN: 1477-870X. DOI: [10.1002/qj.828](https://doi.org/10.1002/qj.828). URL: <http://dx.doi.org/10.1002/qj.828>.
- Paton-Walsh, C et al. (2017). "The MUMBA campaign: measurements of urban, marine and biogenic air Clare". In: *Earth system science data*, pp. 349–362.
- Guérette, Elise-Andrée et al. (2018). "Emissions of trace gases from Australian temperate forest fires: emission factors and dependence on modified combustion efficiency". In: *Atmospheric Chemistry and Physics* 18.5, pp. 3717–3735. ISSN: 1680-7324. DOI: [10.5194/acp-18-3717-2018](https://doi.org/10.5194/acp-18-3717-2018). URL: <https://www.atmos-chem-phys.net/18/3717/2018/>.
- Cheng, M et al. "Factors controlling volatile organic compounds in dwellings in Melbourne, Australia". In: *Indoor Air* 26.2, pp. 219–230. DOI: [10.1111/ina.12201](https://doi.org/10.1111/ina.12201). URL: <https://onlinelibrary.wiley.com/doi/abs/10.1111/ina.12201>.
- Lawson, S. J. et al. (2015). "Seasonal in situ observations of glyoxal and methylglyoxal over the temperate oceans of the Southern Hemisphere". In: *Atmospheric Chemistry and Physics* 15.1, pp. 223–240. ISSN: 1680-7324. DOI: [10.5194/acp-15-223-2015](https://doi.org/10.5194/acp-15-223-2015). URL: <http://www.atmos-chem-phys.net/15/223/2015/>.
- ABS (2013). *Melbourne population*. URL: <http://www.abs.gov.au/ausstats/abs@.nsf?Previousproducts/3218.0>MainFeatures52012-13?opendocument&tabname=Summary&prodno=3218.0&issue=2012-13&num=&view=> (visited on 05/10/2017).

- Schenkeveld, V. M. Erik et al. (2017). "In-flight performance of the Ozone Monitoring Instrument". In: *Atmospheric Measurement Techniques* 10.5, pp. 1957–1986. ISSN: 1867-8548. DOI: [10.5194/amt-10-1957-2017](https://doi.org/10.5194/amt-10-1957-2017). URL: <http://www.atmos-meas-tech-discuss.net/amt-2016-420/> <https://www.atmos-meas-tech.net/10/1957/2017/>.
- Wikipedia (2016). *Solar zenith angle*. DOI: [10.1016/B978-012369407-2/50005-X](https://doi.org/10.1016/B978-012369407-2/50005-X). URL: <http://sacs.aeronomie.be/info/sza.php>.
- Kurosu, T and K Chance (2014). *OMIReadme*. URL: https://www.cfa.harvard.edu/atmosphere/Instruments/OMI/PGEReleases/READMEs/OMHCHO_README_v3.0.pdf.
- Instrument, O M I (2002). "OMI Algorithm Theoretical Basis Document Volume I". In: I.August, pp. 1–50.
- Spurr, R.J.D., T.P. Kurosu, and K.V. Chance (2001). "A linearized discrete ordinate radiative transfer model for atmospheric remote-sensing retrieval". In: *Journal of Quantitative Spectroscopy and Radiative Transfer* 68.6, pp. 689–735. DOI: [10.1016/S0022-4073\(00\)00055-8](https://doi.org/10.1016/S0022-4073(00)00055-8). URL: <https://www.sciencedirect.com/science/article/pii/S0022407300000558>.
- Martin, Randall V. et al. (2002a). "An improved retrieval of tropospheric nitrogen dioxide from GOME". In: *Journal of Geophysical Research D: Atmospheres* 107.20. ISSN: 01480227. DOI: [10.1029/2001JD001027](https://doi.org/10.1029/2001JD001027).
- De Smedt, I. et al. (2015). "Diurnal, seasonal and long-term variations of global formaldehyde columns inferred from combined OMI and GOME-2 observations". In: *Atmospheric Chemistry and Physics* 15.21, pp. 12519–12545. ISSN: 16807324. DOI: [10.5194/acp-15-12519-2015](https://doi.org/10.5194/acp-15-12519-2015). URL: <http://www.atmos-chem-phys-discuss.net/15/12241/2015/acpd-15-12241-2015.pdf>.
- Abad, Gonzalo González et al. (2016). "Smithsonian Astrophysical Observatory Ozone Mapping and Profiler Suite (SAO OMPS) formaldehyde retrieval". In: *Atmospheric Measurement Techniques* 9.7, pp. 2797–2812. ISSN: 18678548. DOI: [10.5194/amt-9-2797-2016](https://doi.org/10.5194/amt-9-2797-2016).
- De Smedt, I. et al. (2012). "Improved retrieval of global tropospheric formaldehyde columns from GOME-2/MetOp-A addressing noise reduction and instrumental degradation issues". In: *Atmospheric Measurement Techniques* 5.11, pp. 2933–2949. ISSN: 18671381. DOI: [10.5194/amt-5-2933-2012](https://doi.org/10.5194/amt-5-2933-2012).
- Zhu, Lei et al. (2016). "Observing atmospheric formaldehyde (HCHO) from space: validation and intercomparison of six retrievals from four satellites (OMI, GOME2A, GOME2B, OMPS) with SEAC4RS aircraft observations over the Southeast US". In: *Atmospheric Chemistry and Physics* 0, pp. 1–24. ISSN: 1680-7375. DOI: [10.5194/acp-2016-162](https://doi.org/10.5194/acp-2016-162). URL: <http://www.atmos-chem-phys.net/16/13477/2016/acp-16-13477-2016.pdf>.
- Barkley, Michael P. et al. (2013). "Top-down isoprene emissions over tropical South America inferred from SCIAMACHY and OMI formaldehyde columns". In: *Journal of Geophysical Research Atmospheres* 118.12, pp. 6849–6868. ISSN: 21698996. DOI: [10.1002/jgrd.50552](https://doi.org/10.1002/jgrd.50552). URL: <http://dx.doi.org/10.1002/jgrd.50552>.
- Chen, D. et al. (2009). "Regional CO pollution in China simulated by the high-resolution nested-grid GEOS-Chem model". In: *Atmospheric Chemistry and Physics Discussions*

- 9.2, pp. 5853–5887. ISSN: 1680-7324. DOI: [10.5194/acpd-9-5853-2009](https://doi.org/10.5194/acpd-9-5853-2009). URL: <http://dx.doi.org/10.5194/acp-9-3825-2009>.
- Giglio, Louis, James T. Randerson, and Guido R. Van Der Werf (2013). “Analysis of daily, monthly, and annual burned area using the fourth-generation global fire emissions database (GFED4)”. In: *Journal of Geophysical Research* 118.1, pp. 317–328. ISSN: 21698961. DOI: [10.1002/jgrg.20042](https://doi.org/10.1002/jgrg.20042).
- Wuebbles, Donald J and Katharine Hayhoe (2002). “Atmospheric methane and global change”. In: *Earth-Science Reviews* 57.3-4, pp. 177–210. ISSN: 0012-8252. DOI: [10.1016/S0012-8252\(01\)00062-9](https://doi.org/10.1016/S0012-8252(01)00062-9). URL: <https://www.sciencedirect.com/science/article/pii/S0012825201000629?via%3Dihub>.
- Horowitz, Larry W. et al. (1998). “Export of reactive nitrogen from North America during summertime: Sensitivity to hydrocarbon chemistry”. In: *Journal of Geophysical Research* 103.D11, pp. 13451–13476. ISSN: 0148-0227. DOI: [10.1029/97JD03142](https://doi.org/10.1029/97JD03142). URL: <http://doi.wiley.com/10.1029/97JD03142> <http://www.agu.org/pubs/crossref/1998/97JD03142.shtml>.
- Crounse, John D et al. (2011). “Peroxy radical isomerization in the oxidation of isoprene”. In: *Physical Chemistry Chemical Physics* 13.30, pp. 13607–13613. ISSN: 1463-9076. DOI: [doi : 10 . 1039 / c1cp21330j](https://doi.org/10.1039/c1cp21330j). URL: <http://dx.doi.org/10.1039/C1CP21330J>.
- Taraborrelli, D. et al. (2012). “Hydroxyl radical buffered by isoprene oxidation over tropical forests”. In: *Nature Geoscience* 5.3, pp. 190–193. ISSN: 17520894. DOI: [10.1038/ngeo1405](https://doi.org/10.1038/ngeo1405). URL: <http://dx.doi.org/10.1038/ngeo1405> <https://www.nature.com/articles/ngeo1405.pdf>.
- Jozef, Peeters et al. (2014). “Hydroxyl Radical Recycling in Isoprene Oxidation Driven by Hydrogen Bonding and Hydrogen Tunneling: The Upgraded LIM1 Mechanism”. In: *Journal of Physical Chemistry*.
- Guenther, Alex (2016). MEGAN. URL: <http://lar.wsu.edu/megan/>.
- Eastham, Sebastian D., Debra K. Weisenstein, and Steven R H Barrett (2014). “Development and evaluation of the unified tropospheric-stratospheric chemistry extension (UCX) for the global chemistry-transport model GEOS-Chem”. In: *Atmospheric Environment* 89, pp. 52–63. ISSN: 13522310. DOI: [10.1016/j.atmosenv.2014.02.001](https://doi.org/10.1016/j.atmosenv.2014.02.001). URL: <http://dx.doi.org/10.1016/j.atmosenv.2014.02.001>.
- Spurr, R. J D (2002). “Simultaneous derivation of intensities and weighting functions in a general pseudo-spherical discrete ordinate radiative transfer treatment”. In: *Journal of Quantitative Spectroscopy and Radiative Transfer* 75.2, pp. 129–175. ISSN: 00224073. DOI: [10.1016/S0022-4073\(01\)00245-X](https://doi.org/10.1016/S0022-4073(01)00245-X).
- Martin, Randall V et al. (2003). “Global inventory of nitrogen oxide emissions constrained by space-based observations of NO₂ columns”. In: 108.2, pp. 1–12. DOI: [10.1029/2003JD003453](https://doi.org/10.1029/2003JD003453).
- De Smedt, I et al. (2008). “Twelve years of global observations of formaldehyde in the troposphere using GOME and SCIAMACHY sensors”. In: *Atmos. Chem. Phys.* 8.16, pp. 4947–4963. ISSN: 1680-7324. DOI: [10.5194/acp-8-4947-2008](https://doi.org/10.5194/acp-8-4947-2008). URL: <http://www.atmos-chem-phys.net/8/4947/2008/>.
- Miller, Christopher Chan et al. (2016). “Glyoxal yield from isoprene oxidation and relation to formaldehyde: chemical mechanism, constraints from SENEX aircraft observations, and interpretation of OMI satellite data”. In: *Atmospheric Chemistry*

- and Physics Discussions* x, pp. 1–25. ISSN: 1680-7375. DOI: [10.5194/acp-2016-1042](https://doi.org/10.5194/acp-2016-1042). URL: <http://www.atmos-chem-phys-discuss.net/acp-2016-1042/>.
- Zhu, Lei et al. (2013). "Variability of HCHO over the Southeastern United States observed from space : Implications for VOC emissions". In: vol. 1.
- Shao, Yaping et al. (2007). "Numerical simulation of the October 2002 dust event in Australia". In: *J. Geophys. Res.* 112.D8. DOI: [10.1029/2006jd007767](https://doi.org/10.1029/2006jd007767). URL: <http://dx.doi.org/10.1029/2006jd007767>.
- Carlisle, Wendy (2012). *The coal seam gas rush*. URL: <http://www.abc.net.au/news/2011-11-24/coal-seam-gas-by-the-numbers-map/3664318>.
- Zheng, Y. et al. (2015). "Relationships between photosynthesis and formaldehyde as a probe of isoprene emission". In: *Atmospheric Chemistry and Physics* 15.15, pp. 8559–8576. ISSN: 16807324. DOI: [10.5194/acp-15-8559-2015](https://doi.org/10.5194/acp-15-8559-2015).
- Abbot, Dorian S. (2003). "Seasonal and interannual variability of North American isoprene emissions as determined by formaldehyde column measurements from space". In: *Geophysical Research Letters* 30.17, pp. 1999–2002. ISSN: 0094-8276. DOI: [10.1029/2003GL017336](https://doi.org/10.1029/2003GL017336). URL: <http://doi.wiley.com/10.1029/2003GL017336>.
- Curci, G. et al. (2010). "Estimating European volatile organic compound emissions using satellite observations of formaldehyde from the Ozone Monitoring Instrument". In: *Atmospheric Chemistry and Physics* 10.23, pp. 11501–11517. ISSN: 16807316. DOI: [10.5194/acp-10-11501-2010](https://doi.org/10.5194/acp-10-11501-2010).
- Stavrakou, T. et al. (2015). "How consistent are top-down hydrocarbon emissions based on formaldehyde observations from GOME-2 and OMI?" English. In: *Atmospheric Chemistry and Physics* 15.20, pp. 11861–11884. ISSN: 1680-7324. DOI: [10.5194/acp-15-11861-2015](https://doi.org/10.5194/acp-15-11861-2015). URL: <http://www.atmos-chem-phys.net/15/11861/2015/acp-15-11861-2015.html>.
- Thomas, W et al. (1998). "Detection of biomass burning combustion products in Southeast Asia from backscatter data taken by the GOME spectrometer". In: *Geophysical Research Letters* 25.9, pp. 1317–1320. DOI: [10.1029/98GL01087](https://doi.org/10.1029/98GL01087). URL: <http://onlinelibrary.wiley.com/doi/10.1029/98GL01087/epdf>.
- Streets, David G et al. (2013). "Emissions estimation from satellite retrievals: A review of current capability". In: *Atmospheric Environment* 77, pp. 1011–1042. DOI: [10.1016/j.atmosenv.2013.05.051](https://doi.org/10.1016/j.atmosenv.2013.05.051). URL: <http://dx.doi.org/10.1016/j.atmosenv.2013.05.051>.
- Kaden DA, Mandin C, Nielsen GD, et al. (2010). *HCHO exposure guidelines*. URL: <https://www.ncbi.nlm.nih.gov/books/NBK138711/> (visited on 10/10/2018).
- Lee, Anita et al. (2006b). "Gas-phase products and secondary aerosol yields from the photooxidation of 16 different terpenes". In: *Journal of Geophysical Research Atmospheres* 111.17, pp. 1–18. ISSN: 01480227. DOI: [10.1029/2006JD007050](https://doi.org/10.1029/2006JD007050).
- Pegoraro, E. et al. (2004). "Effect of drought on isoprene emission rates from leaves of *Quercus virginiana* Mill." In: *Atmospheric Environment* 38.36, pp. 6149–6156. ISSN: 13522310. DOI: [10.1016/j.atmosenv.2004.07.028](https://doi.org/10.1016/j.atmosenv.2004.07.028). URL: <http://linkinghub.elsevier.com/retrieve/pii/S1352231004007198>.
- Liu, Junhua et al. (2015). "Origins of tropospheric ozone interannual variation over Réunion: A model investigation". In: *Journal of Geophysical Research*, pp. 1–19. DOI: [10.1002/2015JD023981](https://doi.org/10.1002/2015JD023981). URL: <http://onlinelibrary.wiley.com/doi/10.1002/2015JD023981/abstract>.

- Thompson, A. M. et al. (2014). "Tropospheric ozone increases over the southern Africa region: Bellwether for rapid growth in Southern Hemisphere pollution?" In: *Atmospheric Chemistry and Physics* 14.18, pp. 9855–9869. ISSN: 16807324. DOI: [10.5194/acp-14-9855-2014](https://doi.org/10.5194/acp-14-9855-2014).
- Danielsen, Edwin F. (1968). *Stratospheric-Tropospheric Exchange Based on Radioactivity, Ozone and Potential Vorticity*. DOI: [10.1175/1520-0469\(1968\)025<0502:STEBOR>2.0.CO;2](https://doi.org/10.1175/1520-0469(1968)025<0502:STEBOR>2.0.CO;2).
- Lefohn, Allen S. et al. (2011). "The importance of stratospheric-tropospheric transport in affecting surface ozone concentrations in the western and northern tier of the United States". In: *Atmospheric Environment* 45.28, pp. 4845–4857. ISSN: 13522310. DOI: [10.1016/j.atmosenv.2011.06.014](https://doi.org/10.1016/j.atmosenv.2011.06.014). URL: <http://dx.doi.org/10.1016/j.atmosenv.2011.06.014>.
- Langford, A. O. et al. (2012). "Stratospheric influence on surface ozone in the Los Angeles area during late spring and early summer of 2010". In: *Journal of Geophysical Research* 117.3, pp. 1–17. ISSN: 01480227. DOI: [10.1029/2011JD016766](https://doi.org/10.1029/2011JD016766).
- Zhang, L et al. (2014). "Sources contributing to background surface ozone in the US Intermountain West". In: *Atmospheric Chemistry and Physics* 14.11, pp. 5295–5309. DOI: [10.5194/acp-14-5295-2014](https://doi.org/10.5194/acp-14-5295-2014). URL: <http://dx.doi.org/10.5194/acp-14-5295-2014>.
- Lin, Meiyun et al. (2012). "Springtime high surface ozone events over the western United States: Quantifying the role of stratospheric intrusions". In: *Journal of Geophysical Research* 117.19, pp. 1–20. ISSN: 01480227. DOI: [10.1029/2012JD018151](https://doi.org/10.1029/2012JD018151).
- Galani, E. (2003). "Observations of stratosphere-to-troposphere transport events over the eastern Mediterranean using a ground-based lidar system". In: *Journal of Geophysical Research* 108.D12, pp. 1–10. ISSN: 0148-0227. DOI: [10.1029/2002JD002596](https://doi.org/10.1029/2002JD002596). URL: <http://www.agu.org/pubs/crossref/2003/2002JD002596.shtml>.
- Terao, Yukio et al. (2008). "Contribution of stratospheric ozone to the interannual variability of tropospheric ozone in the northern extratropics". In: *Journal of Geophysical Research* 113.D18. DOI: [10.1029/2008jd009854](https://doi.org/10.1029/2008jd009854). URL: <http://dx.doi.org/10.1029/2008jd009854>.
- Tang, Q. and M. J. Prather (2012). "Five blind men and the elephant: What can the NASA Aura ozone measurements tell us about stratosphere-troposphere exchange?" In: *Atmospheric Chemistry and Physics* 12.5, pp. 2357–2380. ISSN: 16807316. DOI: [10.5194/acp-12-2357-2012](https://doi.org/10.5194/acp-12-2357-2012). URL: <http://dx.doi.org/10.5194/acpd-11-26897-2011>.
- Frey, W. et al. (2015). "The impact of overshooting deep convection on local transport and mixing in the tropical upper troposphere/lower stratosphere (UTLS)". In: *Atmospheric Chemistry and Physics* 15.11, pp. 6467–6486. ISSN: 1680-7324. DOI: [10.5194/acp-15-6467-2015](https://doi.org/10.5194/acp-15-6467-2015). URL: <http://www.atmos-chem-phys.net/15/6467/2015/>.
- Das, Siddarth Shankar et al. (2016). "Influence of tropical cyclones on tropospheric ozone: possible implications". In: *Atmospheric Chemistry and Physics* 16, pp. 4837–4847. DOI: [10.5194/acp-16-4837-2016](https://doi.org/10.5194/acp-16-4837-2016). URL: www.atmos-chem-phys.net/16/4837/2016/.

- Mihalikova, M et al. (2012). "Observation of a tropopause fold by MARA VHF wind-profiler radar and ozonesonde at Wasa, Antarctica: comparison with ECMWF analysis and a WRF model simulation". In: *Annales Geophysicae* 30.9, pp. 1411–1421. DOI: [10.5194/angeo-30-1411-2012](https://doi.org/10.5194/angeo-30-1411-2012). URL: <http://www.ann-geophys.net/30/1411/2012/>.
- Vaughan, G., J. D. Price, and A. Howells (1993). "Transport into the troposphere in a tropopause fold". In: *Quarterly Journal of the Royal Meteorological Society* 120.518, pp. 1085–1103. ISSN: 00359009. DOI: [10.1002/qj.49712051814](https://doi.org/10.1002/qj.49712051814).
- Beekmann, M. et al. (1997). "Regional and global tropopause fold occurrence and related ozone flux across the tropopause". In: *Journal of Atmospheric Chemistry* 28.1-3, pp. 29–44. ISSN: 01677764. DOI: [10.1023/A:1005897314623](https://doi.org/10.1023/A:1005897314623).
- Baray, J. L. et al. (2000). "Planetary-scale tropopause folds in the southern subtropics". In: *Geophysical Research Letters* 27.3, pp. 353–356. ISSN: 00948276. DOI: [10.1029/1999GL010788](https://doi.org/10.1029/1999GL010788).
- Zanis, P. et al. (2014). "Summertime free-tropospheric ozone pool over the eastern Mediterranean/middle east". In: *Atmospheric Chemistry and Physics* 14.1, pp. 115–132. ISSN: 16807316. DOI: [10.5194/acp-14-115-2014](https://doi.org/10.5194/acp-14-115-2014).
- Akritidis, Dimitris et al. (2016). "On the role of tropopause folds in summertime tropospheric ozone over the eastern Mediterranean and the Middle East". In: *Atmospheric Chemistry and Physics* 16.21, pp. 14025–14039. DOI: [10.5194/acp-16-14025-2016](https://doi.org/10.5194/acp-16-14025-2016). URL: <http://www.atmos-chem-phys.net/16/14025/2016/>.
- Tyrlis, Evangelos et al. (2014). "On the linkage between the Asian summer monsoon and tropopause fold activity over the eastern Mediterranean and the Middle East". In: *Journal of Geophysical Research* 119.6, pp. 3202–3221. ISSN: 2169897X. DOI: [10.1002/2013JD021113](https://doi.org/10.1002/2013JD021113). URL: <http://doi.wiley.com/10.1002/2013JD021113>.
- Price, J. D. and G. Vaughan (1993). "The potential for stratosphere-troposphere exchange in cut-off-low systems". In: *Quarterly Journal of the Royal Meteorological Society* 119.510, pp. 343–365. DOI: [10.1002/qj.49711951007](https://doi.org/10.1002/qj.49711951007). URL: <http://onlinelibrary.wiley.com/doi/10.1002/qj.49711951007/abstract>.
- Wirth, Volkmar (1995). "Diabatic heating in an axisymmetric cut-off cyclone and related stratosphere-troposphere exchange". In: *Quarterly Journal of the Royal Meteorological Society* 121.521, pp. 127–147. ISSN: 00359009. DOI: [10.1002/qj.49712152107](https://doi.org/10.1002/qj.49712152107). URL: <http://doi.wiley.com/10.1002/qj.49712152107>.
- Trickl, T. et al. (2014). "How stratospheric are deep stratospheric intrusions?" In: *Atmospheric Chemistry and Physics* 14.18, pp. 9941–9961. ISSN: 16807324. DOI: [10.5194/acp-14-9941-2014](https://doi.org/10.5194/acp-14-9941-2014).
- Mze, N. et al. (2010). "Climatology and comparison of ozone from ENVISAT/GOMOS and SHADOZ/balloon-sonde observations in the southern tropics". In: *Atmospheric Chemistry and Physics* 10.16, pp. 8025–8035. ISSN: 16807316. DOI: [10.5194/acp-10-8025-2010](https://doi.org/10.5194/acp-10-8025-2010).
- Smit, Herman G J et al. (2007). "Assessment of the performance of ECC-ozonesondes under quasi-flight conditions in the environmental simulation chamber: Insights from the Juelich Ozone Sonde Intercomparison Experiment (JOSIE)". In: *Journal of Geophysical Research* 112.19, pp. 1–18. ISSN: 01480227. DOI: [10.1029/2006JD007308](https://doi.org/10.1029/2006JD007308).
- WMO, World Meteorological Organization (1957). "Meteorology A Three-Dimensional Science". In: *Geneva, Second Session of the Commission for Aerology* 4, pp. 134–138.

- Bethan, S., G. Vaughan, and S. J. Reid (1996). "A comparison of ozone and thermal tropopause heights and the impact of tropopause definition on quantifying the ozone content of the troposphere". In: *Quarterly Journal of the Royal Meteorological Society* 122.532, pp. 929–944. ISSN: 00359009. DOI: [10.1002/qj.49712253207](https://doi.org/10.1002/qj.49712253207). URL: <http://doi.wiley.com/10.1002/qj.49712253207>.
- Tomikawa, Yoshihiro, Yashiro Nishimura, and Takashi Yamanouchi (2009). "Characteristics of Tropopause and Tropopause Inversion Layer in the Polar Region". In: *SOLA* 5, pp. 141–144. DOI: [10.2151/sola.2009-036](https://doi.org/10.2151/sola.2009-036). URL: <http://dx.doi.org/10.2151/sola.2009-036>.
- Lelieveld, Jos and Frank J. Dentener (2000). "What controls tropospheric ozone?" In: *Journal of Geophysical Research* 105.D3, pp. 3531–3551. ISSN: 01480227. DOI: [10.1029/1999JD901011](https://doi.org/10.1029/1999JD901011). URL: <http://doi.wiley.com/10.1029/1999JD901011>.
- Struthers, H. et al. (2004). "Past and future simulations of NO₂ from a coupled chemistry-climate model in comparison with observations". In: *Atmospheric Chemistry and Physics* 4.8, pp. 2227–2239. ISSN: 1680-7324. DOI: [10.5194/acp-4-2227-2004](https://doi.org/10.5194/acp-4-2227-2004). URL: <http://www.atmos-chem-phys.net/4/2227/2004/>.
- Bey, Isabelle et al. (2001). "Global Modeling of Tropospheric Chemistry with Assimilated Meteorology: Model Description and Evaluation". In: *Journal of Geophysical Research* 106, pp. 73–95. ISSN: 0148-0227. DOI: [10.1029/2001JD000807](https://doi.org/10.1029/2001JD000807).
- Rienecker, Michele (2007). "File Specification for GEOS-5 DAS Gridded Output". In: pp. 1–54. URL: https://gmao.gsfc.nasa.gov/products/documents/GEOS-5.1.0_File_Specification.pdf.
- Press, William H et al. (1992). *Numerical Recipes in C (2Nd Ed.): The Art of Scientific Computing*. New York, NY, USA: Cambridge University Press. ISBN: 0-521-43108-5.
- Tang, Q. and M. J. Prather (2010). "Correlating tropospheric column ozone with tropopause folds: The Aura-OMI satellite data". In: *Atmospheric Chemistry and Physics* 10.19, pp. 9681–9688. ISSN: 16807316. DOI: [10.5194/acp-10-9681-2010](https://doi.org/10.5194/acp-10-9681-2010).
- Jaffe, Daniel a. and Nicole L. Wigder (2012). "Ozone production from wildfires: A critical review". In: *Atmospheric Environment* 51, pp. 1–10. ISSN: 13522310. DOI: [10.1016/j.atmosenv.2011.11.063](https://doi.org/10.1016/j.atmosenv.2011.11.063). URL: <http://dx.doi.org/10.1016/j.atmosenv.2011.11.063>.
- Edwards, D. P. (2003). "Tropospheric ozone over the tropical Atlantic: A satellite perspective". In: *Journal of Geophysical Research* 108.D8, p. 4237. ISSN: 0148-0227. DOI: [10.1029/2002JD002927](https://doi.org/10.1029/2002JD002927). URL: <http://doi.wiley.com/10.1029/2002JD002927>.
- Sinha, Parikhit et al. (2004). "Transport of biomass burning emissions from southern Africa". In: *Journal of Geophysical Research* 109, p. D20204. ISSN: 01480227. DOI: [10.1029/2004JD005044](https://doi.org/10.1029/2004JD005044).
- Mari, C H et al. (2008). "Tracing biomass burning plumes from the Southern Hemisphere during the AMMA 2006 wet season experiment, Atmos". In: *Atmospheric Chemistry and Physics* 8, pp. 3951–3961. ISSN: 1680-7324. DOI: [10.5194/acpd-7-17339-2007](https://doi.org/10.5194/acpd-7-17339-2007).
- Reutter, P. et al. (2015). "Stratosphere-troposphere exchange (STE) in the vicinity of North Atlantic cyclones". In: *Atmospheric Chemistry and Physics* 15.19, pp. 10939–10953. ISSN: 16807324. DOI: [10.5194/acp-15-10939-2015](https://doi.org/10.5194/acp-15-10939-2015).

- Škerlak, Bojan et al. (2015). "Tropopause folds in ERA-Interim: Global climatology and relation to extreme weather events". In: *Journal of Geophysical Research* 120.10, pp. 4860–4877. ISSN: 21698996. DOI: [10.1002/2014JD022787](https://doi.org/10.1002/2014JD022787).
- Wauben, Wiel M F, J Paul F Fortuin, and Peter F J Van Velthoven (1998). "Comparison of modeled ozone distributions observations". In: *Journal of Geophysical Research* 103, pp. 3511–3530.
- Hu, Lu et al. (2017). "Global budget of tropospheric ozone: evaluating recent model advances with satellite (OMI), aircraft (IAGOS), and ozonesonde observations". In: *Atmospheric Environment*, pp. 1–36. DOI: [10.1016/j.atmosenv.2017.08.036](https://doi.org/10.1016/j.atmosenv.2017.08.036).
- Roelofs, Geert Jan and Jos Lelieveld (1997). *Model study of the influence of cross-tropopause O₃ transports on tropospheric O₃ levels*. DOI: [10.1034/j.1600-0889.49.issue1.3.x](https://doi.org/10.1034/j.1600-0889.49.issue1.3.x).
- Elbern, H, J Hendricks, and A Ebel (1998). "A Climatology of Tropopause Folds by Global Analyses". In: *Theoretical and Applied Climatology* 59.3, pp. 181–200. ISSN: 1434-4483. DOI: [10.1007/s007040050023](https://doi.org/10.1007/s007040050023). URL: <http://dx.doi.org/10.1007/s007040050023>.
- Olsen, Mark a. (2003). "A comparison of Northern and Southern Hemisphere cross-tropopause ozone flux". In: *Geophysical Research Letters* 30.7, p. 1412. ISSN: 0094-8276. DOI: [10.1029/2002GL016538](https://doi.org/10.1029/2002GL016538). URL: <http://doi.wiley.com/10.1029/2002GL016538>.
- Lee, Hanlim et al. (2015). "Investigations of the Diurnal Variation of Vertical HCHO Profiles Based on MAX-DOAS Measurements in Beijing: Comparisons with OMI Vertical Column Data". In: *Atmosphere*. URL: [10.3390/atmos6111816](https://doi.org/10.3390/atmos6111816).
- Schreier, Stefan F. et al. (2016). "Estimates of free-Tropospheric NO₂ and HCHO mixing ratios derived from high-Altitude mountain MAX-DOAS observations at mid-latitudes and in the tropics". In: *Atmospheric Chemistry and Physics* 16.5. ISSN: 16807324. DOI: [10.5194/acp-16-2803-2016](https://doi.org/10.5194/acp-16-2803-2016).
- SPEI Drought Index*. URL: <http://spei.csic.es/home.html> (visited on 12/19/2017).
- Chance, K. et al. (2000). "Satellite observations of formaldehyde over North America from GOME". In: *Geophysical Research Letters* 27.21, pp. 3461–3464. ISSN: 00948276. DOI: [10.1029/2000GL011857](https://doi.org/10.1029/2000GL011857). URL: <http://dx.doi.org/10.1029/2000gl011857>.
- Bei, N, G Li, and L T Molina (2012). "Uncertainties in SOA simulations due to meteorological uncertainties in Mexico City during MILAGRO-2006 field campaign". In: *Atmospheric Chemistry and Physics* 12.23, pp. 11295–11308. DOI: [10.5194/acp-12-11295-2012](https://doi.org/10.5194/acp-12-11295-2012). URL: <http://www.atmos-chem-phys.net/12/11295/2012/>.
- Cao, Hansen et al. (2018). "Adjoint inversion of Chinese non-methane volatile organic compound emissions using space-based observations of formaldehyde and glyoxal". In: *Atmospheric Chemistry and Physics (Discussions)*. DOI: [10.5194/acp-2017-1136](https://doi.org/10.5194/acp-2017-1136). URL: <https://www.atmos-chem-phys-discuss.net/acp-2017-1136/acp-2017-1136.pdf>.
- Müller, J. F., J. Peeters, and T. Stavrakou (2014). "Fast photolysis of carbonyl nitrates from isoprene". In: *Atmospheric Chemistry and Physics* 14.5, pp. 2497–2508. ISSN: 16807316. DOI: [10.5194/acp-14-2497-2014](https://doi.org/10.5194/acp-14-2497-2014).
- Sander, R et al. (2005). "Technical note: The new comprehensive atmospheric chemistry module MECCA". In: *Atmospheric Chemistry and Physics* 5.2, pp. 445–450. ISSN: 1680-7324. DOI: [10.5194/acp-5-445-2005](https://doi.org/10.5194/acp-5-445-2005). URL: <http://www.atmos-chem-phys.net/5/445/2005/>.

- Sandu, A and R Sander (2006). "Technical note: Simulating chemical systems in Fortran90 and Matlab with the Kinetic PreProcessor KPP-2.1". In: *Atmospheric Chemistry and Physics* 6.1, pp. 187–195. DOI: [10.5194/acp-6-187-2006](https://doi.org/10.5194/acp-6-187-2006). URL: <http://www.atmos-chem-phys.net/6/187/2006/>.
- Jöckel, P et al. (2006). "The atmospheric chemistry general circulation model ECHAM5/MESSy1: consistent simulation of ozone from the surface to the mesosphere". In: *Atmospheric Chemistry and Physics* 6.12, pp. 5067–5104. DOI: [10.5194/acp-6-5067-2006](https://doi.org/10.5194/acp-6-5067-2006). URL: <http://www.atmos-chem-phys.net/6/5067/2006/>.
- Jöckel, Patrick, Rolf Sander, and Jos Lelieveld (2004). "Technical Note: The Modular Earth Submodel System (MESSy) – a new approach towards Earth System Modeling". In: *Atmospheric Chemistry and Physics Discussions* 4.6, pp. 7139–7166. ISSN: 1680-7324. DOI: [10.5194/acpd-4-7139-2004](https://doi.org/10.5194/acpd-4-7139-2004).
- Giglio, Louis, Ivan Csiszar, and Christopher O. Justice (2006). "Global distribution and seasonality of active fires as observed with the Terra and Aqua Moderate Resolution Imaging Spectroradiometer (MODIS) sensors". In: *Journal of Geophysical Research: Biogeosciences* 111.2, pp. 1–12. ISSN: 01480227. DOI: [10.1029/2005JG000142](https://doi.org/10.1029/2005JG000142).